Lawrence Berkeley National Laboratory
Recent Work

Title
An Infrared Free Electron Laser for Chemical Dynamics Research Laboratory: Design Report

Permalink
https://escholarship.org/uc/item/9z43g391

Author
Vaughan, D.

Publication Date
1992-04-01

An Infrared Free-Electron Laser

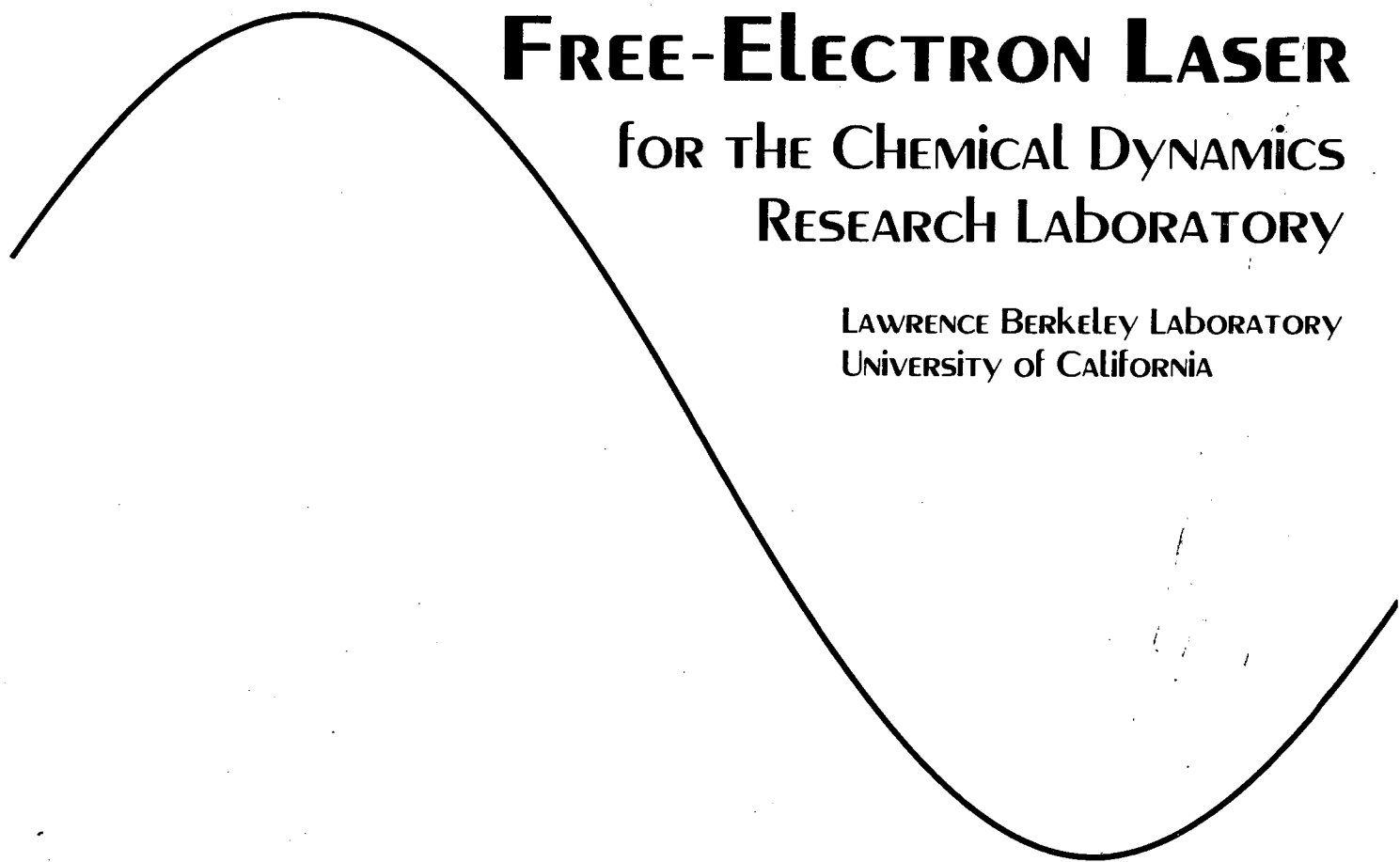## for the Chemical Dynamics Research Laboratory

DISCLAIMER

AN INfRARE D

FREE-ELECTRON LASER

for the Chemical Dynamics
Research Laboratory

LAWRENCE BERKELEY LABORATORY
University of California

A Note on the Contributors

RESEARCH and design studies at LBL that focus on free-electron lasers for various scientific applications are led by the Exploratory Studies Group, headed by Swapan Chattopadhyay of the Accelerator and Fusion Research Division. The FEL design described in detail in Chapters 3 and 4 of this report is the result of efforts by an accelerator physics and engineering team coordinated by Kwang-Je Kim, Deputy Group Leader of the ESG. Contributing to those efforts, and to this document, were Rod Byrns, Swapan Chattopadhyay, Richard Donahue, John Edighoffer, Richard Gough, Egon Hoyer, Kwang-Je Kim, Wim Leemans, John Staples, Brian Taylor, Ming Xie, and the engineering staff of the Advanced Light Source. In addition, Geoffrey Krafft of CEBAF collaborated in some of the simulation studies described in Chapter 4. Chapter 5 describes a control system adapted from a design developed for the ALS by Steven Magyary. Chapter 6, "Safety and Quality Assurance," reflects contributions from many individuals, most of them members of LBL's Environmental Health and Safety Division.

The motivation for this FEL design study was science. The description in Chapter 2 of the scientific opportunities such a machine will offer is a summary of thinking by many scientists interested in combustion research and chemical dynamics; the synthesis is due to Charles Harris, Andrew Kung, and Yuan T. Lee.

Richard Gough, manager of the CDRL project, provided overall leadership for this effort. This report was compiled and edited by Douglas Vaughan.

CONTENTS

1.

OVERVIEW

THROUGHOUT the history of scientific inquiry, electromagnetic radiation has been the dominant tool for probing nature's secrets. Visible light, at first unaltered by human artifice, then refracted by the lenses of telescopes and microscopes, played the leading role until this century. Today, we have learned to interrogate nature's universe, from the cosmic to the subatomic, with radiation of all wavelengths, from x-rays to microwaves. In some respects, though, visible light still plays at center stage. The first lasers were visible-light lasers, and no tunable lasers have yet operated much beyond the red end of the visible spectrum. Practical sources of *broadly tunable, coherent* light, therefore, remain essentially unavailable at ultraviolet and x-ray wavelengths, or at wavelengths beyond the near-infrared.

This situation, however, is soon to change. The development of periodic magnetic devices known as wigglers and undulators, together with advances in particle accelerator technology and design, now offers the possibility of laserlike sources at both longer and shorter wavelengths. Third-generation synchrotron radiation sources, beginning with LBL's Advanced Light Source (ALS), will soon produce radiation in the ultraviolet and x-ray regions that is significantly akin to laser light. Further, free-electron lasers (FELs) have already operated successfully at infrared and microwave wavelengths, and their application to scientific research on a large scale, especially in the infrared, awaits only their incorporation into suitable user facilities.

This document describes such an FEL, proposed as part of the Chemical Dynamics Research Laboratory (CDRL), a user facility that also incorporates several advanced lasers of conventional design and two beamlines for the ALS. The FEL itself addresses the needs of the chemical sciences community for a high-brightness, tunable source covering a broad region of the infrared spectrum—from 3 to 50 μm. All of these sources, together with a variety of sophisticated experimental stations, will be housed in a new building to be located adjacent to the ALS. The radiation sources can be synchronized to permit powerful two-color, pump-probe experiments that will further our fundamental understanding of chemical dynamics at the molecular level, especially those aspects relevant to practical issues in combustion chemistry.

The technical approach adopted in this design makes use of superconducting radio-frequency (SCRF) accelerating structures. The primary motivation for adopting this approach was to meet the user requirement for wavelength stability equal to one part in 10^4. Previous studies concluded that a wavelength stability of only one part in 10^3 could

be achieved with currently available room-temperature technology. In addition, the superconducting design operates in a continuous-wave (cw) mode and hence offers considerably higher average optical output power. It also allows for various pulse-gating configurations that will permit simultaneous multiuser operation. A summary of the comparative performance attainable with room-temperature and superconducting designs is given in Table 1-1.

The FEL described in this report provides a continuous train of 30-ps micropulses, with 100 μJ of optical energy per micropulse, at a repetition rate of 6.1 MHz. The device can also deliver pulses at a cw repetition rate of 12.2 MHz, with a peak power of 50 μJ per micropulse. In both cases, the average optical output power can exceed 600 W. The length of the micropulse can also be varied. For shorter micropulse lengths (from 30 ps to below 2 ps), chirping techniques can be used that will still provide up to 100 μJ per micropulse. Grating techniques can be used to provide longer pulse lengths, up to ~100 ps, but only at the expense of a linear decrease in output power.

A layout of the proposed FEL is shown in Fig. 1-1. The injector prepares a properly bunched electron beam at 6 MeV that matches the phase space requirements of the

Table 1-1. Performance characteristics of FELs based on room-temperature and superconducting linacs.

	Room-temperature linac	Superconducting linac
Accelerator:		
Type	SW side-coupled	SCA
Frequency [MHz]	1300	500
Maximum energy [MeV]	~50	~55
General properties:		
Wavelength, λ [μm]	3–50	3–50
Line width	Transform-limited	Transform-limited
Wavelength stability, $\delta\lambda/\lambda$	10^{-3}	10^{-4}
Intensity stability	0.1	$\leq$0.1
Average optical power [W]	$\leq$20	$\geq$600
Micropulse properties:		
Energy [μJ]	100 (at 50 MeV)	100
Duration [ps]	10–25	30 ($\leq$2 ps via pulse compression)
Repetition rate [MHz]	36.6	6.1
Macropulse properties:		
Energy [J]	0.36	—
Duration	100 μs	>10 ms
Repetition rate	60 Hz	Flexible to cw

2
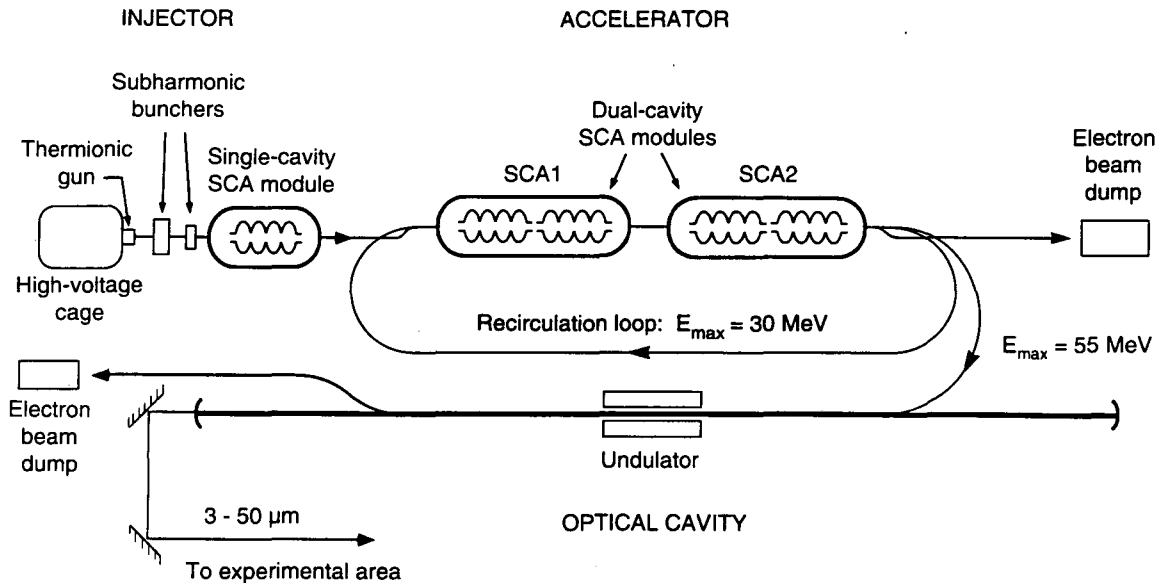
Figure 1-1. Schematic plan view of the infrared free-electron laser, located in the basement vault of the Chemical Dynamics Research Laboratory building. [XBL 921-5511]

accelerator section. The injector includes a thermionic gun; two subharmonic, room-temperature buncher cavities; and a single-cavity, 500-MHz SCRF accelerating module. The accelerator section consists of two dual-cavity, 500-MHz SCRF modules that accelerate the beam to ~30 MeV in a single pass. In the injector and accelerator sections, the SCRF cavities are designed to operate with nominal accelerating gradients of 5 and 5.25 MV/m, respectively.

An achromatic and isochronous beam transport section then recirculates the beam for a second pass through the accelerator section for further acceleration to ~55 MeV. A similar beam transport system then delivers the fully accelerated beam to a 2-meter undulator that forms part of a 24-meter-long optical cavity. Optical power is outcoupled through a hole in one of the cavity end mirrors and transported to the experimental area.

The total estimated cost of the FEL is about $25 million, in FY1992 dollars. This estimate includes all accelerating and optical components, as well as the radio-frequency power and cryogenic systems. It also includes the costs of the associated design and engineering efforts required to make this a reliable user facility, and an appropriate allowance has been made for contingencies, consistent with DOE guidance and practice. The overall project schedule for the CDRL requires five years to complete, with construction beginning in FY1994. The total estimated cost of the FEL, adjusted for inflation in accordance with this schedule, is approximately $31 million in "then-year" or "as-spent" dollars.

2.

INTRODUCTION

On the following pages, we outline some of the research opportunities that await construction of an IRFEL, together with the other facilities associated with the CDRL. Of particular note, this agenda of proposed research imposes special requirements on the performance of the IRFEL; the most important of these are listed in section 2.1.2. In sections 2.2 and 2.3, we then briefly describe the proposed FEL facility and tabulate its most significant performance parameters—parameters that fully meet the needs of the chemical dynamics research community.

2.1 SCIENTIFIC OPPORTUNITIES WITH THE IRFEL

The proposed research program for the CDRL ranges from basic reaction dynamics studies to experiments aimed at providing data that may ultimately lead to reductions in pollution from power plants and automobile engines, at the same time improving their efficiency. The following paragraphs offer a brief review of the research to be made possible with the IRFEL in particular; for a more comprehensive and detailed overview of research opportunities at the CDRL, see the *Combustion Dynamics Facility Scientific Program Summary* [1990].

Over 90% of all energy utilized in the U.S. today is generated by combustion. The National Energy Strategy, the latest Clean Air Act, and many state and local laws require that combustors be designed and operated with unprecedented fuel efficiency and low levels of emitted pollutants. If these requirements are to be met, combustion chemistry and its interaction with fluid flow must be understood at a much deeper level. For example, the oxides of nitrogen (NO_x) and sulfur (SO_x) are major components of pollutants, and industry continues to search for tailor-made fuels that reduce NO_x and SO_x emissions. To aid in the search, accurate critical paths for the oxidation of nitrogen and sulfur compounds in fuels and exhausts must be established. Fundamental information on potential energy surfaces, barrier heights, reaction dynamics, and kinetics will ultimately serve as the foundation for effective NO_x and SO_x abatement strategies.

Soot is another important combustion-generated pollutant—one that is now better understood as a result of recent basic research. Studies of the C–H bond strength in acetylene have now led to a new model for soot formation from acetylene fuel, and more research may someday allow us to control soot formation in this and similar processes.

In short, all combustion-related phenomena—engine knock and CO emission to name but two—are linked to fuel-consuming processes that begin with free-radical reactions. Many different reaction products and many different chemical processes are involved, but clearly an understanding of the fuel cycle cannot be complete without a thorough fundamental study of the chemistry of combustion.

At the CDRL, the scientific research program will focus on gaining a rigorous molecular-level understanding of combustion and other energetic molecular processes. These studies will build foundations of basic knowledge to underlie scientific and technological leadership in the combustion-systems and control-technology industries.

Researchers at the CDRL will explore these topics by

- Determining the structure and chemical behavior of highly reactive polyatomic radicals and unusual transient species.

- Providing microscopic details of mechanisms and dynamics for elementary chemical reactions and primary photodissociation processes.

- Probing the nature of intra- and intermolecular energy relaxation.

- Searching for bond-selective or mode-selective means to modify and manipulate chemical reactivity.

- Establishing a sound theoretical foundation for understanding chemical reactivity and as a basis for experimental efforts.

- Developing novel methodologies and tools to investigate important but currently unsolvable problems in chemical and combustion dynamics.

Input from the user community has been the key to preparing the scientific program for the CDRL. Particularly important roles were played by recent national workshops and symposia, including the Workshop on Opportunities for Chemistry Related Combustion Science (July 1986), the Workshop on Chemical Reaction Dynamics (November 1988), a chemistry user community review (October 1989), and a combustion dynamics workshop in April 1990. These workshops and reviews identified research in combustion and reaction dynamics as critically dependent upon advanced technologies and techniques, including free-electron lasers.

The CDRL will allow, for the first time, the integrated and simultaneous use of dedicated IRFEL and synchrotron-radiation beamlines for pump-probe experiments, as shown conceptually in Fig. 2-1. One mode will use the ALS photon beam as the pump and the IRFEL photon beam as the probe; in this mode, researchers will be able to study the vibrational structure of highly excited and superexcited molecules. The other mode— IRFEL pump and ALS probe—will yield infrared spectra of transient species (combustion diagnostics); new information on ionization potentials and bond energies (reactivity) of transient species; new vibrational spectra of ions; and insight into regioselective photochemistry. Experiments involving new-generation crossed molecular beams can also be integrated with studies using the IRFEL.
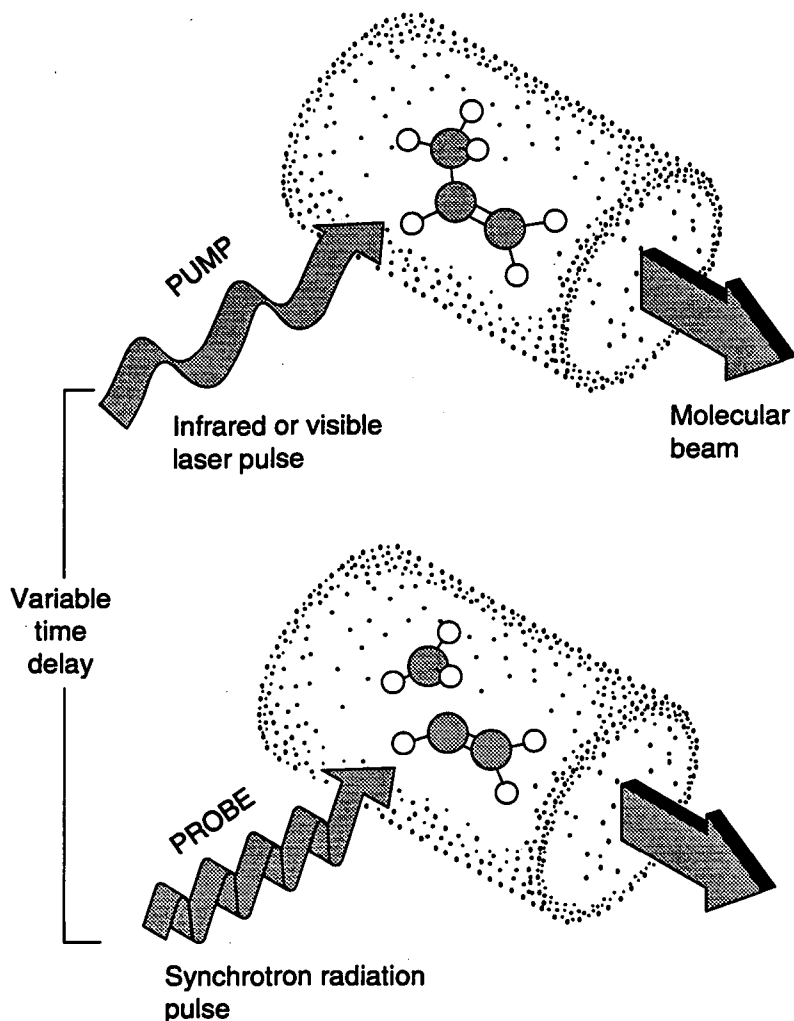
Figure 2-1. Diagram of a "two-color," pump-probe experiment. One source of radiation is used to excite or ionize the molecules in a molecular beam, and a second is used to characterize, or "probe," the resulting species. [XBL 9012-6761B]

2.1.1 Proposed Research

A number of proposals for using the IRFEL, either independently or in conjunction with the other resources of the CDRL, have been put forth, especially at the workshops mentioned above. The following paragraphs summarize just a few of the ideas that have been suggested; their variety and uniqueness underscore the unprecedented opportunities that await the chemical dynamics community.

Infrared Multiphoton Excitation (IRMPE). IRMPE and dissociation under collision-free conditions will be made much more widely applicable by the IRFEL. Thus far, this powerful technique has been used only to study molecular species that can be excited by a CO_2 laser, which has limited tunability. The IRFEL, with its broad tunability, will

expand the range of applicability across the entire periodic table, providing experimental access to practically all molecular species. Using the IRFEL, chemists and surface scientists will be able to probe basic molecular dissociation processes and produce unusual transient species such as organic free radicals, reactive intermediates, and radical-containing clusters.

Important IRMPE applications using the IRFEL include

- Studies of dissociation dynamics and reaction mechanisms of aromatic hydrocarbons, which are abundant in low-grade fuels.

- Selective decomposition of undesirable minor species of molecules in gaseous matter.

- Separation of isotopes.

- Regioselective chemistry, in which vibrational modes at specific sites in a molecule are excited by a properly chosen IRFEL wavelength; these experiments might be combined with photoionization initiated by a VUV beam from the ALS.

Chemistry and Spectroscopy of Surfaces. Surface studies, which will also be enhanced by the IRFEL, are significant because surfaces play an important role in many chemical processes involved in the combustion cycle, including particulate formation and the creation and destruction of pollutants. Optical techniques, being nondestructive and widely applicable, are very attractive for this research.

A relatively new, yet fully developed, technique for surface vibrational spectroscopy—detection of a coherent output whose frequency is the sum of the laser input frequencies—provides vibrational "fingerprints" of surfaces and selective detection of adsorbed molecular species. However, one of the advantages of the technique, its high degree of surface specificity, also hampers its use—another handicap resulting from the narrow tuning range of currently available infrared lasers. The IRFEL would be a major breakthrough in this technique, allowing the study of any molecule or radical. A particularly exciting application, for which few other techniques exist, is spectroscopy of buried interfaces. The picosecond time structure of the beam would also make this technique extremely useful for studies of surface dynamics, as well as for following reaction paths step by step, which is necessary for truly understanding a reaction. The technique is not limited to gas-solid interactions; any interfaces accessible to light could be studied.

Prospects for the IRFEL in semiconductor studies include "hole-burning" experiments, performed with infrared and visible laser light, that would allow the first direct measurements of the coupling between electronic and vibrational degrees of freedom. Another possibility is real-time dynamic study of excitation and relaxation phenomena associated with defects in semiconductors, using the IRFEL and standard lasers.

Vibrational Dynamics of Reactions in Solution. It is currently infeasible to probe vibrational dynamics in solutions on an extremely fine time scale because of the lack of high-power infrared sources at the appropriate vibrational frequencies. The IRFEL, in combination with existing lasers and the ALS, will allow direct studies of such

phenomena, greatly increasing our understanding of how chemical reactions proceed in solution.

Two-Color Threshold Photoelectron Spectroscopy. The CDRL will enable investigation of a set of asymmetric vibrational modes of ground state ions that cannot be excited directly from the vibrational ground state of the neutral molecule; the energy of these modes is unknown for many ions, even some as simple as CO_2^+. The IRFEL beam will be used to excite an infrared mode of the molecule; subsequent ionization by an ALS beam (to which the IRFEL beam is synchronized) will produce the new vibrational state.

Two-Color Fluorescence Studies. Superexcited molecules can dissociate not only into ions, but also into other entities, including electronically excited neutral fragments. This form of decay is usually the sole route below the ionization limit, and it can even compete with ionization several electron volts above the ionization limit. Population of a specific vibrational-rotational state with infrared laser light, followed by further excitation with synchrotron light, can produce a superexcited state whose dispersed neutral decay products fluoresce. This means of studying excited dissociation channels has been established at other synchrotron radiation facilities as a powerful tool in the understanding of predissociation dynamics, and it would be enhanced significantly with the IRFEL.

Spectroscopy of Gas-Phase Free Radicals. Research on gas-phase free radicals will benefit greatly from the combined availability of the ALS and the IRFEL; in fact, the combination has been referred to as a "universal free-radical spectrometer." In these experiments, a cold molecular beam containing a small concentration of radicals will be excited by intense light from the IRFEL, tunable across the absorption spectrum. Since the density of radicals in the beam is not high enough to allow the direct measurement of absorption, a VUV beam from the ALS will be used to detect the infrared-excited states of molecules by selectively ionizing the vibrationally excited radicals. (The VUV photons will not ionize the ground-state radicals.) Then, narrow-line-width infrared lasers will be used for higher-resolution studies at frequencies found with the tunable "search" beam of the IRFEL.

Cluster Energetics and Dynamics. Neutral and ion clusters are formed by pulsed laser desorption of solid material, followed by nucleation and cooling in a high-pressure flow of helium gas. The IRFEL can then be used to excite the clusters, which can subsequently be dissociated or ionized by the ALS or a high-power laser. Spectroscopic and structural information can thus be extracted. Such measurements interact with one another in a very helpful way. Excited-state studies of ion clusters have led to significant insights into the structure and dynamics of transition states.

These studies can dramatically enrich our fundamental understanding of matter interactions, bridging the gap between the gas-phase properties of atoms and molecules and the very different worlds of aerosols, liquids, and solids. The structure, energetics, and kinetics of carbonaceous clusters have important consequences for modeling soot-producing flames. Similar approaches can be used to look at metal clusters, which are of

great fundamental importance and have possible energy-oriented applications in catalysis and other areas.

Optical Diagnostics. At present, optical techniques are recognized as best for probing reacting media in a nonperturbing way. Their application is limited, however, by the fact that the spectroscopic data base necessary for their application exists for very few species containing more than two atoms. At the CDRL, unparalleled resources will be brought to bear on spectroscopic investigations of radicals and other transient species important in combustion. The IRFEL will, for example, allow scientists to excite the internal modes of transient species in a way that simulates the combustion environment. The information obtained will be useful in its own right in expanding our understanding of the properties of these species, but it will also provide a crucial data base for developing optical diagnostic probes for species in flames.

2.1.2 Performance Requirements

Much of the research described above will require the simultaneous use of unique facilities, such as the ALS beamlines, the IRFEL, advanced conventional lasers, and molecular-beam experimental stations. In general, the proposed research will benefit from high wavelength resolution in all the photon sources. In addition, special requirements are imposed on the IRFEL if its full promise is to be realized in pursuing combustion-related fundamental research.

The key characteristics required of the IRFEL include

- A wavelength range from at least 3 to 20 μm

- Wavelength stability equal to a fraction of the resolution

- High peak and average power

- Picosecond pulse duration

- Continuous tunability over any 20% segment of the wavelength range

- Capability to be synchronized to the pulse train of the other CDRL sources

2.1.3 Scientific Horizons for the CDRL

In conclusion, it should be reemphasized that the IRFEL is part of a larger facility, offering an enormous range of research possibilities. Besides providing important —indeed, unique—opportunities for understanding the dynamics of combustion, the available resources will advance the broader field of chemical dynamics in general, and the opportunities for related benefits to science and society are considerable. Combustion studies will be only one of many beneficiaries of newly developed techniques and spectroscopic information that emerge from experiments designed to study dynamical processes in the condensed phase, in novel solid-state materials, semiconductors, metal clusters, inorganic crystals, and polymers. These experiments will further broaden the utility of the facilities and will provide unmatched U.S. leadership in the study of dynamic chemical processes for many years to come.

2.2 FACILITY DESCRIPTION

The electron beam systems of the FEL must be enclosed by a considerable thickness of radiation shielding to protect operators and users of the facility. These shielding requirements impose a significant constraint on the design of the FEL facility. It was necessary to develop a layout that makes economical use of space, yet allows for easy maintenance and, at the same time, leaves the door open to future expansion of the basic system. Accordingly, the FEL will be housed in a concrete vault that also serves as part of the foundation of the CDRL building. The walls and roof of this vault will be formed with approximately 10 feet of conventional, poured-in-place concrete, and access to this area will be carefully controlled and monitored: No access will be possible during operation, and only controlled access will be permitted at other times. Therefore, systems that require occasional tuning or maintenance during operation are located outside the shielded vault area. Components inside the shielded vault include the injector and accelerator sections, all electron beam transport components, the undulator and optical cavity, and the electron beam dumps.

Consideration was given to a variety of layout arrangements, the most attractive of which were variations of two basic configurations, shown schematically in Fig. 2-2. The first is a linear arrangement in which the injector, accelerator, and optical axes are nearly collinear, and in which the electron beam does not reverse direction between the SCRF
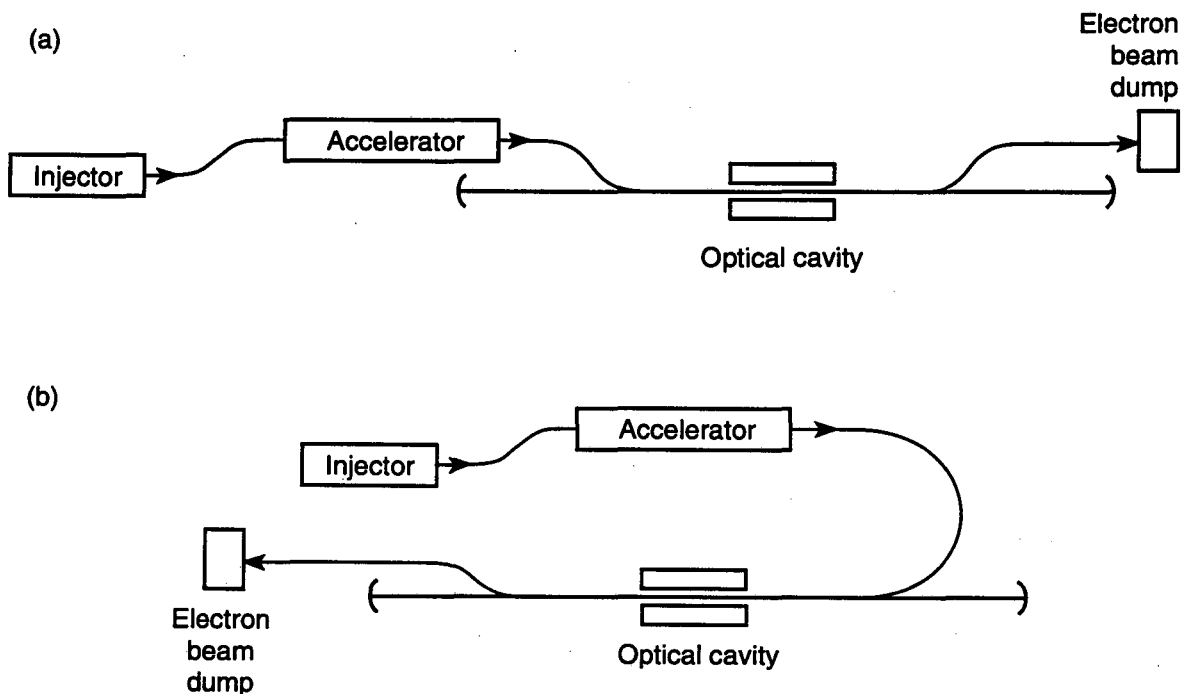

Figure 2-2. Schematic illustrations of (a) linear and (b) folded design configurations for the FEL. [XBL 921-5512]

cavities and the undulator. The second arrangement is a "folded" configuration in which the electron beam is bent by 180° before passing through the undulator section. The folded configuration is more compact and requires considerably less concrete shielding, whereas the linear configuration allows a somewhat simpler electron beam transport system and offers a clearer opportunity to exploit the possibilities of a future second undulator. Preserving this opportunity is very desirable, as it would provide users with two independently tunable infrared sources, driven quasi-simultaneously by the same accelerator. In the linear configuration, with its larger vault, a second full-energy optical cavity could readily be accommodated downstream of the accelerator, parallel to the first cavity. In the folded configuration shown in Fig. 2-2b, a second undulator could be added only in the recirculation loop and optimized for use in the 10- to 50-μm wavelength range. If a second undulator/optical cavity with full-energy capability were considered essential and economically justified, the linear arrangement would be preferred. For reasons of economy, however, we adopted a folded arrangement for the present design. The additional cost of the beam transport system in this configuration is modest and does not offset the savings associated with the smaller vault required for the more compact design.

A layout of the folded FEL configuration is shown in Fig. 2-3, as it would appear inside the vault designed as part of the basement of the CDRL building. Separate shielding is provided at one end of the vault for a closed-loop water system used to operate two beam dumps. These dumps are identical and designed to safely absorb a 55-MeV beam with 800 kW of power. They are housed inside separate concrete bunkers within the main vault. One of these dumps is located near the exit of the accelerator and will be used primarily for commissioning, development, and debugging. The second dump is located near the point where the electron beam exits the optical cavity; this dump will become the primary dump once routine operation is established. Access to the beam dumps will be required only infrequently. They will therefore be kept under separate lock and key, and access will be permitted only to persons accompanied by a designated safety officer.

Space is also required outside the vault for a variety of power, control, and cryogenic systems, together with their associated equipment racks. Most of these systems are shown in Fig. 2-4, which shows a plan view of the basement level of the proposed CDRL building. Five commercially available 500-MHz power amplifiers, each utilizing two klystrons, are located in a 20 × 50 foot room just outside the shielding wall adjacent to the SCRF cavities. This room also houses the associated equipment racks, the klystron crowbar system, and water control systems for thermal stabilization of the room-temperature subharmonic bunchers. The power supplies for these bunchers are located nearby in a separate 20 × 20 foot room. Power from the amplifiers is transmitted to the cavities by means of waveguides. Circulators and "magic tees" are used to prevent reflected power from damaging the klystron amplifiers. An electrical substation that supports all of the building electrical systems (including the FEL) is also located in the basement level of the building, as can be seen at the top of Fig. 2-4.

The cryogenic systems provide both helium at 4 K and liquid nitrogen at 80 K. Commercially purchased liquid nitrogen will be delivered by a house supply line from a nearby storage tank to points throughout the building. The helium will be generated on site by a 600-W refrigerator/compressor system. The helium system consists of the

12
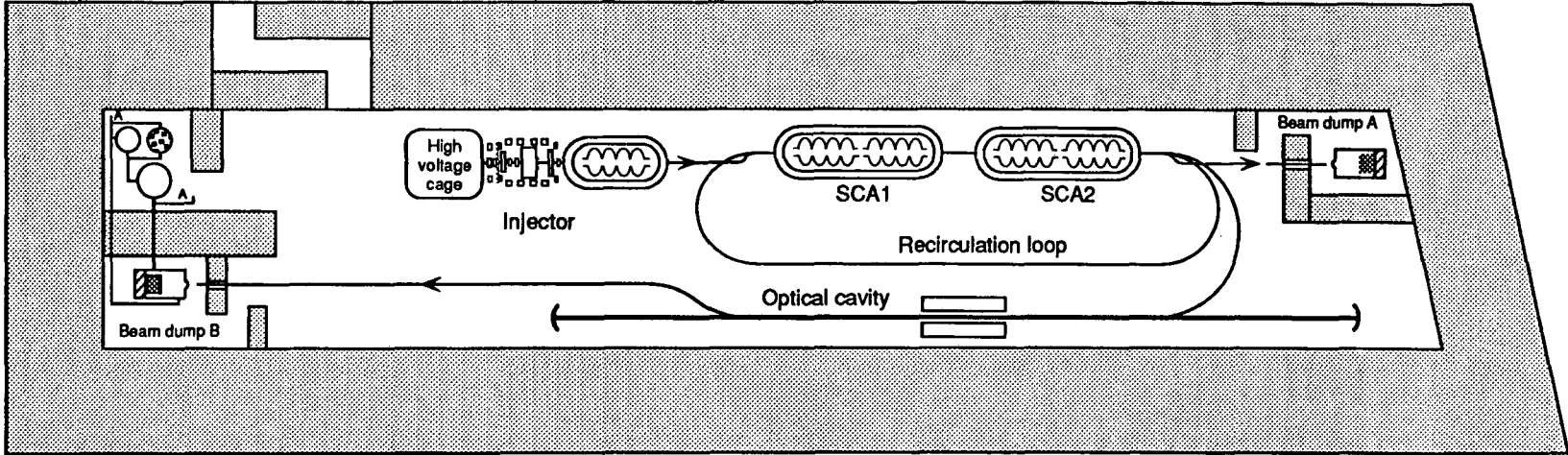
Figure 2-3. Layout of the FEL inside the vault of the CDRL building.

ELECTRICAL SUBSTATION

COLD BOX

MECH.
RM

SERVICE
ELEVATOR

ELEV.
MACH.
RM

MECHANICAL RM

BOILER RM

UP

KLYSTRON RM

POWER
SUPPLIES

VACUUM PUMPS

BEAM
DUMP

IRFEL VAULT

BEAM
DUMP

BASEMENT FLOOR
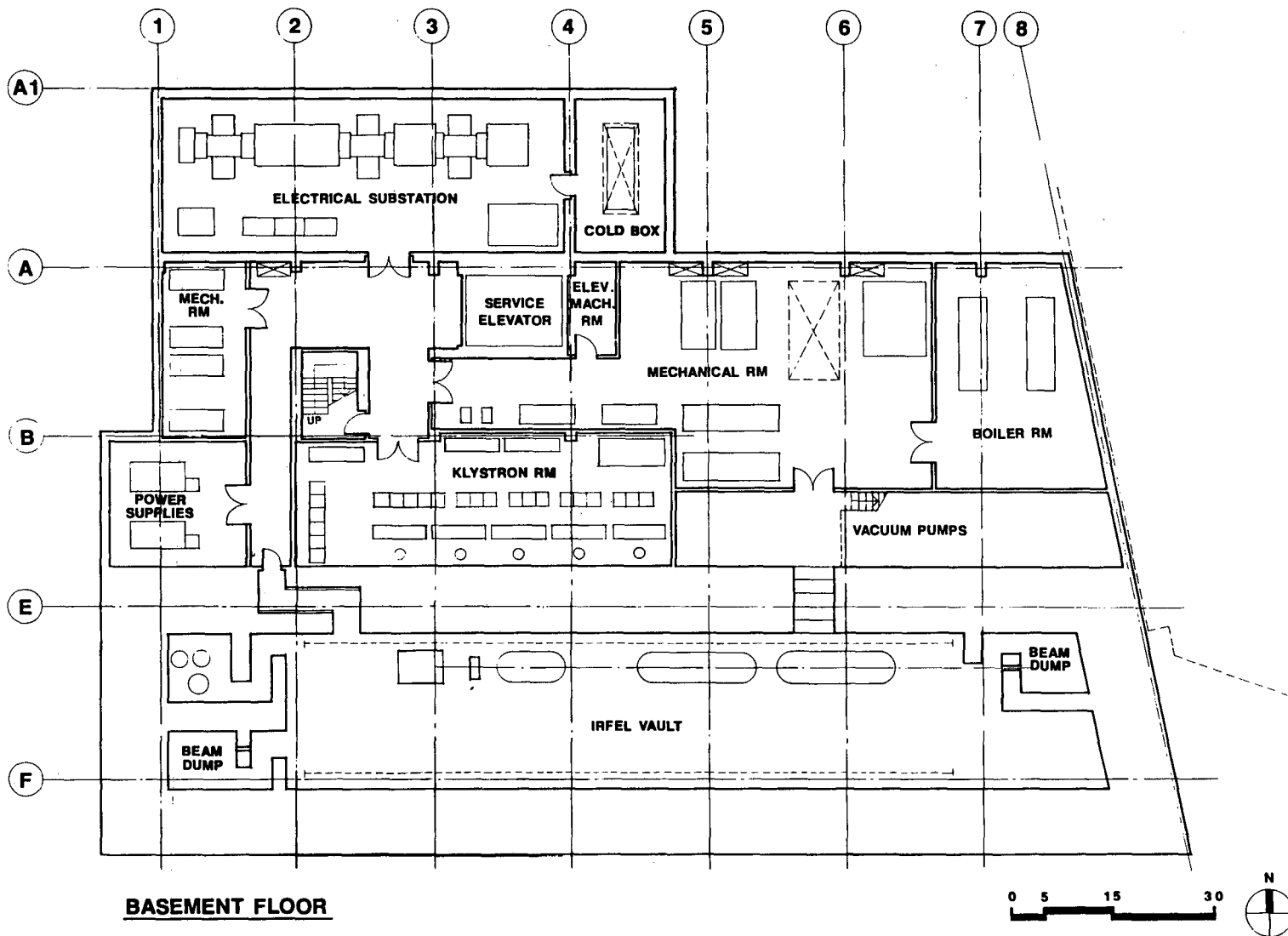
0   5   15   30

N

Figure 2-4. Plan view of the basement level of the proposed CDRL building.

refrigerator/compressor, gaseous helium storage, and connecting cryogenic plumbing. The refrigerator is located in the basement level of the building approximately 70 feet from the cryostats in the vault (see Fig. 2-4). To isolate both noise and vibration, the compressor is located in a separate utility building approximately 200 feet away.

Equipment racks for other systems, primarily the electron beam transport system, are located on the basement level beneath an elevated platform used to support mechanical vacuum pumps servicing equipment in the experimental hall on the main floor. The FEL control room is also located on the main floor of the building, directly above the FEL, and is adjacent to the experimental hall to promote good communication with the users.

2.3 IRFEL PERFORMANCE PARAMETERS

The IRFEL proposed here will provide intense, tunable, and coherent radiation in the infrared region of the spectrum between 3 and 50 μm as direct laser output. Further, this wavelength range can be extended to 1.5 μm, should that be desirable, by optical harmonic generation techniques. Extension to lower energies—wavelengths longer than 50 μm—is also direct and straightforward but will probably suffer from reduced performance and reliability, since such an extension must rely on careful and controlled use of a very-low-energy electron beam.

The general characteristics of the IRFEL are listed in the right-hand column of Table 1-1 in section 1. In addition, the infrared pulses from the FEL will be delivered with a special time structure, allowing synchronization with the ultraviolet pulses from the ALS and with other lasers at the CDRL. The IRFEL pulse structure and its synchronization with the ALS are depicted in Fig. 2-5.

The FEL is driven by a relativistic electron beam, prepared with phase space properties to allow lasing, by an injector, an electron linac, and a carefully designed transport system. The basic electron beam parameters, including the requirements on its stability, are given in Table 2-1. The stability requirements and the other parameters are elaborated on in section 3.1. The constraint on beam energy stability is driven by the required laser wavelength stability $\delta\lambda/\lambda \leq 10^{-4}$, the charge stability by the acceptable laser intensity fluctuations, the repetition rate modulation stability by the fundamental physics of FEL gain, and the steering stability by the requirements on matching in the optical cavity and on directional stability of the FEL output.

The goal of the entire accelerator system is to provide stable, high-quality pulses of electrons to the FEL cavity. The free electrons are produced in a conventional thermionic electron gun. The parameters of the electron gun are listed in Table 2-2. The gun produces electron pulses with a duration of 1.5 ns, at an average current of 1.6 A (2.5 nC of charge); the pulses are squeezed into 33-ps, 30-A bunches by a sequence of three bunchers operating at fundamental frequencies of 61, 171, and 500 MHz. The 500-MHz buncher is a superconducting structure; the other two operate at room temperature. Details regarding buncher design and their operating parameters can be found in section 3.2.

The bunched low-energy electron beam then enters the linac for further acceleration. The design of the main accelerating RF structure is based on the need to maximize

Micropulse rep.
rate = 6.1 MHz

$E_{micro} = 100 \ \mu J$

$P_{avg} \geq 600 \ W$

~30 ps

164 ns

RF linac (500 MHz)
FEL pulse in every 82nd bucket

Every 82nd ALS bucket
Total 328 buckets

ALS (500 MHz)
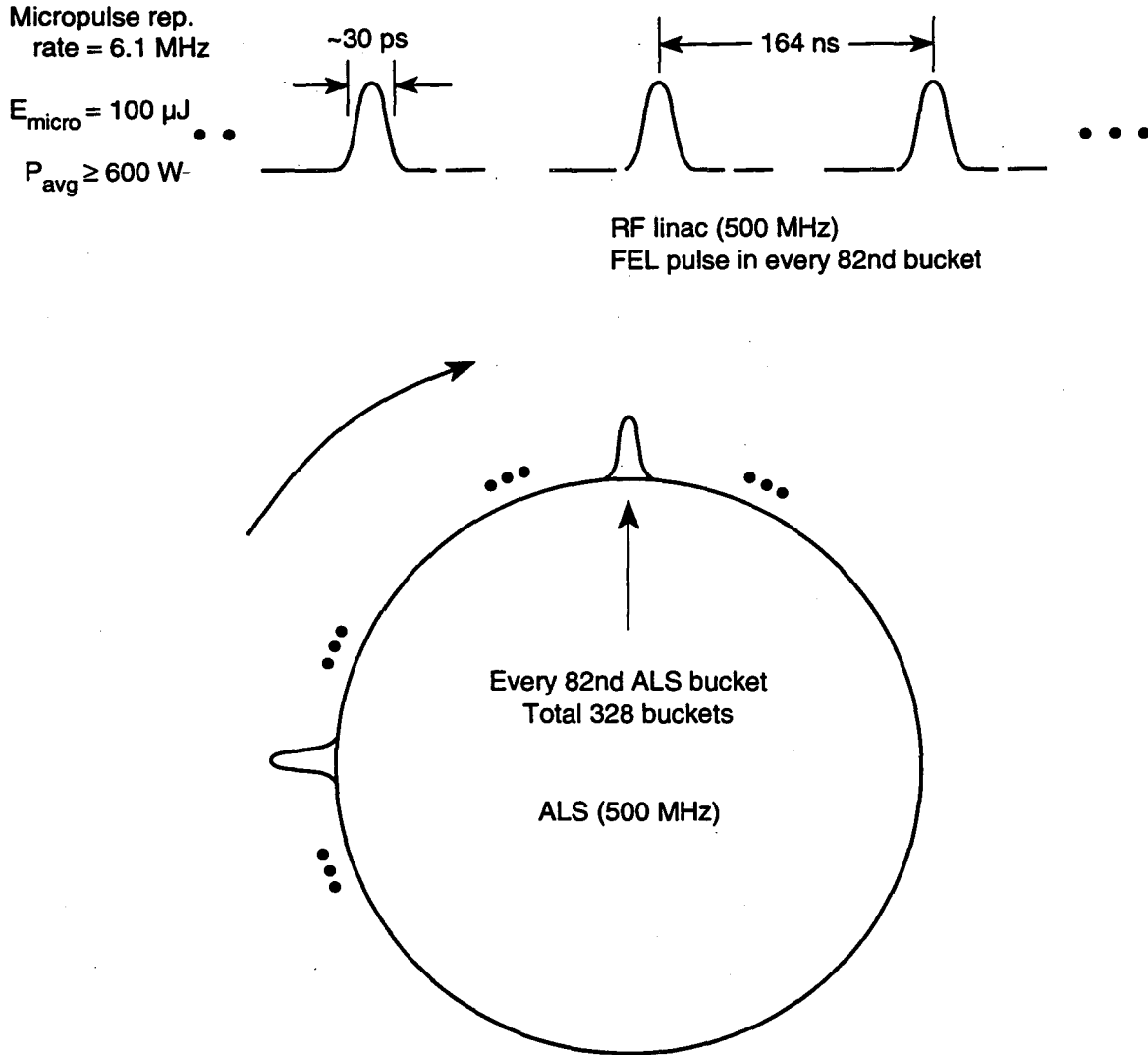
*Figure 2-5. Schematic depiction of the time structure of pulses from the FEL,
showing their synchronization with ALS pulses. [XBL 921-5513]*

Table 2-1. Major electron beam parameters.

Maximum energy [MeV]	55.3
Energy spread, $(\Delta\gamma/\gamma)_{FWHM}$, at 55 MeV [%]	0.35
Micropulse peak current [A]	30–60
Charge per micropulse, q [nC]	1–2
Micropulse duration (FWHM) [ps]	33
Micropulse repetition rate [MHz]	6.1
Normalized emittance, $\gamma\sigma_x\sigma_{x'}$, $\gamma\sigma_y\sigma_{y'}$ [mm·mrad]	11
Stability:[a]	
Beam energy, $\delta E/E$	$\leq 5 \times 10^{-5}$
Charge, $\delta q/q$	<0.05
Freq. modulation of pulse rep. rate, $\delta\omega_{RF}/\omega_{RF}$	$<10^{-7}$
Positional steering, $\delta x/\sigma_x$	≤ 0.1
Angular steering, $\delta x'/\sigma_{x'}$	≤ 0.1

[a]For slow fluctuations on a time scale longer than 1.6 μs or for frequencies lower than 0.1 MHz.

Table 2-2. Electron gun parameters. The gun is a conventional thermionic gun with a Pierce electrode geometry and dispenser cathode.

Voltage [kV]	300
Nominal pulse length [ns]	1.5
Nominal charge/pulse [nC]	2.5
Nominal average pulse current [A]	1.6
Cathode diameter [cm]	1
Gun pulser frequency [MHz]	6.1
Average RF gun power [kW]	6
Average electron current [mA]	15

stability and control. We selected a low-frequency (500-MHz) structure, based on standing-wave superconducting cavities. Standing-wave structures usually allow better control, compared with traveling-wave structures or waveguides. The choice of a superconducting, rather than room-temperature, structure was based on considerations of electron beam energy stability: Continuous-wave (cw) operation of superconducting cavities allows more time for feedback control, as well as a higher feedback loop gain over a narrow bandwidth, and hence assures better stability. This will be discussed in more detail in section 3.1. Further, by use of time gating and other techniques, cw operation will allow the FEL beam to be exploited simultaneously by multiple users.

The frequency choice for the accelerator was again based predominantly on stability considerations: Low frequencies imply large transverse dimensions and a greater cavity volume. Thus, the cavity stores more energy, relative to the beam, and wake-field effects arising from the proximity of metallic boundaries to the beam are minimized—both of which improve stability. The cost penalty due to larger structures is not significant for superconducting cavities. The basic parameters for the superconducting RF linac are summarized in Table 2-3. The linac system design is described in detail in section 3.3, and the details of the associated cryogenic system are covered in section 3.5.

The injector-accelerator complex is responsible for conditioning the electron beam so that it has a suitable distribution around the nominal operating point. However, selecting the good beam core requires further removal of undesirable tails from the energy distribution and the temporal profile, using appropriate filters. These are discussed in sections 3.2 and 3.3. In addition, diagnostic equipment, on-line and off-line, for monitoring the electron beam are distributed throughout the facility and are described in detail in section 3.4. A detailed description of the beam dump, as well as the facility shielding, are provided in section 3.7.

Once suitably prepared, the beam must be carefully transported from the linac exit to the undulator in the optical cavity. This transport must be "achromatic," so as not to introduce any transverse jitter due to magnet fluctuations, and "isochronous," so as not to produce any additional pulse lengthening. In addition, the transport system must match the transverse profile of the electron beam to the optical cavity laser mode, it must be tunable to cover the full 3- to 50-μm wavelength range, and it must bring the beam back to the linac entrance with near-identity transformation for acceleration to higher energies. The transport line is thus constrained by many challenging demands. The design described in section 3.6 meets all of these requirements.

The transported beam interacts with the undulator magnetic field in the FEL optical cavity to generate the optical beam, as shown schematically in Fig. 2-6. The goal of the FEL design is to provide wide wavelength coverage while minimizing operational interruptions. At a fixed electron energy, the wavelength can be tuned between λ_{min} and $\lambda_{max} = 2.28\lambda_{min}$ by varying the magnet gap from 23 to 36 mm. As shown in Table 2-4, the entire wavelength range from 3 to 50 μm can be covered by operating the accelerator at four different energies. By changing the electron beam energy by $\pm 1\%$, one can also fine tune the wavelength by $\pm 2\%$. (In addition, an energy-modulating cavity can be envisioned to switch electron beam energy, and hence the wavelength of the optical beam, on a pulse-to-pulse basis.) Major parameters for the undulator and the optical cavity are summarized in Table 2-4. The physics of the FEL, the design of the undulator

Table 2-3. Superconducting linac parameters.

Type	Niobium cavities
Frequency [MHz]	500
Accelerating gradient [MV/m]	5.25
Unloaded quality factor,[a] Q_0	2×10^9
Shunt impedance/Q, R/Q [Ω/cell]	125
No. of cells/cavity	4
No. of cavities/cryostat	2
No. of cryostats	2
Operating temperature [K]	4
Electron energy at linac exit, first pass [MeV]	30
Voltage/cell [MV]	1.5
Stored energy/cell [J]	5.7
Average electron beam current [mA]	12.2

[a]Loaded quality factor Q_L, with 12 mA of average electron beam current, is expected to be 10^6.
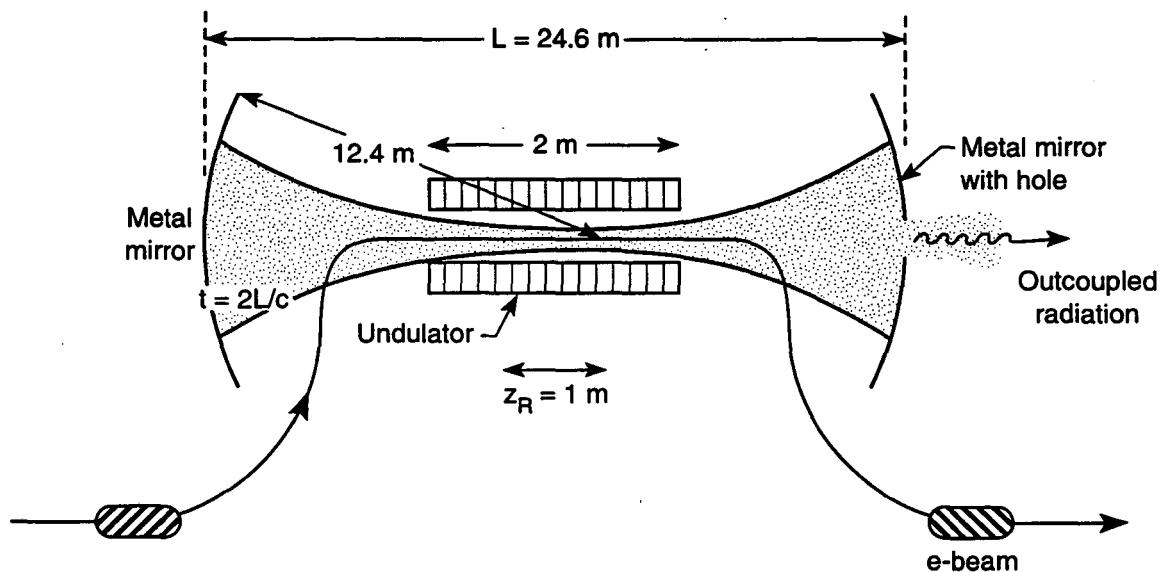
Figure 2-6. Schematic of the FEL optical cavity; z_R is the Rayleigh length and t is the round-trip time for the infrared radiation. [XBL 921-5514]

Table 2-4. Undulator and optical cavity parameters.

Cavity geometrical length [m]	24.6
Raleigh length [m]	1
Total round-trip loss [%]	~10
Hole output coupling efficiency [%]	~50
Single-pass FEL gain [%]	~50
Undulator type	SmCo-steel hybrid (Halbach design)
Undulator period, λ_u [cm]	5
No. of undulator periods	40
Wavelength ranges [μm]for beam energies:	
55.3 MeV	3–6.84
39.1 MeV	6–13.7
27.7 MeV	12–27.4
19.6 MeV	24–54.7

and the optical cavity, and issues related to outcoupling and optical diagnostics are discussed in detail in sections 4.1–4.4.

Every effort has been made in the present design to keep the facility as flexible as possible from an operational point of view. Pulse duration, peak current, and beam energy can all be adjusted over a wide range by varying the gun grid voltage, buncher RF phases, buncher voltages, relative phasing of the accelerator tanks, focusing magnet strengths, etc. These changes can be implemented on-line with relative ease. Our design also allows for the future incorporation of a second undulator and optical cavity—a useful prospect for a multiuser facility.

3.

ACCELERATOR SYSTEMS

WE define accelerator systems as those components of the IRFEL facility responsible for delivering the electron beam to the undulator, together with associated diagnostics and safety systems. This section is devoted to a description of these systems. Underlying their design are a number of accelerator physics issues, most notably stability requirements. These accelerator design issues are discussed in section 3.1. In the next two sections, we then describe the injector and RF linac systems, emphasizing especially the beam physics requirements that constrain the designs. Diagnostics and feedback systems are described in section 3.4, followed by the cryogenic system in section 3.5. The requirement for beam recirculation raises serious accelerator physics issues and imposes severe constraints on the design of the electron beam transport lines of the FEL. Careful beam simulations were required to ensure that neither single-bunch nor multibunch instabilities would threaten the system. The results of these simulations and a description of the beam transport system are included in section 3.6. Finally, section 3.7 describes the shielding requirements, together with the design of the electron beam dumps.

3.1 ACCELERATOR DESIGN ISSUES

Assuring the stability of the optical beam is perhaps the central design issue for the FEL. In line with the demands of experiments planned for the CDRL, fluctuations in the FEL output spectrum and in the intensity must be held to less than 10^{-4} and 10^{-1}, respectively. Accordingly, stringent requirements must be imposed on the stability of the electron beam. These requirements dictate the use of superconducting RF structures and cw operation.

3.1.1 Electron Beam Stability Requirements

The effect of electron beam fluctuations on FEL performance depends upon whether the fluctuations occur on a time scale faster or slower than the response time of the FEL. The FEL response time is given by the cavity Q time, $t_Q = 2L/c\alpha$, where L is the length of the optical cavity and α is the fractional loss per round trip. In the frequency domain, the

characteristic frequency f_Q is related to t_Q by $2\pi f_Q\, t_Q \cong 1$. For the design described here, for which $L = 24.6$ meters and α is typically about 0.1, we have $t_Q \cong 1.6\ \mu s$ and $f_Q \cong 0.1$ MHz.

Thus, we distinguish between slow and fast fluctuations as follows: Slow fluctuations are changes in the electron beam parameters that occur on a time scale longer than 1.6 μs, or, equivalently, at frequencies lower than 0.1 MHz. The effect of such fluctuations on FEL output is equivalent to a dc change in the electron beam parameters. Fast fluctuations, by contrast, are changes in the beam parameters that occur on a time scale shorter than 1.6 μs, or at frequencies higher than 0.1 MHz. The main effect of fast fluctuations is to reduce the gain, in a manner similar to energy spread or emittance.

Here we wish to consider two types of slow fluctuations—fluctuations in the energy of the electron beam and fluctuations in the interval between electron micropulses. Since we require a wavelength stability $\delta\lambda/\lambda$ better than 10^{-4}, and since fluctuations in the electron beam energy E produce optical wavelength fluctuations that are twice as large, the constraint on slow fluctuations in the electron energy is given by

$$\delta E/E < 5 \times 10^{-5} \tag{3-1}$$

Fluctuations in the interval T between electron micropulses is equivalent to fluctuations in the cavity length, or detuning, according to the relation $\delta T = 2\delta L/c$. As described in section 4.1, fluctuations in L should lie in region II of the detuning curve (Fig. 4-1), the width of which is $0.1g\lambda N$ (see section 4.1.2). Thus

$$\delta T < 0.2g\lambda N/c \tag{3-2}$$

where g is the FEL gain per pass, λ is the optical wavelength, and N is the number of undulator periods. Note that the constraint on fluctuations in T is a constraint on the variation in micropulse arrival times. It is thus equivalent to a constraint on the error in the RF frequency:

$$\frac{\delta\omega_{RF}}{\omega_{RF}} = \frac{\delta L}{L} < \frac{0.1g\lambda N}{L} \tag{3-3}$$

Taking $g = 0.3$, $\lambda = 3\ \mu m$, $N = 40$, and $L = 24.6$ m, we find

$$\frac{\delta\omega_{RF}}{\omega_{RF}} < 10^{-7} \tag{3-4}$$

Fast fluctuations in the electron beam energy produce the same effects as does energy spread. Accordingly, the tolerance on fast fluctuations in the beam energy is equivalent to the tolerance on the energy spread, which in our case is 5×10^{-3}. The tolerance on fast fluctuations in the micropulse timing, $\delta T/T$, is determined by requiring that the overlapping of the optical beam with the electron beam be accurate to within one-tenth of the pulse length, that is, $\delta T/T \le 2 \times 10^{-5}$. The tolerances on fast fluctuations are therefore much less stringent than those on slow fluctuations.

User requirements also demand that intensity fluctuations in the optical pulses be minimized. To limit the intensity fluctuations caused by charge fluctuations in the electron beam to less than 5%, we require

$$\delta q/q < 0.05 \tag{3-5}$$

where q is the bunch charge.

Finally, transverse stability of the electron beam must be maintained to ensure the corresponding stability of the output. The requirement imposed by the user community on the fluctuations in the position δx and the angle $\delta x'$ of the electron beam are

$$\delta x \le 0.1\,\sigma_x \tag{3-6}$$

and

$$\delta x' \le 0.1\,\sigma_{x'} \tag{3-7}$$

where σ_x and $\sigma_{x'}$ are the rms values of the beam's transverse size and angular divergence, respectively.

3.1.2 Comparison of Superconducting and Room-Temperature Designs

Figure 3-1 is a schematic representation of an RF cavity interacting with an electron beam and an external power source. Neglecting for a moment the feedback loop, and writing the field quantities in the form

$$e^{i\omega t} \times (\text{quantities varying slower than } \omega) \tag{3-8}$$

the cavity voltage V satisfies

$$\left(\tau\frac{d}{dt} + 1 + iQ_L\frac{\omega-\omega_0}{\omega_0}\right)V = \frac{2\beta}{1+\beta}(V_+ - Z_0 I_B) \tag{3-9}$$

with

$$\beta = \frac{Z_c}{Z_0} = \frac{Q_0}{Q_{ext}}$$

$$Q_L = \frac{Q_0}{1+\beta}$$

$$\tau = \frac{2\,Q_L}{\omega_0}$$

$$V_+ = \sqrt{2\,Z_0\,P_+}$$
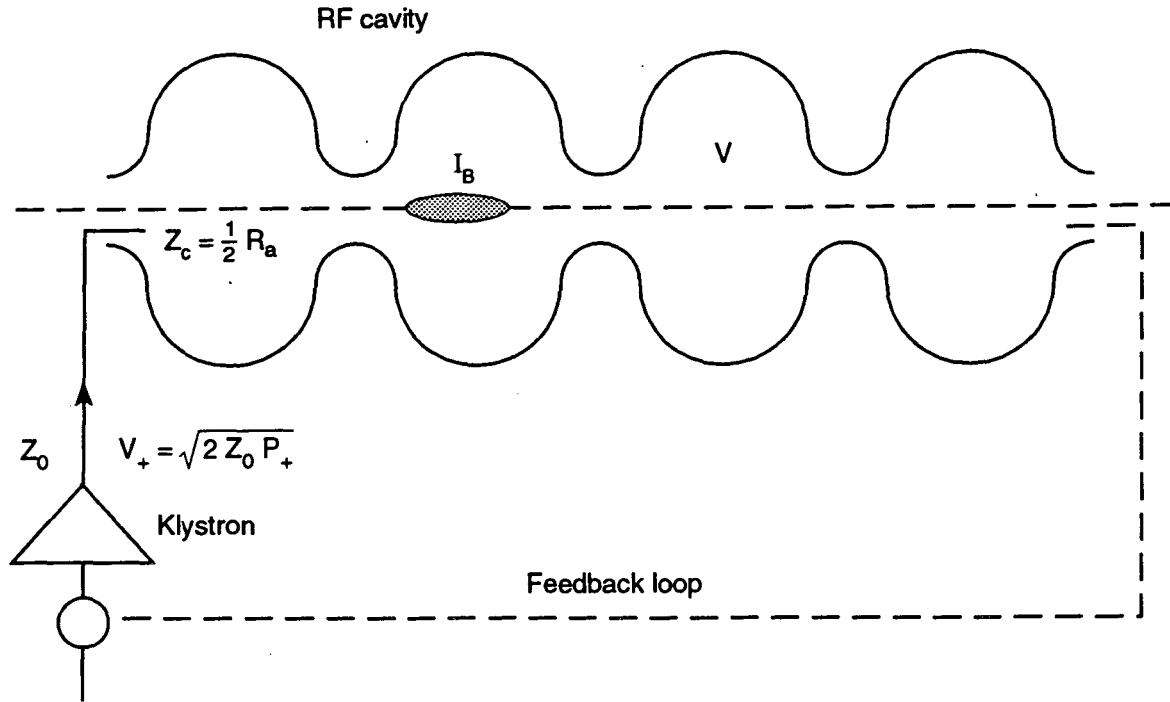
Figure 3-1. A schematic of an RF cavity. V = peak cavity voltage; I_B = beam current; $R_a = 2Z_c$ = cavity shunt impedance; Z_0 = wave impedance of the input line; V_+ = voltage of the input wave; P_+ = klystron power. [XBL 921-5515]

In the above, τ is the cavity decay time, Q_L is the loaded Q, Q_0 is the unloaded Q, Q_{ext} is the external Q, ω is the RF frequency, ω_0 is the resonance frequency, β is the coupling coefficient, Z_0 is the wave impedance of the input guide, Z_c is the cavity impedance, V_+ is the voltage wave traveling toward the cavity, I_B is the beam current, and P_+ is the klystron power. We assume that the reflected wave, $V_- = V - V_+$, is fully absorbed as it passes through a circulator (not shown in the figure). The power dissipated in the cavity wall is

$$P_c = \frac{1}{2}\frac{V^2}{Z_c} \tag{3-10}$$

The time scale for the RF cavity response is given by the cavity decay time τ or by the cavity bandwidth

$$\Delta f_c = \frac{1}{2\pi\tau} \equiv \frac{f_c}{2\,Q_L} \tag{3-11}$$

Note that Δf_c and τ are the RF cavity equivalents of f_Q and t_Q, respectively, for the optical cavity discussed in the previous section. For slow fluctuations, that is, those for which $f \ll \Delta f_c$, the derivative term in Eq. 3-9 can be neglected. For operation at the resonance, $\omega = \omega_0$,

$$V = \frac{2\beta}{1 + \beta} (V_+ - Z_0 I_B) \qquad (3\text{-}12)$$

The optimum value of the coupling coefficient β is determined by requiring that there be no reflected wave, that is, that $V_- = 0$. Thus,

$$\beta = 1 + \frac{2Z_c I_B}{V} = 1 + \frac{P_B}{P_c} \qquad (3\text{-}13)$$

where $P_B = I_B V$ is the power gained by the electron beam in the cavity. For a room-temperature cavity, P_B/P_c is usually small, so that $\beta \cong 1$. On the other hand, P_c is negligible for the superconducting cavities described in section 3.3, so that $\beta \gg 1$.

The fluctuations δV in the cavity voltage due to fluctuations in the beam current I_B, when $f \ll \Delta f_c$, is [Krafft et al., 1990]

$$\frac{\delta V}{V} = -\frac{\beta - 1}{\beta + 1} \frac{\delta I_B}{I_B} \qquad (3\text{-}14a)$$

The factor $(\beta - 1)/(\beta + 1)$ is referred to as the coefficient of the slow disturbance before feedback. The voltage fluctuation after feedback is given by

$$\frac{\delta V}{V} = -\frac{1}{G} \frac{\beta - 1}{\beta + 1} \frac{\delta I_B}{I_B} \qquad (3\text{-}14b)$$

The quantity $(1/G)[(\beta - 1)/(\beta + 1)]$, referred to as the coefficient of slow fluctuation after feedback, is a measure of the achievable RF stability.

Feedback reduces the voltage fluctuations. The gain characteristics of the loop are as follows: The peak gain G within the fluctuation bandwidth Δf ($= \Delta f_c$ for the slow fluctuation) must be sufficiently large to reduce the fluctuations to an acceptable level. At higher frequencies, the gain generally falls off as $1/f$, and it must decline to unity at the frequency f_1, where the loop phase shift becomes $180°$. Several factors contribute to the loop phase shift, including the length of the loop, high-order-mode resonances, etc. It turns out that f_1 is about 1 MHz for the cases we are interested in [Simrock et al., 1990]. This is illustrated in Fig. 3-2. The allowable peak gain G is therefore

$$G = \frac{1 \text{ MHz}}{\Delta f_c} \qquad (3\text{-}15)$$

The cavity bandwidth Δf_c is much narrower in the superconducting case than in the room-temperature case. Thus, although the voltage fluctuation (Eq. 3-14a) is larger in the superconducting case, the feedback is much more effective, leading to stability that is better by an order of magnitude compared with the room-temperature case.

Equation 3-14a is not applicable when the fluctuations are faster than the cavity response, that is, when $f \gg \Delta f_c$. In this case, let δq be the fluctuation in the bunch charge
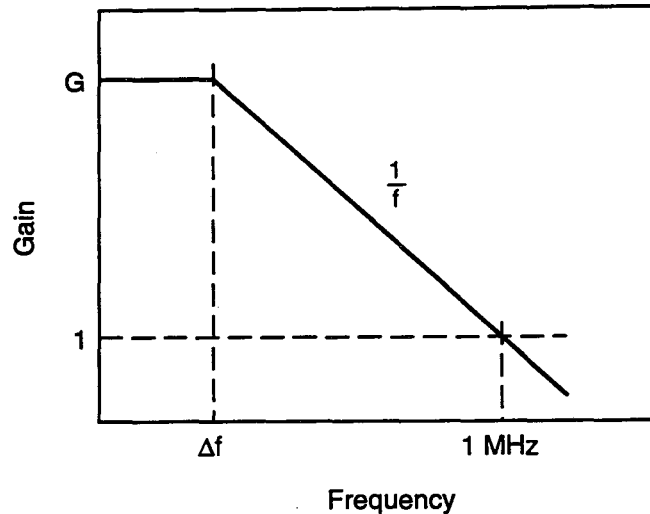
Figure 3-2. Typical Bode plot for the RF feedback circuit, illustrating the 1/f roll-off of the gain. The gain must decrease to unity at f ≅ 1 MHz to ensure the stability of the feedback loop. [XBL 921-5517]

passing through the cavity. The voltage fluctuation calculated from the fluctuation of the stored energy is

$$\frac{\delta V}{V} = \left(\frac{1}{2} \frac{R}{Q} \frac{\omega_0 \, q}{V} \right) \frac{\delta q}{q} \qquad (3\text{-}16)$$

where $R/Q \equiv 2Z_c/Q_0$ is the shunt impedance. The quantity within the parentheses is referred to as the coefficient of the fast disturbance. In general, this turns out to be a small number, so that feedback is not required for fast fluctuations. The coefficient of the fast fluctuation scales as ω_0^2. For the superconducting case, an accelerator system based on a lower RF frequency ω_0 is feasible because of the low cavity loss P_c. Thus, the superconducting option is also superior also from the point of view of controlling fast fluctuations.

Table 3-1 provides a quantitative comparison of the stability performance of different RF options: (i) the previously documented CDRL FEL design using room-temperature 1.3-GHz structures [*Conceptual Design Report: Chemical Dynamics Research Laboratory,* 1991]; (ii) the FEL design documented here, which uses superconducting 0.5-GHz structures; (iii) a possible CDRL FEL design using superconducting 1.5-GHz structures; and (iv) the CEBAF accelerator design using superconducting 1.5-GHz structures. For the room-temperature design, the coefficient of the slow disturbance before feedback is about 0.1, the allowed gain G is about 14, and the coefficient of the slow disturbance after feedback is $0.1/13.8 \cong 7.2 \times 10^{-3}$. Assuming the current fluctuation to be about 0.1, we find that the fluctuations in the RF voltage can only be reduced to about 10^{-3}. For the superconducting CDRL design, the achievable stability should be $0.1 \times 2.5 \times 10^{-4} \cong 2.5 \times 10^{-5}$, which is smaller by more than an order of magnitude and also meets the constraints imposed by user requirements. The fast

Table 3-1. Accelerator performance parameters for four FEL designs.

	CDRL RT 1.3 GHz	CDRL SC 0.5 GHz	CDRL SC 1.5 GHz	CEBAF SC 1.5 GHz
RF wavelength [m]	0.231	0.600	0.200	0.200
Q_0	2.0×10^4	2.0×10^9	2.0×10^9	2.4×10^9
R/Q (per cell) [Ω]	289	125	100	96
R (per cell) [MΩ]	5.78	2.5×10^5	2.0×10^5	2.3×10^5
Accelerating gradient [MV/m]	8	5.25	6	5
Voltage per cell [MV]	0.923	1.50	0.600	0.500
Power dissipated per cell [W]	1.47×10^5	9.0	1.80	1.09
Stored energy per cell [J]	0.361	5.73	0.382	0.276
Beam current [mA]	36	12	12	0.8
Power transferred to beam (per cell) [kW]	33.2	18.0	7.2	0.40
Coupling parameter, β	1.23	2000	4000	370
Loaded Q	8.99×10^3	9.99×10^5	5.00×10^5	6.48×10^6
Filling time [μs]	2.2	636	106	1370
Cavity bandwidth [kHz]	72.3	0.250	1.50	0.116
Coeff of fast disturbance (at 1 nC)	1.28×10^{-3}	1.31×10^{-4}	7.85×10^{-4}	9.04×10^{-4}
Allowed gain, G	13.8	4000	666	8630
Coeff of slow disturbance				
before feedback	0.1	1.0	1.0	1.0
after feedback	7.2×10^{-3}	2.5×10^{-4}	1.5×10^{-3}	1.2×10^{-4}

fluctuations are also smaller for the 0.5-GHz superconducting option because of the lower RF frequency.

The third column of Table 3-1 shows that the slow fluctuations after feedback for a possible CDRL design using superconducting structures of higher frequency are about $0.1 \times 1 \times 1/700 = 1.4 \times 10^{-4}$, which does not meet the requirement of Eq. 3-1. The stability improves for the CEBAF design (column 4), which also uses 1.5-GHz superconducting cavities, because the beam current for nuclear physics applications is

lower. The beam current enters into the stability because it influences the value of β (Eq. 3-13) and thus limits the maximum gain G in light of Eq. 3-15.

3.2 INJECTOR SYSTEM

The injector system is of critical importance to the overall performance of the FEL. The brightness, energy spread, current, and bunch length of the electron beam are all primarily determined by the performance of the injector. In the injection system, space charge terms are large, and the growth of the transverse and longitudinal emittances are most significant. The requirements at the end of the injector, based on overall system requirements, are summarized in Table 3-2.

3.2.1 Design Approaches

We evaluated several design approaches in light of the performance demands of Table 3-2. The design ultimately adopted uses a conventional thermionic cathode, subharmonic bunchers, and fundamental acceleration. This arrangement is shown schematically in Fig. 3-3. It is possible to meet or exceed all of the design requirements with this approach. The injector output characteristics are given in Table 3-3.

An alternative approach that was considered would have made use of an RF superconducting cavity with an internal photocathode. This approach entails using a cryogenic photocathode in a very-high-gradient half-cell superconducting structure. The laser pulse length would be 50–100 ps, and the accelerating gradient would be 10–15 MV/m (15–20 MV/m at the photocathode). This approach was attractive from a beam physics point of view, for it would have eliminated most of the difficulties associated

Table 3-2. Injector output requirements, based on overall system performance requirements.

Energy stability	5×10^{-5}
Peak current, at 2 nC [A]	>60
Charge [nC]	1–2
Bunch length [ps]	≤33
Normalized rms emittance [mm·mrad]	<25
Energy spread	
at 30 MeV	≤0.5%
at 6.4 MeV	<120 keV (FWHM)
Energy [MeV]	>6
Bunch frequency [MHz]	6.10 (499.65/82)
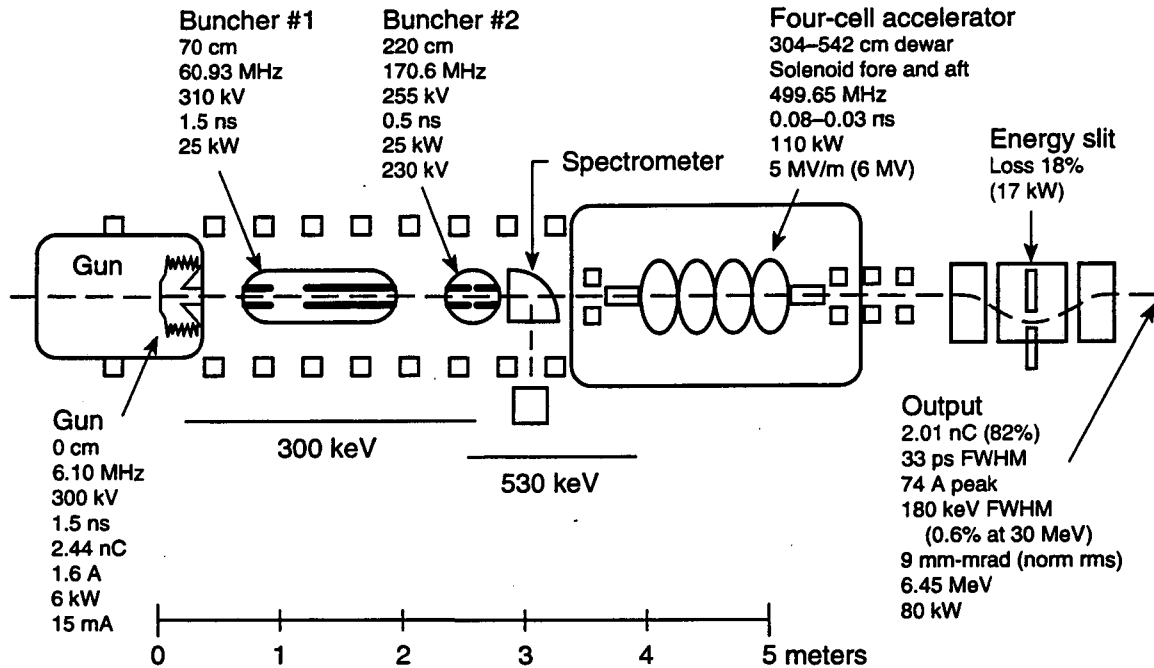
Figure 3-3. Schematic of the FEL injector. [XBL 922-5620]

Table 3-3. Performance characteristics of the FEL injector.

Charge per bunch [nC]	2.0
Bunch length [ps]	33
Average current [mA]	12
Peak current [A]	74
Bunch repetition rate [MHz]	6.10
Energy spread, at 30 MeV	180 keV or 0.6%
Normalized rms emittance [mm·mrad]	9
Energy [MeV]	6.45
Power (after slits) [kW]	80
Loss on slits	18% (17 kW)

with space charge forces in the adopted design. However, both the cryogenic photocathode and the superconducting structure suffer from uncertain lifetimes. The known mechanisms of contamination are suppressed at cryogenic temperatures, but photocathode and superconducting structure lifetimes have not been demonstrated in this

configuration. Work is in progress at the University of Wuppertal [Chaloupka et al., 1988] and at CEBAF on developing this technology, but it is likely to remain insufficiently advanced to serve as the basis for a reliable user facility for the next three to five years.

The third plausible approach would have incorporated a high-voltage dc photocathode just upstream of the second buncher in the design of Fig. 3-3 The dc gun voltage would be 500–600 kV, with a gallium arsenide photocathode and a 100- to 300-ps laser pulse. This injector configuration is also being developed at CEBAF [Sinclair, 1987] and the University of Illinois [D. Engwall, Ph.D thesis in progress]. This technology may be mature within one or two years, though many uncertainties remain.

Both photocathode approaches require lasers with very high average power. Although such lasers have been successfully demonstrated, the laser cost is high and the reliability is lower than needed for a user facility. A backup laser would be required to ensure the requisite reliability.

3.2.2 Injector Design and Modeling Results

The adopted injector design has several unique properties. First, it operates cw at a high average current (15 mA). The charge per bunch can be as high as 2.5 nC or 1.6×10^{10} electrons (allowing for a 20% loss before reaching the accelerator). The frequency (499.65 MHz) is lower than the typical injector (1300–3000 MHz), and the gun voltage is higher than the typical 100–150 kV. The accelerating structure is superconducting, and because it is to be an "off-the-shelf" design, the structure is not graded for β and the entrance beam pipe is large and long. This leads to large fringe fields at the entrance to the accelerating structure that decelerate the beam by about 200 keV before acceleration begins. Also, in this region, all magnetic fields are excluded by the superconductor. Therefore, to avoid significant space charge growth, the beam energy must be about 500 keV before the beam enters this region. Accordingly, the gun voltage is high and the second buncher provides additional acceleration.

The gun bunch frequency was picked to synchronize with the ALS synchrotron radiation pulses, which have a 12.19-MHz frequency when the storage ring is filled with eight equally spaced electron bunches. Half this frequency (6.10 MHz) was chosen for the injector gun to reduce the required RF power. The buncher frequencies are then the 10× and 28× multiples of the 6.10-MHz bunch frequency. The first buncher frequency was chosen such that the entire gun charge, assuming a 1.5-ns-wide pulse and 300-ps rise and fall times, would fall within ±20° of phase. The frequency of the second buncher is about three times that of the first, owing to the ~3× bunching between bunchers. The four-cell accelerating structure is matched to the ALS frequency of 499.65 MHz.

The gun provides 15 mA in a pulse train at 300 kV. As mentioned above, the bunches are 1.5 ns wide (FWHM), with rise and fall times (10–90%) of 300 ps. These characteristics produce a 2.4-nC bunch with a peak current of 1.6 A. A 2-cm^2 gridded thermionic cathode provides the needed current. TRW has built and tested a gun that runs at 500 kV with this bunch format. Their pulser uses step recovery diodes to produce the fast rise and fall times. Their pulser and gun designs meet the present FEL

requirements, and they have demonstrated a higher voltage capability than required here [Lazar et al., 1991].

Both bunching cavities use quarter-wavelength coaxial cavities in the fundamental TEM mode, where the center coax is the beam pipe, with a gap at one end (see Fig. 3-4). The lengths of the first and second bunchers are 123 and 44 cm, respectively.

The four-cell superconducting structure is modeled after the DESY four-cell structure built by Dornier [Willeke and Proch, 1991]. We also adopted the design gradient of 5 MV/m and Q_0 of 2×10^9 for the present design. To ensure good transport into the four-cell structure, a solenoid was added within the cryostat, around the stainless-steel thermal isolation beam pipe near the junction to the superconducting niobium. This solenoid is shielded from the RF superconductor to avoid quenching problems. It will run at a few hundred gauss and will be turned off during cool-down. It will put an extra 10 W (approximately) into the liquid nitrogen shield.

We used PARMELA as the primary computer tool to investigate the phase space development of the electron beam as it traverses the injector. URMEL was used to generate the fundamental-mode field profile. PARMELA uses the first 40 spatial harmonics derived from URMEL to calculate all of the RF fields.

Simulations show a low-energy tail on the bunch from the injector that must be removed before further acceleration. A chicane with a high-power energy slit capable of scraping up to 30 kW, or 25%, of the beam is therefore needed between the injector and the accelerator. This chicane must produce a dispersion of 30 cm per fractional momentum change at the location of the slit. The layout of the chicane and the slit is shown in Fig. 3-5. Positioned three standard deviations from the beam axis, the slit removes electrons in the tail of the spectrum more than 150 keV below the mean of
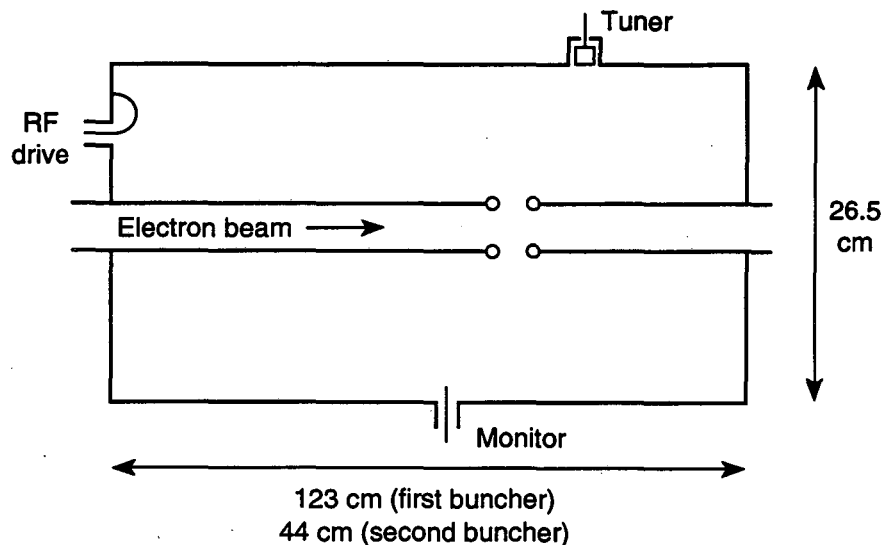

Figure 3-4. Schematic of the first and second subharmonic bunchers. [XBL 921-5561]
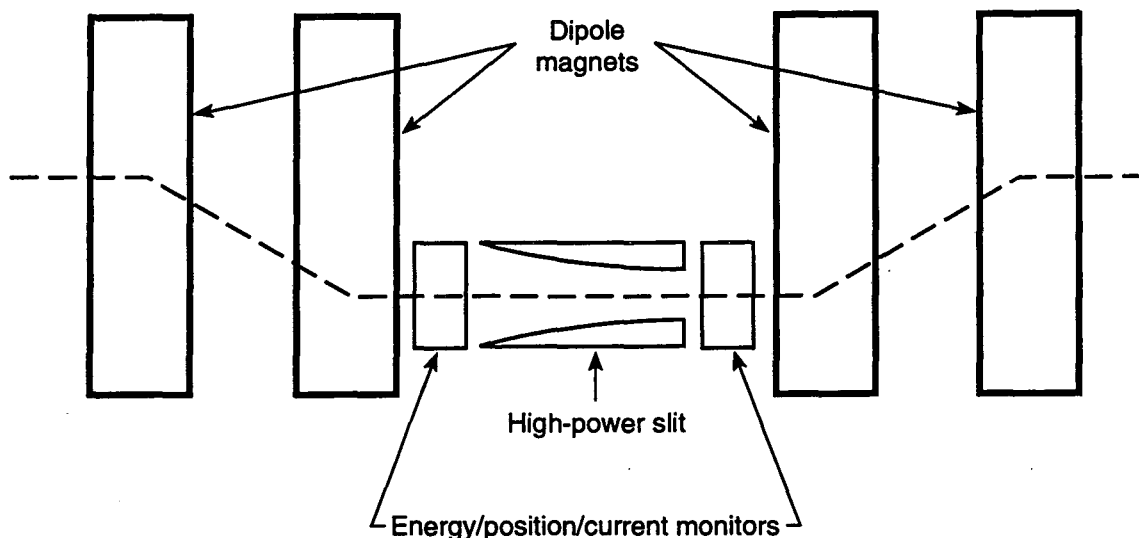
Figure 3-5. Schematic of the chicane at the injector exit, showing the configuration of the high-power slit. [XBL 921-5562]

the energy distribution. The high-power slit is an adaptation of the water-cooled copper photon stops within the ALS ring, which are capable of handling 500 W/cm^2 [DiGennaro and Swain, 1990]. The slit is approximately 1 meter long, and its cross-sectional shape conforms to a 15° arc of a 4-meter-radius circle, with one end tangent to the beam. The power density will thus remain everywhere well below the 500-W/cm^2 limit. Local x-ray shielding will be provided, but the 6.4-MeV beam will produce no neutrons and no component activation.

Figure 3-6 shows the PARMELA output for the injector, both up- and downstream of the energy slit (Figs. 3-6a and 3-6b, respectively). Downstream of the slit, the energy spread is 180 keV. When the cosine curvature of the RF acceleration to 30 MeV is folded in, the energy spread becomes 0.6% at the FEL. The bunch is 33 ps long (FWHM), with a peak current of 74 A, a bunch charge of 2.01 nC, and a normalized rms emittance of 9 mm·mrad. The beam energy is 6.45 MeV, which corresponds to a beam power of 80 kW.

3.2.3 Sensitivity/Stability Analysis

Using PARMELA we performed a sensitivity/stability analysis of the injector to determine, among other things, the phase and amplitude requirements for the bunchers and four-cell structure. Each parameter was varied in turn, while all other parameters were held fixed, to establish how large a deviation could be tolerated in that single parameter. Limits on the tolerable deviations were determined by the tolerances on the injector output; injector tolerance requirements were dictated in turn by stability requirements on the electron beam and, ultimately, the FEL. The first column in Table 3-4 lists these injector output requirements. As will be seen below, voltage stability, bunch timing stability, and the FEL detuning curve imposed the tightest limits on the injector parameters.
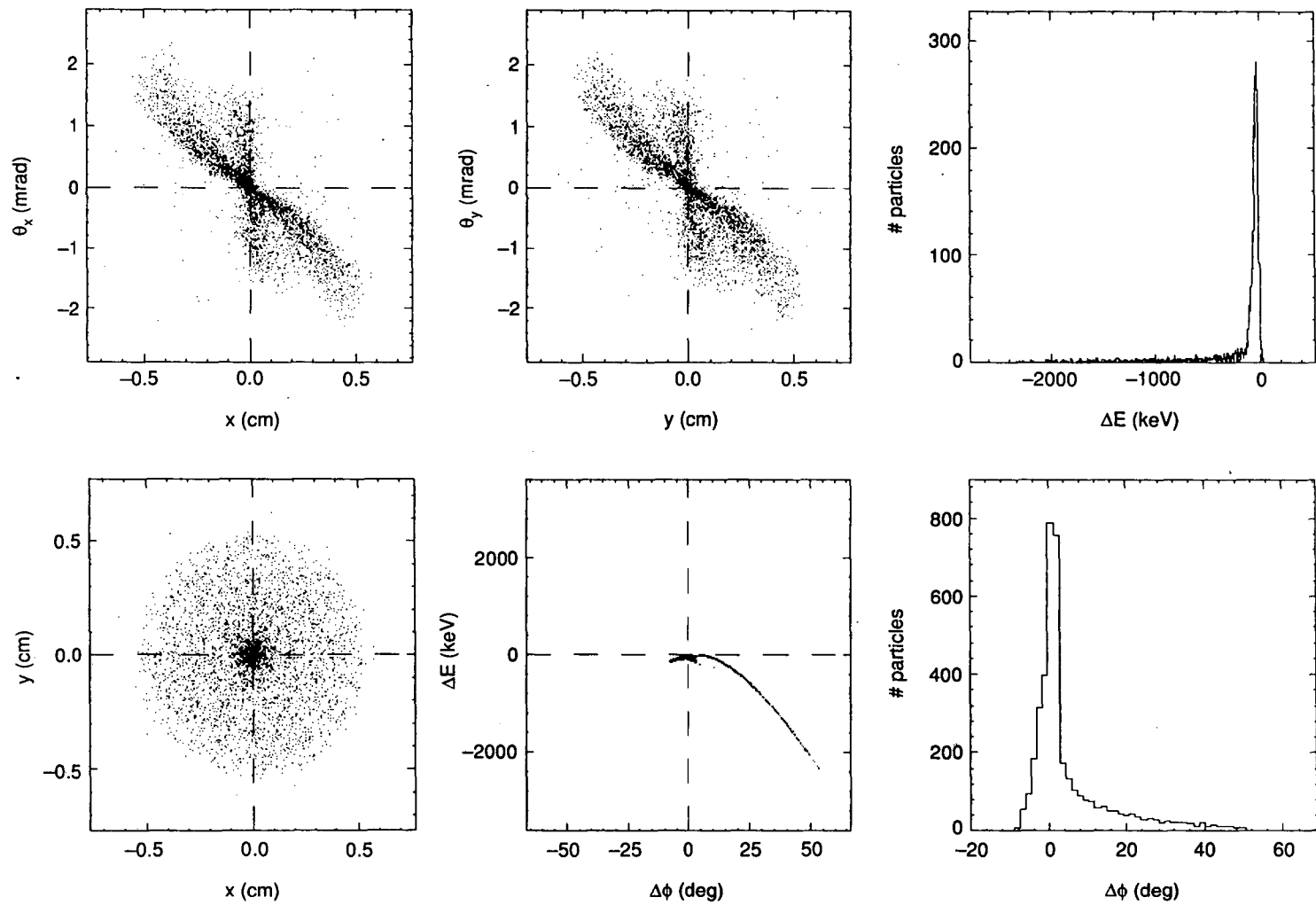
Figure 3-6a. Electron beam characteristics at the injector exit, upstream of the slit. The scatter plots at the upper left and upper center show the x and y phase space profiles, and the plot at the lower left shows the x-y beam profile. The plot at the lower center depicts the energy as a function of particle phase (z position). At the far right, histograms display the energy and phase distributions of the particles. [XBL 922-5587]
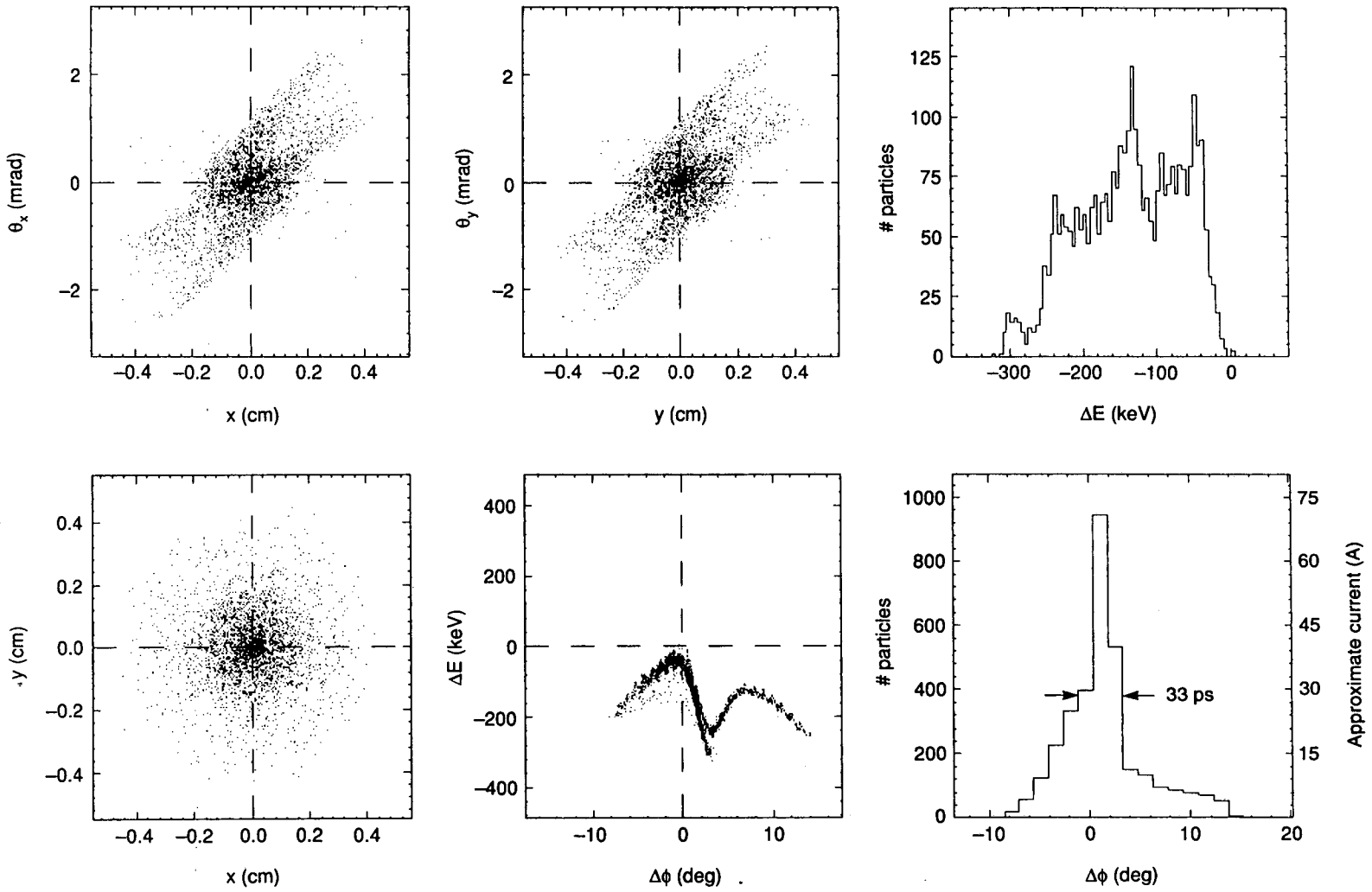
Figure 3-6b. Electron beam characteristics at the injector exit, downstream of the slit. See Fig. 3-6a for explanation. [XBL 922-5588]

Table 3-4. *Results of a stability analysis of the FEL injector. Each column represents a single operational parameter; each figure in the column then gives the tolerable variation in that parameter, given the allowable variation in a single output parameter (listed at left). The most stringent requirements are highlighted.*

	Tolerance on injector output	Gun pulser phase (deg)	Buncher #1 phase (deg)	Buncher #2 phase (deg)	Four-cell phase (deg)	Gun voltage (kV)	Buncher #1 amplitude (kV)	Buncher #2 amplitude (kV)	Four-cell amplitude (MV/m)	Gun current (%)	Gun bunch length (%)
1	Charge, <1%	2.6	0.22	0.45	0.32	0.45	1.9	1.1	0.20	1.0	0.26
2	Voltage, <1×10^{-4}	**1.2**	0.040[a]	**0.15**	**0.16**	0.16	**0.58**	**0.50**	**0.00053**	**0.82**	**0.14**
3	Bunch length, <5%	4.9	0.29	1.7	1.4	1.4	5.8	5.0	0.68	5.8	4.4
4	Bunch timing, <3 ps	32	**0.14**	1.3	1.4	0.75	4.7	2.3	0.15	21	8.2
5	Emittance, <5%	2.0	0.25	1.3	1.3	0.92	2.6	71	3.8	12	1.8
6	Energy spread, <10%	20	1.8	5.9	5.0	4.6	14	12	0.68	24	6.4
7	Beam size, <10%	9.3	1.1	4.5	7.0	3.6	10	29	0.43	18	6.5
8	Beam divergence, <10%	6.9	0.85	5.7	3.8	2.9	12	34	0.26	16	6.1
9	FEL detuning curve[b]	4.0	0.23	0.43	1.2	**0.048**	9.0				0.52
10	Buncher beam loading[b]									3.0	
	Derived requirement[c]	0.60 (3.4 ps)	0.070 (3.2 ps)	0.075 (1.3 ps)	0.080 (0.44 ps)	0.024 (0.008%)	0.29 (0.094%)	0.25 (0.098%)	2.5×10^{-4} (0.005%)	0.41 (0.41%)	0.070 (0.07%)

[a]Removed by changing buncher phase by 1° to curve maximum, thus defining the required operating phase.

[b]See text for explanation.

[c]Equal to one-half of boldface entry above to allow compounding of errors. See text for discussion.

In addition, we considered the beam loading effects in the bunchers, together with the resulting requirements on gun current and gun timing stability. This led to more restrictive stability requirements on gun current and voltage than did the single-parameter analysis alone, where the buncher's phase and amplitude were held constant.

For these analyses, three time regimes are important: times short compared to the FEL optical decay time, times longer than the optical decay time but shorter than the RF fill time of the cavity in question, and times long compared with the RF fill time. The RF fields in an RF cavity are under feedback control for times longer than the cavity's fill time, and for shorter times, the cavity fields are constant, apart from possible beam loading changes. The gun current, voltage, and timing can change rapidly, and these fluctuations are important for times longer than the optical decay time. For the intermediate times, the gun fluctuations may be important and can cause beam loading amplitude and phase changes in the RF cavities. For times longer than the RF fill time, the gun parameters, the phase of the RF drive, and the amplitude may vary. In addition, the tune of the cavity can fluctuate in response to microphonics.

Although the PARMELA analysis is not sensitive to the time scale of these instabilities, the stability requirements shown in Table 3-4 are for times longer than the optical decay time. The FEL performance is largely insensitive to faster beam fluctuations, which are stabilized by the optical storage. Consequently, for times shorter than the optical decay time, the stability requirements are more relaxed and do not impose restrictive requirements. See section 3.1.1 for a more detailed discussion.

The tolerance on gun current due to buncher beam loading (row 10 in the table) was obtained as follows: For times between the optical cavity decay time (1.6 μs) and the buncher fill time (52 μs), phase fluctuations in the first buncher are dominated by charge fluctuations from the gun. The beam loading in this buncher is such that its phase is changed by 0.0072° per nanocoulomb of change in charge. This is true for times short compared with the feedback phase correction time, taken to be close to the cavity fill time. To keep the buncher phase variation within 0.14°, the most restrictive requirement in Table 3-4, the maximum allowable charge deviation over the fill time is 19 nC, or 0.059 nC/bunch, which in turn requires gun current stability equal to 3%. As a result, buncher loading does not impose the most restrictive requirement on gun current stability (the voltage stability requirement is four times more restrictive).

The gun voltage fluctuations are limited by the FEL detuning curve (see section 4.1), which requires that the pulse arrival frequency at the FEL be constant to 1.2×10^{-7}. The maximum allowable timing error over the optical cavity decay time is then $1.2 \times 10^{-7} \times 1.6\ \mu s = 0.19$ ps. For the gun voltage, if we scale from the bunch timing entry in Table 3-4 (0.75 kV for 3-ps stability), this implies a stability requirement of 48 V, which becomes the most restrictive constraint on this parameter.

The bold entries in Table 3-4 are the most restrictive. To allow for compounding of errors, each injector parameter requirement is then taken to be half of the most restrictive entry. The resulting requirements are shown in the bottom two lines of Table 3-4. Figures in the final line are expressed in picoseconds (for the first four parameters) or percent change (for the rest).

Constraints on the injector parameters approach state-of-the-art levels. However, workers at Stanford [Frisch and Edighoffer, 1990] and CEBAF [Bisognano et al., 1991] have achieved better than the required amplitude and phase control. In addition, TRW

[Lazar et al., 1991] has demonstrated a suitable gun pulser with the required tolerances. The approaches used in these successful efforts offer a proven path to meeting the requirements of Table 3-4.

3.3 RF LINAC SYSTEM

Superconducting RF was chosen for the accelerating system primarily because it provides the only sure means of achieving the required wavelength stability of 10^{-4}. As shown in Table 3-5, existing superconducting accelerators have produced electron beam energies sufficiently stable to meet the constraints implied by this requirement. In particular, the RF stability we require has been demonstrated at Stanford and CEBAF, both in amplitude and in phase, though not at the average power levels we demand. Our requirements, as determined by the stability analysis of the section 3.2.3, are for an amplitude stability of 5×10^{-5} and a phase stability of $0.08°$ in the main accelerator. (The energy stability must

Table 3-5. Selected parameters for operating and proposed superconducting RF linear accelerators. Parameters for the operating linacs were taken from Tuckmantel [1991].

	Frequency (MHz)	Gradient without beam (MV/m)	Gradient with beam (MV/m)	Current (mA)	No. of cavities	Q_0	Operating experience (hr)	Stability
Stanford (SCA)	1300	3.5	2.5[a]	0.2	7	2×10^8	3×10^6	3×10^{-5}
Cornell (CESR)	1497	8.0	5.0	20	few	5×10^9	$\sim 10^2$	10^{-4}
Darmstadt	300	5.6	4.2	low	11	$1-2\times10^9$	4×10^3	1×10^{-3}
CERN (SPS)	352	7.1	5.5[b]	6	1	3×10^9	2×10^4	$< 10^{-4}$
CERN (LEP)	352	5	3.6[b]	6	4(of 156)	$2-3\times10^9$	4×10^2	10^{-2}
KEK (Tristran)	508	9.25	4.7[b]	5	32	2×10^9	1×10^4	10^{-2}
DESY (HERA)	500	5	3.5	low	16	1×10^9	4×10^2	—
CEBAF	1497	9.0	5.0	0.1	2(of 350)	6×10^9	2×10^2	$< 3\times10^{-5}$
Cornell B factory (proposed)[c]	500	10	10	1980	16	2×10^9	0	$< 10^{-4}$
CDRL IRFEL (proposed)	500	5.5	5.25	24	5	2×10^9	0	5×10^{-5}

[a]Limited by an old design with multipactoring problems.

[b]Believed to be limited by stray synchrotron radiation, because of the low quench limit of the cavity closest to the bend; the CDRL FEL will produce little significant synchrotron radiation.

[c]See *CESR-B: Conceptual Design for a B Factory Based on CESR* [1991].

be twice a good as the required wavelength stability, since the FEL wavelength is inversely proportional to the square of the electron energy.) The higher average power we demand means that our Q_L and the cavity fill times are less than those at Stanford or CEBAF. This in turn means that the cavity is more tightly coupled to the RF drive, thus reducing the phase shift due to microphonics, because the resonance is broader. Some trade-off of gain for bandwidth is required, so that the gain at low frequencies is comparable to the Stanford and CEBAF values, which means reducing the bandwidth of the feedback loop below that of the cavity. See section 3.1 for a complete discussion of these considerations.

Table 3-5 further suggests that the other IRFEL design goals are likewise reasonable, though no single accelerator has demonstrated all of our design goals simultaneously, in part because none was designed specifically for an FEL. The most significant extension of existing technology will be to produce the high average current, and therefore the high average beam power, that we require. This average current is much higher than has been produced by any accelerator apart from CESR. Reaching the design current will demand that great care be taken to control higher-order modes and to optimize beam transport—both topics to be discussed in detail below.

The field of superconducting RF linac design is moving forward rapidly, and a gradient of 5–6 MV/m is now considered routine. Gradients of 7–9 MV/m are expected to be commonplace within three to five years. (Indeed, Cornell has proposed a B factory to operate at 10 MV/m [*CESR-B*, 1991].) Several manufacturers currently produce superconducting cavities, and most will guarantee performance at 5–6 MV/m and a Q_0 of 2×10^9, which will satisfy our design requirements for 5.25 MV/m and $Q_0 = 2 \times 10^9$. Examples include Siemens (Interatom), Dornier, Mitsubishi, NTG, and Babcock and Wilcox. Figure 3-7 shows a 500-MHz, four-cell structure manufactured by Interatom for INFN/Frascati, and Fig. 3-8 is a cutaway of a 500-MHz, four-cell structure manufactured by Dornier for the HERA project at DESY. The RF structures ultimately chosen for the IRFEL will be based on a proven, off-the-shelf design from an experienced manufacturer. Indeed, we expect our needs to be met at the time of construction by units in production for CERN, DESY, CEBAF, or another large facility. By this means, we expect to minimize the cost, as well as to ensure the reliability of the structures.

3.3.1 Design Overview

Figure 3-9 shows the layout of the accelerator section, together with the injector discussed in section 3.2. Table 3-6 summaries the accelerator parameters. These parameters are derived from the required wavelength range of the FEL (3–50 μm), the required energy per optical pulse (100 μJ at 6 MHz delivered to the user), and the constraint on wavelength stability (10^{-4}), together with practical considerations of feasibility and cost. The injector, for example, must be capable of 2 nC of charge per bunch to produce the required optical energy per pulse over the full wavelength range. The peak current must be at least 20 A so that the FEL gain exceeds the cavity losses. The FEL also requires that the unnormalized rms emittance be less than one-quarter of the wavelength and that the energy spread (FWHM) be less than $1/2N$, where $N = 40$, the
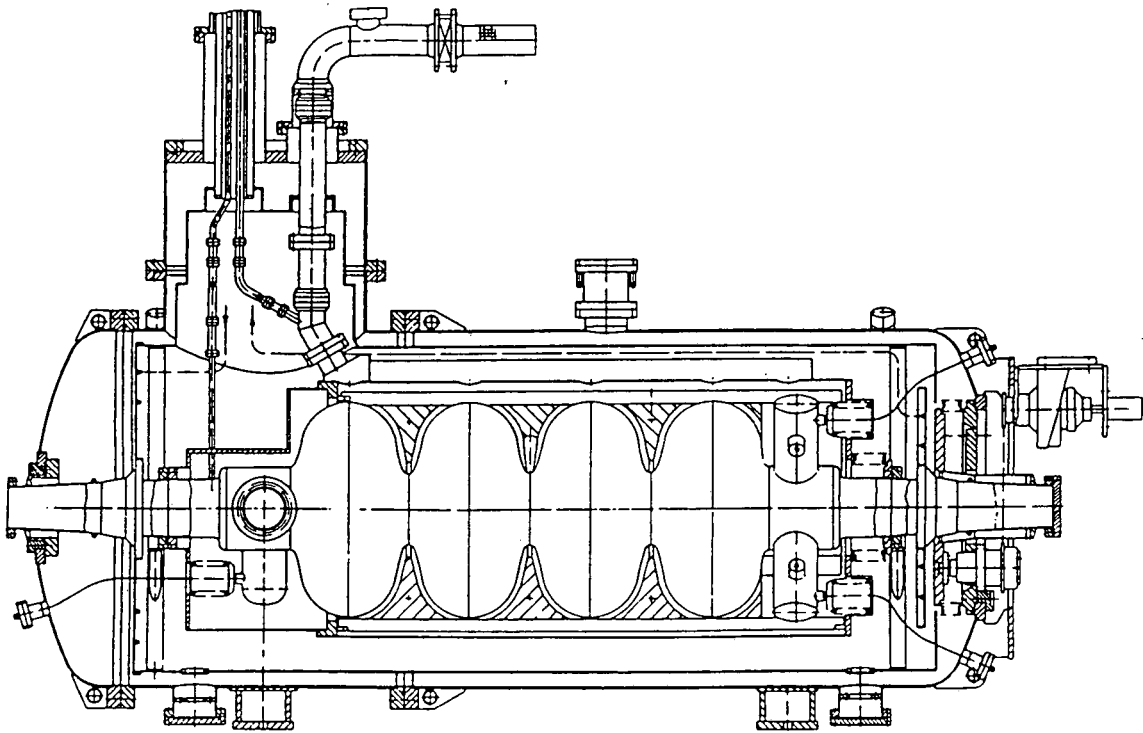
Figure 3-7. Cutaway of a 500-MHz superconducting accelerator module produced for INFN/Frascati.
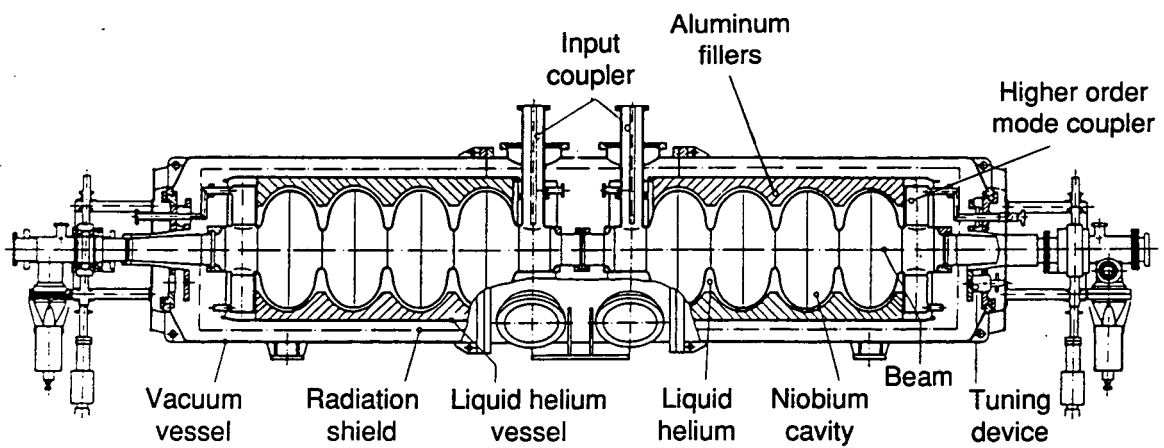
Figure 3-8. Cutaway of a 500-MHz superconducting accelerator module produced for HERA.

Cryogenic system

He 4 K

LN_2 →

Recirculation loop

Buncher #1

Electron gun

Buncher #2

500-MHz accelerating cavities

500-MHz accelerating cavities

cw electron beam to undulator

Accelerator buncher cavity

Coupler (M.C. & HOM)

Coupler (M.C. & HOM)

CW pulsed power supply

100 kW

100 kW

100 kW

100 kW

100 kW

ALS master oscillator

RF system

Figure 3-9. Schematic illustration of the RF accelerator system, together with the injector described in section 3.2.
[XBL 922-5609]

Table 3-6. Design parameters for the superconducting RF accelerator section.

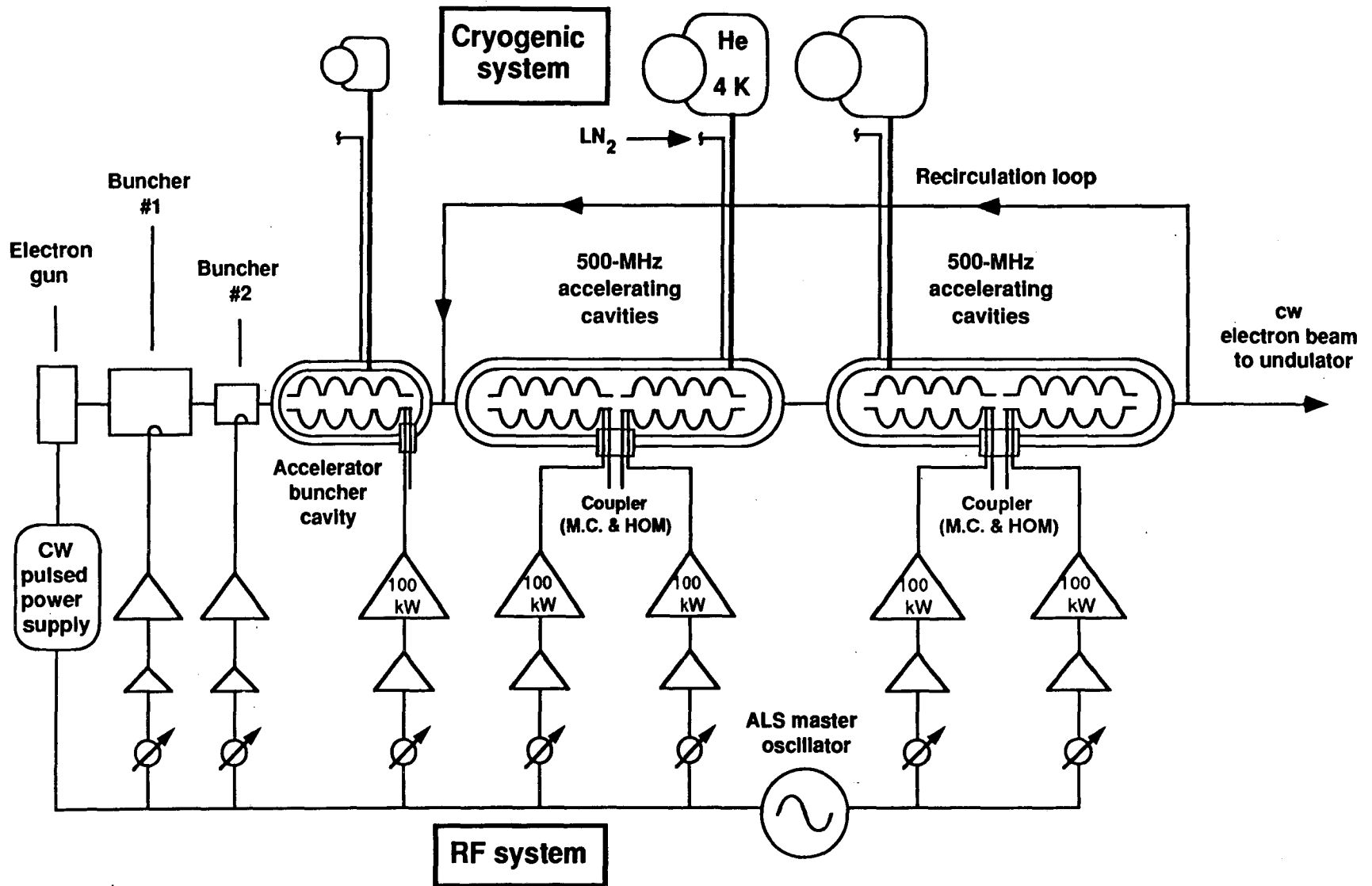|	
Accelerating gradient [MV/m]	>5
Frequency [MHz]	499.65
Peak beam current [A]	>60
Charge per bunch [nC]	>2
Bunch repetition rate [MHz]	6.10 (82nd subharmonic)[a]
Bunch length [ps]	<33
Normalized emittance, rms [mm·mrad]	<25
Beam energy [MeV]	15–55 MeV
Energy spread, FWHM	<0.5%
Energy fluctuations[b]	$<5 \times 10^{-5}$
Frequency stability	$<1 \times 10^{-7}$
Charge fluctuations	<5%
Spatial jitter	<10% of beam size
Angular jitter	<10% of beam divergence

[a]Can also be operated at 12.19 MHz at half the nominal bunch charge.

[b]Fluctuations on time scales longer than the optical decay time (~1.6 μs); the constraint on higher-frequency fluctuations is relaxed by an order of magnitude.

number of undulator periods. The stability requirement on the electron pulse frequency arises from the FEL optical cavity detuning width, which must be accurate to 3 μm out of 24.6 meters, or about 10^{-7}. And finally, the charge fluctuations and the spatial and angular jitter were specified to avoid significant FEL performance fluctuations.

Figure 3-10 shows the limits on beam power and charge per bunch as functions of wavelength. At wavelengths shorter than 10 μm, the RF drive power limits the beam loading per accelerator cavity to 73.2 kW and therefore restricts the charge per bunch that is produced by the injector to less than 2 nC. The power decreases in going from 10 to 3 μm because the injector, which operates at fixed voltage (5.25 MV/m), delivers less power. This reduction can be mitigated to the extent that the injector can be run at a higher voltage at the reduced charge per bunch. For wavelengths longer than 10 μm, the
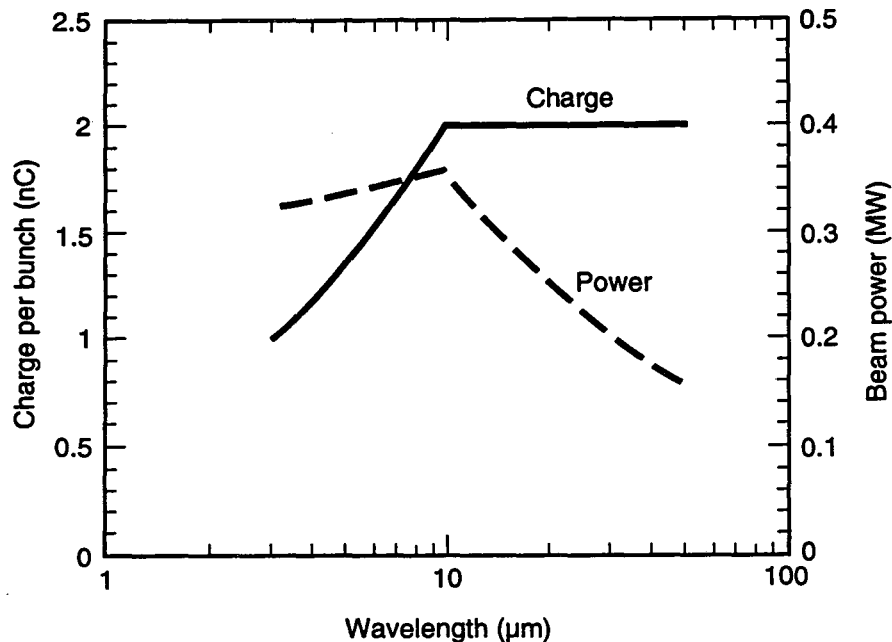
Figure 3-10. Plot of beam power and charge per bunch as functions of optical wavelength. For wavelengths shorter than 10 µm, the RF drive power limits the beam loading per cavity to 73.2 kW and thus restricts the charge per bunch that comes from the injector. At longer wavelengths, the limit is the injector design limit of 2 nC per bunch. [XBL 921-5563]

limits arise from the injector design limit of 2 nC per bunch. By reducing the injector voltage or by providing more RF power, more charge per bunch could be made available, albeit at the cost of increased emittance and energy spread. The FEL output roughly follows the power curve of Fig. 3-10, with about 0.5% converted to optical power and about 0.2% delivered as usable laser power to the user. Section 4.1 discusses FEL output performance in more detail.

3.3.2 Recirculation

The IRFEL requires a recirculation loop to operate at wavelengths shorter than 10 μm (see Figs. 1-1 and 3-9). This leads to potential instabilities. First, because of the beam's second pass, the average current in the accelerator structures is doubled, driving some higher-order modes (HOMs) more strongly. Second, the beam can couple a transverse kick received during the first pass to a displacement on the second pass, potentially leading to a regenerative recirculation instability. Third, a beam loading, or longitudinal recirculation, instability can be driven if an energy-sensitive beam current loss occurs in the transport section. That is, a small change in energy can cause a concomitant change in the fraction of the beam recirculated, thus causing a change in beam loading, which, in turn, causes an additional change in the accelerating voltage. Under certain conditions of phasing and gain, this instability can become uncontrolled. At Los Alamos, this

instability was observed when an energy slit was placed in the recirculation loop during energy recovery FEL tests.

The first instability mentioned requires that the HOM coupling be designed for the higher current, or that the required loaded Q's be halved. Data for the loaded DESY cavity [Willeke and Proch, 1991] indicate that the HOMs are sufficiently damped for us to adopt the DESY design as is. (More recent designs appear to offer even better performance, and our final design will take advantage of the latest available technology.) With the DESY couplers, the instability threshold is about 1 A; our design current is only 24 mA.

A study of the regenerative recirculation instability is described in detail in section 3.6.1. Using the parameters of the DESY structure and a simple recirculation loop, we obtained a threshold of about 340 mA for this instability [Krafft and Xie, 1991]. In addition, the transport optics described in section 3.6.2 is designed as a unity transport from the first pass to the second; this will further suppress this instability. Nonetheless, the threshold for this instability is fairly sensitive to the length of the recirculation loop, especially the equivalent number of RF cycles. It is thus important that the transport loop be adjustable by several RF wavelengths. One wavelength of adjustment is needed just to set the recirculated beam at the peak accelerating phase. Such an adjustment can be made by mechanically moving both recirculation bends by 15 cm. We have therefore allowed for a half-meter of translation in each bend, enough to change the path length by about three RF cycles.

The third potential instability, the longitudinal recirculation instability, can be eliminated by ensuring that very little beam is lost around the transport loop. This is necessary in any case because of the extremely high electron beam power. Only a few hundred watts can be lost in the transport line without causing physical damage. This level corresponds to less than 0.1% of the beam power, well below the 5–10% loss necessary to encounter this third instability. To minimize beam loss, the transport apertures must be equal to 4σ or 5σ, assuming roughly Gaussian tails on the transverse beam distribution. Accordingly, the transport loop described in section 3.6 has a minimum aperture of 5σ (larger in most places). As discussed in section 3.4, x-ray monitors along the transport line will detect even very small beam losses, and interlocks will protect the beam pipe and vacuum chamber.

3.3.3 Superconducting RF Issues

Microphonics constitute a potentially significant contribution to the RF amplitude and phase errors. We are currently collaborating with Stanford, TRW, and Brookhaven in exploring ways to minimize microphonics. The most likely modifications to current practice will be to use rigid stiffening ribs to interconnect the cells' outer rims; this will increase the mechanical resonant frequency and reduce the amplitude of vibrations coupled into the structure. Second, much of the mechanical coupling to the cavities' surroundings will be minimized by making the pipe and cryostat connections very flexible.

Multipactoring has also been a problem with superconducting RF structures, but cavity geometries have now been demonstrated that avoid multipactoring at accelerating gradients above 10 MV/m. Such geometries incorporate spherical or rounded cavity

shapes and thus eliminate the mid-plane multipactoring that plagued the flat mid-plane geometries used in early structures. The off-the-shelf design we adopt will have demonstrated freedom from this problem.

The input couplers must provide 100 kW of power to each structure. The couplers most widely used today have been tested to 70–80 kW and are rated at 150 kW. In addition, available designs exist for couplers rated at up to 500 kW. As part of the LBL-Stanford-TRW-Brookhaven collaboration, we are working to improve the 70- to 80-kW couplers to handle higher power levels. The present design also includes adjustable RF cavity coupling for the input couplers. This approach broadens the range of gradients and beam-loading levels to which we can properly match the RF. It also allows RF processing of the structures at high fields with very low input power to avoid damaging the cavities during processing.

The HOM couplers will be selected from available designs, such that all HOMs are damped to Q's less than 2000. The HOM couplers will be tested as part of the ongoing collaboration with Stanford, TRW, and Brookhaven.

Tuning requires a fast tuner and a slow tuner. The rigid ribs used to mitigate the microphonics will reduce the tuning to the end half-cells. This will reduce the tuning range from about 500 kHz to about 20 kHz. After the structures have been properly bench tuned, they will need only about 10 kHz of cold tuning to hit the design frequency. The fast tuner must have an amplitude comparable to that of the microphonics, estimated to be about 200 Hz, which corresponds to a few tens of micrometers of cavity wall displacement. Fast tuning will be done with piezoelectric tuners at speeds up to a few hundred hertz to cancel the dominant microphonics modes.

The cryostats, transfer lines, and refrigeration systems are commercially available. The cryogenic system is described fully in section 3.5. High vacuum will be used throughout the transport and accelerator, with electrostatic precipitators at the ends of the cryostats to prevent dust from entering the superconducting structures. Should chemical polishing of the superconducting structures be necessary, it will be done off-site, at the manufacturing facility or other suitable site.

3.3.4 RF Drive

Figure 3-9 shows the layout of the RF system. The frequency of the accelerator structures is 499.65 MHz, derived from the ALS master oscillator. (As discussed in section 3.2, the gun pulser frequency is derived by dividing down the accelerator frequency by a factor of 82; the buncher frequencies are then phase locked to 10 and 28 times the gun pulser frequency.) A number of choices of RF sources are available, including klystrons, solid-state klystrodes, and hard-tube triodes. Klystrons were chosen because of their reliability, low cost, and proven success in this application.

The RF feedback loop is shown in Fig. 3-11. The klystrons are two 64-kW EEV K3772 tubes, combined through a magic tee to provide the necessary 100 kW of RF at the input coupler to the superconducting structure. Several probes will sense the field in the superconducting structure, which is compared with the field set point. The field will be compensated by adjusting the RF input to the klystrons. Both Stanford and CEBAF have used this type of control circuit to achieve the level of phase and amplitude stability

RF feedback

Power
VSWR

System interlocks
Waveguide arc
Window temp
High vac
Tuner limit
He pressure
Quench

50 kW
water
load

Ferrite
circulator

RF control
module

20 W

EEV
K3772
64 kW
Klystron

20 W

EEV
K3772
64 kW
Klystron

RF drive distribution 500 MHz

RF reference 70 MHz

Magic
Tee

WG

HOM
filter

Superconducting cavity

100 kW
water
load

Mod anode
and
heaters

Cathode HVPS
10 Klystrons
27 kV   60 A

Cooling
system

M

HOM load

Tuner
motor

Low
power
RF
system
control

HP amp
control

Interlocks
and safety

Cavity
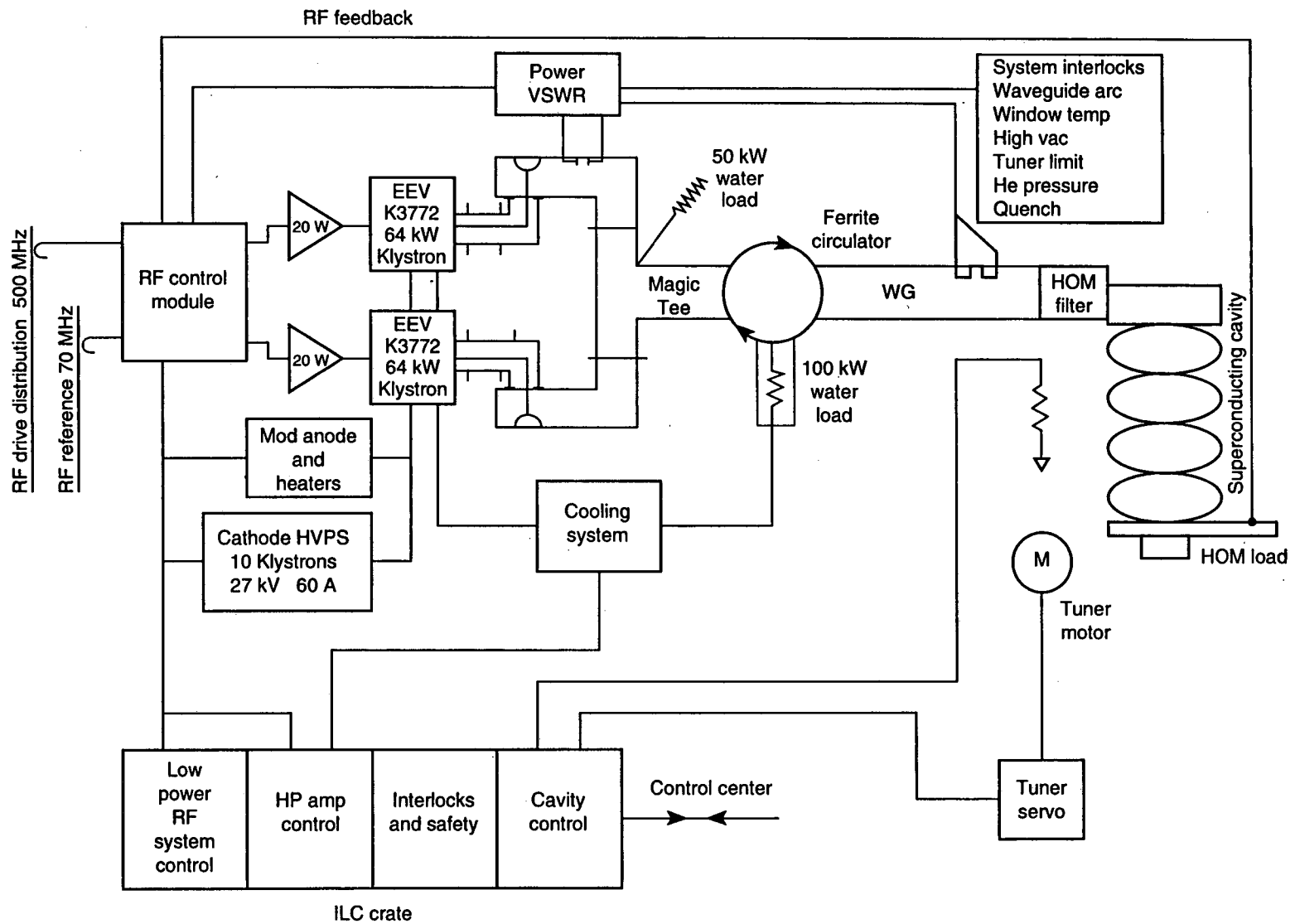control

Control center

Tuner
servo

ILC crate

Figure 3-11. Schematic of the high-power RF system for the superconducting accelerator. [XBL 9111-6853]

we require. In addition, a tuning feedback loop is included to minimize the frequency shifts of the structure, caused by microphonics and helium pressure changes. This will be done by matching the phase of the cavity probes with the phase of the power into the input coupler. The phase shift is proportional to the tune shift for small tune deviations from the drive frequency. This feedback loop will minimize the reflected power as well.

The first buncher operates at 60 MHz, the second at 170 MHz; each requires 25 kW of power. Again, two tubes at the appropriate frequencies are combined with hybrids and fed into the cavities. The setups are shown in Fig. 3-12. The stability requirements from section 3.2 for the two bunchers are 10^{-3} in amplitude and 0.07° in phase.

3.4 ELECTRON BEAM DIAGNOSTICS AND FEEDBACK

3.4.1 General Considerations

Since the electron beam power can approach a megawatt during routine FEL operation, the beam must, at all times, be kept far from the walls. Any significant loss can melt the vacuum enclosure almost instantaneously. As a consequence, the design incorporates an unusually large number of noninterfering position and current monitors. In addition, x-ray monitors will be used to detect beam loss and to provide fast interlocks. The transport system provides for a minimum clearance of 5σ—in most places, much more than that. Assuming that the wings of the beam are gaussian, beam loss will be limited to less than 100 W throughout the transport. Avoiding loss in the region of the undulator is particularly important. Accordingly, a cooled collimator is provided at the undulator entrance. During tune-up, intercepting monitors will be used at extremely low repetition rates.

Beam position, momentum, emittance, energy spread, charge, bunch length, current, and bunch timing all require measurement, continuous monitoring, and in some cases, active feedback. All beam parameters will be monitored at a resolution two to five times better than that demanded by stability requirements.

Monitoring and diagnostics requirements can be summarized by categorizing the instrumentation as follows:

- Stripline monitors to provide beam current and position information throughout the injector, accelerator, undulator, and transport sections.

- Insertable fluorescent TV screens and steering magnets throughout.

- Low-energy spectrometer between the second buncher and the four-cell accelerator for injector tuning.

- Stripline monitors to make energy measurements using transport dispersion, downstream of the injector and in the 180° bends.

- Synchrotron radiation monitors to provide energy and energy spread measurements using transport dispersion, in the 55-MeV bend.

- Fluorescent TV monitors to provide emittance measurements based on spot size and quadrupole strength, downstream of the injector and downstream of the accelerator section.
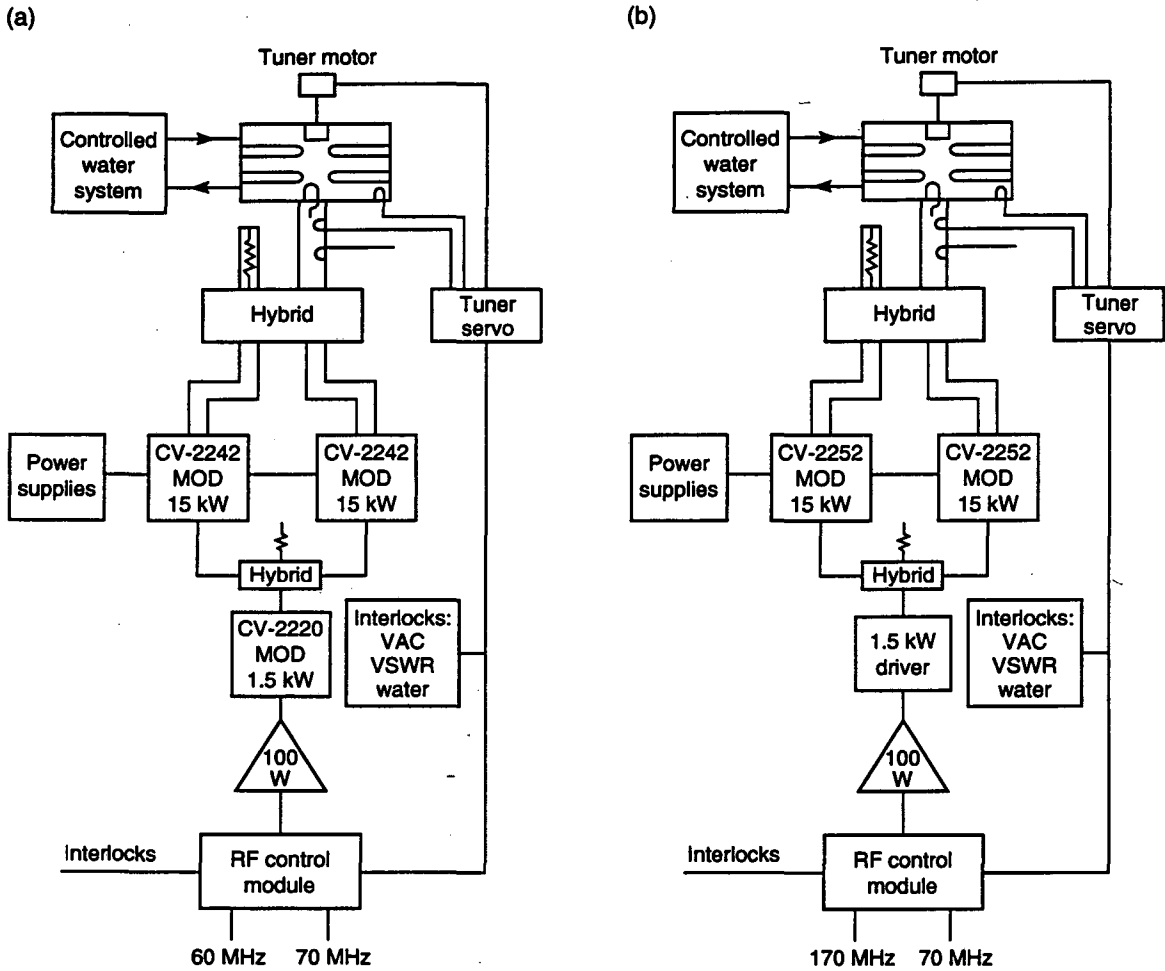
Figure 3-12. Schematic of the RF power system for the (a) first and (b) second bunchers. [XBL 9111-6854/5]

The main noninterfering diagnostics are four-section stripline position/current monitors, eight in the injector, a pair up- and downstream of each bend, two at the maximum-momentum-resolution points within each bend, one in the middle of the recirculation loop, one each up- and downstream of the undulator, six in the beam combiners, and four in the beam dumps. A steering corrector is associated with each monitor. In summary, the facility requires 41 striplines, 4 synchrotron imaging monitors, and 25 phosphor screens.

3.4.2 Diagnostic Measurements

The full range of beam parameters must be monitored closely during both commissioning and operational phases; during routine operation in particular, complete diagnostics not only provide the only means of meeting the user-imposed stability requirements, but also ensure the safety of the hardware.

Emittance will be determined by the transverse profile of the beam as a function of an upstream quadrupole strength. At low repetition rates, the profile will be displayed on the phosphor screens; at high current and high energy, it will appear on the synchrotron radiation imaging monitors. In addition, in the long straight sections with at least eight quadrupoles, the emittance can be determined by the quadrupole signal on the stripline monitors.

Momentum will be measured nondestructively by using the stripline position information in the bends. As a backup to this important measurement, the synchrotron radiation image will also provide momentum information. The requirement that the energy be stable to 5×10^{-5} requires this measurement to have a resolution of $1-2 \times 10^{-5}$. This in turn requires that the dipole power supplies be regulated to $1-2 \times 10^{-5}$, that the position monitors be accurate to $5-10$ μm, that the dipoles be thermally stable to about 0.5°C, and that the magnet alignment be thermally and vibrationally stable to $5-10$ μm. A minimum of three striplines, along with entrance angle and position information, are required to get a momentum measurement. Momentum signals must be developed and processed rapidly so that they can be used for feedback. A fast matrix multiplication of the sensor positions will provide the required momentum error signal. The matrix coefficients will be under computer control and will be determined directly from beam measurements.

Energy spread will be measured by the synchrotron light monitors. Also, at the high dispersion points in the bends, the ellipticity can be measured by the quadrupole signal on the stripline monitors; from this the energy spread can be inferred.

Current will be measured by the striplines and by fast current transformers. During commissioning, a Faraday cup will be used. Current loss will be monitored by the x-ray detectors.

A streak camera looking at the synchrotron light in the last bend will be used to measure bunch length. The bunch length from the injector can be measured during tune-up at low repetition rates, using the main accelerator shifted by 90°. A fast photodiode looking at the synchrotron light near the entrance to the undulator will also be used to monitor the bunch arrival timing, to an accuracy of 2–5 ps.

Processing the stripline signals involves forming the sum and the difference of signals from opposing strips. The processing is done by a network of broadband ferrite-type hybrid junctions. The resulting sums and differences are sampled and held with a minimum detectable charge of 100 fC at the bunch frequency. These sampled signals can be used directly in feedback systems or digitized for further processing. The position measured by the stripline is calculated approximately from the formula difference/sum $= 2\Delta x/r$, where r is the pipe radius. Assuming that a 2-nC bunch will generate an estimated 0.2-nC charge on each sample-and-hold, the difference/sum resolution is (100 fC)/(0.2 nC) = 5×10^{-4}. The resolution in Δx is half that, or 2.5×10^{-4} of the pipe radius. For a 2-cm pipe, the resolution is about 5 μm. Averaging could improve this further. Position resolution of 5–10 μm is required for the energy feedback loop (see below); therefore, resolution should be adequate for charges greater than 1–1.5 nC, below which averaging will be necessary.

Synchrotron light can be used to image the beam profile nondestructively, as well as its temporal structure. At 55 MeV the critical wavelength is 350 nm and the critical angle, 8.7 mrad. Using a 10% bandwidth optical filter around 400 nm will give about 3.6×10^6 photons/bunch. This beam will be monitored by three instruments. First, a gated CCD camera will capture single-bunch profiles, as well as averaging many pulses. Second, a fast linear diode array will generate transverse one-dimensional profiles at a 10-kHz rate. This can also be used for measuring energy and energy spread. Third, a fast photodiode capable of 15- to 30-ps rise times will, with poor resolution, directly measure the bunch temporal profile and timing jitter to about one-tenth of that, or about 3 ps. Also, a streak camera will be used, giving a resolution of about 2 ps.

The injector includes a low-energy 90° spectrometer between the second buncher and the four-cell cryostat. The spectrometer is necessary for measuring the phase and amplitude of the bunchers and for measuring low-energy beam bunching.

3.4.3 Feedback System

The time constants of the RF structures and the optical cavity determine the required speed of the feedback system. Table 3-7 lists the pertinent parameters. Feedback is provided in layers, starting with power supplies, followed by RF control loops, energy feedback, and finally optical feedback. These layers serve different functions and have different time constants.

Table 3-7. Time constants for the bunchers, accelerator, and optical cavity.

Fill times ($2Q_L/\omega$) [μs]	
First buncher	~52
Second buncher	~18
Accelerator	~636
Optical cavity decay time [μs]	1.6

Regulation of the power supplies for the magnets, gun voltage, and klystrons will be provided by standard commercial control of voltage and current ripples. The primary problems are related to the ac line frequency and its harmonics. Regulation equal to 10^{-3}–10^{-4} is typical of commercial units; 10^{-5} is available at higher cost and will be needed in two places: the dipoles within the injector-to-accelerator dogleg and in the final bend upstream of the undulator. Energy measurements at these points, which can be no better than the dipole magnet stability, must be accurate to 1–2×10^{-5}. Current stability requirements for the remaining magnets will be met with commercially available units with 10^{-3}–10^{-4} regulation.

As discussed in section 3.2.3, the gun voltage is required to be stable to ±24 V out of 300 kV, or $\pm0.008\%$. To achieve this level of control requires a temperature-controlled and temperature-compensated high-voltage resistive divider, controlling a 200-V, 15-mA series regulator supply. To be fast enough, this loop must be between the high-voltage deck and the cathode. The relevant time is the optical cavity decay time.

The RF amplitude and phase stability requirement for the klystron power supply, without further feedback, would require voltage stability equal to 4×10^{-5} ($2/5 \times 2 \times 5 \times 10^{-5}$). Regulating the voltage to 0.1% makes the RF amplitude and phase control gain requirements modest.

Radio-frequency feedback is the second layer in the feedback structure. We require control of RF amplitude, phase, and tuning. The RF controls used by CEBAF have demonstrated stability at the level we require, namely, 5×10^{-5} in amplitude and $0.05°$–$0.10°$ in phase. (The derivation of these requirements was discussed in section 3.2, and they are summarized in Table 3-4.) The CEBAF control system converts amplitude and phase into in-phase and out-of-phase components, a process that breaks the normal coupling between amplitude and phase controls, allowing greater independence of the two loops. For our design, we have adopted the CEBAF system without significant change.

An additional tuning loop is controlled by the phase difference between the cell and the input RF. The difference is zero at the peak of the tuning curve and varies linearly away from the peak. This can be used on a fast tuner to counter microphonics. This loop will minimize the reflected power, as well.

Energy feedback serves as the third layer of feedback control. Just downstream of the injector and just upstream of the optical cavity, the energy will be measured continuously with a sensitivity of 1–2×10^{-5}. The resulting momentum error signals can be fed back to any of the accelerator structures, the bunchers, or even the gun. Long-term stability is best served by feeding back to the superconducting structures, whereas the fastest response is available by feeding back to the gun. Accordingly, the injector will be stabilized by feedback to the gun and the four-cell structure; the accelerator will be stabilized by feedback to one of the structures. Within the gun itself, given that the high voltage will require an intermediate gun anode, the best feedback approach is to capacitively couple to this anode with a time constant somewhat smaller than the optical decay time. Such feedback will provide a fast response by means of small current changes that will correct the energy fluctuations. On a time scale longer than the fill time, feedback to the superconducting structure will provide similar correction. In terms of feedback gain, the two loops display a crossover point at about half the structure fill time. This is illustrated in Fig. 3-13.
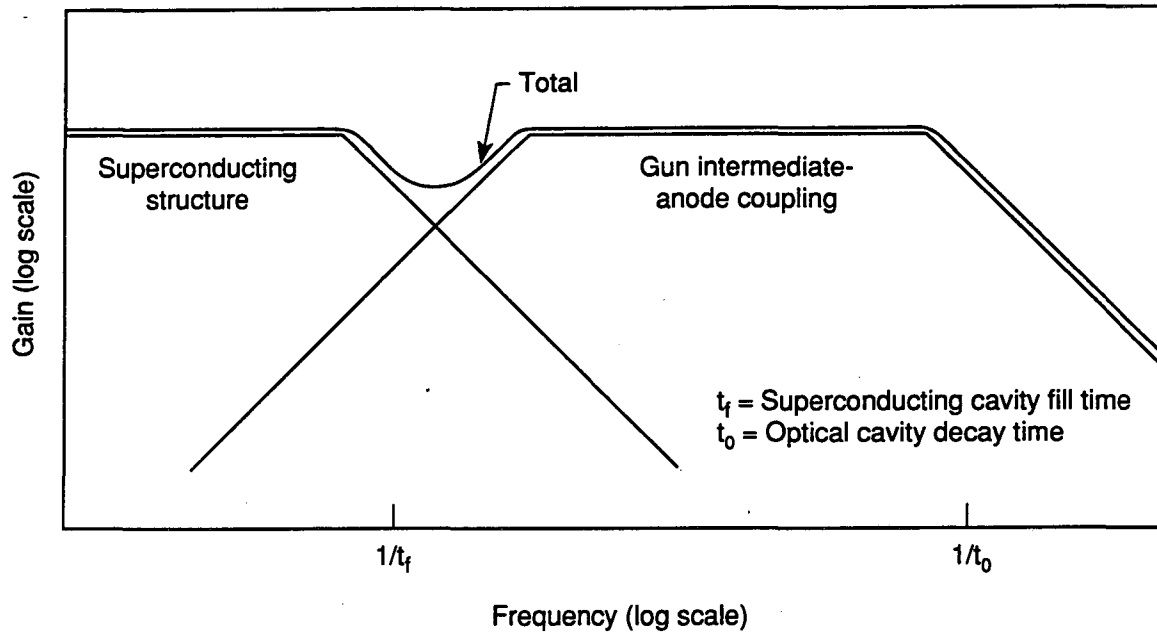
Figure 3-13. The gain of the energy feedback loops as a function of frequency. The total gain is the sum of the gains for loops operating on the four-cell superconducting cavity and on the intermediate-voltage gun anode. [XBL 922-5571]

The final feedback layer is provided by the FEL parameters themselves—the only parameters of interest to the users and the ultimate source of all other design requirements. The two most important parameters are FEL power and wavelength stability. The variables that control these parameters are the electron beam current and energy. FEL power feedback to the gun current will occur on a time scale longer than the structure fill time to avoid conflict with the energy loop described just above.

Wavelength control requires that we continuously monitor the FEL wavelength to an accuracy of 10^{-5}. A 1-meter grating monochromator with 2×10^4 lines (20 cm at 100 lines/mm) will provide sufficient dispersion. The output slit will be removed. To measure wavelength stability, the spectral light is divided into long- and short-wavelength halves, then focused onto two mercury cadmium telluride detectors, which are then differenced to get a wavelength error signal. (At wavelengths longer than 20 μm, helium-cooled, doped germanium detectors will be used.) This signal is then added to the amplitude of the one of the structures, as in the energy feedback loop.

In addition, for any given experiment in which a single FEL parameter is critical, that parameter can be used in a feedback loop. For example, if a user is measuring the autocorrelation, which is sensitive to the peak power and the bunch length, it will be possible to control either the power or the bunch length to maintain a constant autocorrelation. Flexibility is the key to providing the best FEL beam to a wide variety of users.

3.5 CRYOGENIC SYSTEM

The cryogenic system required to cool the superconducting components of the IRFEL consists of the cryostats that house the RF cavities, a refrigerator and gas storage system, and a distribution system. As discussed below, each subsystem makes use of standard, operationally proven units. A simplified schematic of the system is shown in Fig. 3-14.

The cryostats function as high-vacuum housings for the RF cavities (see, for example, Figs. 3-7 and 3-8). The main components of each include (i) a vacuum vessel with a cavity anchor adjustment system and beam alignment reference points, (ii) an 80-K liquid nitrogen–cooled thermal radiation shield, (iii) a magnetic mu-metal shield, (iv) penetrations for RF power couplers, (v) a liquid helium vessel for cooling the cavities, (vi) an insulating vacuum system with pump connections and instrumentation, (vii) a separate beam vacuum system with instrumentation and isolating gate valves at each end, and (viii) instrumented isolating and control valves with connecting bayonets for helium and nitrogen supply and return.

Table 3-8 lists parameters for cryosystems at DESY, KEK, and CERN.
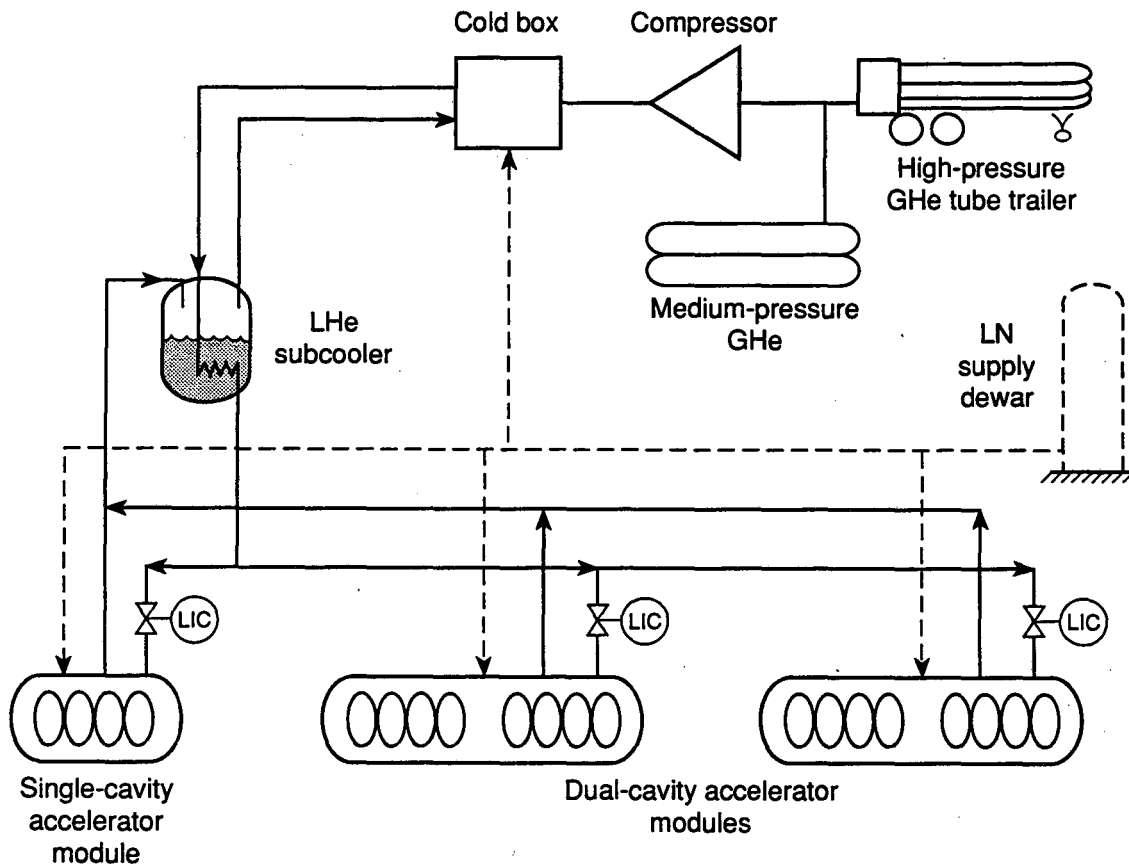

Figure 3-14. Schematic of the IRFEL cryogenic system. LN = liquid nitrogen; GHe = gaseous helium; LHe = liquid helium; LIC = level-indicating controller. [XBL 922-5570]

Table 3-8. Parameters for DESY, KEK, and CERN cryosystems; MLI is multilayer insulation.

	DESY	KEK	CERN
Operating frequency [MHz]	500	508	350
Operating temperature [K]	~4.5	~4.5	~4.5
Max. operating pressure [bar]	~3.0	~3.0	~3.0
Cavity material	Nb	Nb	Nb/Cu
Cryostat insulation	Vacuum/MLI	Vacuum/MLI	Vacuum/MLI
Cryostat radiation shield	He, 40/80 K	LN, 80 K	MLI only
Cryostat magnetic shield	μ-metal	μ-metal	—
Input RF coupler cooling	He, 20 K	H_2O	—
HOM RF coupler cooling?	Yes	Yes	Yes
Static freq. adjustment	Mechanical	Mechanical	Ni thermal
Dynamic freq. adjustment	—	Piezoelectric	Magnetostrictive
Filler for low He inventory	Aluminum	None	Curved He vessel
LHe inventory/cryostat [liters]	200	830	—
He cooling system	Bath	Bath	Bath
No. of cells per cavity	4	5	4
No. of cavities per cryostat	2	2	4
Manufacturer(s)	Dornier	Mitsubishi	Interatom Ansaldo CERCA

3.5.1 Heat Loads and Choice of Operating Temperature

The boiling points of coolants at one atmosphere establish common fixed operating temperatures—for example, 78 K for nitrogen and 4.2 K for helium. Other temperatures are achieved by varying the pressure according to the vapor pressure curve. However, varying the pressure on the coolant liquid is sometimes difficult and expensive. Moreover, when increasing the pressure on helium, the critical temperature, 5.2 K, is soon reached (at 2.26 bars). At lower pressures, helium goes from He I to He II, a unique state of superfluidity, at 2.17 K and 0.05 bar. The lowest practical (engineering) temperature for helium is 1.8 K (0.016 bar). Reaching these lower temperatures requires considerable effort, together with a significant investment in heat exchangers and vacuum pumps. In terms of the IRFEL, an obvious constraint on the operating temperature of the

cavities is that it must be well below the superconducting transition temperature for niobium, 9.2 K.

Rode and Proch [1989] derived the optimum operating temperatures for given values of accelerating gradient, frequency, and Q (the quality factor). For CERN, as an example, operating at 5 MV/m and 350 MHz, the ideal temperature is 4.5 K; at CEBAF, operating at 1500 MHz, it is 2.0 K. For the IRFEL described here, operating at 5.25 MV/m and 500 MHz and with $Q = 2 \times 10^9$, similar considerations led us to select 4.5 K, an operating temperature easily achieved with a standard helium refrigerator.

The most important aspect of cooling system design is a careful calculation of the expected heat loads. Holding the temperature constant requires a balance between the total heat load of the cryomodules and the capacity of the cryogenic refrigerator to remove the heat generated. Extra capacity is needed to assure reliability and the proper cool-down speed, and to allow for possible future upgrades in gradient. The three primary heat loads arise from the static load, the temperature-independent residual surface resistance, and the temperature-dependent (Bardeen-Cooper-Schrieffer) surface resistance. The static load stems from metallic conduction (center supports, tuners, power coupler, etc.), radiation, and convection. The residual surface resistance is caused by small local resistive areas where impurities, defects, or surface dirt disturbs the RF current and superconducting properties. The temperature-dependent resistance is due to unbound Cooper pairs of electrons. It increases with increasing frequency and decreases as the operating temperature decreases.

The power loss per unit length on the cavity wall can be based on the INFN-Frascati design [Byrns, 1989]. In terms of cavity impedance:

$$P = \frac{E_a^2}{(R/Q)Q_0} \tag{3-17}$$

where $E_a = 5.25$ MV/m is the accelerating gradient, $R/Q = Z = 383$ Ω/m is the geometric characteristic impedance, and $Q_0 = 2 \times 10^9$ is the unloaded quality factor at 4.2 K. The power loss for each 1.2-meter cavity is thus 43 W, or 215 W for the five cavities of the injector and accelerator systems. (According to Eq. 3-17, operation at higher gradients or any deterioration in Q_0 can cause large changes in the dynamic heat load.)

Table 3-9 summarizes the estimated cryogenic heat loads.

3.5.2 Refrigerator and Storage System

A 600-W helium refrigerator should provide reserve capacity and a safety margin that allows for system entropy gain, decay of Q, vacuum leaks or static heat increases, higher gradients, etc. Such refrigerators are now readily available, and reliable systems can be obtained to meet our performance goals in terms of capacity, operating mode, and temperature.

The refrigerator system (see Fig. 3-14) comprises a compressor, which compresses helium gas at ambient temperature to ~15 bars; a vacuum-insulated cold box, containing counterflow heat exchangers, expansion engines, and Joule-Thomson valves to produce coolant at 2.5 bars; purifiers; and automatic controls. The expanders may be turbines or

Table 3-9. Estimated heat loads for the five RF cavities (2.5 cryostats) of the injector and accelerator systems. All loads are given in watts.

	at 4.5 K	at 80 K
Static loads		
Control/isolation valves (8)	8	20
Bayonet connections (8)	8	15
25-m supply line (incl. "U" tubes)	8	15
25-m return line	8	—
Subcooler	10	—
Cryostats[a]		
12 W per cryostat	30	—
120 W per cryostat	—	300
Total static load	**72**	**350**
Dynamic (RF on)		
RF loss per cavity (43 W per cavity)	215	—
HOM loss (3 W per cryostat)	8	—
Tuners and misc. (8 W per cryostat)	20	—
Total refrigeration loads	**315**	**350**

[a]From Byrns et al. [1991].

reciprocating pistons, but we have specified the latter. Reciprocating engines are less sensitive to process gas system impurities, they are more efficient (throughout a wide mass-flow range), and they can be maintained on-site. Joule-Thomson valve expansion in the cold box will be at 2.5 bars to supply supercritical helium to the cryostats, as in the DESY-HERA system [Byrns et al., 1991].

The helium compressor is an oil-flooded screw type, self-contained and skid mounted for easy installation and service. Screw compressors, now the industry standard, have a slide valve for variable capacity and complete oil removal systems to assure impurity levels well below 0.5 ppm. Flow delivery for 600 W should be 64 g/s at 220 psig and 310 K. The compressor room is located remotely and will be completely sound shrouded to reduce the exterior sound level to a value below 70 dB.

A cryogenic purifier-adsorber is part of the cold box and will remove all trace impurities (N_2, O_2, H_2O, argon, etc.) above 80 K. A bypass valve will permit on-line regeneration. The control system will use a simple industrial microprocessor or even

relays, as there should be only two primary loads—static and dynamic. Transient operations such as cool-down and warm-up can be set up manually.

Helium gas will be supplied by a helium tube trailer, with a capacity of about 36,000 std ft^3 at 2200 psi. Gas will feed from the tube trailer via a high-pressure line and demand valve directly to the helium refrigerator. In addition, six 1000-gal warm-gas storage tanks will allow all the liquid helium in the cold system (~600 liters) to be stored as gas (at 250 psi) and will also serve as a ballast volume for the compressor and refrigerator operations.

3.5.3 Distribution System

A three-pass transfer line, insulated by high vacuum and with multilayer insulation, connects the cold box to the three cryostats. It contains one supply pass for liquid nitrogen, together with supply and return lines for the helium at 4.5 K. The length is approximately 25 meters. An end box with a thermostatically controlled valve will maintain the supply line temperature at 4.5 K. Connections from the supply line to each cryostat are made with bayonets and flexible "U" tubes. Each cryostat has its own helium system valve box, with a 4.5-K liquid-level-controlled fill valve (expanding to 1 bar) and a 4.5-K return isolation valve. Other valves will permit individual warm-up, cool-down, and pump and purge operations with gaseous helium at 300 K.

The distribution system also contains an in-line subcooler just upstream of the first cryostat, to assure good temperature control of the liquid helium supply and to provide some ballast volume to suppress oscillations in the return liquid helium transfer line. This should serve to damp microphonics and frequency shifts in the cavities.

Liquid nitrogen will be used for the 80-K cryostat shields (350 W) and for precooling continuous flow to the helium refrigerator (1200 W). System needs (350 W + 1200 W = 1550 W) can be met by a flow of about 35 liters/hr from a 3600-gal vertical storage tank on the periphery of the ALS building. Supply to both the cryostats and the helium refrigerator will be via vacuum-insulated lines and automatic demand valves. Gaseous nitrogen will be vented outside the CDRL building to prevent any possible oxygen deficiency hazard.

3.5.4 Automatic Controls and Operating Modes

Control of the cryogenic system will be by automatic valves controlled by liquid level, pressure, or temperature. For the simplest steady-state operating modes—during either FEL operation or standby—the controls will be simple industrial microprocessors or relays. Cool-down or warm-up can be preset manually for the short periods involved. Interfacing for computer control, including control of all pressure, temperature, and liquid-level sensors, will be available to complete the feedback loops and to provide data logging for system diagnostics. ·

The cool-down from 300 to 4.5 K will be handled via gaseous helium–liquid nitrogen heat exchange and final transfer of liquid helium, though it may be necessary to cool first to 150 K and then cool rapidly to 4.5 K, to avoid any H_2 diffusion problems in the niobium shell. (Cool-down from 150 to 4.5 K is expected to take 21.5 hr, based on

experience at DESY.) Each cryostat can be warmed up in a controlled manner with warm gaseous helium from the refrigerator or with the cryostat heaters.

The 4.5-K cryostat in standby mode is affected only by static heat loads (see Table 3-9). Accordingly, to minimize costs, the refrigerator will have a good turn-down ratio in both liquid nitrogen and power consumption. A 600-W refrigerator with 1200 W of liquid nitrogen precooling feed can be expected to produce 300 W without liquid nitrogen.

As mentioned earlier, each cryostat will be separately operable through thermal cool-down, RF pulse, and warm-up, thus allowing complete flexibility for component diagnostics and repair.

3.6 ELECTRON BEAM TRANSPORT

3.6.1 Beam Transport Design Parameters

The constraints and main features of the beam transport design can be summarized as follows:

- The injector supplies a 6-MeV beam with a normalized rms emittance of 30 mm·mrad and a 4% momentum spread (FWHM), plus a long low-energy tail.

- A magnetic compressor follows the injector with matrix element $m_{56} \cong 0.4$, which translates an intentional energy chirp on each bunch to a shortening of the bunch.

- This compressor also contains an energy slit, eliminating beam more than 100 keV below the nominal 6 MeV and thus reducing the current by about 20%. (This low-energy tail is produced by the bunching process in the injector and must be removed.) The slit will be no closer than 3σ from the undeflected beam, with the rms vertical size no smaller than 1 cm to limit the power density on the slit.

- The beam will be accelerated by two 12-MeV superconducting accelerator (SCA) structures, each in a 6-meter-long cryostat. The beam size must be as small as possible in the SCA structures to minimize coupling to fringe fields.

- The beam will be accelerated on the crest of the field in the SCA structures, and the momentum spread will be approximately 0.8% (FWHM) at 30 MeV.

- The beam will be recirculated through two 180° arcs for further acceleration in the same SCA structures, to a maximum of about 55 MeV. In the recirculation loop, the beam will be displaced by 2.35 meters from the SCA axis to provide room for the SCA cryostats, space for a possible future undulator in the 30-MeV beamline, and clearance for the undulator in the 55-MeV beamline.

- The 180° arcs are achromatic and isochronous. The chromatic correction will be sufficient to ensure that the beam transverse and angular displacements do not change by more than 10% of the ellipse parameters for momentum changes of up to 1%. This requires correction through second order in the 180° arcs.

- To satisfy the microtron condition, the path length around the recirculation orbit must be an integer multiple of $\beta\lambda$. The integer must be variable over a narrow range to provide flexibility in avoiding any dangerous higher-order modes in the cavities.

- To avoid transverse beam breakup, the transverse matrix in the recirculating loop is set to unity, which suppresses the second-turn offsets caused by first-turn angular kicks (see section 3.6.3). The symmetric design of the recirculation loop symmetrizes the transfer matrix and forces the matrix to be unity around any point of the recirculating loop.

- The transverse beam function at the undulator must match the undulator gap spacing, with the vertical beam betatron function β_y variable over a range of approximately 0.33 to 0.73 meters, with β_x fixed at 1 meter.

- The 6-, 30-, and 55-MeV beams must be separated as soon as possible up- and downstream of the SCA sections and directed through their own focusing channels to provide maximum independence of tuning and matching.

- Room must be provided in one of the 180° arcs for diagnostic equipment to monitor relative momentum shifts with a resolution of 10^{-5}.

- Because of the high beam power, the stay-clear distance must be at least 5σ throughout the entire beamline.

- The energy spread of the beam entering the undulator at 55 MeV is expected to be 0.4% (FWHM), increasing to 2% downstream of the undulator.

- The design must not preclude an upgrade in which the beam is recirculated (again) for deceleration in the SCA structures, a scenario that would save RF power and avoid activation of the high-energy beam dump.

- The optical cavity length of 24 meters constrains the distance between the 180° arcs. The undulator axis lies 3.44 meters away from the SCA axis, providing sufficient room for all components in the 7-meter-wide vault.

3.6.2 Transport Line Configuration

The transport line was designed and is described below as consisting of separate sections:

- 180° achromatic, isochronous arcs, corrected to second order.

- Transport sections between the SCA cavities and the 180° arcs, and from the 55-MeV 180° arc to the undulator.

- Beam "separators" at the ends of the SCA section.

- Energy slit and magnetic compressor at the exit of the 6-MeV injector.

- Transport lines to the beam dumps.

Figure 3-15 shows the overall beam transport system. The design is highly modular, and each section can be individually tuned and verified. The high degree of symmetry
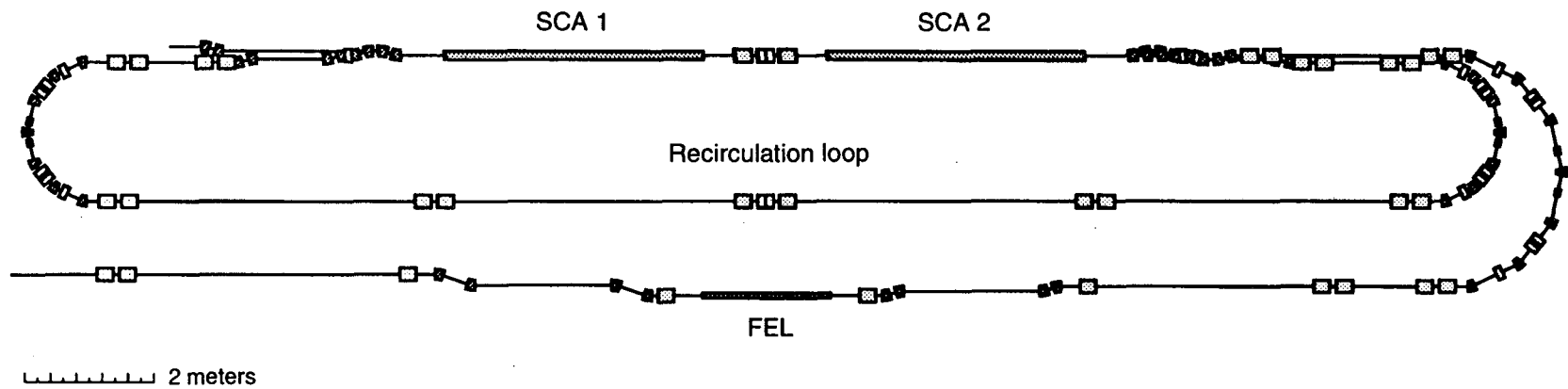
Recirculation loop

FEL

⊔⊥⊥⊥⊥⊥⊥⊥⊔ 2 meters

Figure 3-15. Plan view of the electron beam transport system, showing the location of the magnetic elements. The sizes of the magnets are not to scale. [XBL 922-5582]

results in an optimized optics solution and reduces the number of operating controls and power supplies. The 6-MeV beam enters the combiner through an achromatic dogleg at the upper left of the figure and is accelerated through the two RF cavities to a maximum of 30 MeV. If the beam requires further acceleration, the separator at the exit of the cavities directs it to the recirculation loop and a second pass through the accelerating cavities. Following a second pass, the beam is then directed around a third, broader arc to the FEL undulator. The optical axis of the undulator is translated 22.7 cm from the exit of the final 180° arc to provide clearance for the optical components. The beam emerging from the undulator is achromatically translated 34 cm off the undulator axis to pass around the cavity mirror and is directed to the beam dump.

The Arcs. Three arcs are provided, two mirror-image arcs for the recirculated 30-MeV beam and a 55-MeV arc that directs the beam to the entrance of the undulator. Each 30-MeV arc spans 2.35 meters; the 55-MeV arc, 3.21 meters. Each arc has a symmetric distribution of optical elements about its center and supports a beam envelope symmetric about its center. Each comprises seven identical dipoles, three families of quadrupoles, and one family of sextupoles. The locations of the quadrupoles and sextupoles are symmetric about the arc center point. The seven dipoles are necessary to achieve chromatic correction sufficient to ensure adequate performance at a ±1% momentum spread. A small beam size and smooth envelope are provided by this configuration. Figure 3-16 shows the physical layout of the magnetic components in the 55-MeV arc.

Each arc is achromatic and nearly isochronous, to preserve beam emittance and bunch length. To compensate for the slight non-isochronism in the dogleg translations in the beam separators and the offset of the undulator optical axis from the exit of the high-energy 180° arc, an equal negative non-isochronism is introduced in each of the 180° arcs, thus preserving isochronous transport from the SCA to the undulator. In addition, some additional bunch compression can be obtained by introducing an additional amount of nonzero m_{56} in the arcs, if required.

A pair of sextupoles straddling the central bending magnet in each arc corrects most achromatic terms to second order. This correction also reduces most third-order chromatic aberrations significantly, so that the beam displacement and angular error are held to within 10% of the ellipse parameters for momentum offsets up to ±1.5%.

Sufficient focusing in each arc keeps β_x below 1 meter over most of the arc, with the peak dispersion amplitude equal to 0.5 meter, thus providing convenient locations for stripline beam monitors in any of the three arcs.

The 30-MeV arcs are mechanically movable as a unit to allow variation in the path length around the recirculation loop.

The Transport Sections. The beam is matched from the accelerator section, through the beam separators, into the 30- and 55-MeV arcs by a pair of quadrupole doublets. After the first 30-MeV arc, the beam is transported to the second 180° arc by a symmetric arrangement of quadrupole doublets (and a triplet at the symmetry point). This straight section of the recirculation loop was designed to allow the future insertion of a second undulator and optical cavity.

The beam from the 55-MeV 180° arc is matched into the undulator by an arrangement of five quadrupoles and a four-dipole dogleg. The quadrupoles allow the vertical betatron
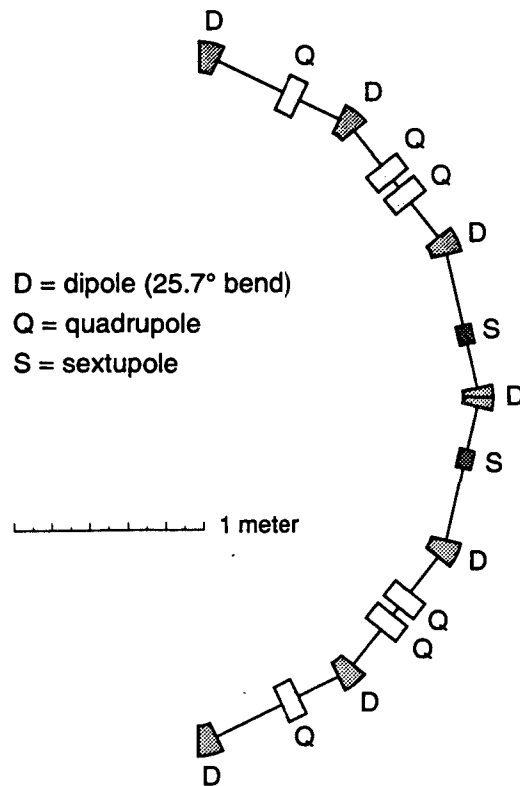
D = dipole (25.7° bend)
Q = quadrupole
S = sextupole

Figure 3-16. Plan view of the high-energy 180° arc. The recirculation arcs are essentially similar. [XBL 922-5583]

function β_y to be smoothly varied over a range from 0.33 to 0.73 meters, depending on the undulator gap spacing, with β_x held at a constant 1 meter. The dogleg is necessary because the optical clearance required near the cavity mirrors is larger than the magnet apertures. Near the undulator, the optical clearance radius is less than the 2.5-cm-radius magnet apertures, thus allowing nearby elements to be on the optical axis.

The total transfer matrix around the recirculation loop is unity, thus suppressing regenerative beam breakup in the SCA sections. The phase advance around the loop is a multiple of 2π, and the betatron amplitudes β_x and β_y are adjusted to the optimal value of 6 meters between the two SCA sections. In addition, the beam is matched in all three 180° arcs to produce a symmetric envelope around each symmetry point. All of these constraints are satisfied by the quadrupole arrangements in the straight sections on each side of the three arcs.

The 6-MeV beam from the injector is directed to the first SCA section by an offset section comprising four identical dipoles, described in more detail below. The 55-MeV beam from the undulator is displaced by 34 cm from the optical axis by an achromatic translation section with a similar configuration.

The Beam Separators. Each of the two SCA sections provides an energy gain of up to about 12 MeV. The 6-MeV beam from the injector is thus accelerated to a maximum of about 30 MeV on the first pass and can then be recirculated and further accelerated to a

61

maximum of about 55 MeV on the second pass. The beam orbits must be separated at the exit of the second SCA section and directed into their respective beam transport systems. Likewise, the beam combiner at the entrance to the first cavity must merge the orbits of the 6-MeV beam from the injector with that of the beam from the recirculation loop.

A single separator design was chosen for both the entrance and the exit of the accelerator section, in part to preserve the option of a future energy-recovery upgrade in which the 55-MeV beam would be returned to the accelerator section for deceleration. (Both combiner and separator are described here as "separators," since the magnetic design is the same in each case.) This separator must merge the orbit of a 6-MeV beam with that of a beam with energy equal to 6 MeV + ΔE, where ΔE is the energy gained in the two SCA cavities. Likewise it must separate beams with energies of 6 MeV + ΔE and 6 MeV + $2\Delta E$. The nominal 30- and 55-MeV beams must be provided with a stay-clear of at least 5σ, along with at least 1 cm of magnetic septum width for further bending. The betatron amplitude at this point is about 12 meters in both planes, and the normalized rms emittance is 30 mm·mrad.

The nominal separator design (Fig. 3-17a) provides first for the separation of the 6-MeV beam, returning higher-energy beams to the axis; it then separates the two remaining beams, returning only the highest-energy beam to the axis. Some of the dipoles are magnetic (iron) septa; the rest are conventional. Not all elements of this nominal design are needed in practice: At the entrance to the accelerator section (Fig. 3-17b), only the 6-MeV injected beam and the beam from the recirculation loop are present; at the exit (Fig. 3-17c), only the two higher-energy beams must be separated.

The magnet group nearest SCA 1 allows the 6-MeV beam to clear a septum and to be translated away from the recirculated beam, which is returned to the axis regardless of its energy. The magnet group downstream of SCA 2 separates "one-pass" and "two-pass" beams, returning the higher-energy beam to the axis and directing it to the larger 180° arc. In this second group, the lower-energy beam is offset 19.8 cm toward the inside of the ring and is directed to the smaller 180° arc. The smallest (worst-case) separation of these two beams is 4.2 cm; it occurs in the middle of the second group of four dipoles when the SCA is providing its maximum 24-MeV energy gain. The two 180° recirculation arcs are identical, so the offsets provided for the recirculated beam at each end of the SCA section are also the same. All dipoles are 12 cm long, running at 0.056 T in the entrance separator and 0.3922 T in the exit separator. The design of Fig. 3-17 satisfies the requirement that the acceleration gain in the cavities may vary, whereas the injection energy is always 6 MeV. Likewise, the design permits a low-energy beam from the accelerator section to be sent directly to the undulator.

The bumps and doglegs of the separators are achromatic, but not isochronous. An equal and opposite non-isochronism is introduced in the 180° arcs, as described above. The separator dipoles themselves strongly focus the beam, which is taken into account in the placement of the quadrupoles used to control the peak beam sizes.

The Energy Slit and Magnetic Compressor. The four-magnet translation for the 6-MeV beam (see Fig. 3-17b) also serves as a magnetic energy compressor and energy selection slit. The m_{56} (isochronous) matrix element for the translation will be set by the final choice of geometry at about 0.4, and the dispersion η_x is about 0.33 meter, where the matched beam amplitude β_x is about 0.55 meter. This is more than sufficient to give a
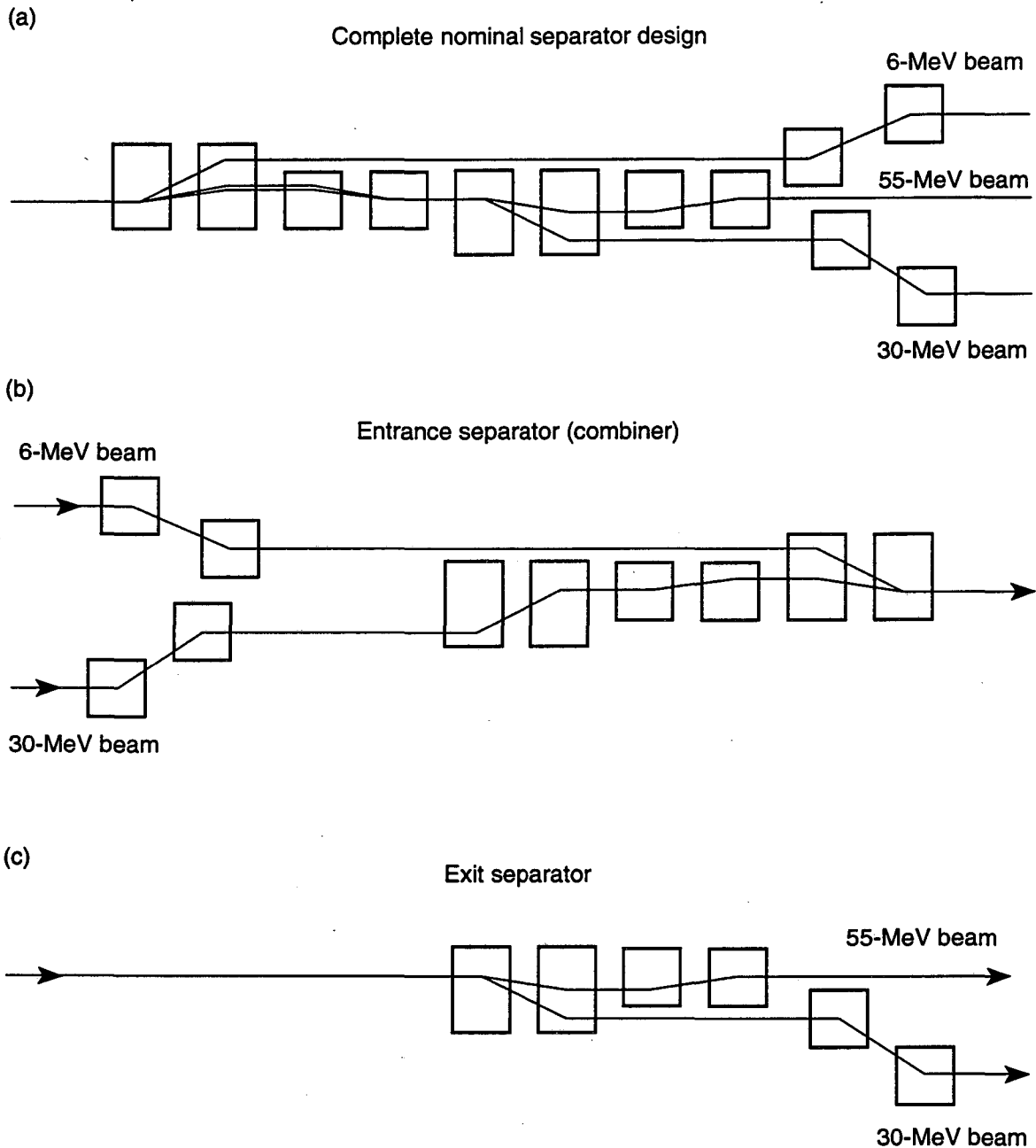
Figure 3-17. Schematics of three separator configurations: (a) the nominal separator design, which provides for the separation of the 6-MeV injected beam, a medium-energy (typically, 30-MeV) beam, and a high-energy (typically, 55-MeV) beam; (b) the entrance "separator," which combines the injected beam and the recirculated beam; and (c) the exit separator, which directs beam to the two arcs downstream of the accelerator section. [XBL 922-5568]

100-keV slit at a 5σ beam radius, with a normalized emittance of 30 mm·mrad. As this double translation is essentially a drift space in the vertical plane, the vertical beam size can be made as large as desired by external focusing to reduce the peak power density on the energy slit.

Transport System to the Beam Dumps. The beam is transported to the beam dumps by a conventional optics configuration. Beam from the accelerator section can be dumped simply by turning off the power to the first dipole in the 180° arc. With an average power of more than 600 kW at the highest energy and current, the beam must be spread over an area of at least 80 cm² at the dump. A raster scanner avoids the demands for precise steering and the long transverse-distribution tails associated with quadrupole or higher-multipole beam spreaders. A fast scanning-failure monitor is also required to protect the target. During commissioning the raster scanner will be installed at the beam dump downstream of the accelerator section. It will then be moved to the second beam dump (downstream of the undulator) for routine operations, and a multipole beam spreader will be installed at the first dump.

Summary. An inventory of the required magnetic elements is given in Table 3-10, along with the number of families needing independent power supplies. The dipoles are all short, typically 10 cm long, with modest fields and less than a 2-cm gap. The

Table 3-10. Inventory of the dipole and quadrupole magnets required for the electron beam transport system, excluding the transport lines from the injector and to the beam dump downstream of the accelerator section.

	Quadrupoles		Dipoles	
	No.	Families	No.	Families
First recirculation arc	6	3	7	1
Second recirculation arc	6	3	7	1
High-energy arc	6	3	7	1
30-MeV SCA line	8	4		
55-MeV SCA line	4	4		
Recirculation line	11	6		
Undulator line	10	8	8	1
Entrance separator	1	1	10	2
Exit separator	1	1	6	2
Total	**53**	**33**	**45**	**8**

quadrupoles are typically 25 cm long, with modest gradients equal to less than 15 T/cm. Magnet elements needed in the beam transport systems from the injector and to the beam dump downstream of the accelerator section, as well as sextupoles, are not included in Table 3-10.

The design of the electron beam transport will easily accommodate future upgrades. In particular, the configuration allows for the future addition of a second undulator in the recirculation loop, adjacent to the undulator currently planned. In addition, the beamline configuration allows inclusion of an energy-recovery deceleration option, which would save RF power and reduce the power deposited in the beam dump.

3.6.3 Beam Dynamics of Recirculation

As described above, the electron beam must pass twice through the accelerator section to reach a beam energy greater than 30 MeV. A recirculation path thus routes the 30-MeV beam back to the entrance of the first RF cavity for further acceleration to energies up to 55 MeV. The major beam dynamics issues of recirculation are (i) the multipass beam breakup (BBU) instability and (ii) electron beam emittance growth. The former arises from the fact that the high-Q superconducting RF structures retain a "memory" of previous beam passage. Under suitable phase conditions, this can lead to a resonance, resulting in beam loss caused by fast growth in the amplitude of coherent beam motion. The second concern, emittance growth, arises from growth of beam phase space due to prolonged sampling of longitudinal and transverse electromagnetic wakefields in the linac.

Multipass Beam Breakup. The threshold current for multipass beam breakup was simulated with the multibunch code TDBBU [Krafft and Bisognano, 1987], using a simple model of a four-cavity accelerator. The accelerator was modeled as a full FODO cell having a 60° phase advance (first pass) and a half-cell length of 6 meters (Fig. 3-18).
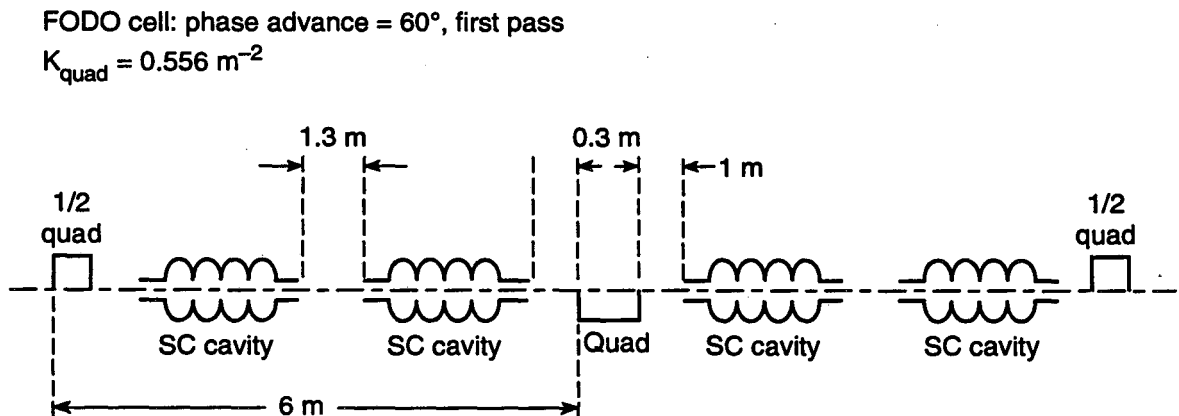

FODO cell: phase advance = 60°, first pass
$K_{quad} = 0.556 \text{ m}^{-2}$

Figure 3-18. Model of the SCRF cavity and magnet configuration, used for simulation of multipass beam breakup. [XBL 922-5569]

The focusing was provided by 30-cm quadrupole magnets with focusing parameter $K = 0.556 \text{ m}^{-2}$ (again, for the first pass only). Within each half-cell were two 500-MHz superconducting cavities, each with an acceleration length equal to 1.2 meters. The cavities were placed 1 meter from the quads on either side of the half-cell and 1.3 meters from each other. Eight (four × 2 polarizations) transverse higher-order modes (HOMs) were assumed to deflect the beam transversely at the center of each cavity. The HOM properties are summarized in Table 3-11. These values, from measurements at DESY on 500-MHz copper cavities [Willeke and Proch, 1991], will be replaced by measurement results from cold superconducting cavities when they become available. (These values also reflect only a selected set, presumed to be harmful, from the full set of HOMs.) The frequencies of the HOMs were assumed to be equal for all cavities, suggesting that the threshold current is underestimated by the simulation, because the frequencies of the HOMs will, in fact, have some spread due to manufacturing differences in the individual cavities. The pass-band mode with the largest R value was chosen, because, all other things being equal, the threshold current is proportional to $1/R$.

The beam was taken to have an injection energy of 5 MeV, and the recirculation time delay was taken as equal to 52 RF periods. Examples of simulation results are shown in Figs. 3-19 through 3-21, where the initial excitation is provided by a displacement of the injected beam. The figures show the momentum of every 500th bunch as a function of bunch number (that is, time). In Fig. 3-19, the current is 90 mA, below the threshold current of 100 mA. In Fig. 3-20, the current is 100 mA, still slightly under the threshold current. The oscillations, which are due to the RF fluctuations, decay relatively slowly compared to those in Fig. 3-19. In Fig. 3-21, the current is 110 mA, and the oscillation grows due to the BBU instability. The 977-MHz horizontal mode in the final cavity is the main electromagnetic mode responsible for the instability.

Table 3-12 summarizes the results of threshold calculations for the conditions described above, and for situations in which recirculation is used to decelerate the beam and in which the injection energy is lower. The deceleration scenario causes a 10-mA reduction in the instability threshold; whereas reducing the injection energy to 2.5 MeV

Table 3-11. Cavity parameters for the IRFEL multipass BBU instability simulation.

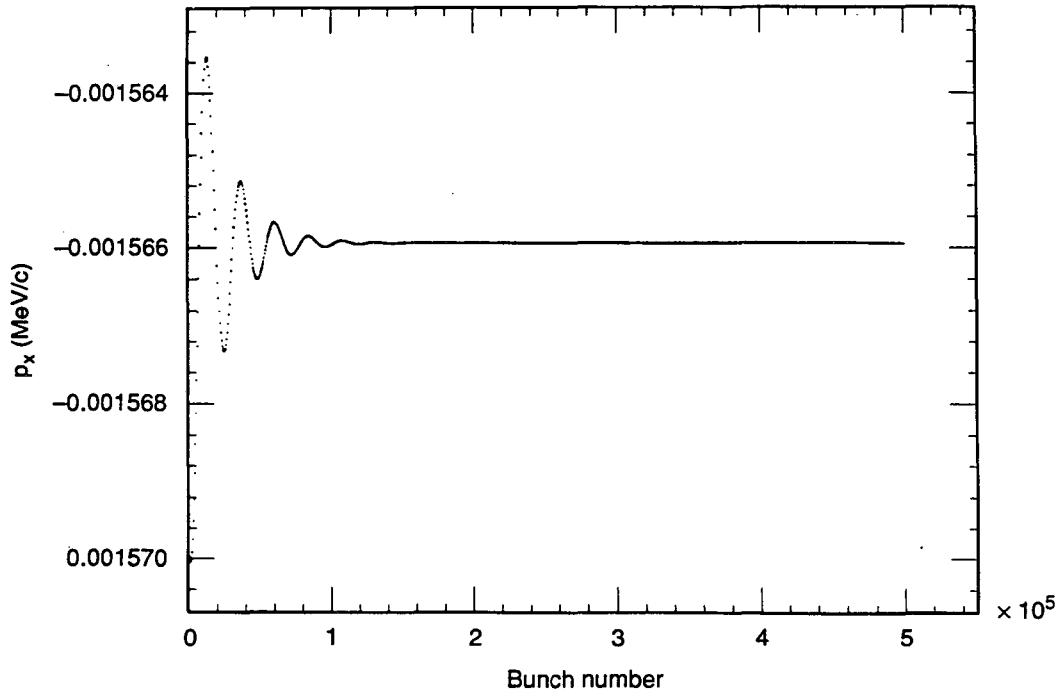| Frequency (MHz)	Polarization	R/Q (Ω)	Q
651	x	17.0	6200
651	y	17.0	6200
729	x	15.4	16000
729	y	15.4	16000
977	x	51.8	16000
977	y	51.8	16000
1107	x	4.8	1000
1107	y	4.8	1000

Figure 3-19. Bunch momentum as a function of bunch number for I = 90 mA.
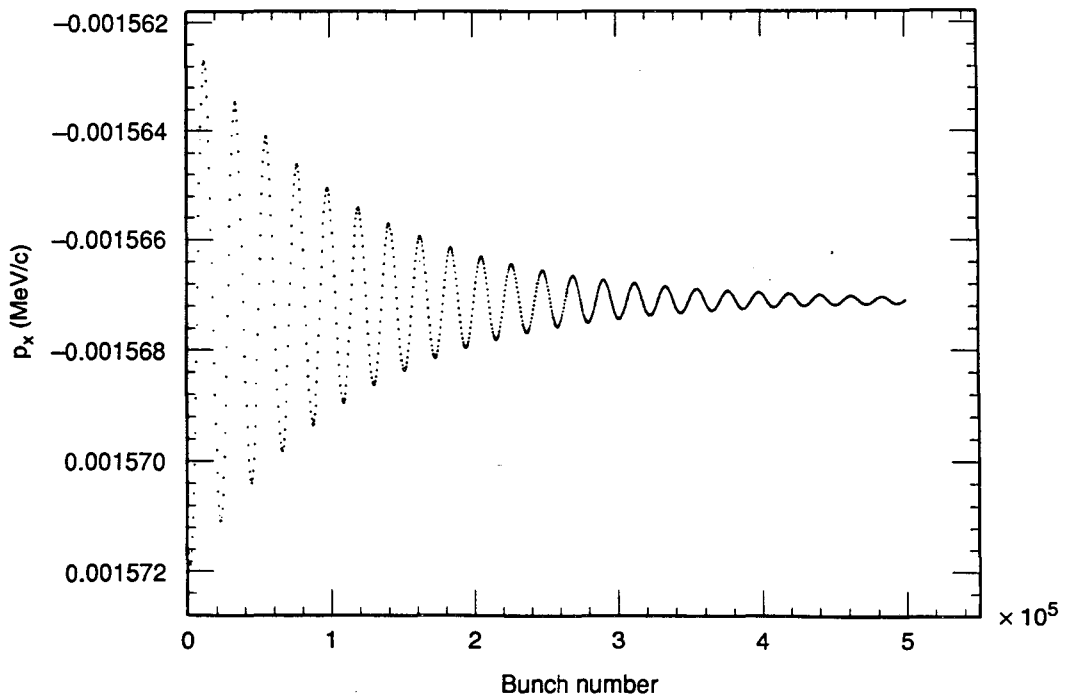*[XBL 922-5584]*

Figure 3-20. Bunch momentum as a function of bunch number for I = 100 mA.
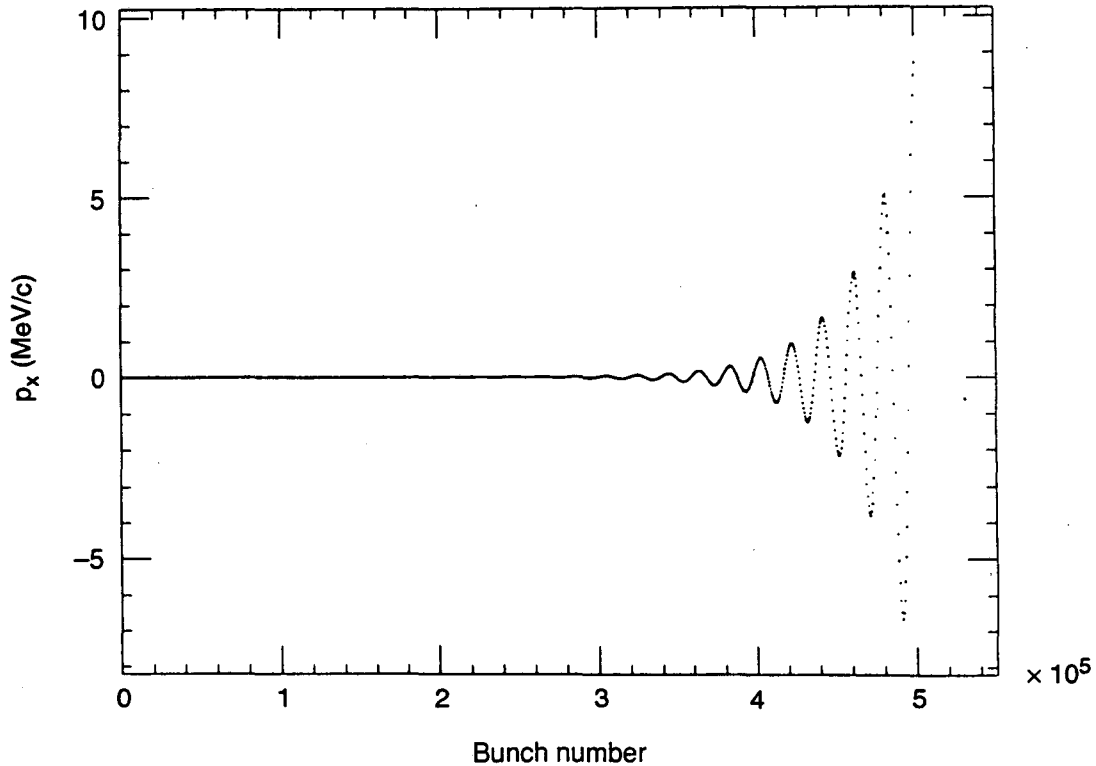*[XBL 922-5585]*

Figure 3-21. Bunch momentum as a function of bunch number for I = 110 mA.
[XBL 922-5586]

reduces the threshold by 5 mA. The threshold is relatively insensitive to the injection energy because the resulting energy difference at the final cavity is only 10%.

The threshold current is much more sensitive to the recirculation time delay. For example, given the conditions first described, but with a time delay of 53 RF periods instead of 52, the threshold current increases to 157 mA. The same mode goes unstable, but sin $(\omega_{HOM}\tau)$ gets closer to zero, thus increasing the threshold [Krafft et al., to be published]. If the time delay is 54 RF periods, the threshold current rises to 340 mA.

Table 3-12. Threshold currents for the multipass BBU
instability, for four operating scenarios.

	Instability threshold (mA)	
	2.5-MeV injection	5-MeV injection
Accelerating recirculation	95	100
Decelerating recirculation	85	90

However, now the 110-MHz horizontal mode is the one that goes unstable. For the 977-MHz mode, sin $(\omega_{HOM}\tau) \cong 0$ at 54 cycles of recirculation time delay.

Finally, simulations were performed with a 30° phase advance on the first pass. The threshold current was found to be 102 mA, suggesting little sensitivity to the phase advance. Also, simulations were undertaken of the case where an accelerating recirculation was followed by two decelerating recirculations. Again, the threshold current was about 100 mA.

Single-Bunch Phenomena. If care is taken to minimize changes in vacuum chamber cross section, then the short-time impedance is due mainly to the cavity contributions. The longitudinal wake for five-cell CEBAF cavities is 4.7 V/pC at 10 ps, providing an overestimate for the four-cell DESY cavities of 1.6 V/pC at 30 ps. The uncorrected full-width energy spread for a 1.6-nC bunch would be 4×10^{-4}, yielding about 1×10^{-4} after correction [Krafft and Bisognano, 1989].

The transverse-wake slope parameter is 1 V/(pC·cm²), again scaled from CEBAF values. When such a slope parameter is used in a series of single-bunch simulations, Fig. 3-22 results. The emittance growth is substantial only for peak currents greater than 200 A, well beyond the operating range of the IRFEL.

Conclusions. The threshold currents for multipass beam breakup were found to be significantly higher than the IRFEL design current of 30 mA; therefore, no further damping of DESY-type cavities is necessary to assure stable operation. Because there are only a few cavities, and because only one HOM in one cavity is the main contributor to
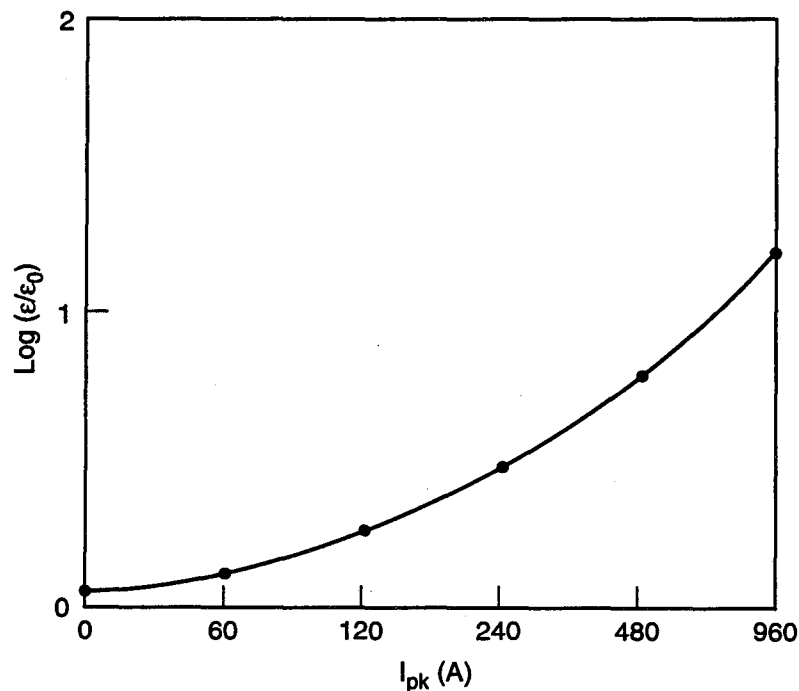

Figure 3-22. Emittance growth as a function of peak current, assuming a transverse-wake slope parameter scaled from CEBAF values. [XBL 922-5575]

the instability, the threshold current is strongly dependent on the recirculation time delay. A recirculation time delay of 54 RF cycles increases the threshold current by a factor of three, to at least 340 mA, where a different mode goes unstable. Our design includes flexibility in adjusting this parameter, to help ensure stable operation with recirculation.

Single-bunch instability was also computed, assuming that the machine impedance arises mainly from the superconducting cavities. For the peak operating currents of the IRFEL, emittance growth will be insignificant compared with the initial emittance, and the energy spread in the bunch should be about 1×10^{-4}.

3.7 SHIELDING AND BEAM DUMPS

3.7.1 Shielding Design Criteria

The DOE limits for occupational workers and for the general public are summarized in Table 3-13 [USDOE Order 5480.11, 1989; USDOE Order 5400.5, 1990]. Since the IRFEL will be located adjacent to the ALS, the personnel and site boundary exposures attributable to the FEL alone must be kept low enough to ensure that the overall exposures (IRFEL + ALS + others) are held to their historically low values. For this reason, our objective was to design the shielding such that radiation exposures outside the shielding will be less than or equal to *100 mrem per 2000 hr*, assuming conservative beam loss scenarios. This will ensure that the FEL's contribution to personnel exposure and site boundary exposure is consistent with the ALARA (as low as reasonably achievable) principle.

3.7.2 Shielding Design: Assumptions and Results

The IRFEL is capable of producing about 600 kW of 55-MeV electrons. For purposes of radiation shielding design, we assumed that beam is lost at a rate of 10% of full beam power (about 60 kW, 55 MeV) continuously at any point inside the accelerator vault. This is a conservative estimate, since most beam components may not withstand the

Table 3-13. DOE radiation exposure limits for occupational workers and the general public.

	Dose
Occupational exposure	
Maximum allowed	$5.0 \ \text{rem} \cdot \text{yr}^{-1}$
Design objective	$1 \ \text{rem} \cdot \text{yr}^{-1}$
	$(0.5 \ \text{mrem} \cdot \text{hr}^{-1})$
Public exposure	
On site	$100 \ \text{mrem} \cdot \text{yr}^{-1}$
Site boundary	$10 \ \text{mrem} \cdot \text{yr}^{-1}$

thermal stresses associated with such a continuous loss. In addition, most beam tuning and collimating will be done at low energies and with low intensities.

Wall and ceiling shielding requirements are based on the radiation levels produced by secondary particles at 90°. Shielding requirements around the beam dumps are based on a continuous 100% loss (600 kW, 55 MeV).

Shielding analyses were based upon the work of Jenkins [1979]. Calculations were performed with a computer program from the Stanford Linear Accelerator Center (SLAC), which incorporates these analytical models. The expressions for determining the dose equivalents from photons (H_γ) and neutrons (H_n) are as follows:

$$H_\gamma = 10^{-11} E \left(\frac{\sin \theta}{R}\right)^2$$

$$\times \left[\frac{133 \exp\left(-\frac{\mu}{\rho} \frac{\rho d}{\sin \theta}\right)}{\left(1 - 0.98 \cos \theta\right)^{1.2}} + \frac{0.27 \exp\left(-\frac{\rho d}{\lambda_1 \sin \theta}\right)}{\left(1 - 0.72 \cos \theta\right)^2}\right] \quad [\text{rem·cm}^2\text{·GeV}^{-1}] \quad (3\text{-}18)$$

where

H_γ = dose equivalent (in rem) due to photons, per GeV-electron, normalized to a distance of 1 cm

E = electron energy, in GeV

R = distance normal to the beamline to outer shield surface, in cm

μ/ρ = 0.0243 cm²·g⁻¹, the mass attenuation coefficient for the Compton minimum in the target material (8 MeV for iron)

d = shield thickness at 90° to the beam direction, in cm

λ_1 = 120 g·cm⁻², the attenuation length of high-energy neutrons in concrete

ρ = 2.25 g·cm⁻³, the density of ordinary concrete

θ = angle with respect to the beam direction

and

$$H_n = 10^{-11} E \left(\frac{\sin \theta}{R}\right)^2 \left[\frac{13.7 \exp\left(-\frac{\mu}{\lambda_1} \frac{\rho d}{\sin \theta}\right)}{A^{0.65}\left(1 - 0.72 \cos \theta\right)^2} + \frac{10 \exp\left(-\frac{\rho d}{\lambda_2 \sin \theta}\right)}{\left(1 - 0.75 \cos \theta\right)}\right.$$

$$\left. + 4.94 \, Z^{0.66} \exp\left(-\frac{\rho d}{\lambda_3 \sin \theta}\right)\right] \quad [\text{rem·cm}^2\text{·GeV}^{-1}] \quad (3\text{-}19)$$

where

λ_2 = 55 g·cm^{-2} for the mid-energy neutrons (1 tenth-value layer = 54 cm concrete)

λ_3 = 30 g·cm^{-2} for giant resonance neutrons (1 tenth-value layer = 29 cm concrete)

A = atomic weight of the target material

Z = atomic number of the target material

Since the maximum energy of the IRFEL is 55 MeV, the terms representing the contributions from mid- and high-energy neutrons were neglected and only giant resonance neutrons were considered [Jenkins, personal communication].

Figure 3-23 shows the dose rate as a function of concrete thickness. The three curves represent different thicknesses of local lead shielding. The top curve is dominated by bremsstrahlung photons that can be effectively reduced by adding lead shielding around points of local continuous loss. However, a point of diminishing returns is reached at about four inches of additional lead, at which thickness the dose equivalent rate is due largely to giant resonance neutrons. To achieve the criterion of 100 mrem per 2000 hr, a level less than or equal to

$$\frac{100 \text{ mrem}}{2000 \text{ hr}} \cdot \frac{1}{60 \text{ kW}} \cdot \frac{1 \text{ rem}}{1000 \text{ mrem}} = 8.3 \times 10^{-7} \text{ rem·kW}^{-1}\text{·hr}^{-1} \qquad (3\text{-}20)$$

is needed. From Fig. 3-23, we find that this corresponds to about 10 feet of concrete. The shield walls and the ceiling will therefore consist of 10 feet of ordinary concrete ($\rho = 2.25$ g·cm^{-3}), and 4 inches of additional lead will surround local loss points such as the collimators. Additional loss points will be identified during commissioning.

3.7.3 Beam Dumps

The dumps and associated systems were designed to absorb and dissipate a 600-kW, 55-MeV, cw electron beam. Ample precedent exists for such a design. SLAC has successfully operated high-power beam dumps of 600 kW and 2.2 MW for an electron energy of 20 GeV [Walz and Lucas, 1969; Walz et al., 1965], and LLNL has considered the design of a 225-MW, 150- to 300-MeV electron beam dump [Van Sant et al., 1989].

For high-average-power, low-energy electron beams, only aluminum or other materials of low atomic number (Z) are suitable as beam absorbers. Power deposition increases with Z and may cause melting or vaporization in high-Z absorbers. For the IRFEL, only water is suitable to absorb the majority of the electron beam power. A 55-MeV electron in water has a minimum collision stopping power of 1.82 MeV·cm^2·g^{-1} [Berger and Seltzer, 1983]. This corresponds to a maximum range of about 27 cm, or about 1 foot. An electron loses energy by two major processes: collisional losses and radiative losses, the latter becoming more important at high energies. The ratio of radiative to collisional losses is about 0.5 [Berger and Seltzer, 1983]. Therefore, about one-third of the power at 55 MeV in water is converted to radiation, that is, bremsstrahlung x-rays. The bremsstrahlung energy spectrum can be characterized as having a preponderance of low-energy photons, asymptotically decreasing to near zero at
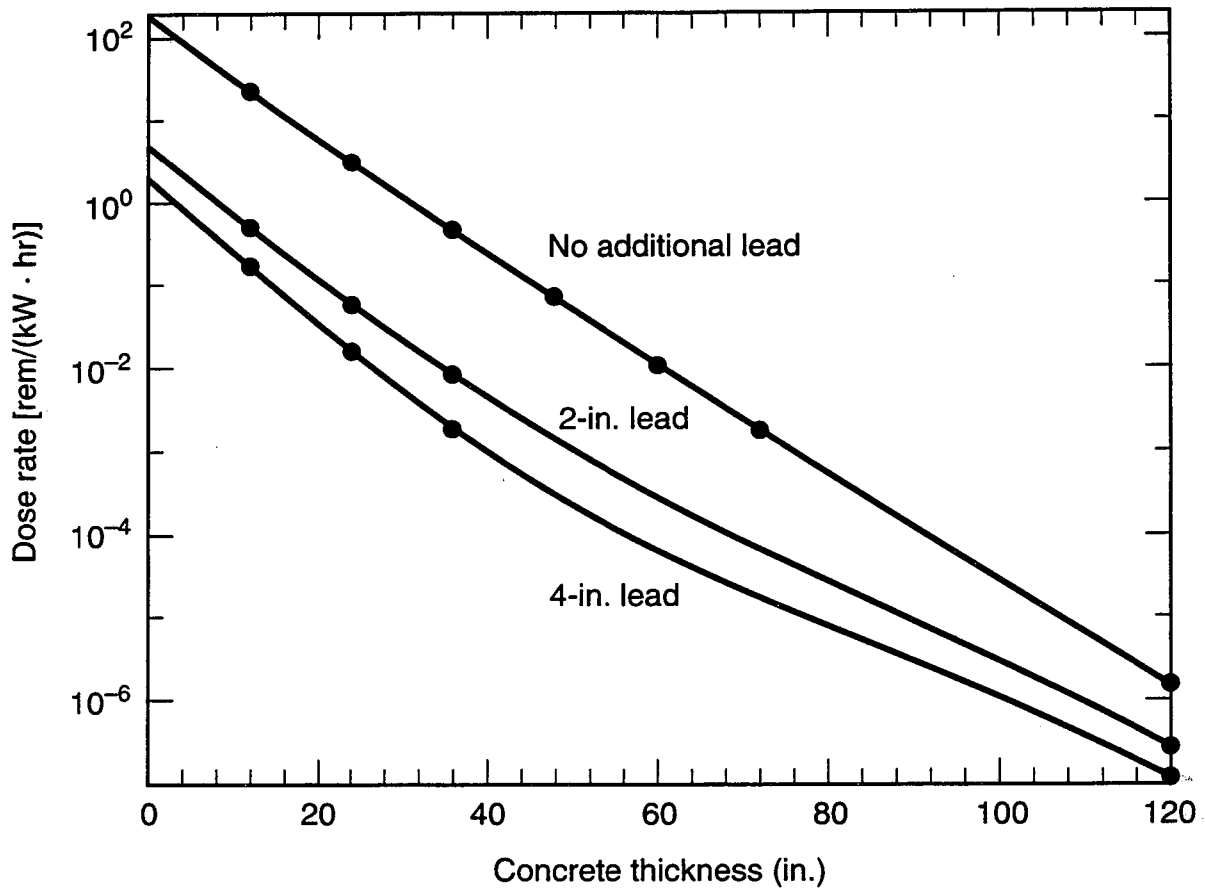
Figure 3-23. Calculated dose rate from the IRFEL, as a function of concrete thickness, for the cases of 0, 2, and 4 inches of additional lead. [XBL 921-5567]

the incident electron energy. Therefore, the length of the dump can be minimized by using high-Z materials at the appropriate depth.

Each beam dump will therefore consist of (i) about two feet of water to range out the incident electrons, absorb a large fraction of the soft bremsstrahlung x-rays, and provide a large coolant reservoir, (ii) a six- to twelve-inch water-cooled aluminum block to absorb a large fraction of the intermediate- and high-energy x-rays, and (iii) a high-Z backstop consisting of two to four inches of tungsten (or other high-Z material) to attenuate the remaining high-energy bremsstrahlung x-rays. (A detailed design must await the results of Monte Carlo calculations to determine energy deposition profiles.) A schematic of the complete system is shown in Fig. 3-24. One dump is located downstream of the FEL and will be in continuous use during routine operation. A second dump, sharing the same surge tank, hydrogen recombiner, heat exchanger, and ion exchange system, is located at the end of the RF linac (see Fig. 1-1). This second dump will be used primarily during commissioning and tune-up.

The primary, or radioactive, loop of the dump is isolated from the secondary, or plant water, loop. In addition, a demineralizer loop provides that some fraction of the cooling
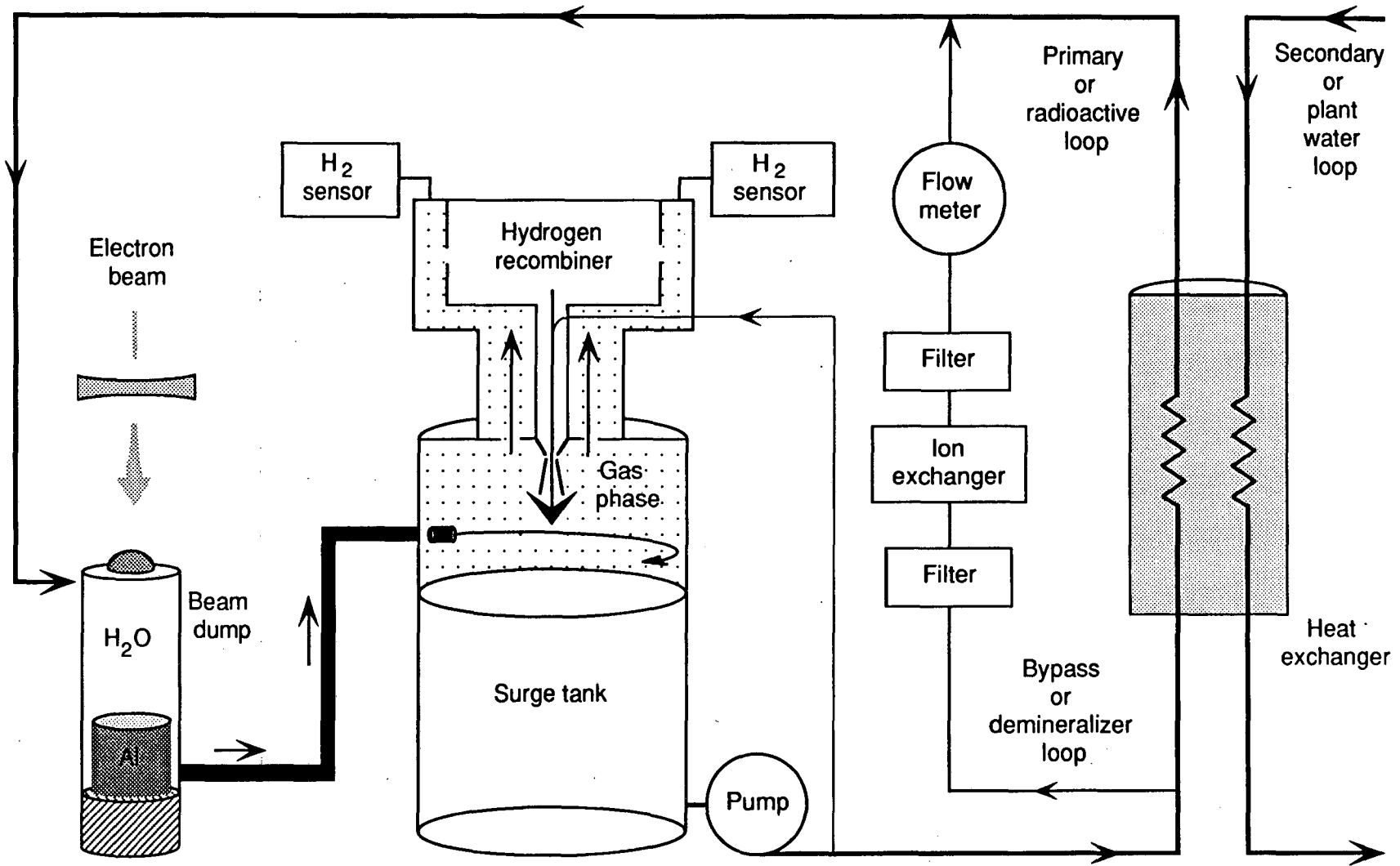
Figure 3-24. Schematic of the beam dump design for the IRFEL. [XBL 924-5658]

water is continuously purified in the ion exchange bed. The surge tank capacity is about 100 gal (75 gal liquid and 25 gal gas) and is sized to accommodate about 25% of the primary-loop water volume. Aluminum-copper electrolysis will be avoided by using stainless-steel plumbing. All welds will be radiographed, and the plumbing will be buried in the floor or wall. Buried plumbing will reduce radiation exposure during routine and unscheduled maintenance.

Figure 3-25 shows the layout of one of the beam dump systems within the accelerator wall. The beam dump and its associated water systems are isolated from the vault, as well as from each other, to ensure that radiation exposures are kept as low as reasonably achievable (ALARA). The vault will contain all water spills in a sump/hold-up tank to ensure that radioactive water is not released to the sanitary sewer or storm drain.

Window Design. A critical element of the beam dump system is the vacuum window into the beam dump. The window must be strong enough (that is, thick enough) to withstand stresses created by the difference in pressure, but thin enough that energy deposition, and hence thermal stresses, are minimized. We chose a 2-mm-thick aluminum window, which will be curved to reduce the stresses caused by pressure differences between the beam dump and the accelerator vacuum.

As the beam penetrates the window, volumetric heating occurs. This heat is removed by the coolant water behind the window. Assuming only convective heat transfer from the back of the window, the heat flux can be determined from

$$\frac{q}{A} = t_w \frac{I_{avg}}{A_b} \rho_w \left.\frac{dE}{dx}\right|_{min} = h \left(T_w - T_\infty\right) \; [W \cdot cm^{-2}] \tag{3-21}$$

where

t_w	= 2 mm, the window thickness
I_{avg}	= 12 mA, the average current
A_b	= beam area, in cm^2
ρ_w	= 27 g·cm^{-3}, the window density
$\left.\dfrac{dE}{dx}\right|_{min}$	= 1.8 MeV·cm^2·g^{-1}, the minimum collision stopping power
h	= convective heat transfer coefficient, in W·cm^{-2}·°C^{-1}
T_w, T_∞	= window and water temperatures, in °C

To minimize thermal stresses and ensure long life, the temperature difference between window and coolant water ($\Delta T = T_w - T_\infty$) will be limited to about 100°C. Assuming a reasonable convective heat transfer coefficient of 1.5 W·cm^{-2}·°C^{-1}, this ΔT can only be achieved by reducing the electron current density, that is, by increasing the area of the beam. The minimum allowable beam area can be determined by solving for A_b in Eq. 3-20:

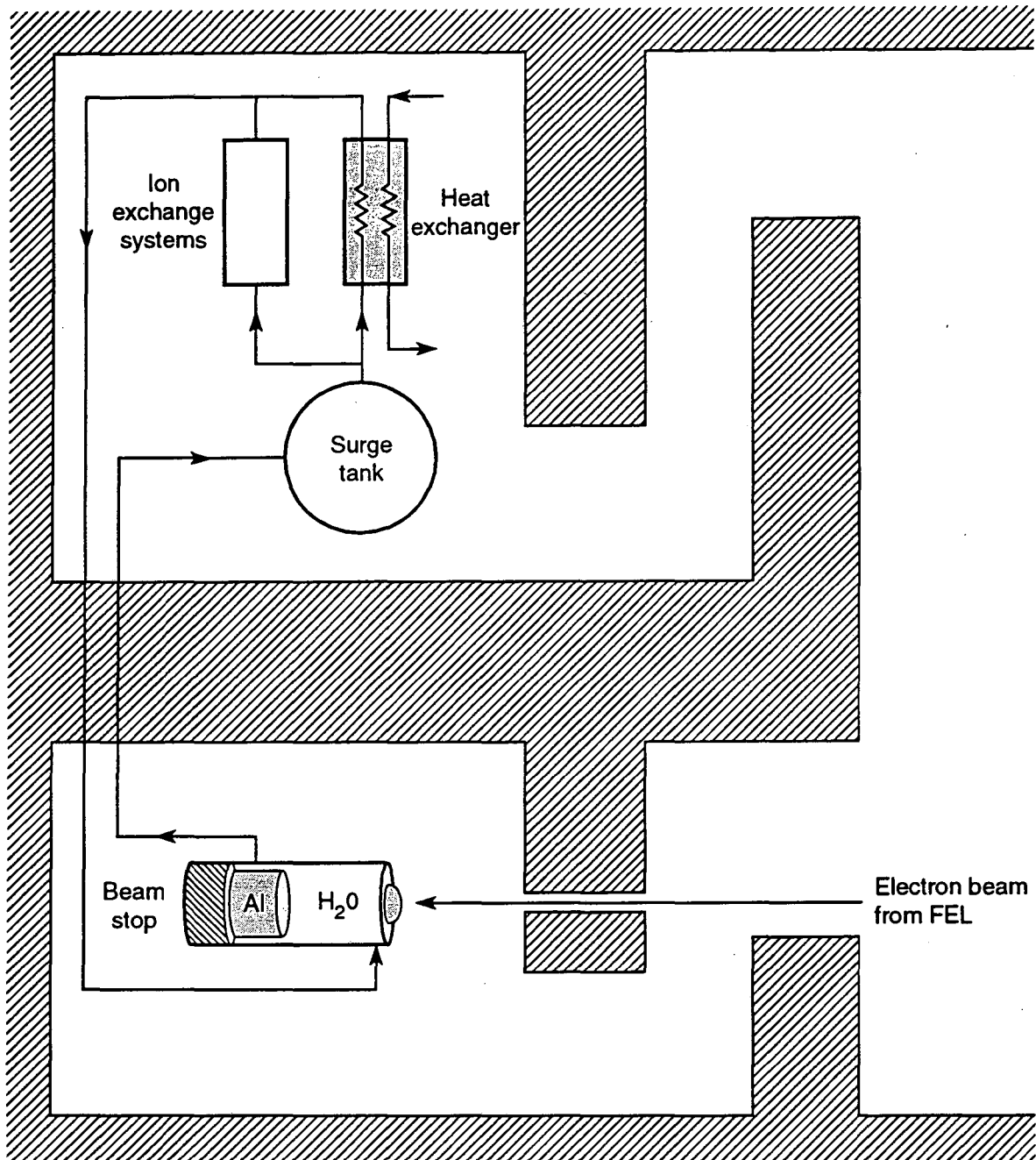$$A_b \geq \frac{t_w I_{avg} \rho_w}{h \, \Delta T} \cdot \left.\frac{dE}{dx}\right|_{min} \tag{3-22}$$

Figure 3-25. Layout of the main beam dump system inside the FEL vault. A second beam dump, sharing the same surge tank, hydrogen recombiner, heat exchanger, and ion exchange system, will be located at the end of the RF linac (see Fig. 1-1). [XBL 922-5610A]

Using values given previously yields a minimum area of 80 cm^2. To be conservative, we adopted a minimum of 100 cm^2, or a minimum diameter of 10 cm. The heat flux calculated from Eq. 3-21 is therefore only 150 W·cm^{-2}.

A series of parallel tubes will be directed toward the back of the window to sweep it with cool water and thus ensure uniform heat convection.

Hydrogen Recombination. Another major design feature of the beam dump system is the hydrogen recombiner. Hydrogen gas is produced in the dumps by radiolysis, because the energy of the incident radiation is greater than the ionization potential of water. After the resulting H_2 saturates the water, it appears as a potentially explosive gas, at a rate of 0.3 liters$\cdot MW^{-1}\cdot s^{-1}$ [Walz and Seppi, 1967]. Hydrogen gas has a lower explosive limit (LEL) of only 4%. When formed in an air environment, it concentrates and can quickly reach explosive levels. Radioactive gases produced in the water system prohibit the venting of this hydrogen. The most common solution in such situations is to catalytically recombine the hydrogen with oxygen to form water. This process has been described in detail [Walz and Lucas, 1969] and is the basis of our design. An isometric view of the SLAC hydrogen recombiner is shown in Fig. 3-26.

This dump has been operating successfully since the mid-1960s. Cooling water from the beam dump enters from the bottom left. Hydrogen gas collects in the gas space and is drawn into the recombiner, where it is heated to the optimum temperature, then over the catalyst bed, where it is mixed with oxygen to form water. Redundant H_2 sensors ensure that the recombiner is working properly at all times.

Future Work. The following areas have been identified as meriting further attention during detailed design work:

- Thermal and stress analyses to determine the fatigue life of the window.

- Detailed Monte Carlo radiation transport calculations to determine energy deposition profiles inside the dump.

- Appraisal of alternative designs for a safe, reliable means of protecting/interlocking the integrity of the vacuum window.
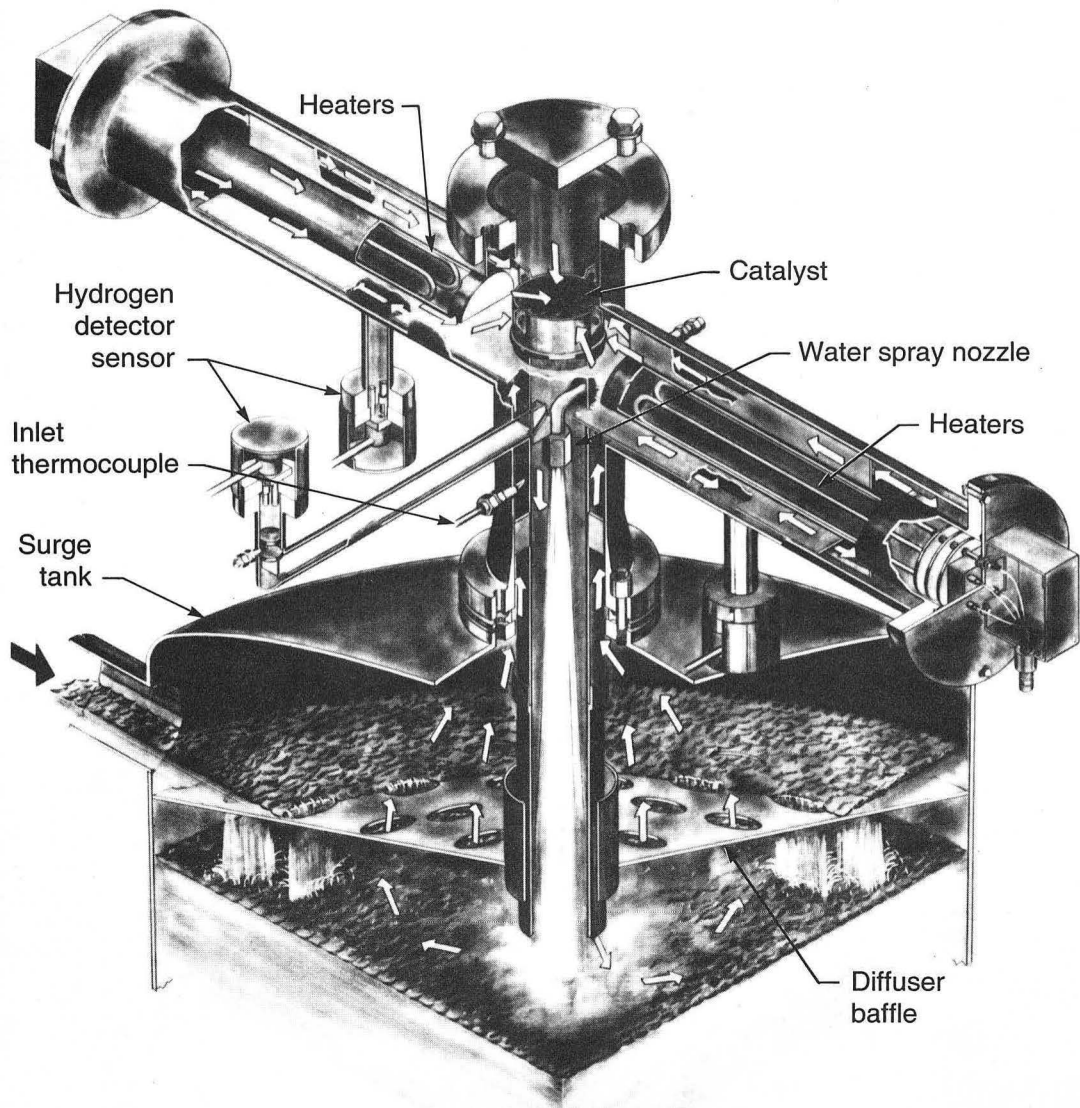
Figure 3-26. Artist's drawing of the catalytic hydrogen recombiner used at SLAC.

4.

FEL SYSTEMS

PREVIOUS sections described the accelerator and the transport optics necessary to produce an electron beam suitable for a free-electron laser. The sections that follow focus on the physical components that constitute the FEL itself—the undulator and the elements of the optical cavity. An introductory section provides a brief overview of FEL physics, concentrating especially on design and modeling issues pertinent to the performance of an IRFEL for chemical dynamics research. Section 4.2 then follows with a description of the undulator design, which draws heavily on the design, engineering, and construction experience gained at the Advanced Light Source. A final central design issue, the choice of a practical outcoupling scheme, is discussed in detail in section 4.3, as an introduction to the description in section 4.4 of the elements of the optical cavity, including the optical diagnostics systems. Finally, section 4.4 also describes the optics design for the transport system that will deliver infrared radiation from the FEL to the users.

4.1 FEL MODELING AND DESIGN ISSUES

In a free-electron laser, electron beams receive a periodic transverse kick in the magnetic field of the undulator so that the electrons' kinetic energy is transferred to the radiation field. The radiation is trapped in an optical cavity and amplified by interacting with the electron beam during successive traversals. A portion of the optical energy in the optical cavity is then coupled out and transported to experimental stations. In this section, we consider the issue of modeling the basic FEL interactions.

4.1.1 Basic Considerations

The FEL wavelength is given by

$$\lambda = \frac{\lambda_u \left(1 + K^2/2\right)}{2\gamma^2} \tag{4-1}$$

where λ_u is the period length of the undulator magnet, γ is the electron's relativistic energy E divided by its rest energy m_0c^2, and K is the dimensionless deflection parameter, related to the peak magnetic field B_0 in the undulator and the electron charge e as follows:

$$K = \frac{eB_0\lambda_u}{2\pi m_0 c} = 0.934 \; B_0 \,[\text{T}] \; \lambda_u\,[\text{cm}] \qquad (4\text{-}2)$$

From these equations, it is clear that the FEL wavelength can be changed either by changing the electron beam energy or by changing the undulator magnet gap (thereby changing K). We shall employ both methods of tuning, changing the undulator gap for broad tuning within each of four ranges established by the choice of electron beam energy and, at a fixed gap, changing the electron beam energy for rapid tuning over a narrow range.

The FEL gain in the small-signal regime is given by (see, for example, Brau [1990])

$$g = 16\sqrt{2} \, \frac{\lambda^{3/2} \lambda_u^{1/2}}{\Sigma} \, \frac{K^2 \,[JJ]^2}{\left(1 + K^2/2\right)^{2/3}} \, \frac{I}{I_A} \, N^3 f \qquad (4\text{-}3)$$

Here N is the number of undulator periods, Σ is the combined transverse area of the mode and the electron beam, I is the peak electron current, I_A is the Alfven current (17,000 A), and

$$[JJ] = J_0\left(\frac{K^2}{4 + 2K^2}\right) - J_1\left(\frac{K^2}{4 + 2K^2}\right) \qquad (4\text{-}4)$$

where the J's are the Bessel functions. The factor f describes the frequency dependence of the gain, with the maximum value $f_{\max} = 0.0675$. If the radiation intensity is to build up in the cavity, the gain must be at least as large as the round-trip loss in the cavity. Indeed, it is desirable to design FELs so that the single-pass gain is as large as possible.

For the electron micropulses to continue to overlap with the optical pulses, the round-trip time of the optical pulses in the cavity must be an integral multiple of the time interval T between the electron micropulses. Thus,

$$nT = 2L_c/c \qquad (4\text{-}5)$$

where L_c is the length of the optical cavity. The integer n is the number of optical pulses simultaneously present in the optical cavity; in our case, $n = 1$ or 2. The timing between the pulses is arranged so that some of the FEL pulses can overlap with ALS pulses.

The Rayleigh length of the optical cavity, z_R, is determined by two considerations, namely, the desirability of minimizing the transverse mode size Σ in the interaction region, as well as the loss in the undulator bore. The optimum value of z_R is

$$z_R \cong L_u/2 \qquad (4\text{-}6)$$

where $L_u = N\lambda_u$ is the length of the undulator.

To avoid gain degradation, the energy spread $\Delta\gamma$ of the electron beam should satisfy

$$\frac{\Delta\gamma}{\gamma} < \frac{1}{2N} \tag{4-7}$$

Effective lasing also requires a good overlap of the optical pulse and the electron beam in transverse phase space. This condition can be written (for the beam waist) as

$$\sigma_x \sigma_{x'} < \frac{\lambda}{4\pi}, \ \sigma_y \sigma_{y'} < \frac{\lambda}{4\pi} \tag{4-8}$$

where σ_x (σ_y) and $\sigma_{x'}$ ($\sigma_{y'}$) are the rms size and angle, respectively, of the electron beam in the x (y) direction. The product $\sigma_x \sigma_{x'}$ ($\sigma_y \sigma_{y'}$) is the rms beam emittance in the x (y) direction.

Given the beam emittance, the maximum overlap occurs when the envelopes of the electron beam and the radiation beam are similar to one another. This condition is achieved by arranging that the horizontal betatron function β_x is at a minimum at the undulator center, having a value

$$\beta_x = z_R = L_u/2 \tag{4-9}$$

In the vertical direction, however, there is a constant focusing produced by the undulator magnetic field, given by

$$\beta_y = \frac{\gamma\lambda_u}{K\pi\sqrt{2}} \tag{4-10}$$

Therefore, the external focusing must be arranged to match this value. Otherwise, the beam envelope develops a modulation and the FEL gain is reduced.

4.1.2 Spectrum and Intensity

When the FEL signal begins to develop, the optical pulse is dominated by the spontaneous radiation, for which the bandwidth is given by

$$\frac{\Delta\lambda}{\lambda} \cong \frac{1}{N} \tag{4-11}$$

As the signal is repeatedly amplified by the FEL gain process, the spectrum becomes narrower:

$$\frac{\Delta\lambda}{\lambda} \cong \frac{1}{N\sqrt{n}} \tag{4-12}$$

where n is the number of round-trips. Eventually, the bandwidth reaches a value corresponding to a coherent optical pulse extending the length $c\tau$ of the electron beam micropulse:

$$\frac{\Delta\lambda}{\lambda} \cong \frac{\lambda}{c\tau} \qquad\qquad (4\text{-}13)$$

Equation 4-13 is usually known as the (Fourier) transform-limited bandwidth. The condition for obtaining this bandwidth is that FEL saturation take place at a strong field, where the intensity-dependent gain reduction becomes significant [Kim, 1991].

We have observed that the optical pulses can, in some cases, develop an exponential tail at the front end. This phenomenon, which occurs when the gain is sufficiently high and the detuning is properly chosen, is caused by the spilling of optical energy through the front end of the electron pulse. The existence of the tail means that the spectral bandwidth can be narrower than that given by Eq. 4-13. Note, however, that the spectral shape due to an exponential tail is Lorentzian; it thus has a long tail in the frequency domain and may be undesirable for certain applications.

In practice, the length of the optical cavity should be slightly shorter, by an amount δL (usually referred to as the cavity detuning), than that implied by Eq. 4-5. The cavity detuning proves to be an important parameter that can be adjusted to control FEL performance. For a small detuning, the approach to saturation is slow and the spectrum exhibits sidebands and sometimes even chaotic modes. The appearance of the sidebands and chaotic modes is a high-intensity phenomenon and is related to the synchrotron oscillation in the ponderomotive potential [Kroll et al., 1981; Goldstein, 1984]. These undesirable effects can be avoided by adjusting the amount of the cavity detuning [Warren et al., 1986; Warren and Goldstein, 1988].

The fraction η of the electron beam's kinetic power P_{el} that is converted into the optical power P_{opt} generated by the FEL interaction is called the efficiency. Thus,

$$P_{opt} = \eta\, P_{el} \qquad\qquad (4\text{-}14)$$

A simple argument shows that the efficiency is about $1/2N$. However, numerical simulations indicate that, when sideband development is suppressed for higher spectral purity, the efficiency is about $1/4N$ or less.

Numerical simulation and analytic calculation of FEL performance [Kim and Xie, 1991] reveal that FEL behavior can be divided into three distinct regions, each characterized by a range of values for the detuning δL:

- Region I, where $\delta L \le 0.1 g\lambda N$, characterized by the appearance of sidebands and a chaotic spectrum, but with high efficiency, $\eta \ge 1/4N$.

- Region II, where $0.1 g\lambda N \le \delta L \le 0.2 g\lambda N$, characterized by a good spectrum and a reasonable efficiency, $1/5N \le \eta \le 1/4N$.

- Region III, where $\delta L \ge 0.2 g\lambda N$, characterized by a good spectrum but low efficiency, $\eta \le 1/5N$.

A curve showing the FEL efficiency as a function of the cavity detuning δL is called the detuning curve. In Fig. 4-1, we show a typical such curve, in which efficiency is plotted in units of $1/2N$. The FEL spectra corresponding to points A and B are shown in Figs. 4-2a and 4-2b, respectively. These figures clearly illustrate the distinct regions discussed
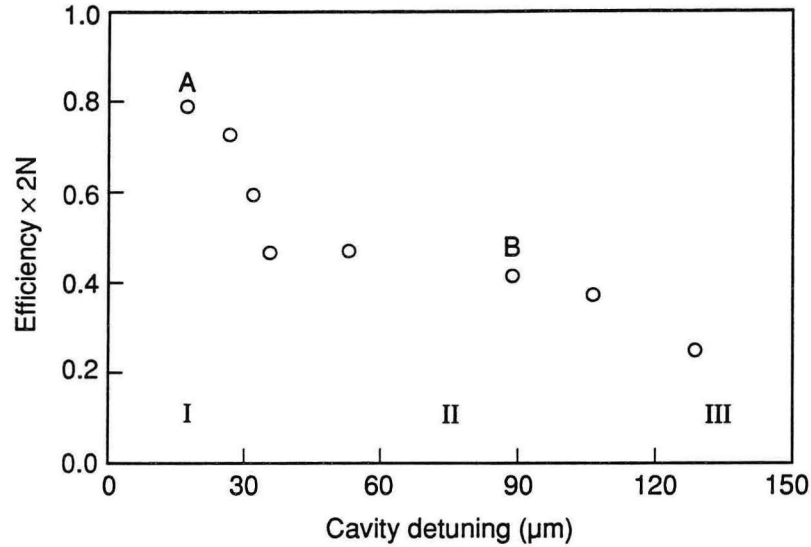
Figure 4-1. Plot of extraction efficiency η as a function of cavity detuning, for λ = 10 μm. Three different regions are denoted with capital Roman numerals. The FEL spectra at the detunings marked by A and B are shown in Fig. 4-2. [XBL 922-5576]

above. (These figures were obtained using the parameters of an earlier FEL design, based on a room-temperature linac [Conceptual Design Report: Chemical Dynamics Research Laboratory, 1991; Kim et al., 1991]).

For the current IRFEL design, a good spectrum is important. Thus, the detuning was chosen to be $\delta L \geq 0.1 g \lambda N$. Accordingly, the efficiency η will be equal to about $1/5N$.

If we denote the total round-trip loss by α, the intracavity power is given by

$$P_{\text{cav}} = \frac{P_{\text{opt}}}{\alpha} = \frac{\eta}{\alpha} P_{\text{el}} \qquad (4\text{-}15)$$

The intracavity optical elements must be designed to withstand the power level given by P_{cav}. The total loss α consists of the useful loss α_c due to outcoupling and other losses α':

$$\alpha = \alpha_c + \alpha' \qquad (4\text{-}16)$$

Thus, the useful output power is given by

$$P_{\text{out}} = \left(\frac{\alpha_c}{\alpha}\right) \eta P_{\text{el}} \qquad (4\text{-}17)$$

The ratio α_c/α, the coupling efficiency, depends on the details of the outcoupling. For the hole-coupling scheme discussed in section 4.3, this ratio is about 0.5.
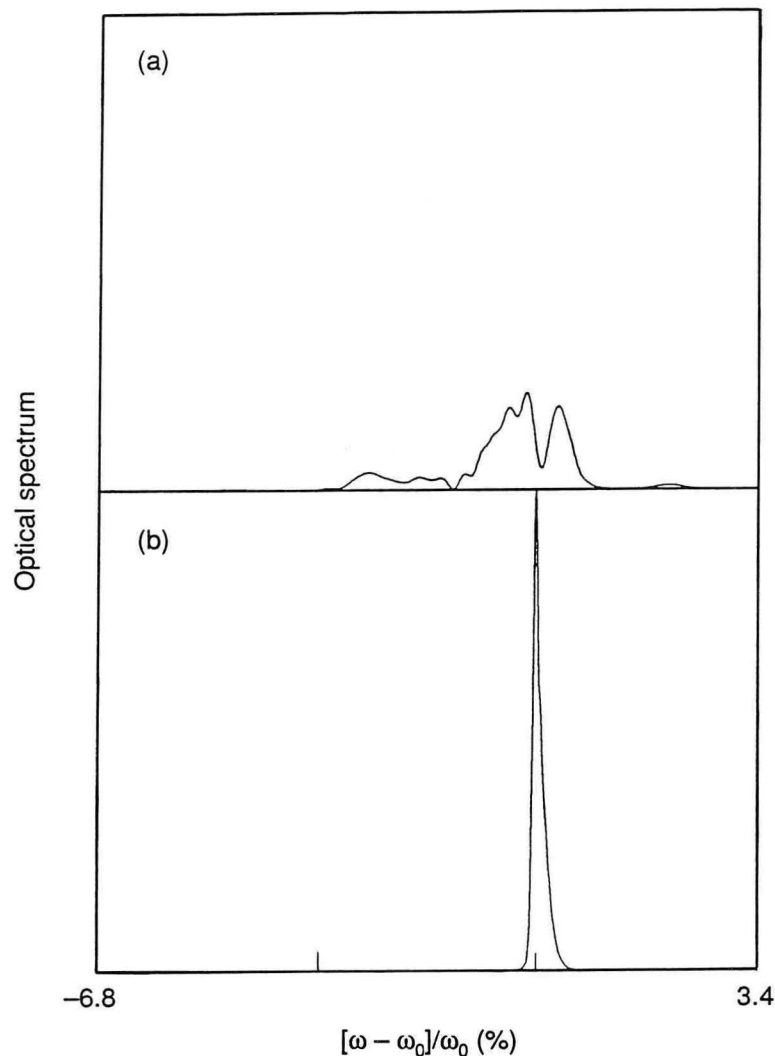
Figure 4-2. The FEL spectra for different cavity detunings, as a function of the relative frequency, for λ = 10 μm, τ = 33 ps, and pulse charge = 1 nC: (a) δL = 18 μm, corresponding to point A in Fig. 4-1; (b) δL = 89 μm, corresponding to point B. [XBL 922-5577]

Finally, the optical power delivered to the experimental station, P_{exp}, is obtained by multiplying the output power by the transport efficiency η_{trans}:

$$P_{exp} = (\alpha_c/\alpha) \, \eta_{trans} \eta P_{el} \qquad (4\text{-}18)$$

Typically, $\eta_{trans} \cong 0.75$.

Denoting the electron kinetic energy, the generated optical energy, and the transported optical energy in a micropulse by W_{el}, W_{opt}, and W_{exp}, respectively, we have

$$W_{opt} = \eta \, W_{el}$$

$$W_{exp} = (\alpha_c/\alpha) \, \eta_{trans} \, \eta \, W_{el} \qquad (4\text{-}19)$$

4.1.3 IRFEL Performance Calculation

Our FEL modeling is based on several numerical simulation codes. The workhorse of the calculation is a code named PLS PRPLP, developed originally by S. Benson [1985]. The code is based on the one-dimensional FEL equations, three-dimensional effects being taken into account by means of a suitable filling factor. PLS PRPLP takes into account the effects of the finite length of electron micropulses, spontaneous radiation, and the electron beam energy spread. The code calculates the evolution of the temporal and spectral profiles of the optical pulses in the cavity.

Table 4-1 summarizes the performance of the IRFEL, as obtained from a simulation calculation using PLS PRPLP. The electron beam parameters used for this calculation are listed in Table 4-2. The magnet parameters and wavelength tuning are discussed in section 4.2.

The net gain shown in Table 4-1 is the total gain g minus the loss α (10% in this case) at the beginning of FEL evolution. The output characteristics represent the optimized performance with respect to cavity detuning. The optimization was achieved by comparing the output at several values of the cavity detuning at the lower end of region II (see Fig. 4-1), and then choosing the one with the maximum output energy (or efficiency) showing no sideband development. The values of δL corresponding to the optimum performance are shown in Table 4-1; they agree with the formula $\delta L \cong 0.1 g \lambda N$, except in the long-wavelength cases.

The spectral bandwidths in Table 4-1 are consistent with the electron beam transform-limited values given by Eq. 4-13 for short wavelengths ($\lambda \leq 10$ μm). For longer wavelengths near 50 μm, the bandwidth is smaller than that expected from Eq. 4-13, owing to the spilling phenomenon and front tail development discussed above.

Table 4-1. FEL performance predicted on the basis of a simulation using the computer code PLS PRPLP. The total round-trip loss was taken to be 10%; the coupling efficiency, 50%.

λ (μm)	E (MeV)	Net gain (%)	δL (μm)	$\Delta\lambda/\lambda$ (%)	Pulse energy (μJ)
3	55.3	17	4.6	0.04	99
6.8	55.3	51	15	0.08	170
6	39.1	44	15	0.06	134
13.7	39.1	116	60	0.13	169
12	27.7	105	40	0.13	176
27.4	27.7	227	150	0.38	154
24	19.6	119	100	0.24	113
54.7	19.6	260	300	0.32	108

Table 4-2. Electron beam parameters used for the simulation of Table 4-2. The pulse length (FWHM) was taken to be 33 ps.

E (MeV)	q (nC)	Normalized rms emittance (mm·mrad)	Energy spread, FWHM (%)
55.29	1	7.0	0.35
39.1	1.414	8.7	0.48
27.65	2	11.1	0.66
19.55	2	11.1	0.93

It has been pointed out that FEL micropulses can develop chirping [Moore, 1988; Szarmes et al., 1990]. A fraction of the bandwidth in Table 4-1 in the short-wavelength cases might be due to this "natural" chirping phenomenon. If so, a narrower bandwidth can be achieved by accelerating the electron beam slightly away from the peak of the RF crest. Note that Eq. 4-13 yields a bandwidth about twice as wide as that expected from a coherent Gaussian pulse.

From the values of the generated optical micropulse energy W_{opt} given in Table 4-1, we find that the FEL efficiency η is consistent with our expectation that it be larger than about $1/5N$. The final transported optical energy W_{exp} can be estimated from Eq. 4-19, assuming $\alpha_c/\alpha = 0.5$ and $\eta_{trans} = 0.75$.

It is possible to increase the FEL efficiency by tapering the undulator magnetic field [Kroll et al., 1981]. For this scheme to work, the intracavity optical intensity must be high, so that the required fraction of the electron beam is trapped in the ponderomotive "bucket." Thus, it might be necessary to reduce the cavity loss while maintaining the coupling efficiency α_c/α at a reasonable value. Tapered operation of the CDRL IRFEL is currently being evaluated.

We have also calculated the variations in the FEL spectrum and power caused by sinusoidal modulation of the electron beam energy and of the timing between the micropulses under different operating conditions. Figure 4-3 is an example of such a calculation. The results are in general agreement with the analysis in section 3.1.1.

4.1.4 Intracavity Gratings

Intracavity dispersive elements such as gratings can be useful for sideband suppression and for wavelength stabilization beyond the level made possible by electron beam control alone. A schematic of the optical cavity with a grating in a Littrow configuration is shown in Fig. 4-4. Here, the light diffracted in the first order remains in the cavity, whereas the zeroth or second order provides a convenient outcoupling mechanism. A proof-of-principle experiment using gratings in an FEL for sideband suppression [Sollid et al., 1989a, 1989b] and for wavelength stabilization [D.W. Feldman, private communication] has been carried out at LANL.

$$\frac{\delta\gamma}{\gamma} = 1/2 \ (5 \times 10^{-4}) \cos 2\pi \ ft$$

f(MHz) = 0.05, 0.1, 0.15, 0.2
Wavelength = 3 μm
Pulse length = 5 ps
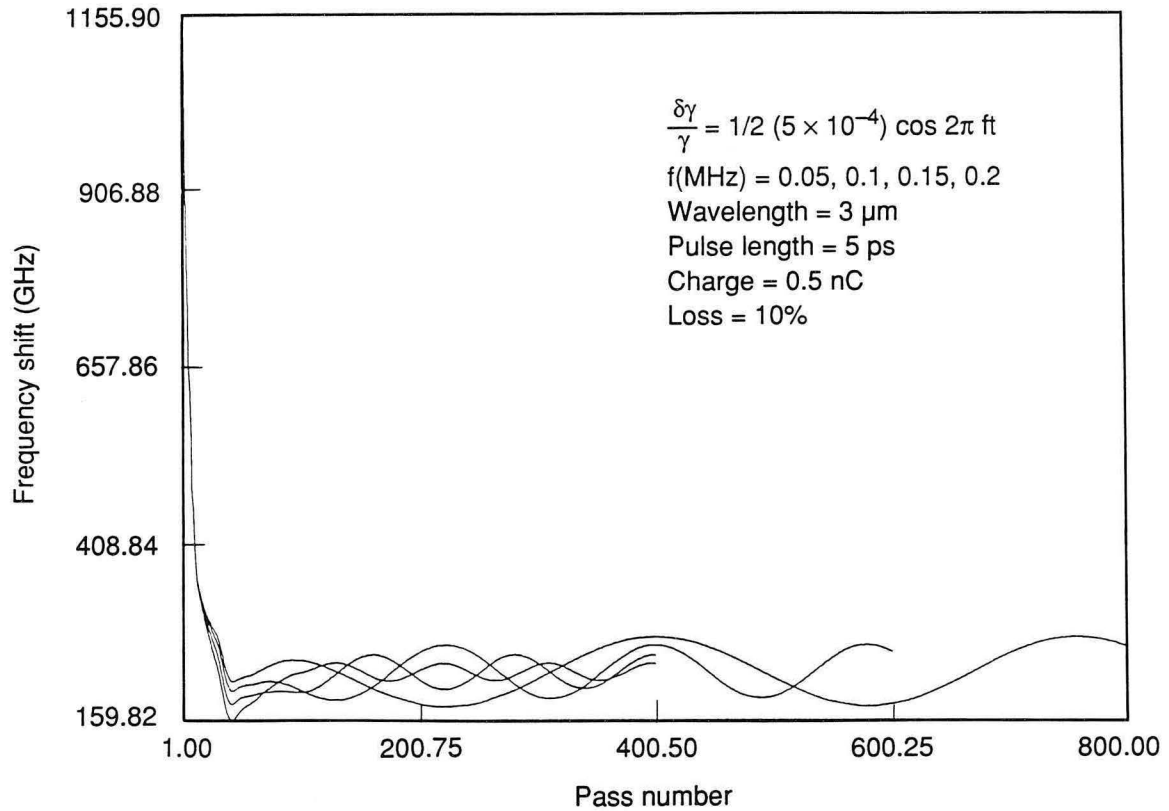Charge = 0.5 nC
Loss = 10%

Figure 4-3. Plot of the FEL frequency shift as a function of pass number, showing the frequency modulation caused by modulation in the electron energy. The conditions assumed for the four curves are described in the figure. [XBL 922-5578]
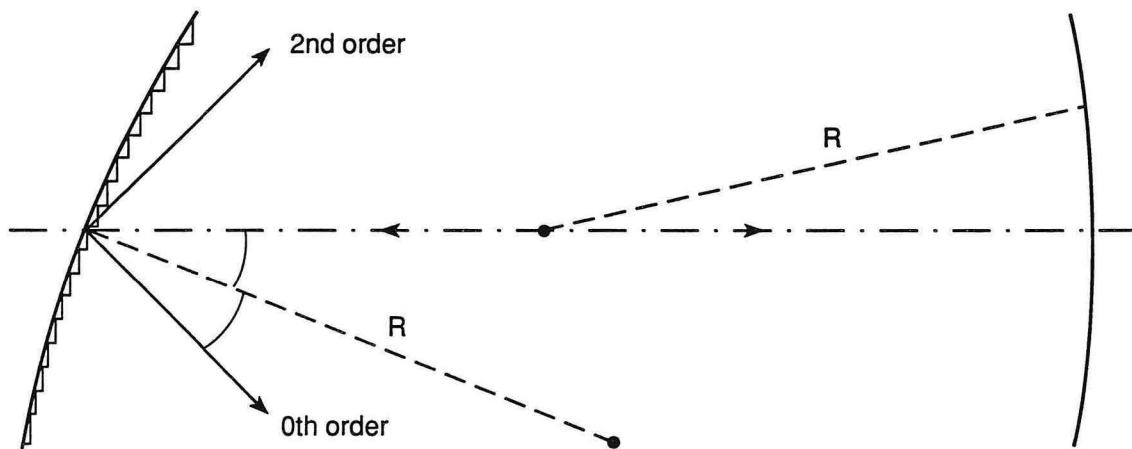

Figure 4-4. Schematic of the FEL optical cavity with a grating in a Littrow configuration. [XBL 922-5579]

The wavelength fluctuation in the presence of an intracavity grating is related to the fluctuation in the absence of a grating, $\delta\omega_0/\omega_0$, by

$$\frac{\delta\lambda}{\lambda} = \frac{g\left(\sigma_g/\sigma_0\right)^2}{1 + g\left(\sigma_g/\sigma_0\right)^2} \frac{\delta\omega_0}{\omega_0} \tag{4-20}$$

where σ_0 is the gain bandwidth ($\sim 1/2N$) and σ_g is the grating bandwidth. At saturation, the gain g in Eq. 4-20 can be replaced by the loss α, which is typically 0.1 for the IRFEL described here. Thus, the wavelength fluctuations can be reduced by a factor of 10 or more below that possible with electron beam control alone, when $\sigma_g < \sigma_0$.

We have calculated the wavelength fluctuations caused by the electron beam modulation in the presence of an intracavity grating by modeling the grating as a frequency filter in PLS PRPLP. The result agrees qualitatively with the behavior predicted by Eq. 4-20.

Gratings with narrower bandwidths, or with finer grooves, will be better in terms of stability. However, excessive pulse stretching, caused by a finer grating, could lead to an unacceptable reduction in the FEL gain [Sollid et al., 1989a, 1989b]. For a Littrow grating configuration, the rms pulse stretching per grating reflection is calculated to be

$$\sigma_{\Delta z} \cong \lambda \sigma_x/d \tag{4-21}$$

where σ_x is the rms beam size at the grating and d is the groove spacing. To avoid a significant gain reduction, $\sigma_{\Delta z}$ should be small compared with the electron pulse length. For the CDRL FEL, this requirement leads to a coarse grating with $d \cong 0.1$ mm for $\lambda \leq 10$ μm, and to even coarser gratings for longer wavelengths.

For a coarse grating with a shallow groove, the grating efficiency can be calculated in a closed form by using an asymptotic form of the Rayleigh expansion [Loewen et al., 1978]. The result for the first order efficiency $|E_1|^2$ near the blaze frequency ω_g is

$$|E_1|^2 = [(\sin \varepsilon)/\varepsilon]^2 \tag{4-22}$$

where $\varepsilon = \pi (\omega - \omega_g)/\omega_g$. If we require the efficiency to be larger than 90%, a single grating can cover the wavelength range

$$-0.17 \leq \frac{\omega - \omega_g}{\omega_g} \leq 0.17 \tag{4-23}$$

Thus, the total tuning range is about 34%.

The efficiency into the zeroth- or second-order reflection is given by

$$|E_0|^2 = |E_2|^2 = \left(\frac{\varepsilon}{\pi}\right)^2 = \left(\frac{\omega - \omega_g}{\omega_g}\right)^2 \tag{4-24}$$

Therefore, up to about 3% of the FEL intensity can be coupled out in each order for external use. However, according to Eq. 4-24, the efficiency vanishes quadratically as ω approaches ω_g.

Three-dimensional effects could be important for FEL operation with intracavity gratings. For example, for a fixed grating, the optical axis corresponding to a wavelength $\lambda \neq \lambda_g$ (where λ_g is the wavelength corresponding to ω_g) is rotated by an angle θ with respect to the original axis, where θ is given by[1]

$$\theta = \frac{L}{4(2R - L)}\left(\frac{\lambda - \lambda_g}{d}\right) \tag{4-25}$$

in which R is the radius of curvature for the grating. The rotation of the optical axis can excite a walking mode around the new axis [Grossman and Quimby, 1984; Warren and McVey, 1987] and should be limited to a value smaller than, for example, the mode divergence angle.

4.2 FEL UNDULATOR

The heart of the IRFEL is a steel–permanent magnet hybrid undulator, consisting of a magnetic structure, a support and drive system, a control system, and a vacuum system. As shown in Fig. 4-5, the magnetic structure is outside the vacuum chamber, which is a small cylindrical pipe extending the length of the undulator. The magnet gap is varied mechanically for wavelength tuning.

4.2.1 Parameter Selection and Tuning

The undulator period length, the wavelength tuning ranges, and the vacuum chamber dimensions are closely related parameters that must be chosen carefully. The diameter of the pipe must be neither too large (to ensure a sufficiently strong magnetic field) nor too small (to avoid excessive diffraction loss). To balance these considerations, we chose the inner diameter of the vacuum chamber to be 21 mm. Allowing for a 1-mm chamber thickness yields a minimum magnet gap $g_{min} = 23$ mm. The corresponding peak magnetic field on the undulator axis, B_0, is 0.45 T. Thus, for the chosen undulator magnet period length $\lambda_u = 5$ cm, the maximum value of the deflection parameter K is, from Eq. 4-2,

$$K_{max} = 2.1 \tag{4-26}$$

To insure a sufficient FEL gain, the minimum value of K, obtained by opening the gap, was chosen as

$$K_{min} = 0.9 \tag{4-27}$$

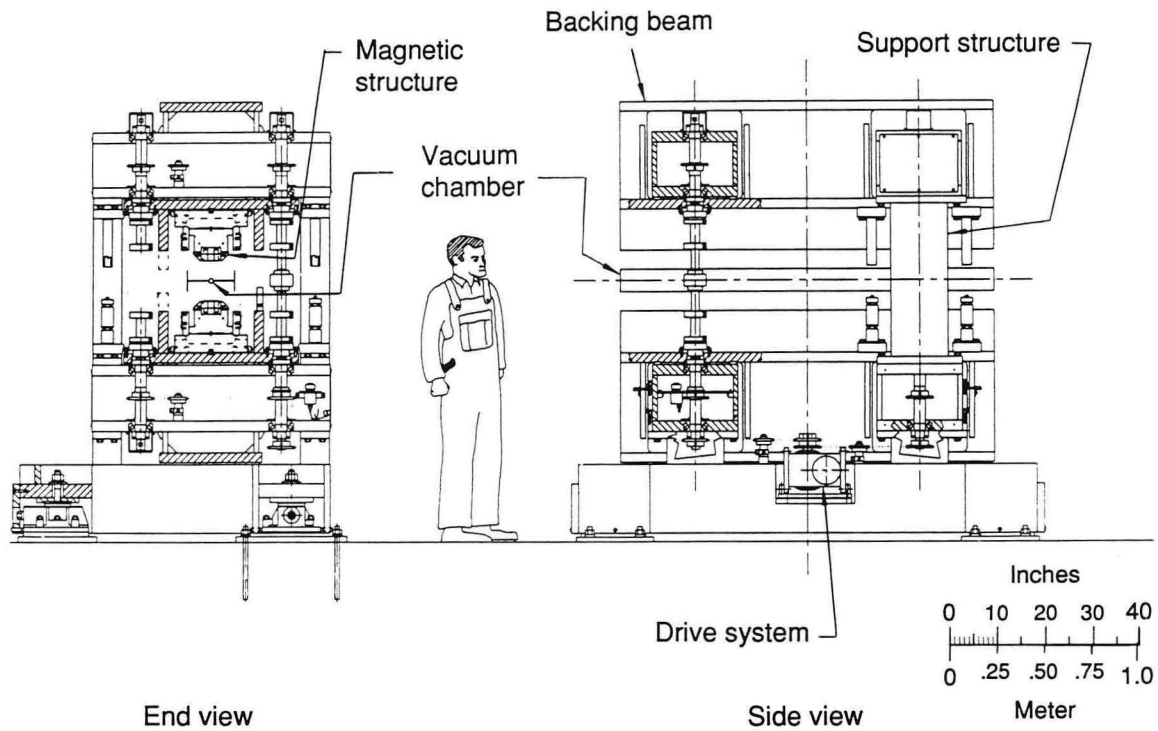[1]We thank R. W. Warren for his help in deriving Eq. 4-25.

Figure 4-5. Cross-sectional end and side views of the IRFEL undulator. [XBL 922-5580]

Thus, at a fixed electron energy E, the wavelength can be varied between $\lambda_{\min}$ and $\lambda_{\max}$, where

$$\frac{\lambda_{\max}}{\lambda_{\min}} = \frac{1 + K_{\max}^2/2}{1 + K_{\min}^2/2} = 2.28 \qquad (4\text{-}28)$$

The entire wavelength range 3–50 μm can therefore be covered by operating the FEL at four energies, as shown in Table 4-3. Ease of wavelength tuning is crucial for the

Table 4-3. Wavelength tuning ranges for four selected electron beam energies.

Electron energy (MeV)	Wavelength tuning range
55.3	3 μm $\leq \lambda \leq$ 6.84 μm
39.1	6 μm $\leq \lambda \leq$ 13.7 μm
27.7	12 μm $\leq \lambda \leq$ 27.4 μm
19.6	24 μm $\leq \lambda \leq$ 54.7 μm

successful operation of a user facility. Accordingly, changes in the undulator gap that are required to satisfy user needs will be carried out under automated computer control. The full undulator scan at a given electron energy will take about one minute.

The dependence of the deflection parameter on the magnet gap is given approximately by

$$K = K_{max} \exp\left[-\frac{\pi(g - g_{min})}{\lambda_u}\right]$$ (4-29)

Thus, the maximum gap corresponding to $K_{min} = 0.9$ is $g_{max} = 36.5$ mm.

4.2.2 Tolerance Requirements

Gap Motion. The change $\Delta\lambda$ in FEL wavelength due to a gap change Δg is, from Eqs. 4-1 and 4-29

$$\frac{\Delta\lambda}{\lambda} = \left(\frac{K^2}{1 + K^2/2}\right)\left[\frac{\pi(\Delta g)}{\lambda_u}\right]$$ (4-30)

We require the wavelength change per step to be about one-tenth of the bandwidth (which is 10^{-3}); thus, the gap change per step must be no larger than about 1 μm.

Random Field Errors. We require that the intensity reduction due to random field errors be less than 10%. This leads to the condition [Kincaid, 1985]

$$q = \frac{n\sigma^2 N^2 K^2}{2(1 + K^2/2)} \leq 0.1$$ (4-31)

where σ is the rms error, n is the harmonic number, and N is the number of undulator periods. Setting $n = 1$, $N = 40$, and $K = 2.01$, we find that the requirement is satisfied by $\sigma \leq 0.9\%$. We chose to set the tolerance at $\sigma \leq 0.5\%$, in case operation at the third harmonic is required. This requirement on random errors is less stringent than that for the U5.0 undulator for the ALS.

Variations in the Undulator Gap. Variations in the undulator gap, such as those caused by weight, will cause a broadening of the homogeneous gain bandwidth. We require this broadening to be less than $1/4N$. Using Eq. 4-30, this requirement demands that $|\Delta g| \leq 35$ μm along the undulator.

Field integral. The first field integral is

$$\int B_y \, dz$$ (4-32)

where y is the vertical direction and B_y accounts for the deflection of the electron beam. We require the deflection angle to be less than one-tenth of the angular divergence of the electron beam ($\sigma_{x'} \leq 450$ mrad). This leads to the requirement

$$\int B_y \, dz \leq 10 \text{ G·cm} \tag{4-33}$$

4.2.3 Mechanical Description

The proposed IRFEL undulator is a shortened version of the ALS U5.0 undulator. Table 4-4 summarizes the proposed engineering design parameters. The major subsystems are

- The magnetic structure, which includes the hybrid pole assemblies mounted on pole mounts that are attached to the backing beams.

- The support and drive system, which includes the framework for supporting the magnetic structure and the mechanism for closing and opening the magnetic gap.

Table 4-4. Engineering design parameters for the IRFEL undulator, based on the design of the ALS U5.0 undulator.

Maximum peak field, at 23-mm magnetic gap [T]	0.475
First harmonic peak field, at 23-mm magnetic gap [T]	0.450
Period length [cm]	5
Number of periods	40
Number of full-field poles	81
Nominal entrance/exit sequence	0, +1/2, −1, +1
Magnetic structure length [cm]	210.8
Pole width [cm]	8
Pole height [cm]	6
Pole thickness [cm]	0.8
Number of blocks per half-period pole	6
End correction range, B_y [G·cm]	1500
End correction range, B_x	None
Steering coil length, if required (short) [cm]	~25
Dipole trim coil length, if required (long) [m]	1.95
Steering and trim field strength [G]	±5
Systematic gap variation tolerance [μm]	35

- The control system, which provides for remote, precise control of the magnetic gap.

- The vacuum system, which includes a small-bore vacuum chamber and its associated vacuum pumping system.

The magnetic structure consists of samarium-cobalt and vanadium permendur poles, arranged in a hybrid configuration similar to that used successfully in the wigglers constructed for the Stanford Synchrotron Radiation Laboratory Beamlines VI and X, as well as that being used for the ALS undulators. Figure 4-6, an ALS U5.0 undulator assembly section, shows the mechanical configuration of the half-period pole assemblies, pole mount, and mount adjusters. All pole surfaces are located in a plane, with a tolerance of ±0.001 in. (25 μm).

A plot of the estimated peak field is shown in Fig. 4-7 as a function of gap. The peak field at the minimum operating gap is 0.475 T, and the peak field of the fundamental at this gap is 0.450 T. To achieve the required field tolerances, the permanent magnet
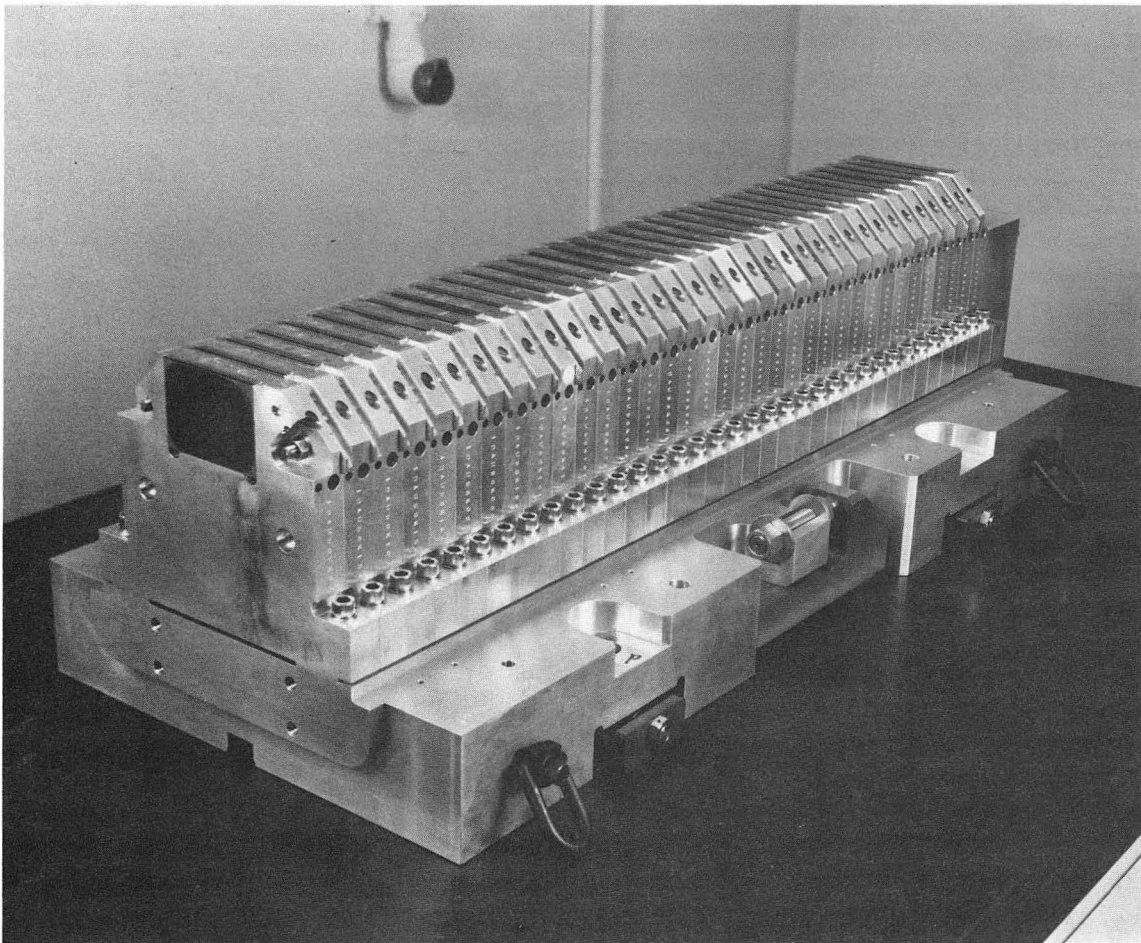
Figure 4-6. An assembly section for the first ALS U5.0 undulator; the IRFEL undulator is expected to be essentially identical. [CBB 910-8311]
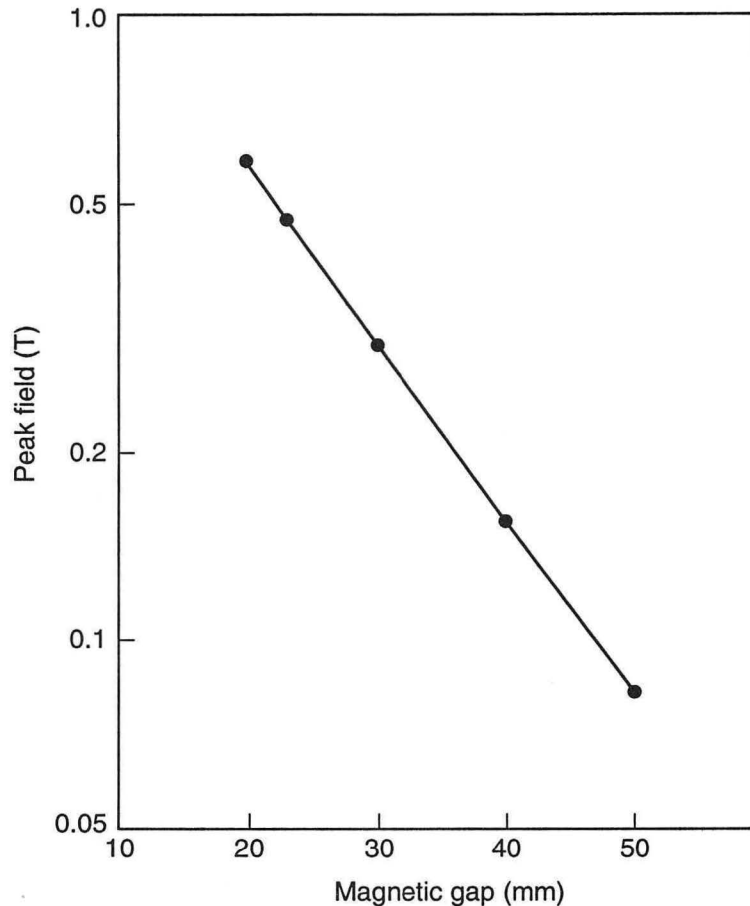
Figure 4-7. Plot of predicted undulator peak field as a function of gap. [XBL 922-5581]

blocks will be measured and sorted, and provisions have been made to correct the fields with pole adjustment and auxiliary coils, if necessary. To date, measurements on the first ALS U5.0 undulator assembly section have shown good control of field errors, and no field corrections have been required. The uncorrelated field errors are only 0.28%.

The 2.15-meter-long backing beams are sized to minimize the gap variation due to magnetic loading. To null the undulator vertical field integral, the IRFEL undulator design includes permanent-magnet end rotators, above and below the midplane at each end of the undulator; each of the four assemblies comprises two permanent-magnet rotators.

The support structure is a shortened version of the 4-post configuration adopted for the ALS insertion devices, as shown in Fig. 4-8. The support structure consists of a base, two lower horizontal beams, four vertical posts, and two upper horizontal beams. Prior to assembly, the four horizontal beams will be inserted through the webbing of the two backing beams that carry the magnetic structure. A magnetic load–compensating spring system is incorporated to buck the gap-dependent magnetic load.

The drive system changes the magnetic gap by rotating right- and left-handed Transrol roller screw/nuts, located in the upper and lower sections of the device,
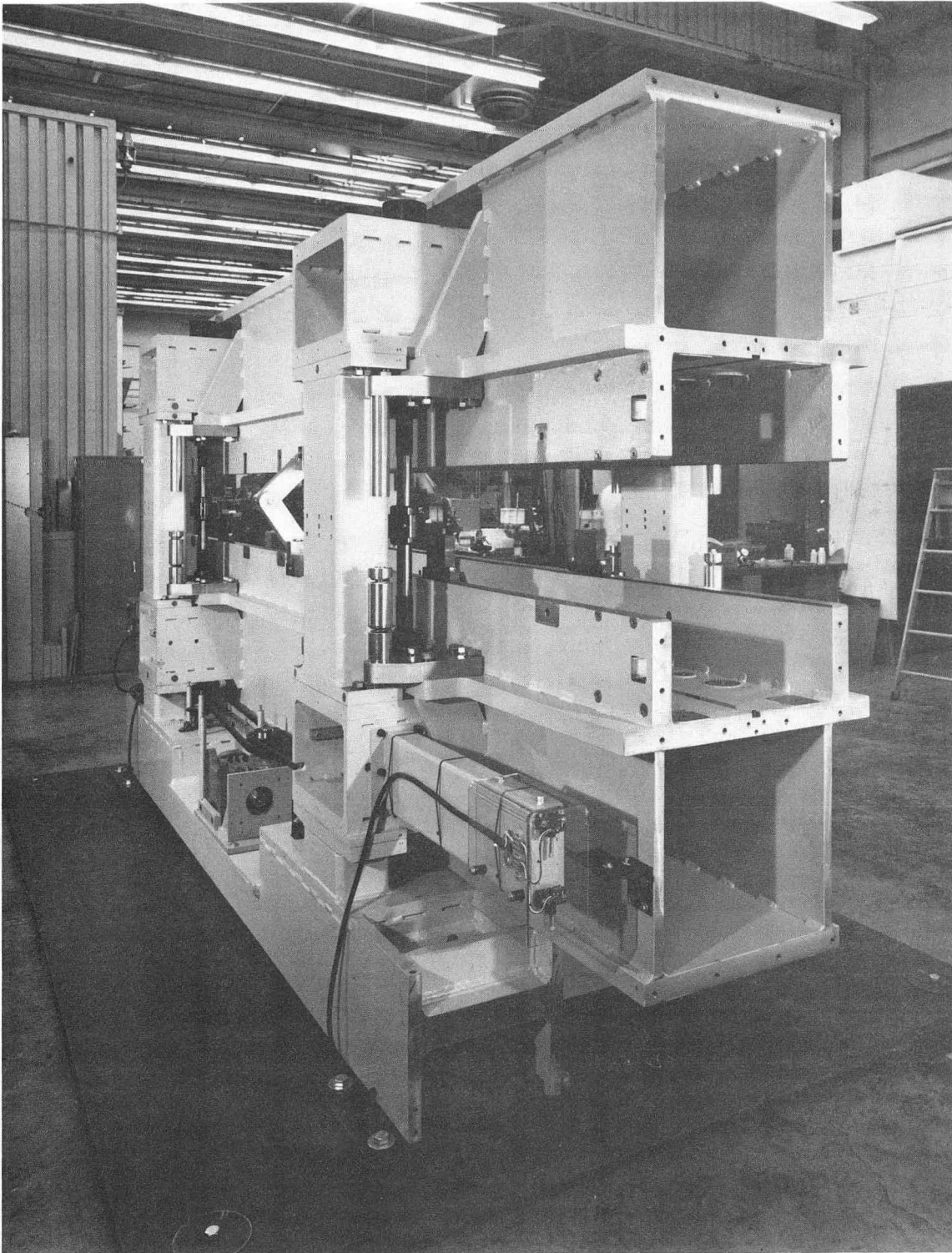
Figure 4-8. The support structure/drive system for an ALS undulator; a shortened version is proposed for the IRFEL undulator. [CBB 910-8205]

respectively. These roller screws are, in turn, interconnected with a system of roller chains, sprocket wheels, couplings, and loaded idler sprocket wheels. A gearbox and stepper motor drives the system. An absolute rotary encoder, with a resolution of better than 0.1 μm, is coupled to one of the roller screws to read the absolute position of the magnet gap.

If it is found to be desirable to taper the undulator magnetic field, a differential drive between the upstream and downstream drive shafts can be readily implemented. A 2% taper of the magnetic field along the length of the insertion device requires a maximum gap variation of about 0.4 mm, equal to about a 40° rotation of one drive shaft with respect to the other.

The goal of the undulator control system is to provide sufficient positional accuracy, resolution, velocity, and range for the motors and encoders used to vary the magnetic gap. The computer-controlled system uses a Compumotor control package, and provisions for interfacing limit switches are included, together with the ability to compensate for backlash and to program acceleration and deceleration curves. A selection of 10 microsteps/step by the control electronics for the stepper motor will provide 2000 steps/revolution, thus ensuring a gap resolution of 0.07 μm.

Initial measurements with the control system operating the first ALS U5.0 undulator support structure/drive system in a open-loop motor-stepping mode have shown a positional reproducibility of 4 μm or less in all tests. To achieve 1-μm gap reproducibility with the IRFEL undulator, a laser interferometer will be provided as an integral part of the control system, to monitor the magnetic gap directly.

The undulator vacuum system includes a small-diameter 321 stainless-steel vacuum chamber, transition sections, and associated pumping and diagnostics—all supported by a stainless-steel framework. Ports for diagnostics are provided at the entrance, center, and end of the undulator. The transition sections include bellows sections, beam position monitors, and vacuum pumping. If required, pumping can also be installed at the center of the undulator vacuum chamber.

4.3 OUTCOUPLING STUDIES

Ease of tuning is a high priority for the CDRL IRFEL. An essential feature of the design, therefore, is an outcoupling scheme that covers the widest possible range of wavelengths. We adopted a hole-coupling approach after an extensive study of its performance, in which we found that it fully meets our requirements [Xie and Kim, 1991a, 1991b]. Here we discuss the results of that study; in section 4.4, we describe the optical cavity itself.

The outcoupling schemes applicable to FELs can be broadly classified as relying on either dielectric materials or metal optics. Among the first class are those based on dielectric mirrors and those using deflection from Brewster plates. Belonging to the second class are schemes based on hole coupling, edge coupling in stable and unstable cavities, and diffraction from intracavity gratings.

The use of dielectric mirrors has been demonstrated at both the Los Alamos FEL project and the Mark III project at Stanford. For this approach to work well, both the coating materials and the substrate material must be compatible with the IRFEL power density in the cavity, and the materials must survive the intense flux of x-rays that is

emitted concurrently with the undulator radiation. This severely limits the choice of materials. In addition, the bandwidth of the dielectric coating is typically about 10% of the central wavelength of the coating. For broad tuning, this means that mirrors must be changed frequently.

The Stanford Mark III FEL (now at Duke University) used an intracavity CaF_2 plate tilted slightly off the Brewster's angle as an output coupler [Benson, 1991]. It worked well between 3 and 8 μm, which was the primary tuning range of the FEL. The drawbacks of this scheme were a tuning range limited by the long- and short-wavelength cutoffs of the CaF_2 and an output that consisted of two to four parallel beams. A future alternative to CaF_2 may be thin-film diamond, which has a unique transparency range and should have good optical properties, as well as being resistant to radiation damage. However, further development of this material is necessary before it can be relied on for practical applications.

Notwithstanding the promise of approaches using dielectric materials, outcoupling schemes based on all-metal optics appear to be the best-suited for FEL applications, because they allow broad tuning and because of their power-handling capabilities. As discussed below, the hole-coupling approach fully satisfies our design requirements, and edge-coupling schemes in stable and unstable resonators also appear promising. The use of intracavity gratings was discussed in section 4.1.4.

4.3.1 Hole Coupling

Basic Considerations. The resonator configuration used to study the performance of hole coupling is shown in Fig. 4-9. The effect of the undulator bore is taken into account approximately by the two apertures shown in the figure. The right-hand mirror has a circular hole for outcoupling. The effective radius of the left-hand mirror can be varied by means of an adjustable aperture, whose role is to control the intracavity mode profile.

A wave profile that reproduces itself after one round-trip in the cavity, except for a multiplicative constant, is called a mode. Modes for a cylindrically symmetric resonator are denoted by the designation TEM$_{mn}$, where m and n are the azimuthal and radial mode numbers, respectively. For each mode, we define the total round-trip loss α and the loss through the hole α_c [Xie and Kim, 1991b]. The coupling efficiency of the mode is then defined as

$$\eta_c = \frac{\alpha_c}{\alpha} \qquad (4\text{-}34)$$

When a random electromagnetic field is injected into a cavity, the profile converges, after some number of cavity round-trips, to the dominant mode with the lowest loss. Two modes are said to be degenerate when their losses are the same. Even if degenerate, however, their round-trip phase advances are in general distinct. Mode degeneracy should therefore be avoided, because the beating of the two degenerate modes causes the field distribution to oscillate rapidly, leading to a corresponding modulation in FEL output.
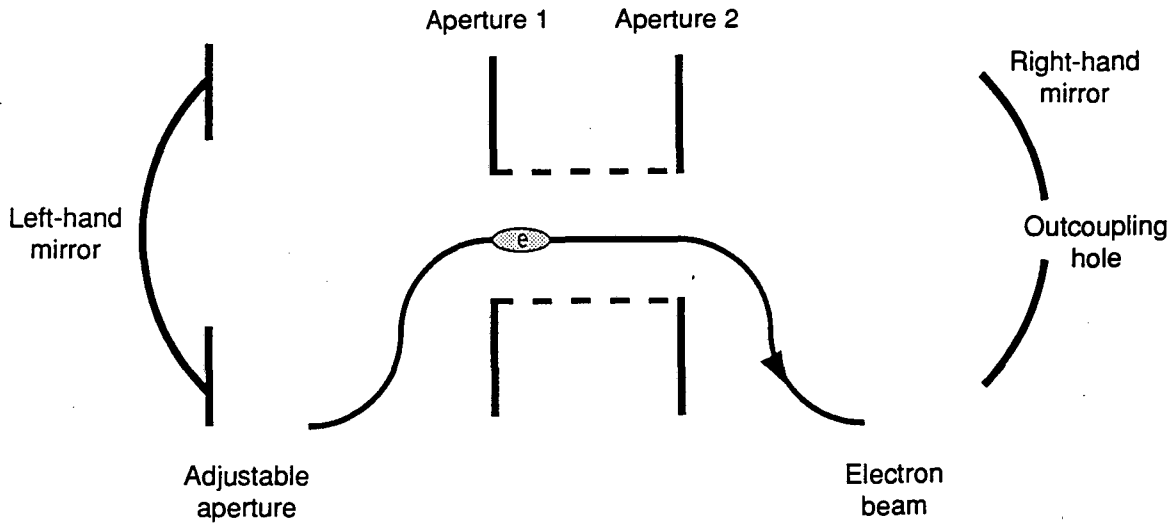
Figure 4-9. Cross-sectional view of a cylindrical IRFEL resonator, as modeled for the simulation code HOLD. The resonator consists of two mirrors and two intracavity apertures. A circular hole is located at the center of the right-hand mirror, and an adjustable aperture is placed in front of the left-hand mirror for mode control. The dashed lines indicate the boundary of an undulator bore simulated by the two fixed apertures. An electron beam traverses the FEL interaction region from aperture 1 to aperture 2. [XBL 922-5606]

Several considerations enter into the optimization of a hole-coupling resonator for the CDRL IRFEL. First, the coupling efficiency should be high enough to allow efficient utilization of the FEL output. Here, we aim for an efficiency in the neighborhood of 50%. Second, the mode profile in the interaction region should be a smooth, Gaussian-like shape for optimum overlap with the electron beam. The fundamental mode TEM_{00} satisfies this requirement. Third, mode degeneracy should be avoided. This can be done by increasing the losses for the unwanted higher-order modes (HOMs) by choosing an appropriate radius for the adjustable aperture.

Whether the outcoupled beam can be efficiently transported to a user station is another important issue in the design of an outcoupling scheme. Since the fundamental Gaussian mode in free space can usually be transported efficiently, it is of interest to know what fraction of the outcoupled optical energy is contained in the fundamental Gaussian mode in the Laguerre-Gaussian expansion. (This expansion contains two free parameters, the mode waist and the Rayleigh length. These parameters are chosen so that the power in the fundamental Gaussian mode is maximized.) With this in mind, we define the Gaussian quality factor for the outcoupled mode as the ratio of the power in the fundamental Gaussian mode to the total power. In the special case where the field distribution is uniform over the hole area (the far-field diffraction pattern in that case is known as the Airy pattern), the Gaussian quality factor is 81%. We find that the Gaussian quality factor is close to this value when the hole radius is below the mode degeneracy point.

Empty-Cavity Simulation. We developed a Fox-Li–type [Fox and Li, 1961] simulation code called HOLD (*HOL*e and *D*iffraction) to evaluate hole coupling and other resonator configurations. For an arbitrary resonator configuration involving apertures and mirrors (with or without holes), the code calculates the dominant mode by iteratively simulating round-trip propagations, starting from a random distribution. When first written, the code neglected the FEL interaction [Xie and Kim, 1991a]; we refer to this as the empty-cavity simulation. Each round-trip propagation in this case consists of a sequence of Fresnel-Kirchhoff integral transforms. FEL gain at saturation is equal to the total loss, which is about 10%. Therefore, neglecting the FEL interaction is expected to be a valid approximation in estimating the resonator performance. Simulations using the empty-cavity HOLD code demonstrate very clearly the phenomenon of degeneracy and the role of adjustable apertures in removing the degeneracy, hence widening the wavelength tuning range.

Figure 4-10 illustrates the wavelength dependence of the performance of hole coupling with an adjustable aperture. The right-hand mirror size was chosen to be sufficiently large to have no effect on performance, whereas the effective size of the left-hand mirror was increased linearly from 6.7 to 10 mm by varying the adjustable aperture,
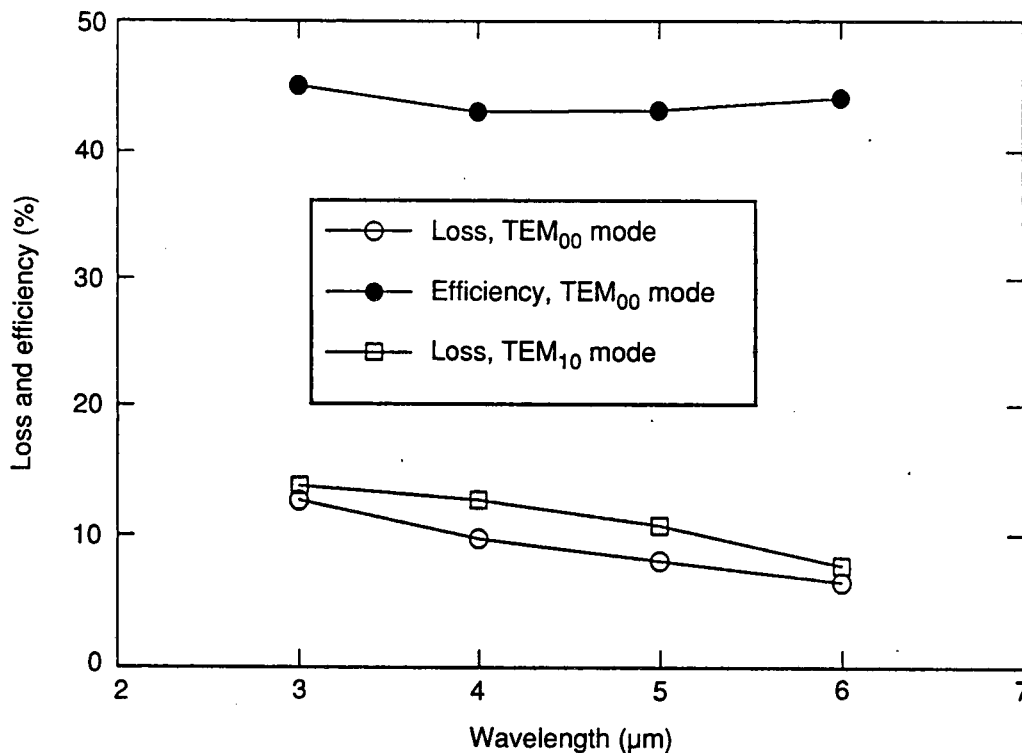

Figure 4-10. Hole-coupling efficiency for the TEM_{00} mode and loss for the TEM_{00} and TEM_{10} modes, at different wavelengths. The radius of the left-hand mirror was increased linearly from 6.7 to 10 mm as the wavelength was varied from 3 to 6 μm. The FEL interaction was neglected in this simulation. [XBL 922-5605]

as the wavelength was tuned from 3 to 6 μm. Note that the coupling efficiency and the loss remain close to 45% and 10%, respectively, varying little over the tuning range. Also, the loss of the TEM_{10} mode is kept higher than that of the TEM_{00}. Although not shown, the losses for other HOMs are higher, given our choice of left-hand mirror size. For comparison, Fig. 4-11 shows the corresponding curves for the case where the left-hand mirror size is fixed at the midpoint value of 8.35 mm. The performance is unacceptable: At the short-wavelength end, the mirror is large enough to allow the TEM_{10} mode to dominate. This mode becomes degenerate with the fundamental mode at $\lambda = 4.3$ μm. On the other hand, the mirror is too small at the longest wavelengths, thus reducing coupling efficiency.

Simulations Including the FEL Interaction. The HOLD code was subsequently modified to include the FEL interaction [Xie and Kim, 1991b]. This was done by replacing the Fresnel-Kirchhoff transportation in the interaction region, in the direction from aperture 1 to aperture 2, by a new map constructed from an FEL integral equation. The map is valid in the small-signal regime.

The most striking result of this modification is the fact that the gain, even if small, can be very effective in suppressing the HOMs among the azimuthally symmetric ($m = 0$) modes when the electron-beam Fresnel number is not too small. This suppression occurs because the overlap with the electron beam is optimal for the fundamental mode. Figures
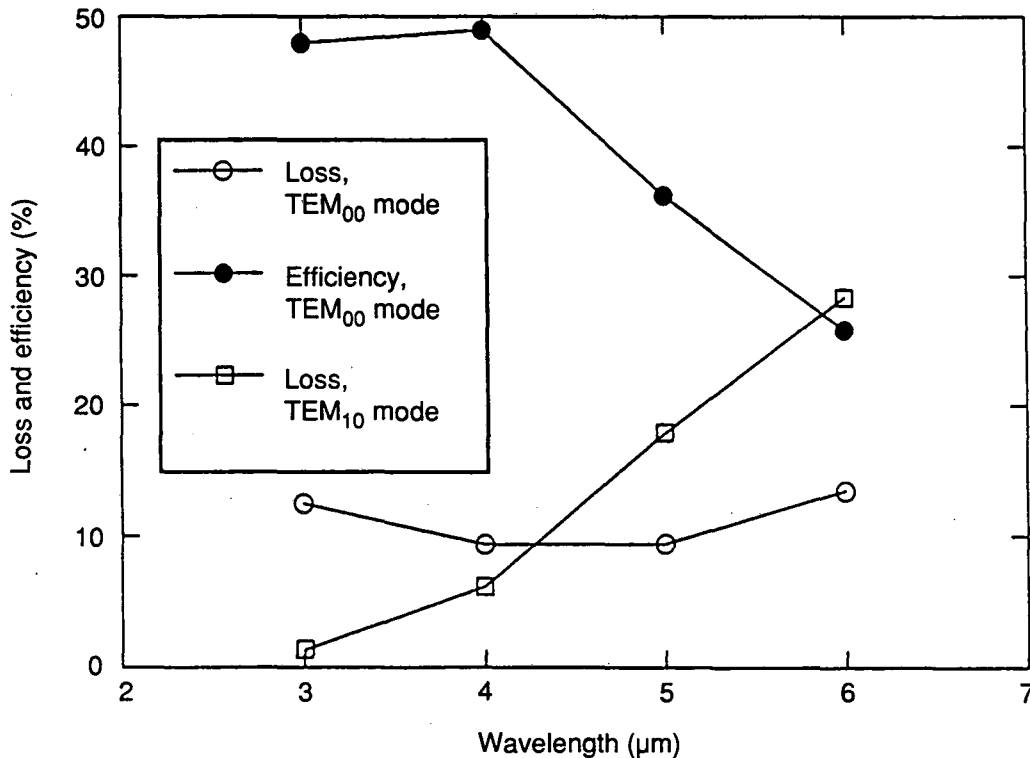

Figure 4-11. Same as Fig. 4-10, except that the radius of the left-hand mirror remained fixed at 8.35 mm for all wavelengths. [XBL 922-5604]

4-12 through 4-14 illustrate the intracavity mode profiles for single-pass gains of 0%, 2%, and 55%, respectively. The resonator configuration is such that the dominant symmetric mode for 0% gain has a large mode number $n = 4$. However, for a gain as small as 2%, the fundamental mode becomes dominant. Comparing Figs. 4-13 and 4-14, we also find that the mode profile changes little when the gain increases from 2% to 55%. The performance of hole coupling is therefore insensitive to the gain, except for the desirable effect of suppressing the symmetric HOMs.

As the electron beam size becomes smaller, the symmetric HOMs can become dominant. In principle, operation with such a mode can provide satisfactory performance, since the mode has a narrow central peak and thus a good hole-coupling efficiency; however, in practice, it will usually be necessary to suppress such modes, since a single resonator mode should remain dominant while the FEL wavelength is being scanned. This suppression can be accomplished by introducing intracavity apertures.

We expect that the asymmetric modes ($m \neq 0$) will not be perturbed significantly by the FEL interaction, because their intensities vanish on axis at the location of the electron beam. The asymmetric HOMs are also suppressed by means of adjustable intracavity apertures.
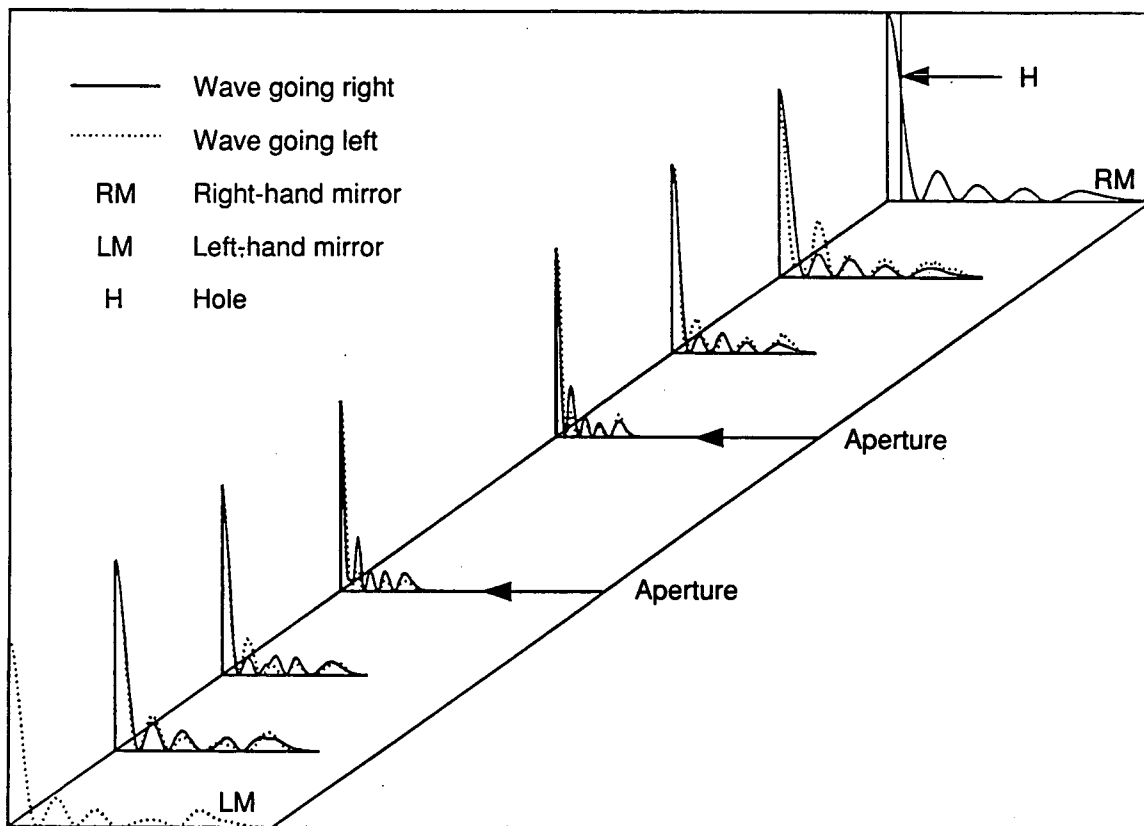

Figure 4-12. Intracavity intensity profiles of the dominant mode at a wavelength of 3 μm, for a gain of 0%. [XBL 922-5603]
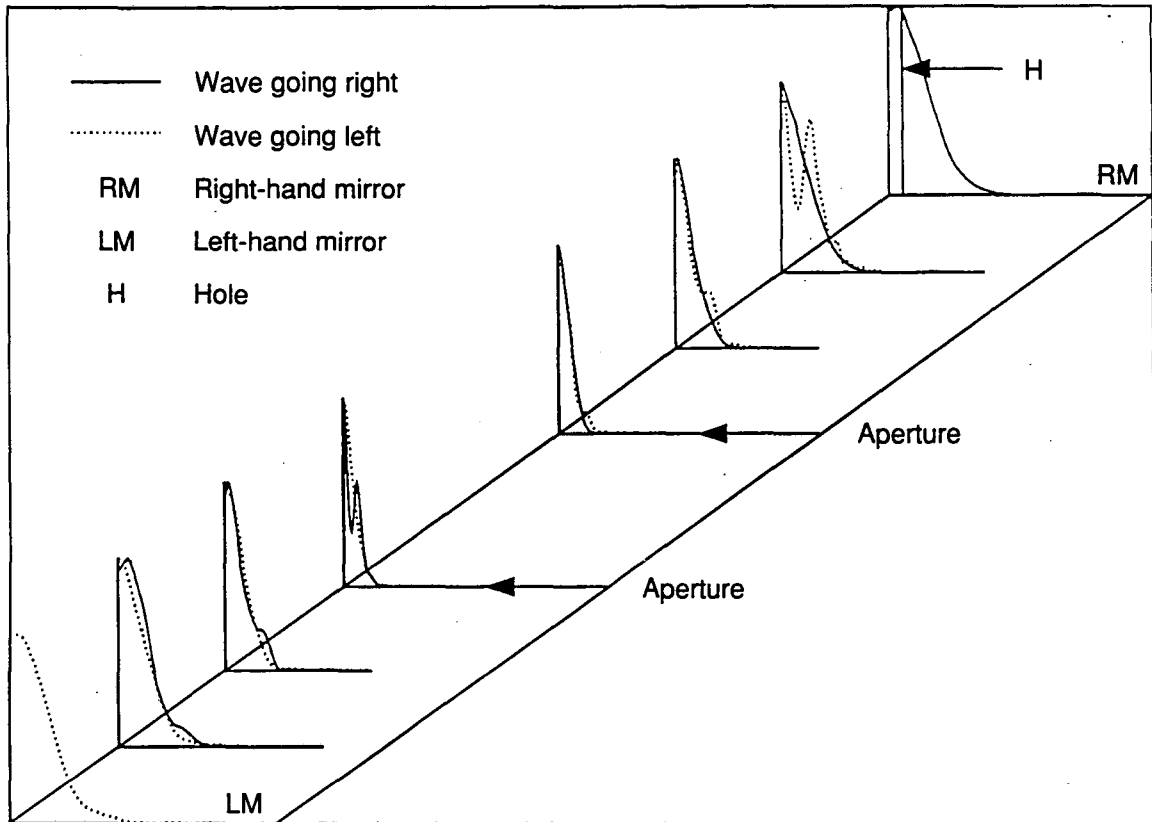
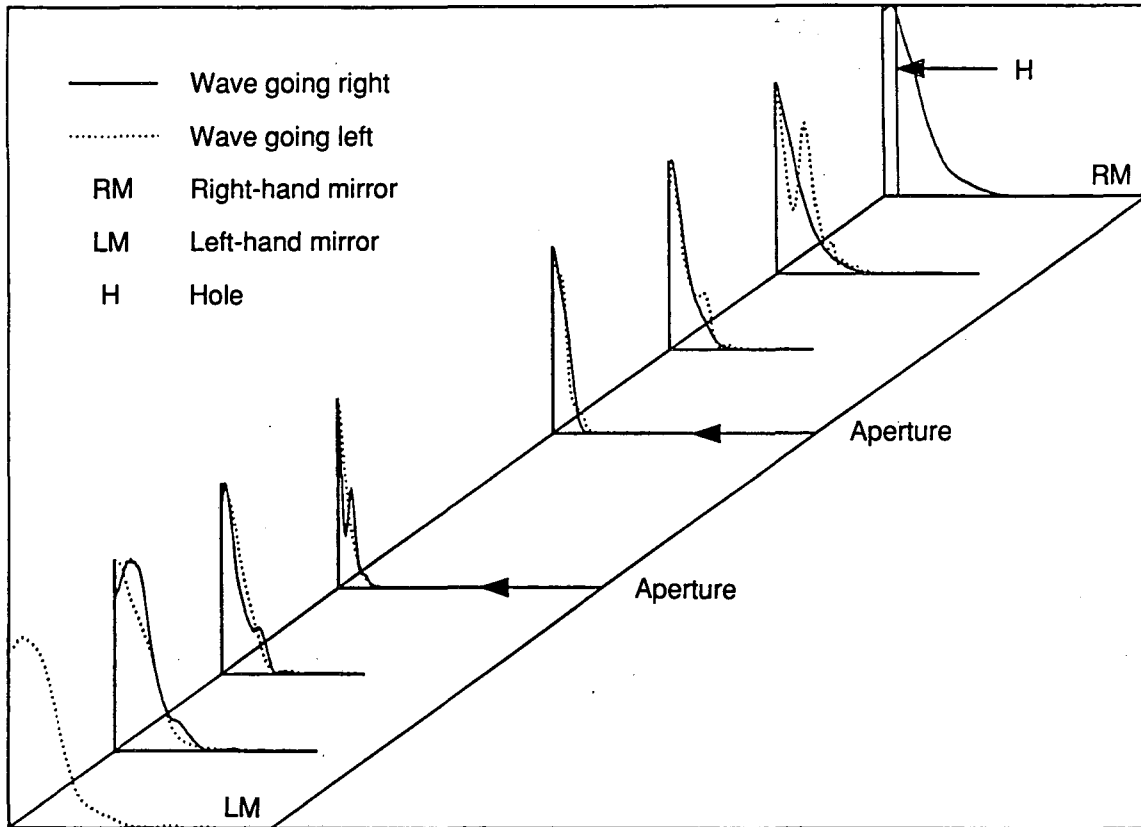*Figure 4-13. Intracavity intensity profiles of the dominant mode at a wavelength of 3 μm, for a gain of 2%. [XBL 922-5602]*

Figure 4-14. Intracavity intensity profiles of the dominant mode at a wavelength of 3 μm, for a gain of 55%. [XBL 922-5601]

As the intensity increases in the oscillator, the gain decreases from pass to pass. The saturated value of the gain at steady state, g_s, is given by

$$(1 - \alpha)(1 + g_s) = 1 \tag{4-35}$$

The mode profile and the resonator performance at saturation can therefore be obtained by computing the dominant mode for a sequence of cases obtained by decreasing the magnitude of the gain parameter until Eq. 4-35 is satisfied. The results of such a calculation were compared with those obtained from the oscillator version [Krishnagopal et al., 1991] of the three-dimensional FEL simulation code TDA [Tran and Wurtele, 1989]. The agreement is excellent when the saturated gain is low. Thus, our use of the linear FEL map to calculate the dominant resonator mode is also justified in the strong-signal regime.

In Fig. 4-15, we show an example of the hole-coupling performance for an FEL at saturation. The resonator configuration for this calculation was same as that for the empty-cavity results shown in Fig. 4-10, except that the left-hand mirror size is allowed to be somewhat larger to take advantage of the FEL gain. Figure 4-15 shows the loss and efficiency for the fundamental mode. We see that the hole-coupling efficiency, about
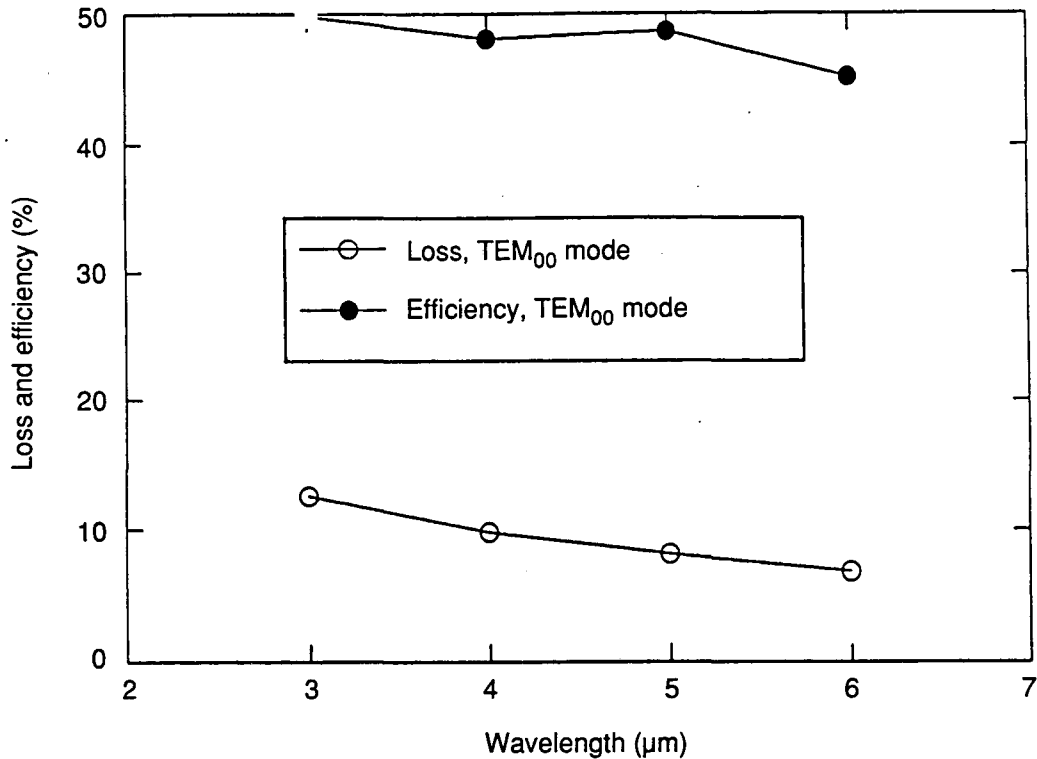
*Figure 4-15. Hole-coupling efficiency and loss for the TEM00 mode, with
intracavity FEL gain, at different wavelengths. The radii of the left-hand mirror
were 7, 8.3, 9.4, and 10.3 mm at wavelengths of 3, 4, 5, and 6 µm, respectively.
[XBL 922-5600]*

50%, is somewhat higher than in the empty-cavity case, whereas the round-trip loss is
practically the same over the entire tuning range from 3 to 6 µm.

To make sure that the TEM_{00} mode remained dominant, we checked the net gain of
both the TEM_{00} and the TEM_{10} mode in the small-signal regime and at saturation. The
results are shown in Fig. 4-16. At small signal, both modes are above threshold (net gain
> 0); however, the TEM_{00} mode has a larger net gain. At saturation, where the net gain
for the TEM_{00} mode is zero by definition (indicated in Fig. 4-16 by the horizontal line),
the TEM_{10} mode is below threshold. Thus, we conclude that the fundamental mode is
dominant.

Design of a Hole-Coupled Resonator for the IRFEL. Table 4-5 gives the basic resonator
parameters for the CDRL IRFEL. The radius of mirror curvature is determined by the
requirement that the Rayleigh length be 1 meter. The radius of the undulator bore
determines the radius of the fixed apertures 1 and 2.

As discussed in section 4.2.1, the full wavelength range of the FEL is divided into
four subranges, each spanning a wavelength region from λ_{min} to $\lambda_{max} \cong 2.28\ \lambda_{min}$. Each
subrange is covered by changing the undulator gap at a fixed electron energy. It is
obviously convenient to design the resonator configuration so that the size of the mirror
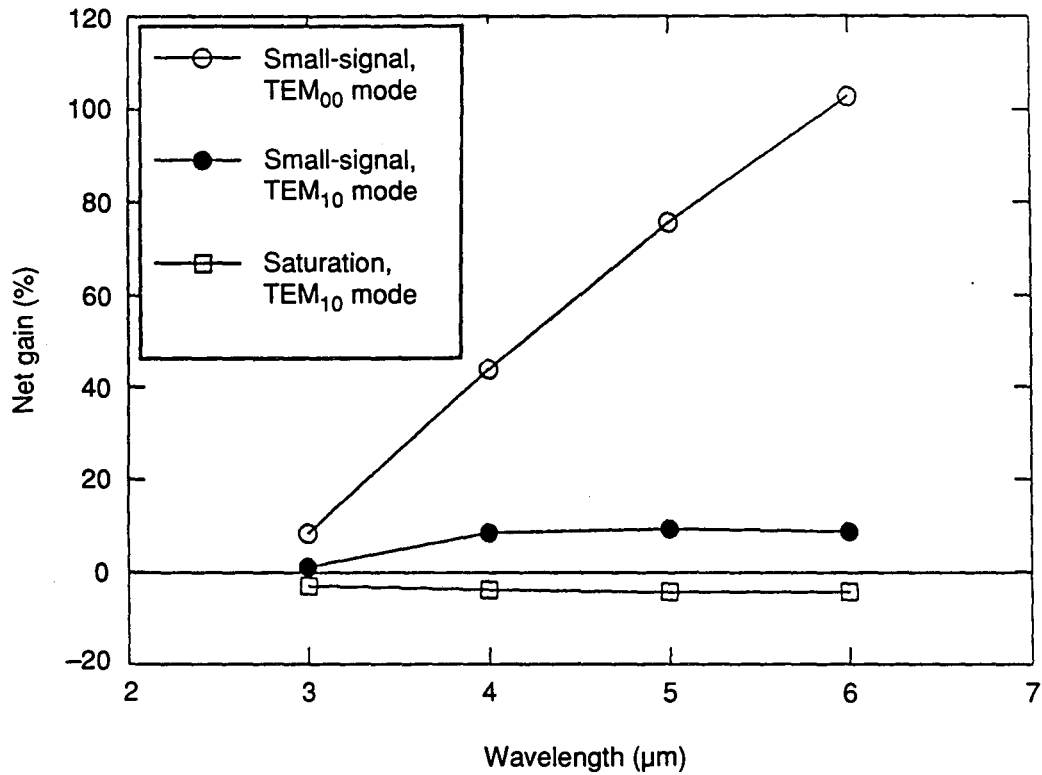
Figure 4-16. The net gains of the TEM_{00} and TEM_{10} modes in the small-signal regime and at saturation, for the same conditions described for Fig. 4-15. By definition, the horizontal line at 0% reflects the net gain of the dominant TEM_{00} mode at saturation. [XBL 922-5599]

Table 4-5. Basic resonator parameters for the CDRL IRFEL.

Cavity length [m]	24.6
Mirror radius of curvature [m]	12.38
Stability parameter, g	–0.987
Rayleigh length, z_R [m]	1
Undulator length [m]	2
Radius of undulator bore [mm]	10.5

coupling hole need not change during the wavelength scan within a given subrange. Thus, the right-hand mirror in Fig. 4-9 need not be changed during the scan. On the other hand, the radius of the adjustable aperture varies continuously during the scan.

The hole-coupling parameters for the CDRL IRFEL are given in Table 4-6. The performance of the hole-coupling resonator is summarized in Figs. 4-17 and 4-18. Figure 4-17 shows the hole-coupling efficiency η_c and the total loss α as functions of the wavelength. Over the entire wavelength range, $40\% \leq \eta_c \leq 60\%$ and $5\% \leq \alpha \leq 15\%$. The resonator parameters were chosen so that degeneracies do not occur during a wavelength scan within a given subrange. Figure 4-18 shows the small-signal gain (the gain at the beginning of the FEL start-up) and loss α as functions of the wavelength. At all wavelengths, the gain is larger than the loss by a margin sufficient to ensure efficient FEL operation.

4.3.2 Additional Outcoupling Schemes Based on All-Metal Optics

For finite-radius mirrors, some radiation energy must spill over the mirror edges. Outcoupling approaches based on this phenomenon are referred to as edge-coupling schemes. Edge coupling can be used in either a stable or an unstable resonator.

Edge Coupling in a Stable Resonator. The case of a stable resonator is illustrated in Fig. 4-19. The radius of the left-hand mirror is taken to be sufficiently large that the loss at the mirror edge is negligible. The radius of the right-hand mirror is chosen to maximize the coupling efficiency, while maintaining the total loss at the desired level.

The parameters for an edge-coupling scheme optimized for the CDRL IRFEL are given in Table 4-7. The radius of curvature for both mirrors is the same as that given in Table 4-5. The coupling performance is shown in Fig. 4-20. As expected, the loss for a fixed mirror size increases as a function of the wavelength, in contrast to the case of hole coupling. Such behavior is desirable, because it is similar to the behavior shown in Fig. 4-18 for the small-signal gain. The efficiency is significantly higher than that in the hole-coupling case, especially at short wavelengths. At long wavelengths, the loss at the fixed apertures (the undulator bore) becomes the limiting factor in the efficiency. For the edge-coupling scheme described here, the wavelength scans encounter no mode degeneracies. Thus, it is unnecessary to introduce adjustable apertures.

Table 4-6. Hole-coupling parameters for the IRFEL.

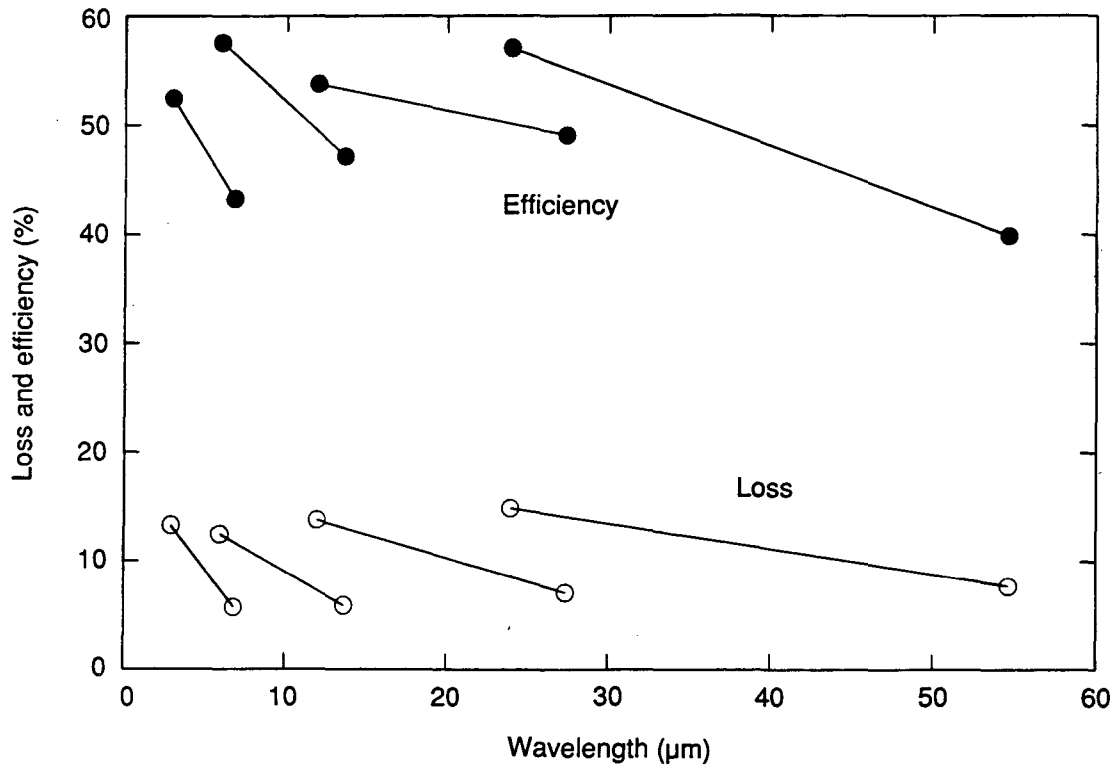| Wavelength range (μm)	Hole radius (mm)	Adjustable aperture radius (mm)
3–6.84	2	19–35
6–13.7	2.8	30–50
12–27.4	4.4	45–65
24–54.7	6	60–100

Figure 4-17. Hole-coupling performance parameters (loss and efficiency) for the CDRL IRFEL, as functions of wavelength. Each line segment represents the wavelength scanning range for a fixed electron beam energy. [XBL 922-5598]
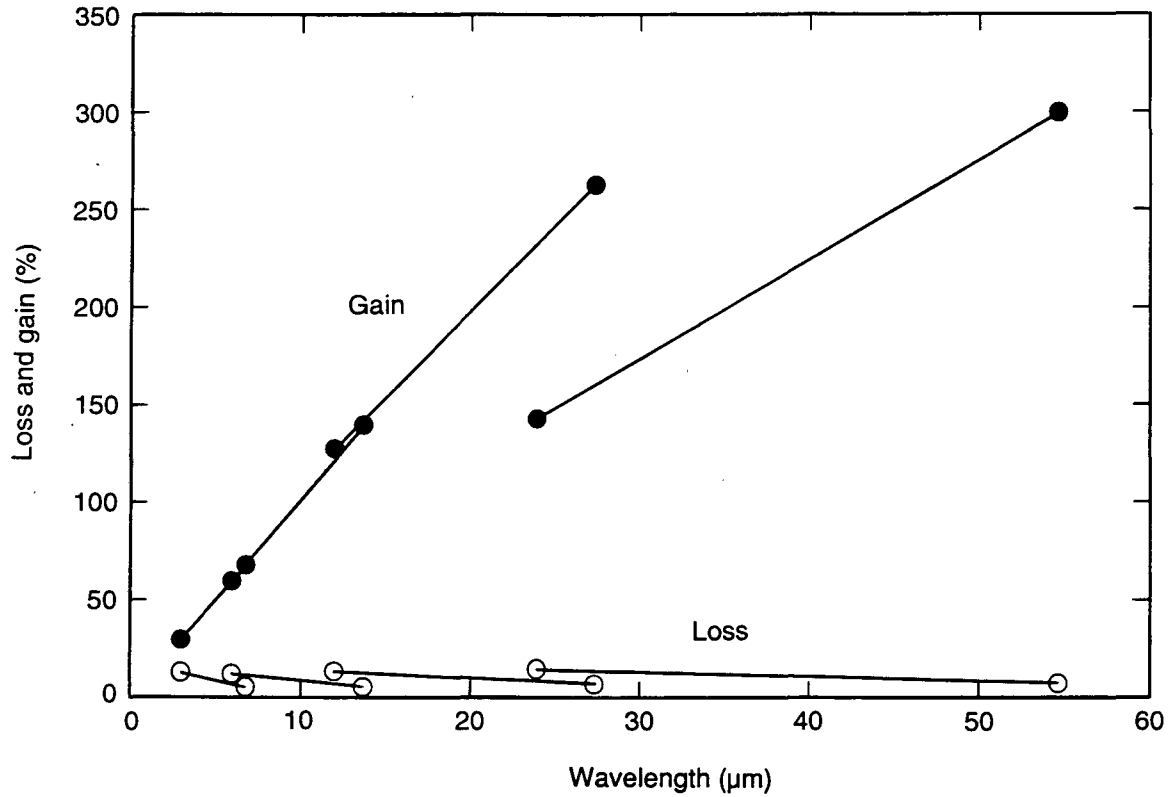
Figure 4-18. Small-signal FEL gain and the loss of a hole-coupling resonator, as functions of wavelength. [XBL 922-5597]
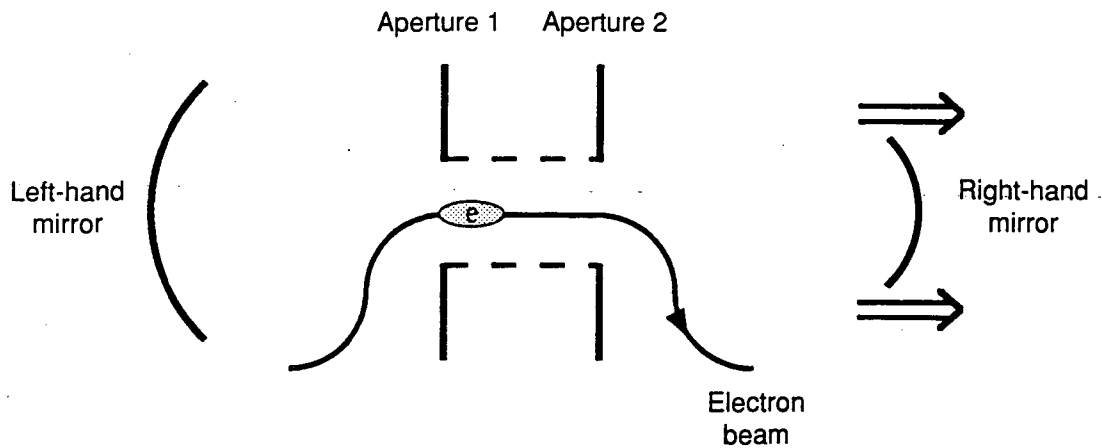

Figure 4-19. Schematic of an edge-coupling arrangement in a stable resonator. [XBL 922-5595]

Table 4-7. Parameters for edge coupling in a stable resonator, optimized for the CDRL IRFEL.

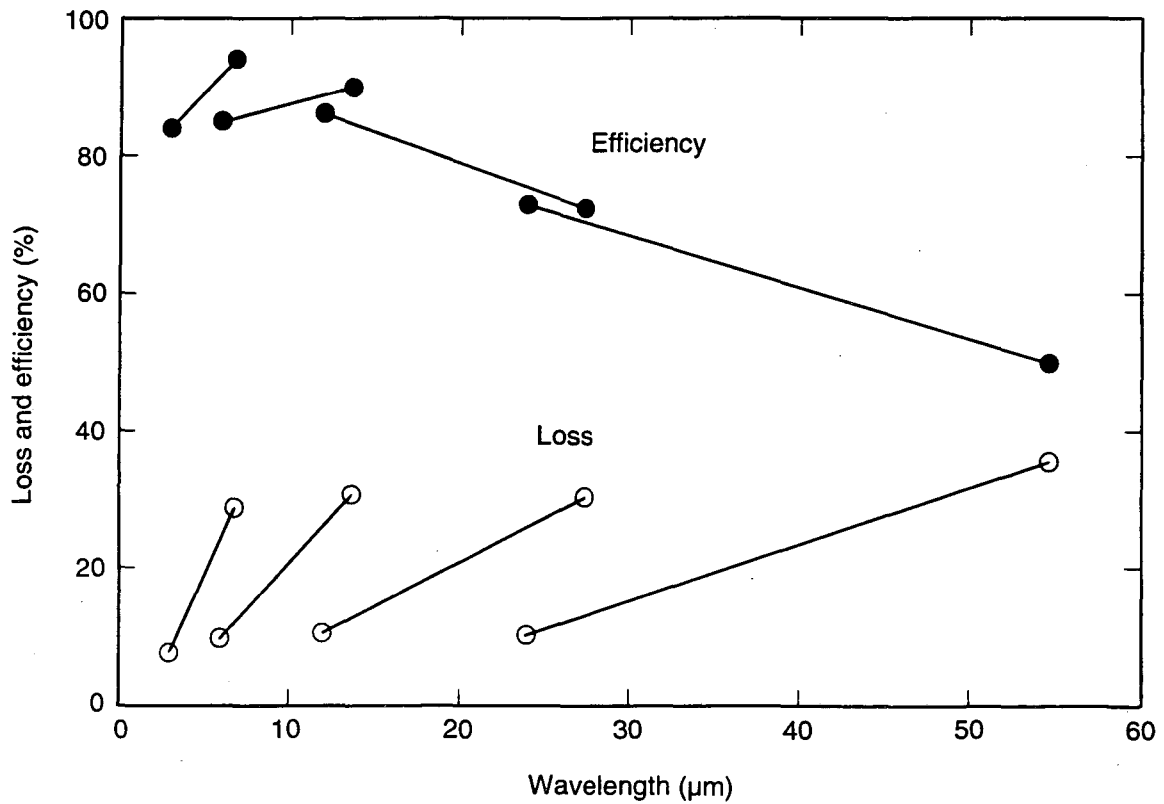| Wavelength range (μm)	Radius of coupling mirror (mm)
3–6.84	14
6–13.7	19
12–27.4	26
24–54.7	36

Figure 4-20. Edge-coupling performance parameters as functions of wavelength. [XBL 922-5594]

The intracavity mode profile is smooth and Gaussian-like, as shown in Fig. 4-21. Such a profile matches well to the electron beam profile.

A drawback of the edge-coupling scheme is the fact that the mode profile immediately beyond the coupling mirror has the shape of a ring, with a poor Gaussian quality factor. However, it is possible to transform the ring profile into a solid profile by using an exotic optical element known as an axicon (Fig. 4-22). Whether the use of an axicon is consistent with the broad tuning requirement of the CDRL IRFEL is an issue that merits careful study.

Edge Coupling in an Unstable Resonator. Unstable resonators have been used in many high-power lasers [Siegman, 1986]. Recently, Siegman [1991] has studied a negative-branch stable-unstable resonator for FEL applications, as shown schematically in Fig. 4-23. The mirrors are toroidal, so that the mode characteristics are different in the horizontal and vertical planes. In the vertical plane (the plane perpendicular to the page in Fig. 4-23), the resonator is stable and has a lowest-order Gaussian mode. In the horizontal plane, which is also the oscillation plane for the undulator, the cavity is a one-sided, low-magnification, confocal, negative-branch unstable resonator, with the internal focal region of the negative-branch resonator providing the focused interaction region with the electron beam.
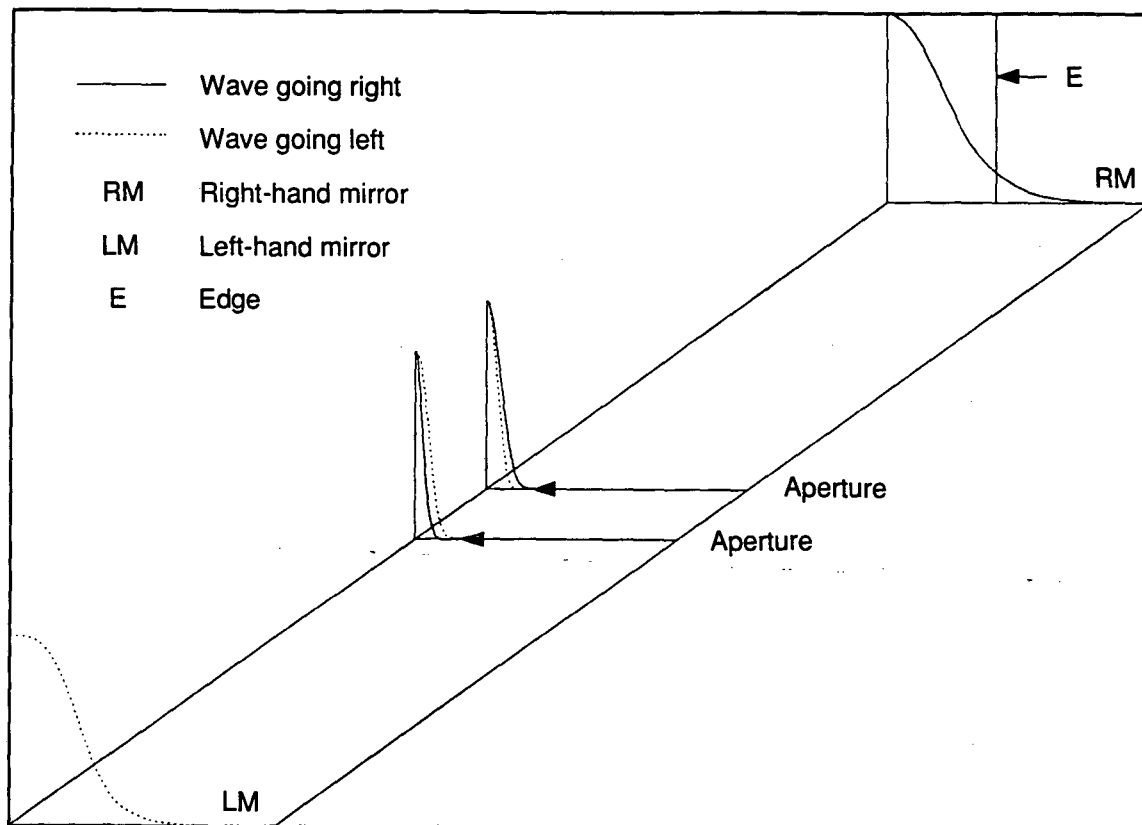

Figure 4-21. Intracavity mode profile at a wavelength of 21.5 μm, for an edge-coupled resonator. [XBL 922-5593]
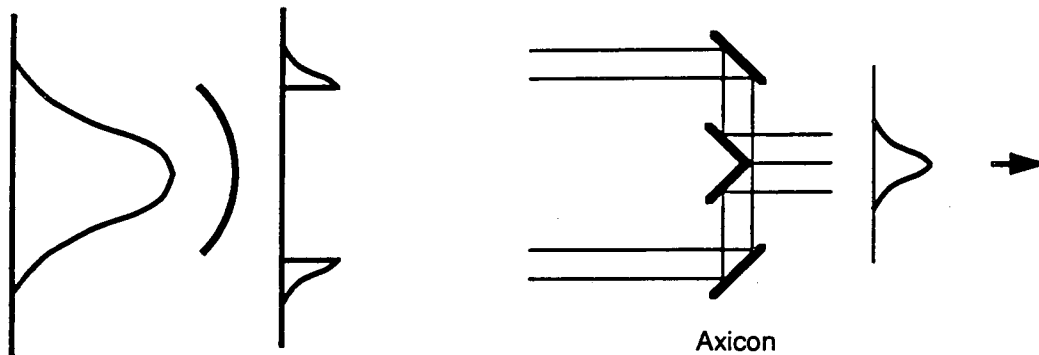
Figure 4-22. Schematic illustration of an axicon, used to improve the mode quality of an edge-coupled beam. [XBL 922-5596]
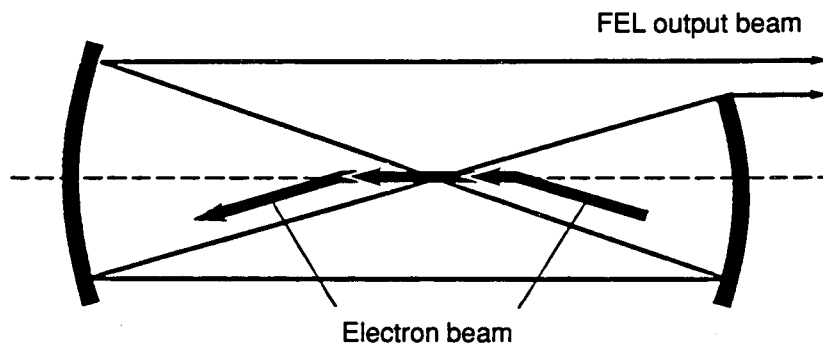

Figure 4-23. Schematic top view of an unstable resonator. By using toroidal mirrors, the cavity can be made geometrically stable, with low loss, in a direction perpendicular to the page, while operating as a one-sided, confocal, negative-branch unstable resonator in the plane of the page. [XBL 922-5592]

Preliminary calculations [Siegman, 1991] indicate that this type of resonator has attractive features for long-wavelength, widely tunable IRFELs, such as the one described here. We intend to carry out a more extensive study in the future to compare the performance of such a resonator with that of the hole-coupling scheme.

4.4 OPTICAL SYSTEMS

In this section, we first describe the optical cavity, explicitly outlining the engineering requirements imposed on the various optical elements and their supports. Next, we describe the diagnostics that will allow us to evaluate FEL performance and that will serve as the front end of a feedback-controlled cavity alignment and stabilization system. Section 4.3.3 then outlines the underlying principles and design of semiconductor switch–controlled pulse slicers and pulse pickers, which will be used to further tailor the FEL output to user requirements. Finally, we briefly describe the beam transport system that will deliver infrared radiation to CDRL researchers.

4.4.1 Specifications for the Cavity Optics

The basic optical cavity layout is shown schematically in Fig. 4-24, and the basic cavity parameters are given in Table 4-8. Of particular importance, the cavity optics can suffer only low losses, and good surface quality is necessary. To ensure a clean optical mode pattern, we require a maximum tolerance of $\lambda/20$, peak-to-peak at 10 μm, for surface flatness, coma, astigmatism, and spherical aberrations. These specifications, however, can currently be met by commercial manufacturers. The maximum spot size on the mirror surface occurs during operation at 50 μm. Gaussian optics predicts a spot size $w_M \cong 5$ cm, which would require 15-cm optics to minimize diffraction losses; however, the simulations described in section 4.3 indicate that diffraction at the exit plane of the undulator bore will increase the spot size and thus require 25-cm optics. Transverse mode control will be handled using intracavity apertures.

For the FEL to operate efficiently, the Rayleigh length z_R should be matched to the undulator length to provide a good overlap between the electron beam and the optical beam. From simulations (again, see section 4.3), we have determined for different wavelength ranges a ratio of the spot size on the mirror to the mirror hole size that maximizes the outcoupled power. As shown in Fig. 4-25, a small deviation ΔR from the design value for the radius of curvature leads to a large deviation in both z_R and the spot size on the mirror (and therefore the fraction of outcoupled power). We therefore require a 0.04% tolerance on the 12.38-meter radius of curvature, which can again be met by commercial manufacturers.

The mirror must also handle high peak and high average intracavity power densities. When the FEL operates in a high-efficiency ($1/2N$) sideband mode, the intracavity power levels are given by

$$P_{cw} = \frac{\text{efficiency}}{\text{loss}} P_{cw}^{\text{beam}} \cong \frac{1.25\%}{10\%} 370 \text{ kW} = 46 \text{ kW} \tag{4-36}$$

$$P_{\text{peak}} = 107 \text{ MW} \left(\sim 10\% \text{ of } P_{\text{peak}}^{\text{beam}} = 1 \text{ GW}\right) \tag{4-37}$$
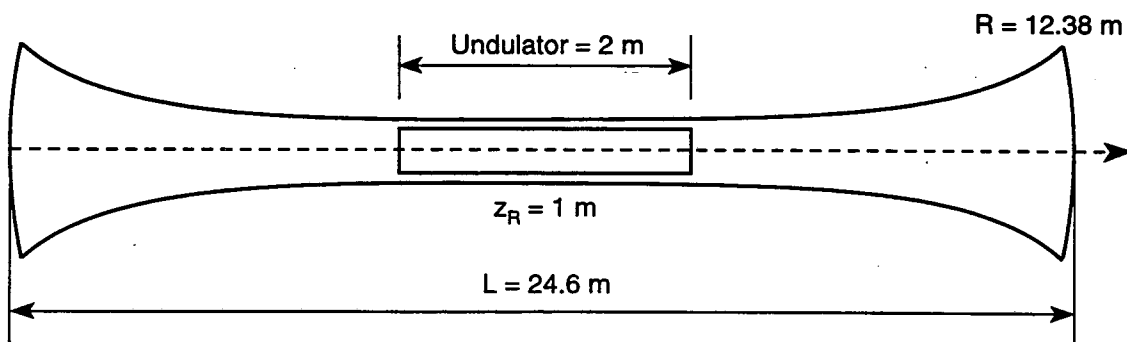

Figure 4-24. Schematic of the basic cavity layout. R = mirror radius of curvature; z_R = Rayleigh length. [XBL 922-5613]

Table 4-8. Cavity dimensions and output parameters.

Wavelength range [μm]	3–50
Cavity length, L [m]	24.6
Undulator length, L_u [m]	2.0
Rayleigh length, z_R [m]	1.0
Radius of mirror curvature, R [m]	12.38
Stability parameter, g	–0.987
Micropulse duration, τ_p [ps]	35
Intracavity cw power, P_{cw} [kW]	46
Intracavity peak power, P_{peak} [MW]	107
Micropulse energy E_{pulse} [μJ]	
at 10 μm and 12.2 MHz	50
at 10 μm and 6.1 MHz	100
Peak output power, P_{peak}^{out} [MW]	2
Repetition rate [MHz]	12.2 or 6.1
CW output power, P_{cw}^{out} [kW]	0.6
Spectral bandwidth at 10 μm, $\Delta\lambda/\lambda$	$\leq 10^{-3}$

and the intracavity power densities on the mirror surface are then given by

$$\left.\frac{dP}{dA}\right|_{cw} = 6.1 \text{ kW/cm}^2 \tag{4-38}$$

$$\left.\frac{dP}{dA}\right|_{peak} = 14 \text{ MW/cm}^2 \tag{4-39}$$

The surface quality we demand can be maintained without active cooling only for average power densities below 200 W/cm^2. We therefore require actively cooled mirrors. The peak power density is well below the single-pulse damage threshold for uncoated OFCH-copper, but the cumulative effect of a 12-MHz pulse train is unclear. Fortunately, the high vacuum that must be maintained in the optical cavity will greatly reduce surface contamination, which is the main source of surface damage.
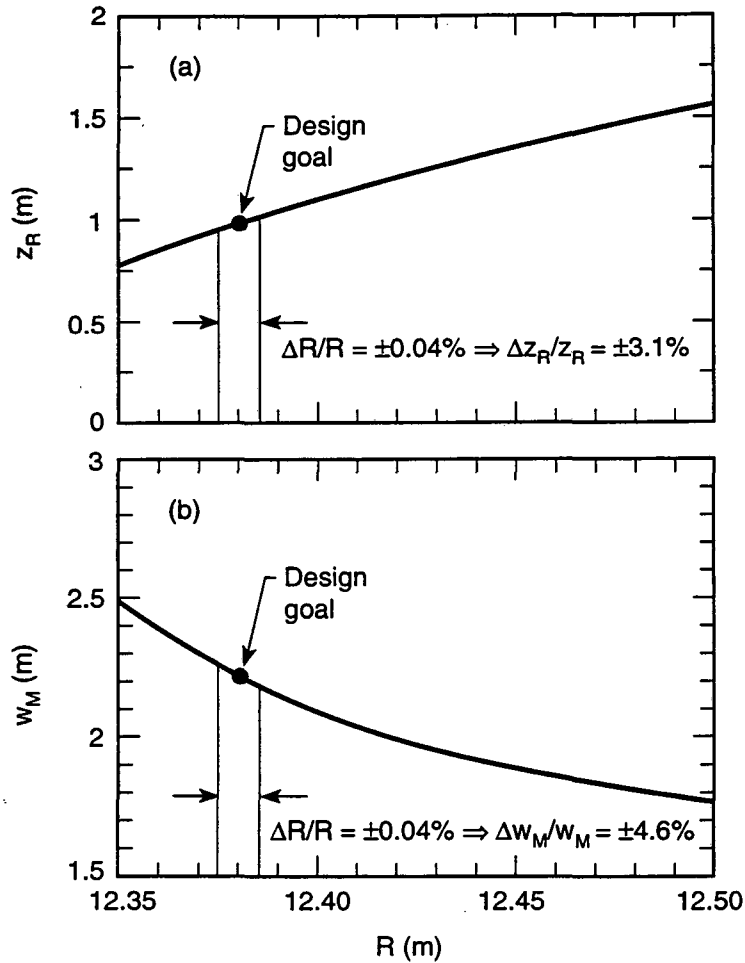
Figure 4-25. (a) The Rayleigh length z_R and (b) the laser spot size on the mirror, w_M, as functions of the radius of mirror curvature, R. The vertical lines indicate a 0.04% tolerance around the design value of 12.38 meters. [XBL 922-5612]

The mirror mounts must allow accurate alignment . As shown in Fig. 4-26, mirror misalignment by an angle θ_M leads to a change in the angle of the optical axis, θ_{OA}, given by

$$\Delta \theta_{OA} \cong \frac{R}{2R - L} \Delta \theta_M \qquad (4\text{-}40)$$

To keep the optical axis within 1/10 of the mode rms angle

$$\sigma = \left(\frac{\lambda}{4\pi z_R} \right)^{1/2} = 890 \ \mu\text{rad} \qquad (4\text{-}41)$$

we demand a pointing accuracy of $\Delta\theta_M < 1.0 \ \mu$rad . (Off-the-shelf mounts are available with a pointing accuracy better than 0.4 μrad.) In addition, the mirror mount must have a true gimbal design and must be able to accommodate large 25-cm water-cooled optics.
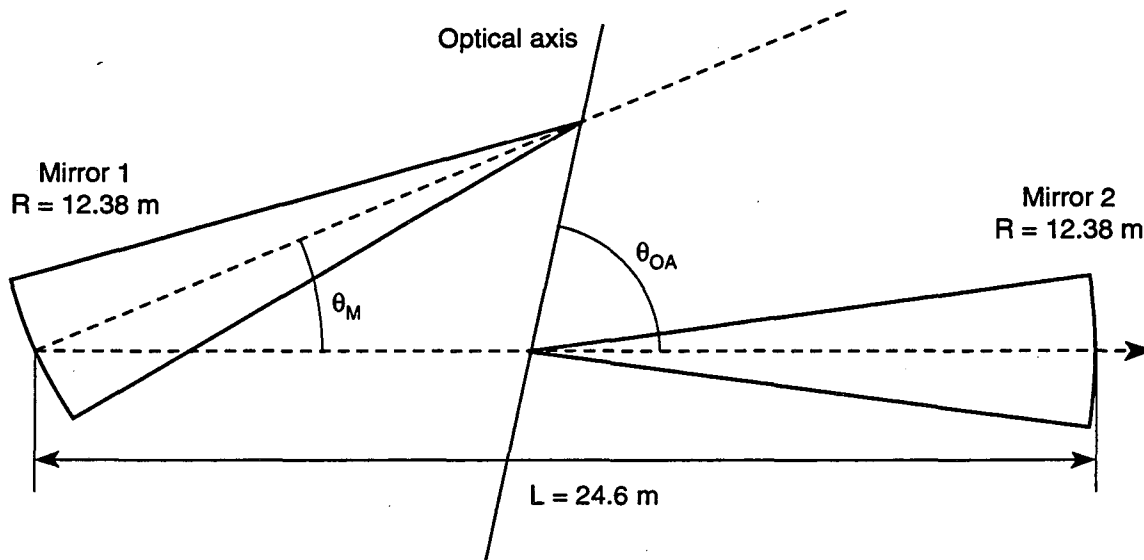
***Figure 4-26. Depiction of the effect of an angular mirror misalignment, θ_M, on
the position of the optical axis. [XBL 922-5614]***

Angular adjustments must have a resolution better than 1 μrad. The mount should allow
remotely controllable, trackable translations in the x, y, and z directions and two
orthogonal rotations. (Here, the laser propagates in the x direction and yz defines the
transverse plane.) Resolution must be 0.1 μm in the x direction and 1 μm in the
transverse plane. An interferometric measuring unit will be used to measure cavity length
changes with a resolution of 0.2–0.3 μm and can also be used to monitor pitch, roll, and
yaw of the mirror mount. The motion control system must allow for a feedback control
system based on the interferometric measurements. A large-aperture (~22-cm), pin-
actuated iris diaphragm will be used for transverse mode control. Finally, all
electromechanical and electro-optical components must be compatible with the radiation
and vacuum environment of the optical cavity. Commercially available mounts,
translation stages, and motion-control modules that interface with personal computers
meet the above specifications. One such assembly is shown in Fig. 4-27.

Two options are available for the support system. The option selected for the
conceptual design involves mounting the mirror mount and stages directly to the vacuum
chamber, then supporting the vacuum chamber with a pneumatically isolated table. The
alternative consists of an electronic vibration-isolation system that supports both the
mirror mount and the translation stages and dynamically damps out system vibrations
inside the vacuum housing. The vacuum housing is then bolted to a concrete block,
which provides static inertial isolation. In both options, the vacuum housing of the
mirrors is isolated from the beam pipe using flexible bellows. A final engineering design
will be based on the adequacy of these two options in damping out vibrations, after we
have measured the actual frequency spectrum and levels of vibrations in the accelerator
vault. A conceptual layout of the first design alternative is shown in Fig. 4-28.

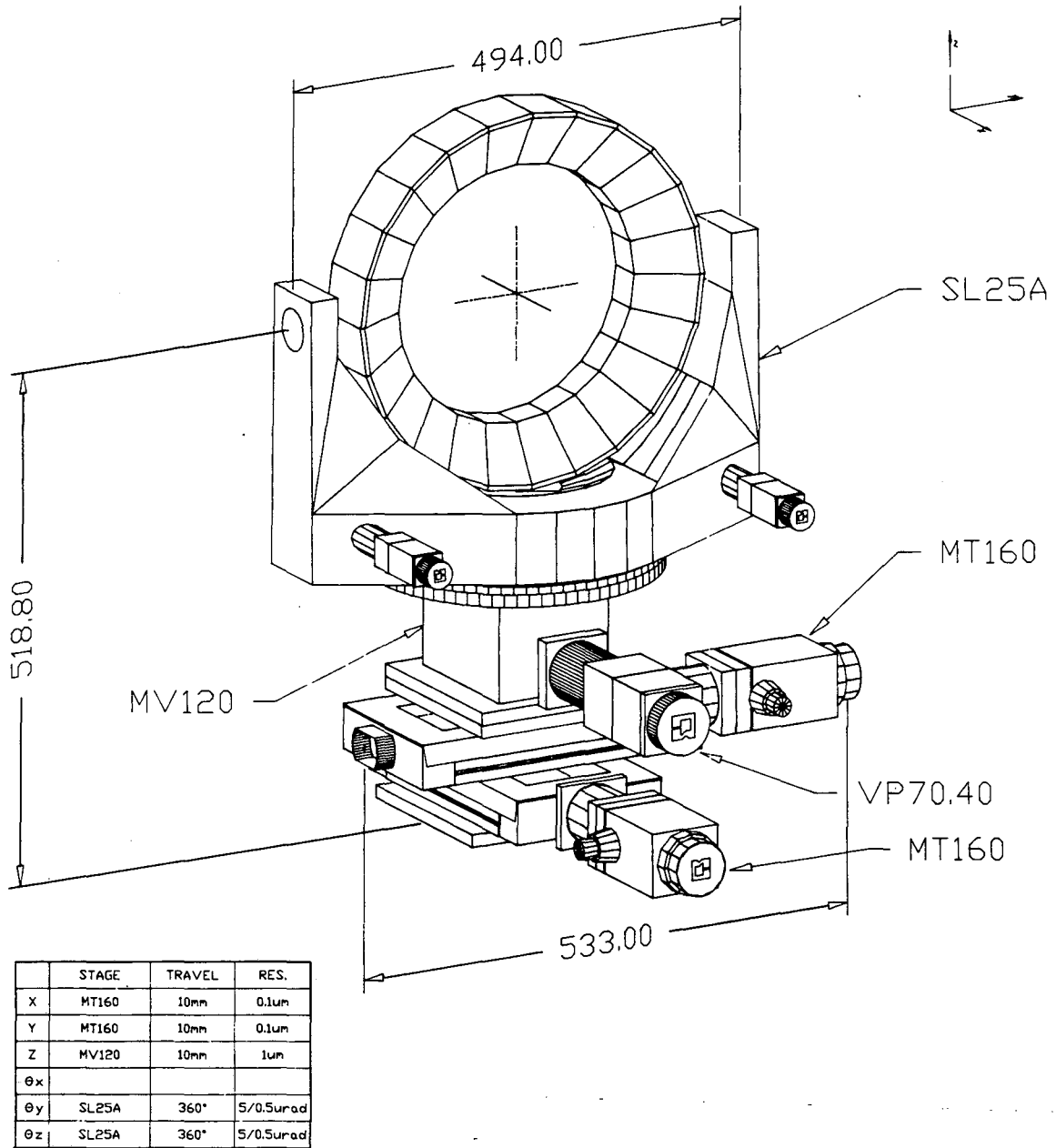|	STAGE	TRAVEL	RES.
X	MT160	10mm	0.1um
Y	MT160	10mm	0.1um
Z	MV120	10mm	1um
θx			
θy	SL25A	360°	5/0.5urad
θz	SL25A	360°	5/0.5urad

Figure 4-27. A mirror mount, available commercially from Klinger Scientific, that meets the specification for the IRFEL optical cavity end mirrors. [XBL 922-5608]
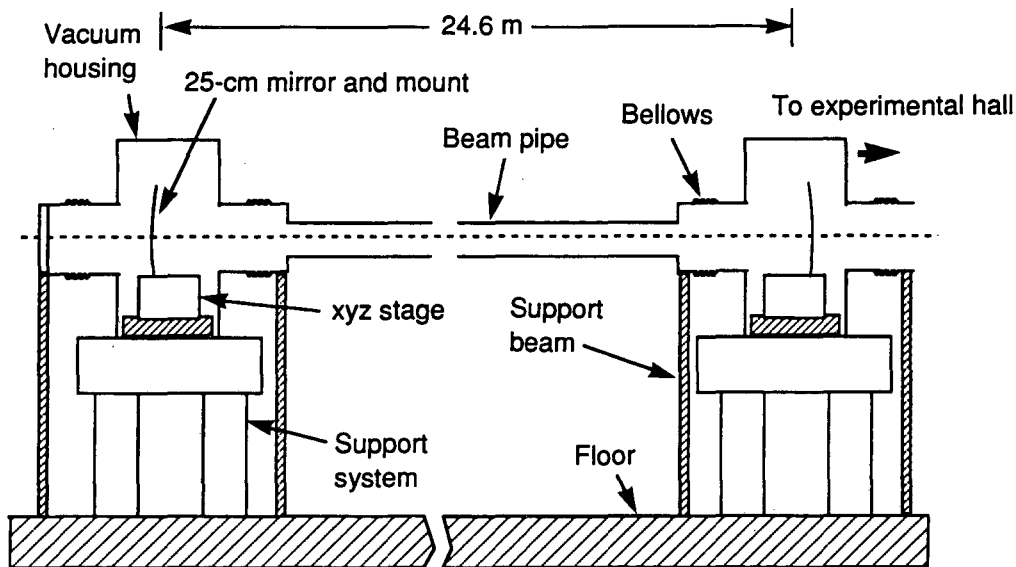
Figure 4-28. Conceptual layout of the mirror mount and support system. [XBL 922-5590]

4.4.2 Optical Alignment and Diagnostics

The basic layout for the optical alignment and diagnostics system is shown in Fig. 4-29. The FEL will be aligned as follows. An optical axis is defined by aligning a cw He-Ne laser and a pulsed or cw CO_2 laser on the undulator axis. (All the radiation diagnostics will be aligned on this axis.) The initial electron beam is then aligned by making the electron beam (at low duty cycle) overlap the He-Ne laser beam on alignment screens. Fine tuning at full electron beam power is then done by maximizing the intensity of the on-axis spontaneous emission. Finally, the optical cavity is aligned, first with a cw visible and/or infrared laser and then by maximizing the FEL output.

Optimizing the performance of the FEL (both during the start-up phase and during normal operation), as well as providing the user with all pertinent FEL output parameters, requires measuring peak and average output power levels, macropulse and micropulse durations, wavelength, time-averaged and instantaneous line widths, and the output beam mode quality. Average output power will be measured with thermopiles, and peak power will be estimated from the average power, once the pulse duration is known. The time evolution of the pulse train will be monitored using room-temperature or cooled intrinsic photoconductors, such as HgCdTe, Ge:Cu, or Ge:B. The signal from these detectors will also be used as the basis for feedback-controlled cavity alignment.

Average wavelength and line width will be measured using a 1-meter spectrograph, with suitable gratings and a one-dimensional pyro-array detector. Resolution for the wavelength measurement ($\Delta\lambda/\lambda$) will be about 10^{-4}. Stabilizing the wavelength at which the FEL operates will require tracking the spectral peak, which can be done with a resolution of 10^{-5}. We plan to measure the spectral properties of each micropulse by
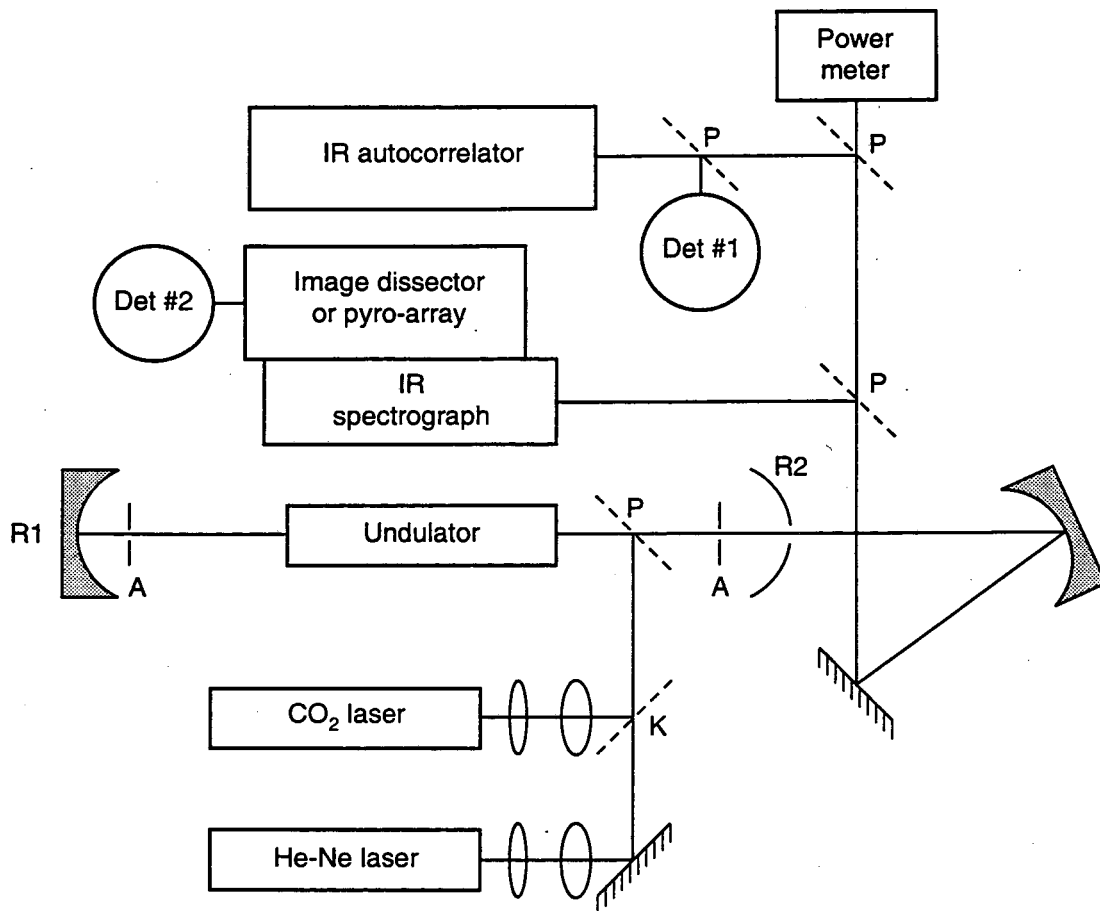
Figure 4-29. Schematic layout of the optical diagnostics. R1 and R2 are the cavity mirrors; the P's are partially reflecting mirrors; K is a kinematic mirror; the A's are transverse apertures; and Det. #1 is an intrinsic photoconductor detector that monitors the pulse train. The spectrograph–pyro-array combination is used to record average spectral information. An image dissector replaces the pyro-array to obtain single-pulse spectral information on a fast single-element detector, Det. #2. [XBL 922-5615]

replacing the pyro-array with an image dissector, set up as shown in Fig. 4-30 [Baldis et al., 1977]. An image dissector switches slices of arbitrary width from a linear infrared image (in this case, a single pulse spectrum) onto a single-element detector, with a time delay between successive slices that depends on the round-trip time within the instrument. The round-trip time thus determines the time resolution, which can be better than 5 ns.

The micropulse duration will be measured using an infrared autocorrelator. The underlying idea in autocorrelation is to split an incident pulse into two half-intensity pulses and then to recombine then in a nonlinear medium. Only when the intensity is high enough (requiring good overlap between the two pulses) will a second-harmonic signal be generated. Two different types of autocorrelators will be constructed: a scanning autocorrelator that employs a time-varying delay unit [Ippen and Shank, 1975]
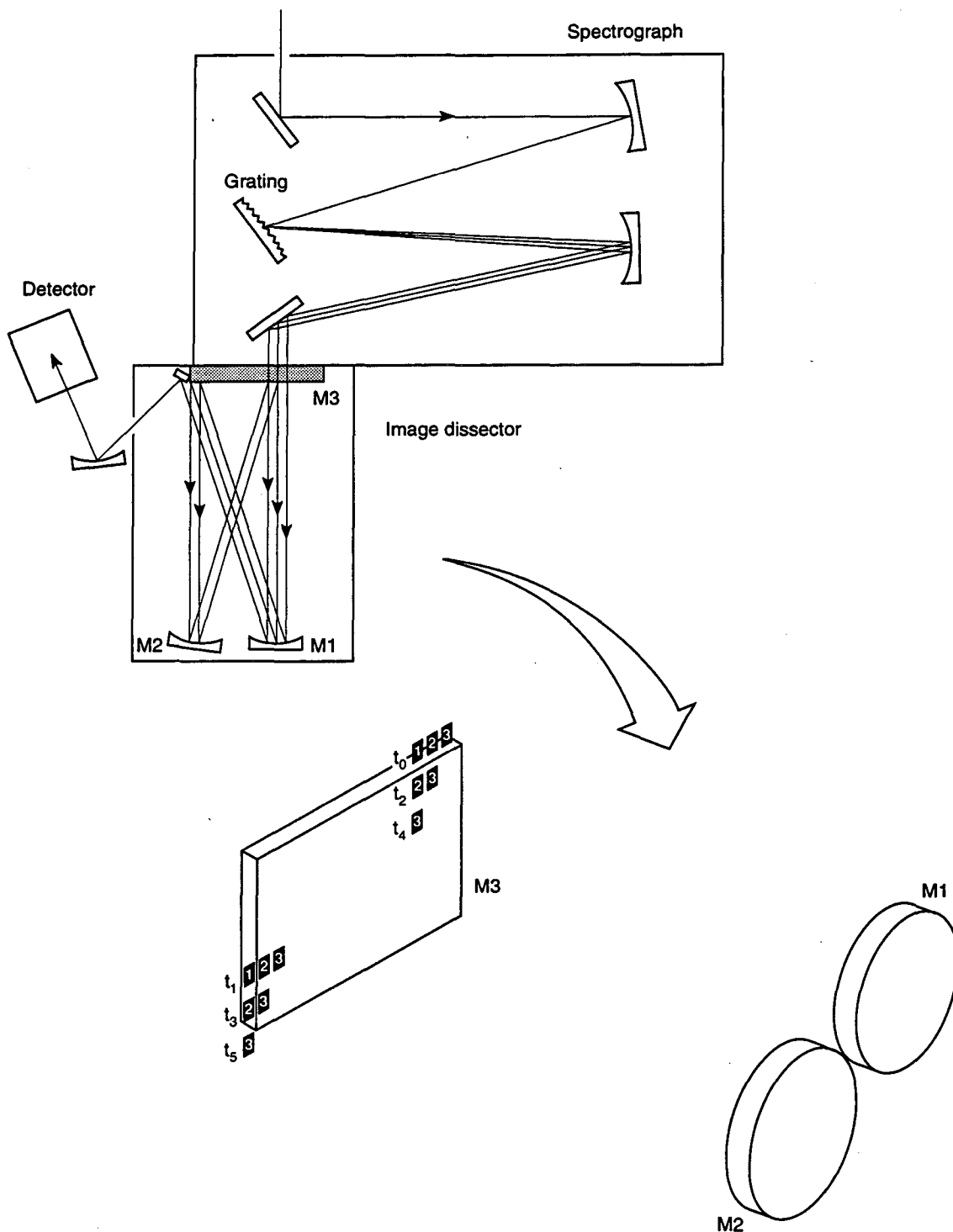
Figure 4-30. Schematic of a single-pulse measurement setup using an image dissector. Slices from a spectral image are sent sequentially to the detector, with a time delay between slices equal to the round-trip time within the instrument. The figure depicts the optical paths of three slices from an infrared spectrum. Slice 1 exits the image dissector at t_1, following a single reflection from mirror M1; slices 2 and 3 are further reflected from mirrors M3, M2, M3, and M1, before slice 2 exits at t_3. Slice 3 requires another round-trip before exiting at t_5. [XBL 922-5616]

and a single-pulse autocorrelator based on non-collinear optical mixing [Kolmeder et al., 1979]. The former requires many pulses to construct the autocorrelation; the two halves of each split pulse receive different time delays, and the relative time delay for succeeding pulses is varied slowly by slowly changing the path lengths the pulses travel (by means of rotating glass blocks, for example). By measuring the second-harmonic intensity as a function of delay, we obtain the pulse width. Typically, one scanning autocorrelation trace can be obtained in 1–10 μs; however, this time scale is comparable to the optical cavity decay time. In a single-pulse autocorrelator, it is the physical length of the region in which the second harmonic is generated that is measured and that yields the pulse length. To truly qualify as a single-shot device again requires the use of an image dissector and a fast single-element detector. Commercially available nonlinear crystals allow frequency doubling of wavelengths up to 12.6 μm (for example, AgGaSe$_2$ can be used in the 3- to 12.6-μm range). Further, recent experiments suggest that CdMnTe could be used to extend the wavelength range to 40 μm [Becla et al., 1992].

4.4.3 Pulse Control

In some experiments, a single pulse, shorter than the nominal infrared micropulse, may be required. Semiconductor switching offers a practical means for providing such pulses [Alcock and Corkum, 1979]. The idea is to create free-carrier pairs in a semiconductor, on a time scale that is short compared with the incident infrared pulse duration, using a visible control pulse (see Fig. 4-31). When the visible photon energy is higher than the band-gap energy, free-carrier absorption terminates transmission; when the plasma density of free carriers reaches the critical density for the infrared radiation, the semiconductor becomes highly reflective.
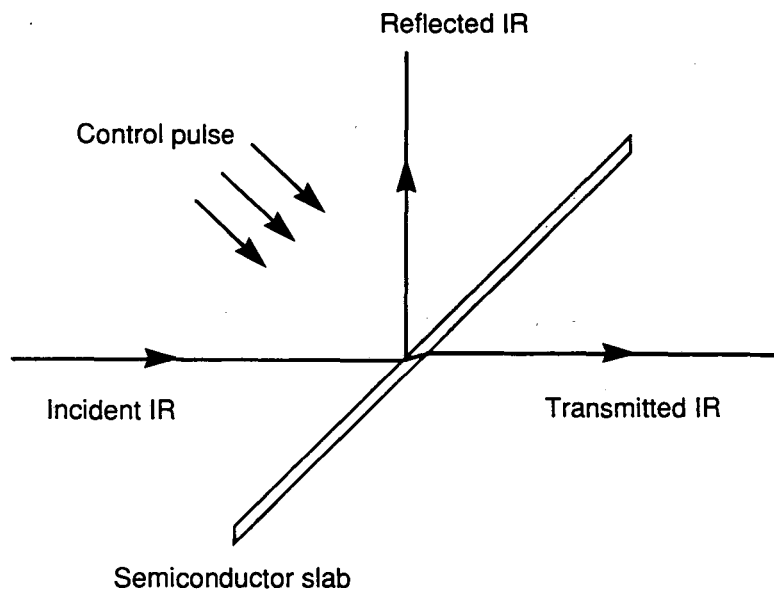

Figure 4-31. Schematic of a semiconductor switch used to provide output pulses shorter than the nominal infrared pulse duration. [XBL 922-5591]

The control pulse should have a power density of 10–50 MW/cm² at visible wavelengths. For example, a 1- to 10-ps pulse at 532 nm, containing a few tens of microjoules in a 1-mm spot, is sufficient to create a fast switch [Corkum, 1983]. The time scales for which switching is practical can be inferred from Fig. 4-32 [Alcock and Corkum, 1979]. Typically, total reflection occurs in about 5 ps and significant attenuation occurs on a 1- to 2-ps time scale.

To produce pulses shorter than the infrared micropulse, two semiconductor switches will be configured as a pulse slicer, as shown in Fig. 4-33. A short pulse is sliced from a longer pulse by using one semiconductor to remove the leading tail of the micropulse (by transmission), and a second to remove the trailing tail (by reflection). This method has been used successfully in generating 1- to 2-ps pulses from 50-ns CO_2 laser pulses at 10.6 μm [Corkum, 1983].

As Fig. 4-32a demonstrates, the surface density of free carriers can remain high for tens of picoseconds, a phenomenon that we will use to our advantage for a pulse picker. As shown schematically in Fig. 4-34, a pulse picker selects one pulse from the infrared pulse train. A single suitable semiconductor in reflection mode serves well as such a device. Since the free-carrier density remains high for tens of picoseconds, the control pulse can be fired onto the semiconductor well before the arrival of the infrared pulse.

According to Alcock and Corkum [1979], faster fall times for the surface density of free carriers may be achieved by choosing semiconductors with a high electron-hole recombination rate or by enhancing the rate (for example, by using a highly polished surface). Such a fast-closing semiconductor switch may be useful as single-element pulse slicers. The availability of such semiconductors would also allow a micropulse duration measurement, based on correlating a short visible-light pulse with the infrared pulse. The
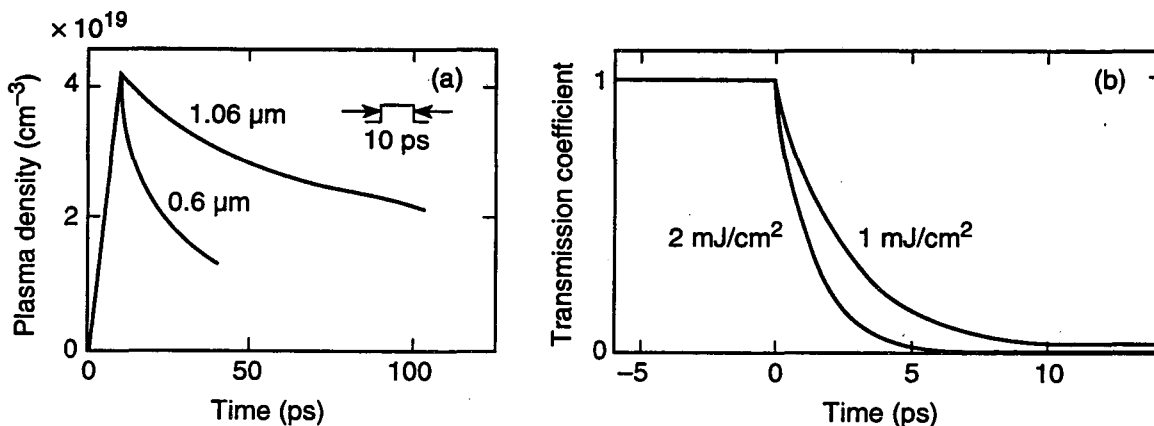
Figure 4-32. (a) Surface density of free-carrier pairs in germanium, plotted as a function of time for a 10-ps, 1-mJ/cm² (absorbed energy), 1.06-µm pulse (upper curve) and for a 10-ps, 0.5-mJ/cm² (absorbed energy), 0.6-µm pulse (lower curve). (b) Transmission coefficient of germanium as a function of time, showing the attenuation of 10-µm radiation due to an intravalence band transition induced by a 10-ps pulse of 1-µm radiation at t = 0. The absorbed energy density was 1 mJ/cm² (upper curve) and 2 mJ/cm² (lower curve). [XBL 922-5617]

Figure 4-33. Schematic layout of a pulse slicer based on a pair of semiconductor switches arranged in series. [XBL 922-5618]

semiconductor would be used as a gate that could be swept across the infrared pulse by changing the delay time between visible and infrared pulses. Semiconductor switching may also be useful as a technique for cavity dumping.

4.4.4 Optical Beam Transport

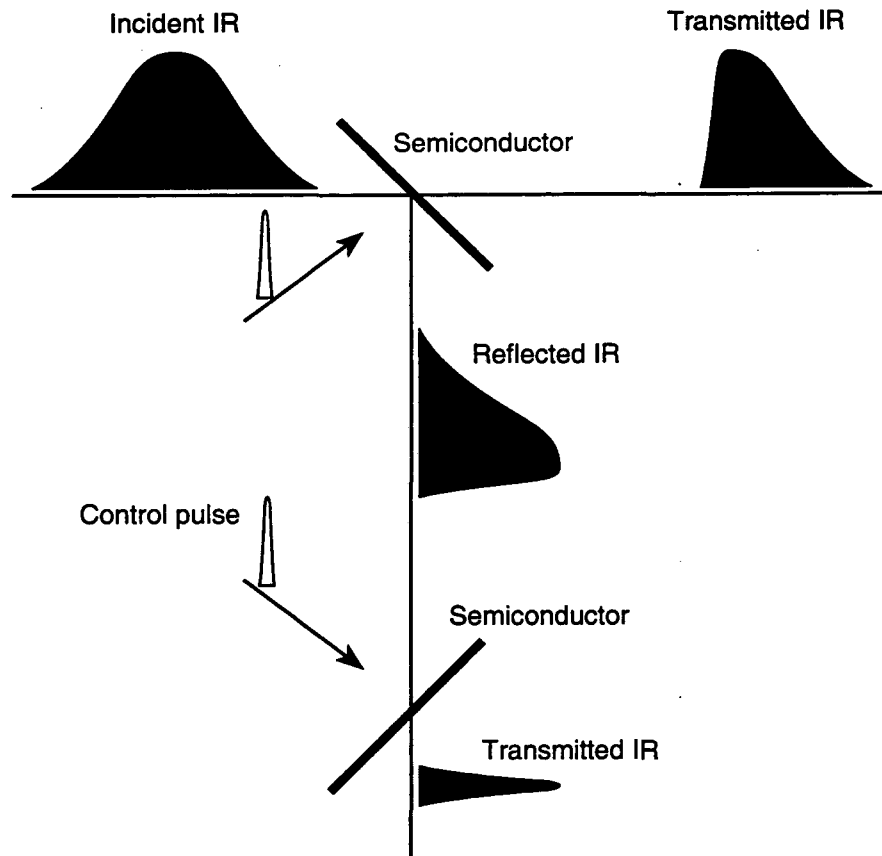The IRFEL output must propagate at least 30 meters to reach the experimental hall; then, depending on the location of the experiment, it must travel an additional 10–20 meters within the hall. To reach laboratories on the second level of the CDRL, the beam must cover yet another 50 meters. Since infrared beams are prone to significant diffraction, a suitable beam transport system must be provided to guide the beam for distances up to 100 meters, at the same time maintaining it at a reasonable size.

Since the diameter of the output-coupling hole is small compared with the mode size, the output can be approximated by an Airy pattern. This output will first be collimated. An image-relay system will then be used to transport the beam to the experimental hall.
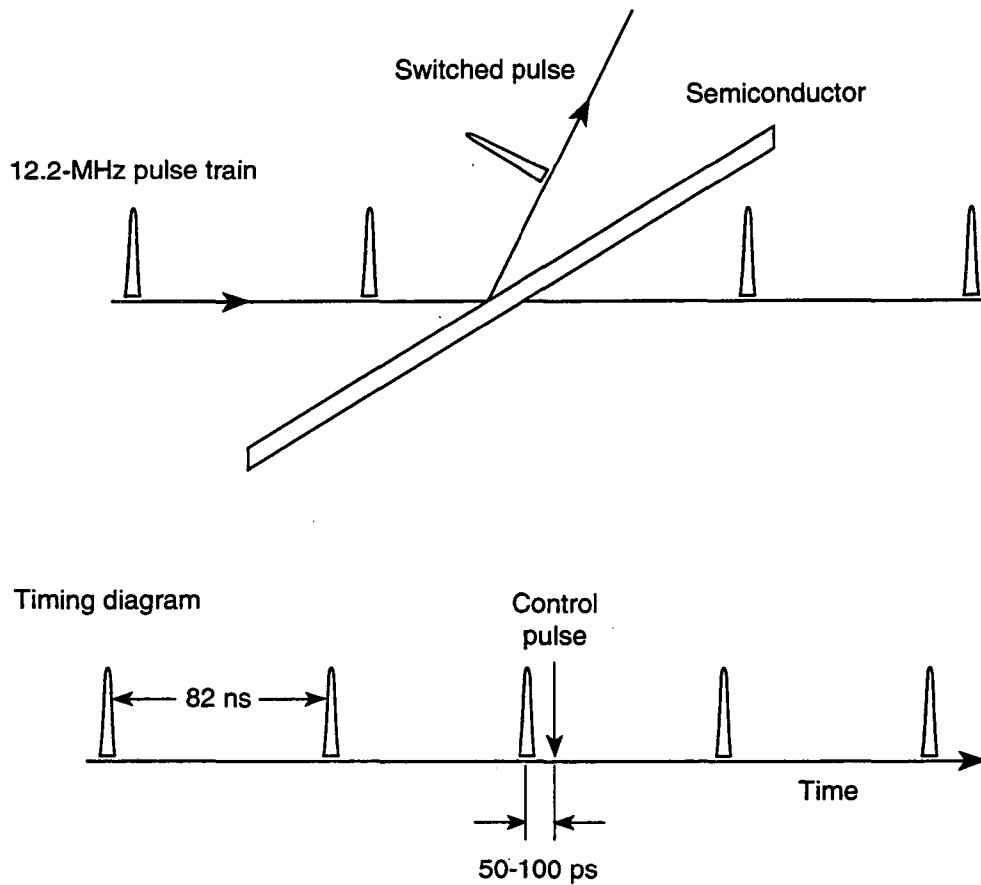
Figure 4-34. Schematic layout of a pulse picker based on a semiconductor switch.
[XBL 922-5619]

Figure 4-35 shows the optical arrangement of the transport system. Because of the fast divergence of beams at infrared wavelengths, image relaying is necessary to maintain the beam at a practical size. Two stages of relay imaging are required to cover 30 meters. From the entrance port in the experimental hall, another image relay system will be used to adjust the beam size and bring it to the experiment. Additional optics will relay the beam to the second level of the building.

For maximum flexibility, all transport optics are high-reflectivity, overcoated copper mirrors, similar in their specifications to the optical cavity mirrors. Reflective optics are used for the lens systems, shown in Fig. 4-36. Each system consists of two matched copper mirrors, separated such that the angle θ is less than 10°, to minimize astigmatism. In this arrangement, the effective focal length of the system is given by $f_{eff} \cong R/4$, where R is the radius of mirror curvature.

Many applications require that the beam-pointing fluctuations be less than 10% of the beam diameter. This dictates the overall stability requirement for the transport system. Angular stability (mechanical and temperature induced) must be better than 5″. Position sensors will be used to guide alignment of the beam through the transport system and to provide occasional long-term directional adjustments.
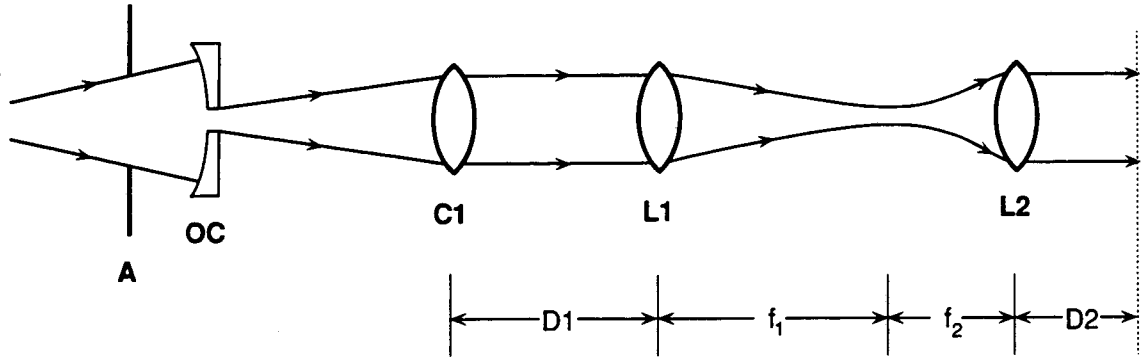
$$D2 = M(f_1 + f_2) - M^2 D1$$

$$M = f_2 / f_1$$

A = Aperture C1 = Collimator

OC = Output coupler L1 , L2 = Lens of focal length f_1 , f_2

Figure 4-35. Optical arrangement for the infrared beam transport system. [XCG 8912-4753]
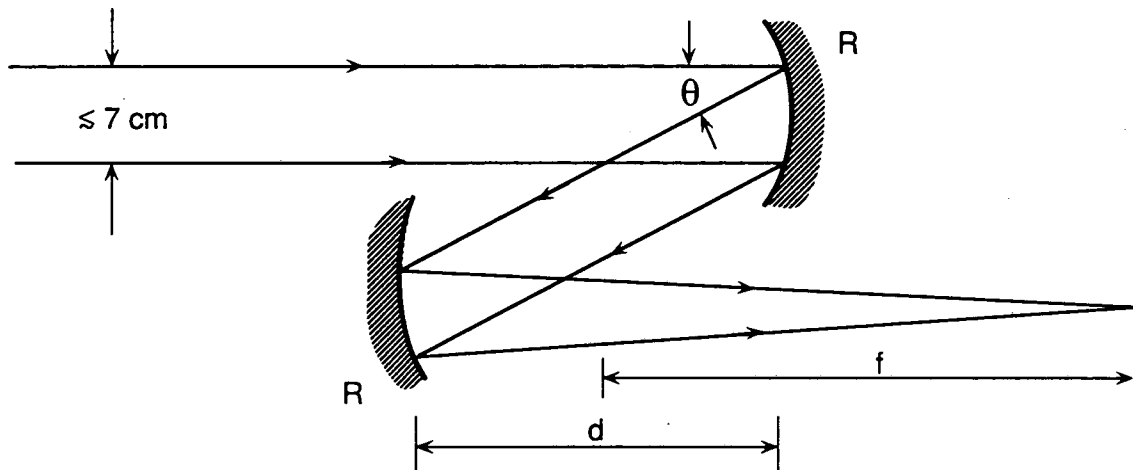
For f >> d, f ≅ R/4

Figure 4-36. Optical arrangement for the infrared beam lens system. [XCG 8912-4754]

The entire beam path will be evacuated to $<10^{-6}$ Torr to minimize absorption losses. A Brewster-angle exit window of an appropriate material (ZnSe for short wavelengths, KrS_5 or CsI for longer wavelengths) separates the transport system vacuum from the experimental apparatus.

5.

CONTROL SYSTEM

THE design of the computerized control system for the IRFEL, which is patterned closely after that of the ALS, provides a means of accessing all machine components so that their values can be set and monitored remotely. This is done by the operator through a console equipped with video displays and data input devices. To allow flexible control, a number of computer programs are provided to the operator. The status of machine devices is displayed, with graphics where appropriate, and software is provided for archival and subsequent retrieval of machine parameters. A typical start-up sequence for machine operation will involve recalling a set of machine parameters from the archives, making a few corrections to it (either by direct operator input or under program control), and sending it to the hardware devices.

The operator interface, comprising the console displays and controls, is structured to permit efficient operation. This requires that a number of different operational scenarios be accommodated. The experienced operator will require instant access, with a minimum of advice from the programs; for the beginning operator, a programmed path will be provided to ease the learning process. A number of programs are available that will provide computer models of the machine (for example, a program that calculates the behavior of a beam through a series of steering and focusing magnets). These make it possible to implement computer tuning, that is, tuning under program control, to make the beam parameters more closely approach the idealized model.

Normal day-to-day operation will require that a set of machine settings be given to the control system as a reference and that a set of tolerances be established on these data. The control system will then advise the operator of any values out of tolerance.

The control system design is based on a highly distributed, microprocessor-based architecture. In the days before the ALS, this approach was pioneered at LBL on the Uranium Beams Project at the Bevalac accelerator complex, and many of its underlying ideas (parallel processing, completely microprocessor-based architectures, distributed data base, bus-based systems, etc.) are now widely used—for example, in the control system of the LEP collider at CERN. The major benefits of such decentralized systems are improvement in system response, substantial simplification in programming, lower maintenance cost over the life of the accelerator, and the ability to adapt to future developments, both in hardware (processors, etc.) and in network technologies and topologies (Ethernet, Fiber Distributed Data Interface or FDDI, etc.).

The design philosophy for the control system is to have a reliable, fast, and user-friendly system, with complete capability for reporting all operating parameters, from initial commissioning through routine, day-to-day operation. All aspects of the linac and undulator will be controlled through a distributed system based on many high-performance microcomputers (using the Intel 80186, 80386, and 80486 microprocessors) operating in parallel. With this very flexible architecture, we can make careful trade-offs between hardware and software, thereby using technology effectively and holding software costs down. In addition, using a compatible family of processors will simplify the interface among the many parts of the system, further reducing software cost and complexity.

To facilitate the development of specialized auto-tuning or modeling applications software, workstations (the IBM PC/AT family and others familiar to accelerator physicists and operators) can be connected to the control system. This is assured by providing for an industry-standard network interface with high-speed access to the accelerator data base. Since these programs will be written mostly in high-level languages (BASIC, FORTRAN, PLM, C, and Pascal), they will be easy to integrate into the main part of the control system if even faster access and higher performance should be desired.

This transition is particularly simple if the workstations utilize Intel-based processors, as does the IBM PC family, since the processor used in the main part of the control system will be an Intel 80486. This microprocessor has the hardware-supported capability to run multiple operating systems simultaneously [MS DOS, UNIX (Xenix), or RMX, a real-time operating system]. Additional features carried forward include

- Local debugging capability

- High-level programming languages

- Homogeneous processor architecture throughout the system

- Ease of maintenance and repair

- Use of workstations

- Data-driven software capability

- Built-in help functions

Furthermore, it will be possible to utilize a substantial amount of existing software to minimize software development costs. The understanding of the processors, architectural features, and computer languages attained in the course of ALS commissioning and prior projects will lead to considerable cost savings and rapid commissioning.

5.1 SYSTEM ARCHITECTURE

The overall system architecture, shown in Fig. 5-1, consists of

- A large number of single-processor units (Intelligent Local Controllers, or ILCs, illustrated in Fig. 5-2).
- A central data base storage/collector (Collector Micro Module, or CMM, Fig. 5-3).
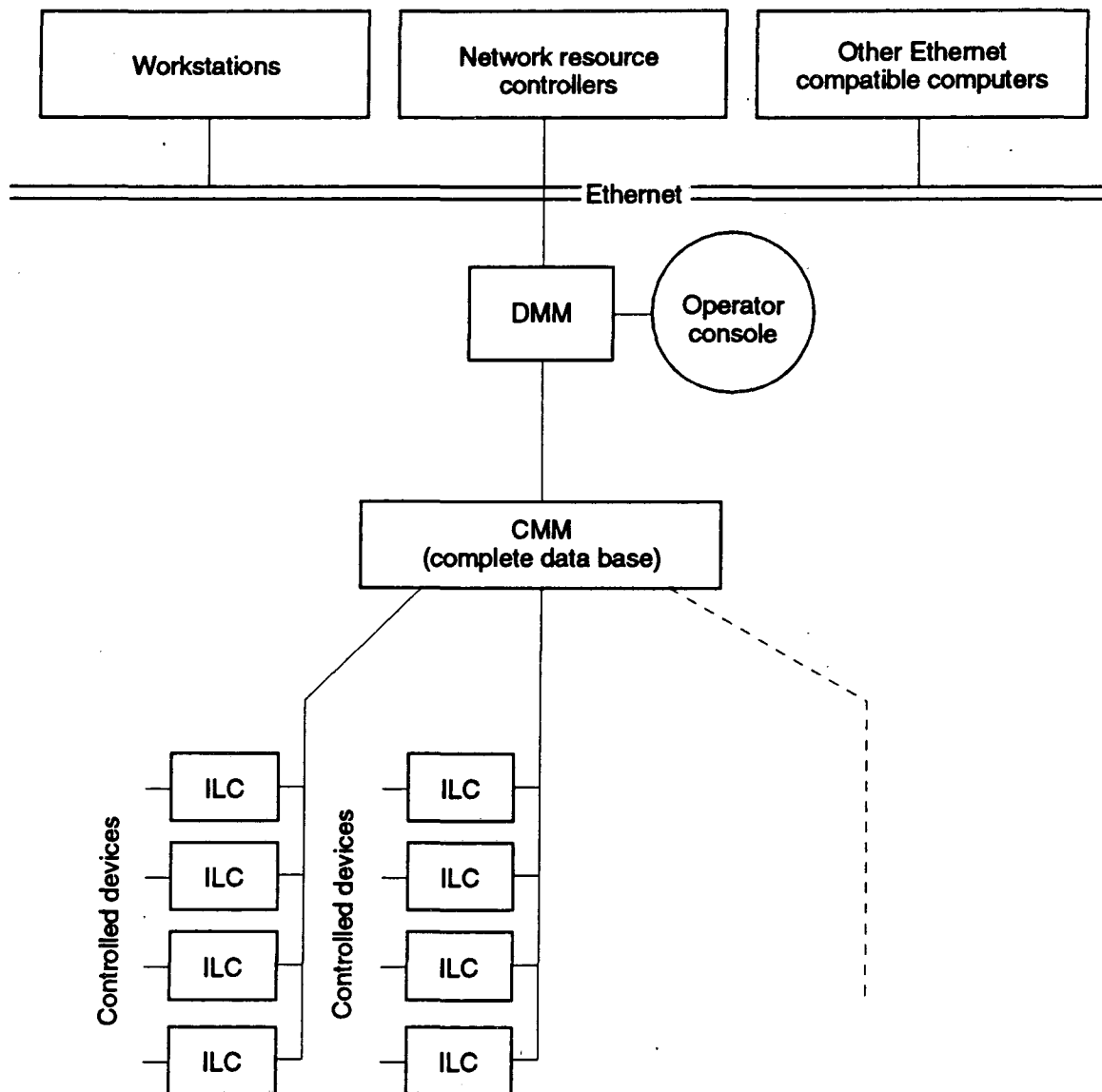- The operator display driver (Display Micro Module, or DMM, Fig. 5-4).

Figure 5-1. Block diagram of the overall control-system architecture. [XBL 902-5416]

```
┌─────────────────────────────────────────────────────────────┐
│  Single high Multibus II (Eurocard format, 3U) circuit board │
│                                                              │
│  ┌────────┐      ┌──────────┐      ┌──────────────┐          │      Serial link
│  │        │◄───► │ 64-KByte │◄───► │ Single-chip  │◄──────   │         to
│  │        │      │ dual port│      │ microcomputer│   ──────►│        CMM
│  │ 80186  │      │   RAM    │      │  (80C152)    │          │
│  │  CPU   │      └──────────┘      │ with on-chip │          │
│  │(16 MHz)│                        │serial interface          │
│  │        │                        │   2Mb/s     │          │
│  │        │      ┌──────────┐      └──────────────┘          │
│  │        │◄───► │ Interface│                                │
│  └────────┘      │  logic   │                                │
│                  │          │  ┌─────┬─────┬────────┐        │
│                  │          │  │     │     │Parallel │        │
│                  │          │  │     │     │  &      │        │
│                  │          │  │ ADC │ DAC │  bit    │        │
│                  └──────────┘  │     │     │ control │        │
│                                ├─────┴─────┴─────────┤        │
│                                │ Eurocard connector  │        │
│                                │        &            │        │
│                                │ accelerator equipment        │
│                                └─────────────────────┘        │
└─────────────────────────────────────────────────────────────┘
```
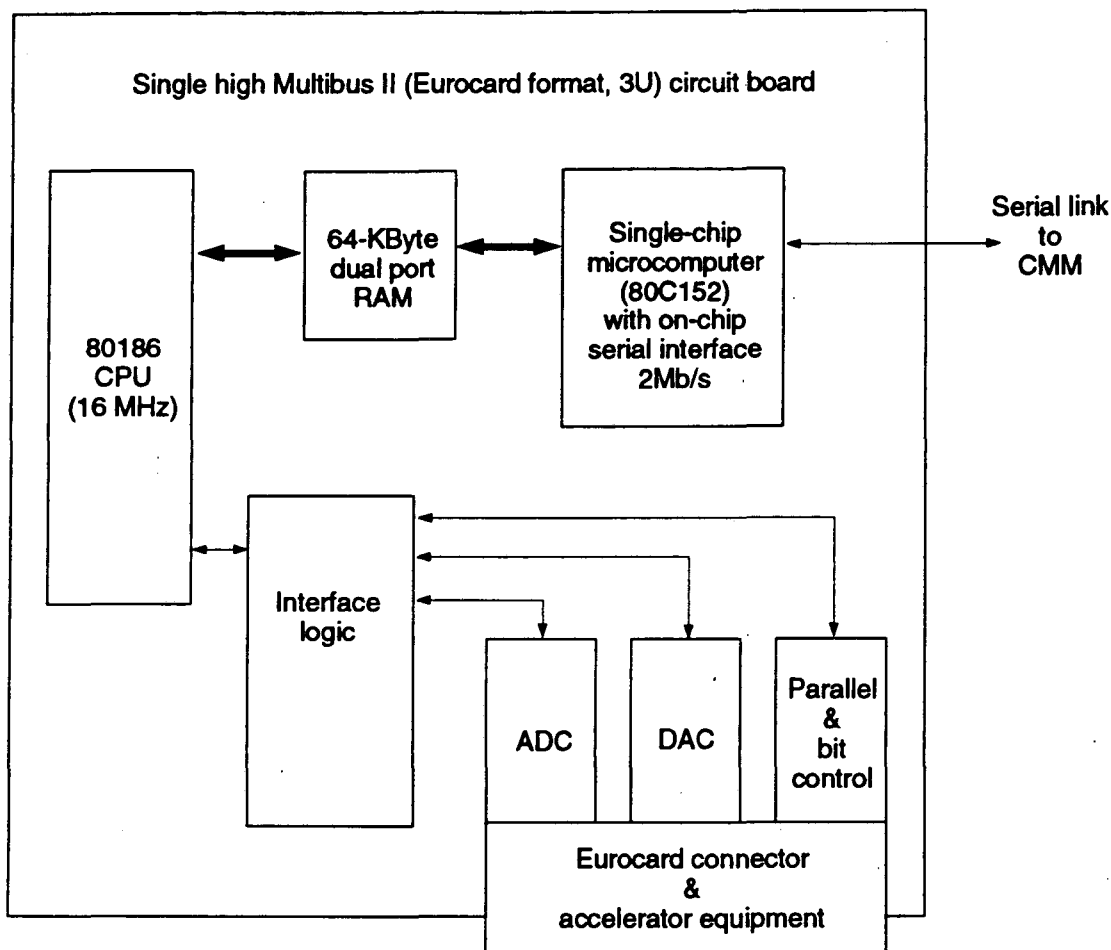
Figure 5-2. Block diagram of an Intelligent Local Controller (ILC). [XBL 902-5415]

The ILCs provide an interface to the accelerator equipment by collecting data and transmitting control instructions. They contain a local data base and reside near the accelerator hardware. A primary function of these units is to continually refresh the data stored in the central data base at the CMM.

The CMM collects the data from all the ILCs. Data are sent to and from the CMM over fiber-optic serial links at a rate of 2 Mb/s. These data are stored in dual-ported memory, so that a fresh copy of the local data bases resides at all times in the CMM.

The DMM services the operator console. Access to the accelerator data base that resides in the CMM is provided via a commercial Multibus-II to Multibus-I extension board. A word of data can be fetched in less than 1 μs. There is one DMM per operator console; each console consists of four operator stations.

An Ethernet or FDDI link connects the workstations, the network resource manager, and the DMMs. Commercial hardware is used to provide communications to and from a
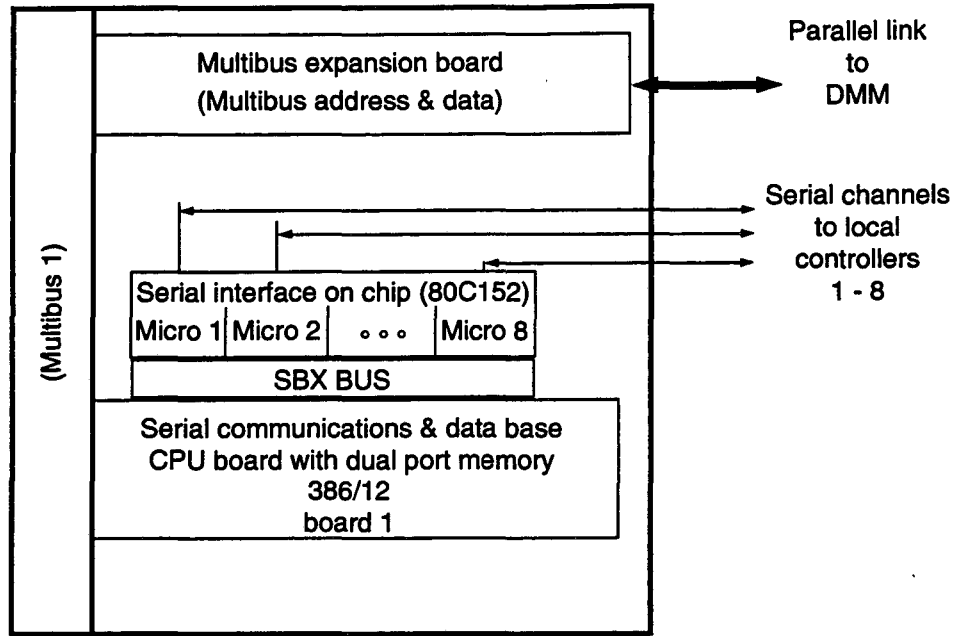
Figure 5-3. Block diagram of a Collector Micro Module (CMM). [XBL 902-5414]

file server/spooler, as well as data base entry and retrieval service between the accelerator and the various workstations and personal computers. The file server/spooler is used to record accelerator data, to log errors, to hold output data, to store applications software and the appropriate tools to aid in its development, and in general, to perform system file management. The workstations and personal computers are used for program development and problem diagnosis. The philosophy is to develop and test programs such as auto-tuning and modeling, with full access to the accelerator data base. Completed and debugged programs can then be installed for use by the operator.

The board-level computers in the control system are very powerful and can easily be augmented by board-level array processors for special functions (such as fast Fourier transforms). The Ethernet or MAP network also provides controlled experimenter access to appropriate control system parameters (such as undulator gap control) or beam-status information.
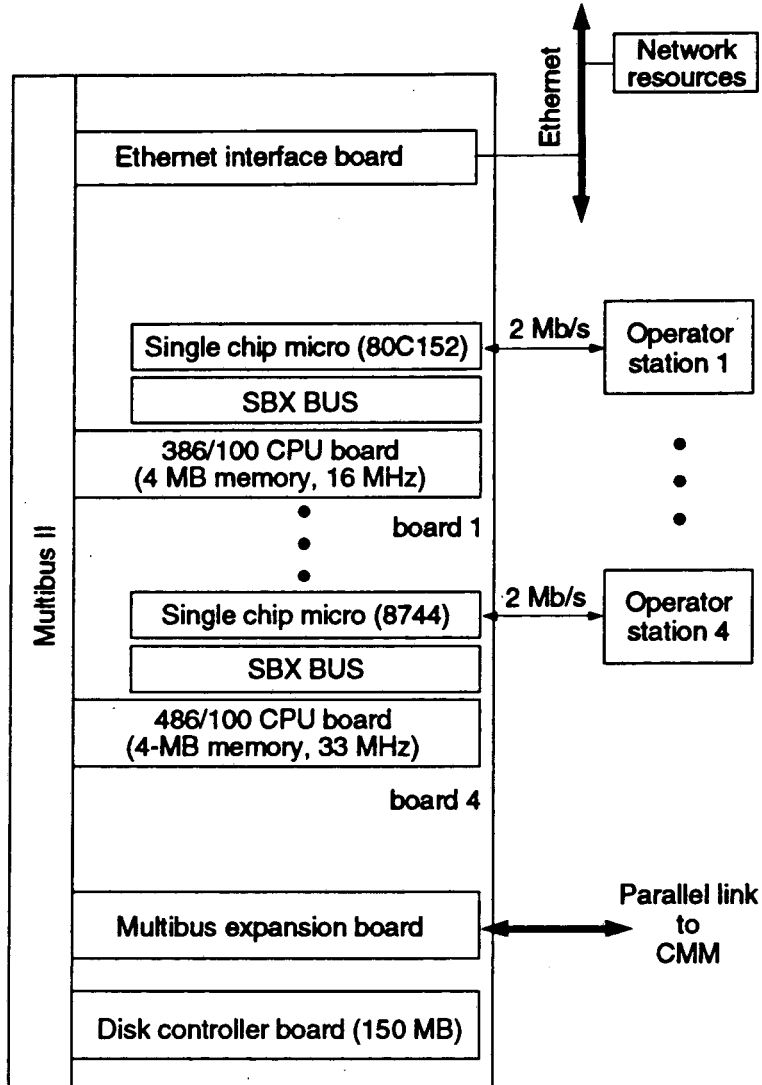
Figure 5-4. Block diagram of a Display Micro Module (DMM). [XBL 902-5417]

5.2 OPERATOR INTERFACE

Operator stations (see Fig. 5-5) provide the human interface to the control system. Each operator station is an 80486-based IBM PC with a high-resolution (1280 × 1024) 19-inch color monitor. For input there will be knob panels, keypads, and mice. The knob panel will have an LED display for each of the knobs (for labeling or display of values), and these displays can be updated under program control when scrolling or using the mouse. A console, made up of four operator stations, will also have space for oscilloscopes, network analyzers, and other instruments.

Operator stations are connected to the DMM by high-speed (2-Mb/s) serial lines; this unique feature of the system allows the placement of such stations almost anywhere in the vicinity of the machine (for instance, as a local control station for any of the major subsystems of the accelerator). The DMM incorporates one high-performance, 80486-based single-board computer (SBC) per station, thereby providing extremely fast (less than 0.1 s) response to operator input. The four SBCs (per DMM) share data and communicate via a commercial Multibus-II–based chassis. These microprocessors,
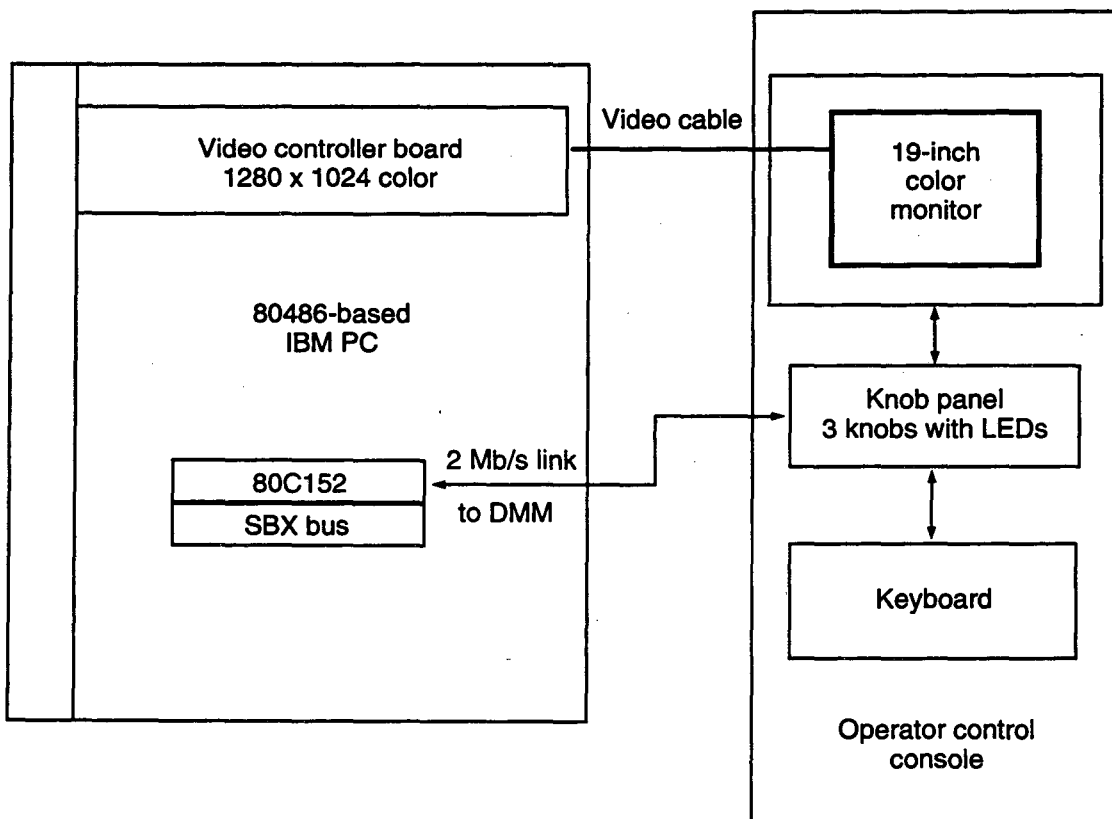

Figure 5-5. Block diagram of an operator control station. [XBL 902-5418]

operating in parallel, provide performance exceeding that of many super-minicomputers, at a very modest price. Each operator station PC contains a video board and an SBC; the latter does the serial communication with the DMM. The knob panel electronics (shown in Fig. 5-6) also contain single-chip microcomputers, so they, in turn, present only relatively high-level information to the operator station PC.

5.3 SUBSYSTEMS

The DMM has access to the data that describe the status of the machine via a Multibus-II to Multibus-1 extension into the CMM. The CMM collects data from the various ILCs and stores them in memory accessible to the DMM. The CMM sends to the ILCs any messages (new set points, etc.) generated by the DMM or the operator stations.

The ILCs monitor and control the operation of the machine. They are directly interfaced to the various components, and because they possess the computing power of a 16-bit minicomputer, they are capable of many control functions, such as monitoring interlocks, data acquisition, closed-loop control, data analysis, and error checking. Only data processed by these ILCs are sent to the CMM. The DMM, therefore, is not burdened with low-level signal-processing tasks. The ILCs control a single, or at the most a few, devices. A modified operator station or laptop computer can interface directly to the ILC links, thereby providing local control and testing. This is particularly useful during machine commissioning and for failure diagnosis (to isolate one chassis from another).

The justification for using many ILCs lies primarily in the complexity of the system. Each ILC deals mainly with one device (or one type of device), making it easy to provide additional computing and network capacity. This kind of power may be desirable during simultaneous ramping of a number of elements. Furthermore, it simplifies the programming task and can shift the software (for example, floating-point conversion,
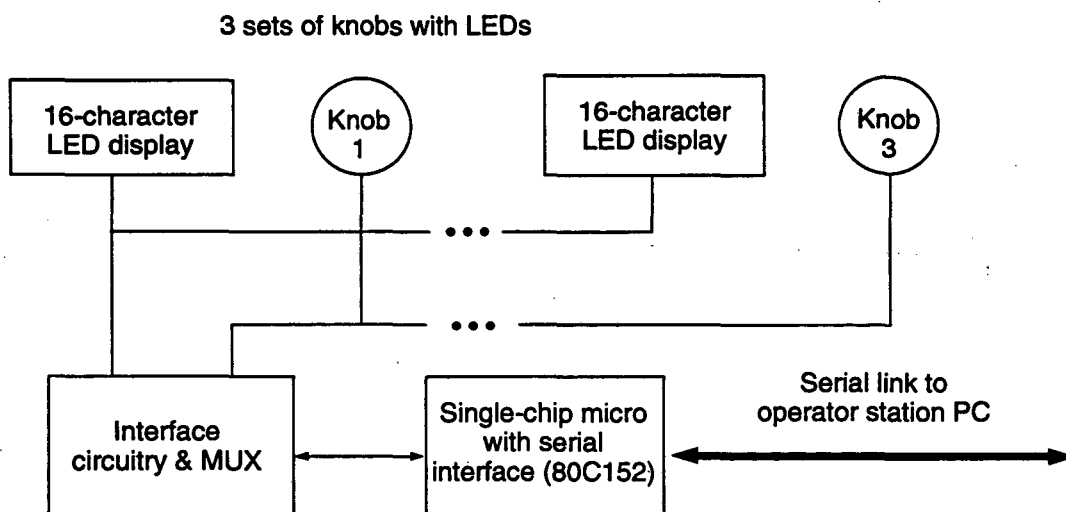

Figure 5-6. Block diagram of an intelligent knob panel. [XBL 902-5419]

error checking, or ADC/DAC processing) from the DMM to the ILC. The results are a reduction of DMM software, improved response to the operator, and simplified hardware maintenance.

The simplified system design allowed by the use of ILCs will be especially important during routine machine operation, when experts who built the control system may become less readily available. The use of ILCs also provides considerable flexibility for future expansion. If the data refresh rate needs to be increased, the number of ILCs on a link can be decreased to accommodate this improvement. Use of the ILC means that only relatively simple boards must be added to provide control functions, and that only a modest amount of software development effort would be required for such expansion.

6.

SAFETY AND QUALITY ASSURANCE

FROM a safety standpoint, the IRFEL presents no significant new problems. All of the potential hazards are ones that have been faced and solved during previous construction projects or experimental activities, at LBL or elsewhere. In all cases, measures have already been developed to protect the health and safety of workers and others, and to guarantee no adverse effects on the environment. In particular, the close association of the IRFEL with the ALS will allow us to take advantage of a number of safety systems that already exist.

6.1 RADIATION SAFETY

The design and operation of all facilities at LBL are governed by the ALARA (as low as reasonably achievable) policy. LBL has always maintained radiation dose limits well below those allowed by regulation.

The most important elements of radiation safety—well-designed radiation shielding, adequate beam dumps, and redundant beam-containment measures—have already been described. The shielding and the beam dumps are discussed in detail in section 3.7, and the diagnostics and interlock systems that serve to ensure adequate beam containment are described in section 3.4.

6.1.1 Personnel Protection System

The design philosophy behind the personnel protection system is that it must protect personnel from all plausible hazards related to the operation of the IRFEL. The primary hazards addressed are those associated with radiation, high voltage, high-stored-energy devices, and moving mechanical parts or assemblies. To achieve its aim, such a system must be fail-safe, redundant, self-checking, reliable, and simple.

Redundancy requires more than one level of checking and protection. The long history of safe operation at facilities with two levels of redundancy led us to adopt such a system for the IRFEL.

Self-checking means that any single system error or failure must be detected before other failures occur that might produce a hazardous situation. This requires that all individual circuits and chains be checked to determine whether they are reporting the same status. On the basis of this criterion, a simple, hard-wired electromechanical system was selected. The safety system uses the industry-standard 24-V dc control voltage and electromechanical relay logic, with complete redundancy (independently wired relay systems with parallel functions) and fail-safe features throughout. Microswitches are used to sense position (open or closed). When semiconductors are used in applications where a failure could render the system inoperative or result in a hazardous situation, the system is designed to fail in a safe condition.

Operational safety procedures specifying, in detail, the steps required for entry into controlled-access zones and the search sequence required for restarting the IRFEL will be prepared prior to operation. Appropriate review and approval procedures will be followed. Procedures for personnel access, interlock bypass, interlock testing, and calibration of radiation detectors will be similar to those used at the ALS, which served as the basis for the descriptions below.

Personnel Access. The radiation safety enclosure for the IRFEL is designed with one main access gate and one emergency exit gate. Each gate's position is sensed by redundant microswitches. During normal operation, access to the IRFEL vault is controlled by the control room. A two-way audio communications system, closed-circuit television camera system, "key tree," and lighted status sign are located adjacent to the main access gate. Access to the vault requires communications with and surveillance by the control room operator. Controlled access requires the following sequence of events:

1. The control room operator relinquishes control of the IRFEL by switching it to the safe mode.

2. Each person entering takes a key from the key tree.

3. The control room operator logs the access and releases the gate for entry.

4. As each person leaves the vault, his or her key is returned to the key tree. Once all personnel have left the vault and returned their keys, the control room operator may return the IRFEL to operational status.

"Crash-off/search" reset boxes are located inside the IRFEL vault, and the main access and emergency exit gates have emergency "crash-out/in" release mechanisms. Activation of a crash-off box or crash-out/in gate release inhibits operation of the IRFEL and requires a search of the IRFEL vault. The search procedure requires that a key from the control room be used in a prescribed manner, thus ensuring that a complete and thorough search-and-secure procedure is followed. The IRFEL can be operated only after the search is completed and the key returned to its key-switch cache in the control room.

Active radiation monitoring outside the IRFEL vault consists of x-ray and neutron detectors. Radiation detected above the allowable limits inhibits operation of the IRFEL.

Interlock Bypass Procedures. Procedures for bypassing radiation interlocks will be prepared in accordance with Chapter 21 ("Radiation Safety—Ionizing and Nonionizing") of the LBL *Health and Safety Manual* [1990]. Interlock bypass procedures will be

136

defined in the *IRFEL Operational Safety Procedures Manual* (OSP). Modifications made to a radiation interlock system (such as temporary defeat for testing) will be carefully documented, approved by authorized personnel, and removed when no longer needed. An interlock bypass must be approved by the second level of supervision. Only properly trained personnel will be allowed to install an interlock bypass. An interlock bypass will be documented on appropriate drawings and logged, and a notice of the installed bypass will be displayed in the control room. A notice of an installed bypass will also be displayed so that any person who normally relies on the bypassed interlock will be informed that a safety device has been disabled. Current LBL policy and practice require that all interlock bypasses be removed when no longer needed; if more than three days are needed to complete the task for which the bypass is installed, a permanent solution must be devised and implemented.

Interlock Testing. All radiation interlocks will be tested at intervals of not more than six months. The testing and maintenance schedule will be incorporated into the IRFEL OSP. Records of all testing will be maintained by the IRFEL Safety Officer. Failures will be reviewed by a safety committee, and any hazards that personnel may have been subjected to during the failure will be evaluated. All installations and alterations will be reviewed by a safety committee composed of qualified personnel. Access to system components will be restricted to personnel authorized to maintain the system.

Calibration of Radiation Monitoring Equipment. Calibration procedures for all radiation monitoring devices will be incorporated into the IRFEL OSP. All radiation monitoring equipment will be tested for calibration at intervals of three months by the IRFEL Safety Officer. Radiation monitoring devices not meeting specifications will be tagged and removed from service. Radiation monitoring equipment will be maintained by trained personnel. The IRFEL Safety Officer will retest and calibrate repaired radiation monitoring devices before returning them to service. Active test sources used for calibration will be handled and stored in accordance with current DOE regulations.

6.1.2 Radiation Safety Training

In accordance with the LBL *Health and Safety Manual* [1990], the implementation plan for DOE Order 5480.11 (Radiation Protection for Occupational Workers) includes appropriate radiation safety training for all regular LBL employees, participating guests, and visitors. All new employees must attend a health and safety orientation program within one month of employment; this program covers the fundamentals of radiation safety. In addition, those workers who might potentially receive a total occupational radiation dose greater than 100 mrem in one year are classified as radiation workers; as such, they are required to take additional radiation safety training and to demonstrate proficiency by passing an examination. Radiation workers are retrained every two years.

6.2 OTHER SAFETY ISSUES

6.2.1 Nonionizing Radiation

The IRFEL will generate radio-frequency radiation at several frequencies, including 499.65 MHz and its harmonics. Areas of potential exposure include the IRFEL vault, the room housing the klystrons, and adjacent areas. Personnel will not be allowed in the vault during operation, and the klystron room and adjacent areas will be surveyed for electric and magnetic fields during IRFEL operation. The American Conference of Governmental Industrial Hygienists threshold limit values (TLVs) will be adopted as the limits for personnel exposure. Engineering and administrative controls will be implemented as necessary to ensure that the TLVs are not exceeded. Periodic measurements will be made to confirm the adequacy of controls.

6.2.2 Confined Space

Areas identified by LBL's Environment, Health, and Safety Division as confined spaces will be governed by LBL Confined Space Entry Procedures. These existing measures ensure the safety of personnel working in confined areas.

6.2.3 Oxygen-Deficient Atmosphere

The superconducting cavities of the IRFEL require significant quantities of liquid nitrogen and helium. Oxygen-deficiency sensors and alarms will be installed in areas where a gas leak might decrease the atmospheric oxygen level to less than 19.5%. Oxygen-deficiency hazard (ODH) training will be provided for all personnel working in ODH areas. Access to such areas will be limited to ODH-trained personnel (or persons accompanied by such personnel).

6.2.4 Toxic Gases

Ozone and oxides of nitrogen are likely to be generated during IRFEL operation. Airborne concentrations of these gases will be measured in areas adjacent to the accelerator vault during operation and in the vault immediately after any shutdown. We anticipate that ozone levels within the vault will decrease to safe levels within five minutes. The American Conference of Governmental Industrial Hygienists TLVs will be adopted as the limits for personnel exposure. Engineering and administrative controls will be implemented if TLVs for toxic gases are exceeded.

6.2.5 Electrical Hazards

Electrical protection is achieved by scrupulous adherence to applicable standards, codes, and directives governing design, operation, and maintenance of electrical equipment,

including the *National Electric Code 1990* [NFPA, 1990] and the *Electrical Safety Requirements for Employee Workplaces* [NFPA, 1988]. All installation and maintenance of electrical equipment is checked by LBL Construction and Maintenance (C&M) supervisory personnel or electronic-maintenance-shop personnel. In addition, all installations and operations must be carried out in accordance with the latest edition of Chapter 8 of the LBL *Health and Safety Manual* [1990], which defines responsibilities of personnel, principles of safety procedure implementation, requirements for design and construction of equipment, and means of accident prevention.

Cabinet doors to high-voltage equipment will be interlocked to turn off circuits when doors are opened. Enclosures containing high-voltage equipment (600 V or higher) will be marked in accordance with *National Electric Code 1990* [NFPA, 1990], paragraph 370-52(e), "Danger High Voltage Keep Out." Enclosures containing lower-voltage equipment will have warning signs of a similar nature. Stored-energy devices such as capacitors will have automatic discharging devices. Grounding and bonding of electrical equipment cabinets and electromechanical devices, including magnet iron, and girder support assemblies, will be in accordance with the National Electric Code.

6.2.6 Fire and Earthquake Safety

Fire safety measures for the IRFEL and its associated systems have been incorporated into the design of the CDRL building itself, which has been classified within ordinary hazard group 3. In particular, the IRFEL control room, power supply room, and FEL vault will be protected by double-interlocked, preaction sprinkler systems.

Facilities associated with the IRFEL, as well as all shielding, will be designed to withstand a site-specific maximum credible earthquake on the nearby Hayward Fault, in accordance with special seismic criteria included in the LBL *Health and Safety Manual* [1990]. A third-party design review of the entire CDRL building will be carried out by a consulting structural engineer experienced in earthquake engineering.

6.3 CONSTRUCTION

Responsibility for monitoring various construction activities at LBL is delegated by line management to several organizations. Project line management will also designate Safety and Quality Assurance Officers who will oversee all aspects of the project. The Purchasing Department is responsible for business matters and thus ensures contractor compliance with administrative contractual requirements. For matters pertaining to conventional construction, Plant Engineering is responsible for quality assurance and for ensuring contractor compliance with contractual terms and conditions related to performance, schedule, and budget. Plant Engineering personnel serve as LBL management representatives for conventional construction activities and the Laboratory's primary contact with the contractor.

LBL's Environment, Health, and Safety (EH&S) Division has primary responsibility for monitoring safety compliance by the construction contractor. The Construction Safety Engineer assigned to EH&S's Occupational Safety Department ensures compliance with LBL, DOE, CAL/OSHA, OSHA, and other applicable safety

requirements. This individual's safety responsibilities are carried out in concert with LBL Plant Engineering, Purchasing, and line management; they include

- Apprising contractors of LBL and DOE safety criteria pertaining to the construction project.

- Requiring the contractor to submit a written Safety Plan.

- Conducting periodic inspections of contractor areas to evaluate the quality of the contractor's safety compliance program.

- Stopping contractor work when situations are noted that pose imminent danger.

- Obtaining contractor accident reports and compiling such information for reporting to DOE.

6.4 EMERGENCY PREPAREDNESS

LBL has developed a Master Emergency Plan and site-specific Building Emergency Plans, which, together, establish emergency procedures to be followed in the event of an earthquake, fire, chemical release, or other potentially hazardous occurrence. The emergency plans conform to DOE Orders and other health and safety code requirements. The CDRL building will have such a Building Emergency Plan that will address site-specific emergencies, the duties of Building Managers and the Building Emergency Team, utility shutdown procedures, evacuation routes, assembly areas, and the location of fire and first-aid equipment. Building Emergency Plans are tested at least annually.

6.5 ENVIRONMENTAL PROTECTION

Protection of the environment, employees, and the public is of paramount concern in all activities at LBL. Accordingly, the OSP for the CDRL will address all pertinent environmental protection laws, regulations, and standards, and all requirements in the LBL *Health and Safety Manual* [1990] relevant to environmental protection will be met, during both construction and operation of the IRFEL.

6.6 QUALITY ASSURANCE

LBL facility operations and research programs are governed by the quality assurance (QA) provisions of the *LBL Institutional Quality Assurance Program Plan* [LBL, 1988]. This plan requires each LBL programmatic division to develop plans and procedures to carry out LBL QA requirements. The Accelerator and Fusion Research Division (AFRD) has developed a divisional QA plan that describes how quality is assured in the conduct of its accelerator operations and research activities.

Typical QA procedures required by the AFRD plan for accelerator operations include

- Operator training.
- Operational checklists.
- Maintenance and periodic reviews of downtime logs to help identify causes of ineffective operation.
- Relevant documentation maintained and accessible at the site of the facility.
- Periodic updates and reviews of operator training procedures, operational checklists, and relevant documentation.
- Maintenance and periodic checks and recalibration of instrumentation to indicate clearly the status of the facility and the permissible range of critical operating parameters.
- Meetings to update operations schedules and to provide periodic emphasis on facility performance and efficiency.

REFERENCES

A. J. Alcock and P. B. Corkum, 1979, *Can. J. Phys.* **57**, 1280.

H. A. Baldis, N. H. Burnett, and M. C. Richardson, 1977, *Rev. Sci. Instrum.* **48**, 173.

P. Becla et al., 1992, to be published in *J. Vac. Science.*

S. Benson, 1991, *Nucl. Instrum. Methods* **A304**, 773.

S. V. Benson, 1985, *Diffractive Effects and Noise in Short Pulse Free-Electron Lasers,* Ph.D. dissertation, Department of Physics, Stanford University.

M. J. Berger and S. M. Seltzer, 1983, *Stopping Powers and Ranges of Electrons and Positrons,* National Bureau of Standards report NBSIR 82-2550-A, 2nd ed.

J. Bisognano et al., 1991, *High-Power UV and IR Free Electron Lasers Using the CEBAF Superconducting Accelerator,* CEBAF report.

C. A. Brau, 1990, *Free Electron Lasers* (Academic Press, Inc., New York).

R. Byrns, 1989, "Review of SC/RF Refrigerator Systems," in *Proceedings of the 4th Workshop on RF Superconductivity,* Tsukuba, Japan.

R. Byrns, H. Huibao, W.-D. Möller, 1991, "Cryogenic Distribution System (CDS) for Eight HERA Superconducting RF Cavity Cryostats," in *Proceedings of the 5th Workshop on RF Superconductivity,* Hamburg.

CESR-B: Conceptual Design for a B Factory Based on CESR, 1991, CESR report CLNS 91-1050.

H. Chaloupka et al., 1988, in *Proceedings of the European Particle Accelerator Conference,* Rome (World Scientific, Singapore).

Combustion Dynamics Facility Scientific Program Summary, 1990, Lawrence Berkeley Laboratory report PUB-5284 (published in collaboration with Sandia National Laboratories).

REFERENCES

Conceptual Design Report: Chemical Dynamics Research Laboratory, 1991, Lawrence Berkeley Laboratory report PUB-5293.

P. B. Corkum, 1983, *Opt. Lett.* **8**, 514.

R. DiGennaro and T. Swain, 1990, *Nucl. Instrum. Methods Phys. Res.* **A291**, 313.

A. G. Fox and T. Li, 1961, *Bell Systems Tech. J.* **40**, 453.

J. C. Frisch and J. A. Edighoffer, 1990, *Nucl. Instrum. Methods Phys. Res.* **A296**, 9.

J. C. Goldstein, 1984, *Proc. SPIE* **453**, 2.

W. M. Grossman and D. C. Quimby, 1984, *Proc. SPIE* **453**, 86.

Health and Safety Manual, 1990, Lawrence Berkeley Laboratory report PUB-3000, including revisions.

E. P. Ippen and C. V. Shank, 1975, *Appl. Phys. Lett.* **27**, 488.

T. M. Jenkins, 1979, *Nucl. Instrum. Methods* **159**, 265.

K.-J. Kim, 1991, *Phys. Rev. Lett.* **66**, 2746.

K.-J. Kim and M. Xie, 1991, *Nucl. Instrum. Methods* **A304**, 146.

K.-J. Kim et. al., 1991, *Nucl. Instrum. Methods* **A304**, 233.

B. M. Kincaid, 1985, *J. Opt. Soc. Am. B* **2**, 1294.

C. Kolmeder, W. Zinth, and W. Kaiser, 1979, *Optics Comm.* **30**, 453.

G. A. Krafft and J .J. Bisognano, 1987, in *Proceedings of the 1987 Particle Accelerator Conference*, IEEE Catalog No. 87CH2387-9, p. 1356.

G. A. Krafft and J. J. Bisognano, 1989, in *Proceedings of the 1989 Particle Accelerator Conference*, IEEE Catalog No. 89CH2669-0, p. 1256.

G. A. Krafft, S. Laubach, and J. J. Bisognano, to be published, "Calculating Beam Breakup in Superconducting Linear Accelerators."

G. A. Krafft, S. N. Simrock, and K. L. Mahoney, 1991, in *Proceedings of the 1990 Linac Conference*, Albuquerque, NM, Los Alamos National Laboratory report LA-12004-C (Conf).

G. A. Krafft and M. Xie, 1991, *Beam Breakup in a Superconducting IRFEL*, Lawrence Berkeley Laboratory ESG Tech Note 176.

S. Krishnagopal, M. Xie, K.-J. Kim, and A. Sessler, 1991, in *Proceedings of the 13th FEL Conference*, Albuquerque, NM.

N. M. Kroll, P. Morton, and M. N. Rosenbluth, 1981, *IEEE J. Quantum Electron.* **QE-17**, 1436.

N. H. Lazar et al., 1991, *Nucl. Instrum. Methods Phys. Res.* **A304**, 243.

LBL Institutional Quality Assurance Program Plan, 1988, Lawrence Berkeley Laboratory.

E. G. Loewen, M. Neviere, and D. Maystre, 1978, *J. Opt. Soc. Am.* **68**, 496.

G. T. Moore, 1988, *Nucl. Instrum. Methods* **A272**, 302.

NFPA, 1988, *Electrical Safety Requirements for Employee Workplaces* (National Fire Protection Association).

NFPA, 1990, *National Electric Code 1990* (National Fire Protection Association).

C. H. Rode and D. Proch, 1989, "Cryogenic Optimization of Cavity Systems," in *Proceedings of the 4th Workshop on RF Superconductivity*, Tsukuba, Japan.

A. E. Siegman, 1986, *Lasers* (Univ. Science Books, Mill Valley, CA).

A. E. Siegman, 1991, *Stable-Unstable Resonator Design for Wide-Tuning-Range Free Electron Lasers*, E. L. Ginzton Laboratory preprint, Stanford Univ.

S. N. Simrock et al., 1990, in *Proceedings of the Second European Particle Accelerator Conference*, Nice, France, p. 824.

C. K. Sinclair, 1987, in *Advanced Accelerator Concepts*, AIP Conf. Proc. No. 156 (American Institute of Physics, New York).

J. E. Sollid et al., 1989a, *Nucl. Instrum. Methods* **A285**, 147.

J. E. Sollid, D. W. Feldman, and R. W. Warren, 1989b, *Nucl. Instrum. Methods* **A285**, 153.

E. B. Szarmes, S. V. Benson, and J. M. J. Madey, 1990, *Nucl. Instrum. Methods* **A296**, 755.

T. M. Tran and J. Wurtele, 1989, *Comp. Phys. Comm.* **54**, 263.

J. Tuckmantel, 1991, "Worldwide Superconducting Cavity Performance Survey," in *Proceedings of the 1st Workshop on LEP Performance*, CERN report SL/91-26(DI).

REFERENCES

USDOE Order 5400.5, 1990, "Radiation Protection of the Public and the Environment," June 5, 1990, Chap. 2.

USDOE Order 5480.11, 1989, "Radiation Protection for Occupational Workers," July 20, 1989.

J. Van Sant et al., 1989, *A Conceptual Design for an Actively Cooled, High-Average-Power, Electron-Beam Absorber,* Lawrence Livermore National Laboratory report UCRL-100416.

D. R. Walz, J. Jurow, and E. L. Garwin, 1965, *IEEE Trans. Nucl. Sci.* **NS-12**(3), 867.

D. R. Walz and L. R. Lucas, 1969, *The Sphere Dump—A New Low-Cost High-Power Beam Dump Concept and a Catalytic Hydrogen-Oxygen Recombiner for Radioactive Water Systems,* SLAC report PUB-555.

D. R. Walz and E. J. Seppi, 1967, *Radiolysis and Hydrogen Evolution in the A-Beam Dump Radioactive Water System,* SLAC report TN-67-29.

R. W. Warren and J. C. Goldstein, 1988, *Nucl. Instrum. Methods* **A272**, 155.

R. W. Warren, J. C. Goldstein, and B. E. Newnam, 1986, *Nucl. Instrum. Methods* **A250**, 19.

R. W. Warren and B. D. McVey, 1987, *Nucl. Instrum. Methods* **A259**, 154.

F. Willeke and D. Proch, 1991, paper presented at the 5th Workshop on RF Superconductivity, Hamburg.

M. Xie and K.-J. Kim, 1991a, *Nucl. Instrum. Methods* **A304**, 792.

M. Xie and K.-J. Kim, 1991b, *Hole-Coupling Performance in the Presence of Asymmetric Modes and FEL Gain,* Lawrence Berkeley Laboratory report LBL-30672; to be published in *Nucl. Instrum. Methods.*